AN ABSTRACT OF THE DISSERTATION OF

Jianghui Du for the degree of Doctor of Philosophy in Ocean, Earth, and Atmospheric Sciences presented on June 6, 2019.

Title: The Global Overturning Circulation Since the Last Glacial Maximum Based on Marine Authigenic Neodymium Isotopes

Abstract approved:

_____

Alan C. Mix Brian A. Haley

The Global Overturning Circulation (GOC) is a major component of the global climate system. Understanding its behavior is pertinent to our prediction of climate change in the future. The lack of long-term observations of GOC in the modern instrumental era necessitates studies of GOC using paleoceanographic records. Of great interest to climate scientists is the history of GOC since the Last Glacial Maximum (LGM, ~22,000 years before present). This is because this period experiences the last major natural global warming event accompanied by an increase of atmospheric CO_2 comparable to that since the industrial revolution, and because this period was characterized by centennial to millennial scale abrupt climate transitions, making it a potential analog of the present human-induced global warming.

The neodymium isotope composition (ε_{Nd}) of authigenic phases in marine sediments has been used as a circulation proxy to reconstruct past change of GOC, but our incomplete understanding of the processes regulating the distribution of ε_{Nd} in the ocean has so far hampered the application of this proxy, such that there is not yet a globally consistent description of past GOC history using this tracer.

In this dissertation, I develop new methods to extract authigenic phases from marine sediments for ε_{Nd} analysis. The methods are designed specifically for sediments from the Pacific Ocean, which often contain disperse volcanic materials that usually cause significant contamination to extracted Nd when using existing methods developed for the other ocean regions. Using a suite of geochemical tools, I identify the sources of extracted Nd, and show that the methods are capable of extracting authigenic Fe-Mn oxyhydroxides with negligible contamination from detrital sediments including volcanic materials. However, when applying the methods to sediments from the Gulf of Alaska, I find that the authigenic ε_{Nd} from modern core top samples are consistent more positive than the local bottom water, suggesting that *in site* diagenesis of volcanic materials affects the ε_{Nd} of authigenic phases. Differences of ε_{Nd} between authigenic phases and bottom water are widespread in the global ocean, thus questioning the traditional assumption that authigenic phases passively record bottom water ε_{Nd}. I suggest that this difference is evidence that there exists a significant sedimentary source of Nd to the ocean, which is linked to the diagenesis of authigenic phases and detrital sediments. I propose a conceptual model to describe how authigenic phases acquire their ε_{Nd} signatures through interactions with bottom water, pore water and detrital sediments. The two key factors controlling the interactions are the benthic exposure time and the reactivity of detrital sediments. I show that this conceptual model is applicable to the distributions of seawater and authigenic ε_{Nd} in the Pacific Ocean.

With the new method and conceptual model, I generate two new authigenic ε_{Nd} records using cores from the Gulf of Alaska at intermediate and abyssal depths, and reconstruct the Pacific circulation since the LGM. I synthesize the existing Pacific authigenic ε_{Nd} records using a box model, in which I separate the non-conservative component from the preformed-conservative mixing component of ε_{Nd}. Using the non-conservative component of ε_{Nd}, I estimate the Pacific circulation rate, together with benthic radiocarbon (^{14}C) records from the same sites. The results show that the transport of Southern Ocean deep waters to the Pacific reduced to ~half of today in the LGM, but increased later in the Northern Hemisphere stadial events to ~2-fold of today during the deglaciation. The inferred circulation changes imply

accumulation of respired carbon in the glacial deep Pacific and its subsequent release during the deglaciation, supporting the conclusion that the Pacific circulation plays a key role in the global carbon cycle since the LGM.

Extending the conceptual model globally, I synthesize published authigenic ε_{Nd} records from the global ocean since the LGM. The dominant modes of variability in these records are extracted using Principal Component Analysis. The first Principal Component (PC1) is related to the LGM-Holocene difference of ε_{Nd}: the glacial deep ocean has consistently more positive ε_{Nd} than the Holocene, and the magnitude of this increase was highest in the subpolar North Atlantic, decreasing toward the Southern Ocean and further so in the Pacific and Indian Oceans. This change is interpreted as the result of an increase of the preformed ε_{Nd} of the deep water produced in the North Atlantic, linked to the southward shift of the deep water formation location in the LGM. The second Principal Component (PC2) is related to the abrupt changes during the Northern Hemisphere stadial events: in these events North Atlantic and North Pacific ε_{Nd} converge. This mode of change is interpreted to be the consequence of strengthening of Southern Ocean overturning circulation, which overcomes the effect of the reduction of North Atlantic overturning, leading to overall stronger overturning of the global deep ocean. The PC1 and PC2 related mechanism are quantified using a global ε_{Nd} box model. The reconstructed GOC since the LGM correlates to changes of atmospheric CO_2 and ocean heat transport, giving key evidence to the long-standing hypothesis that links GOC to these climate variables.

The Global Overturning Circulation Since the Last Glacial Maximum Based on Marine Authigenic Neodymium Isotopes

by
Jianghui Du

A DISSERTATION

submitted to

Oregon State University

in partial fulfillment of
the requirements for the
degree of

Doctor of Philosophy

Presented June 6, 2019
Commencement June 2019

Doctor of Philosophy dissertation of Jianghui Du presented on June 6, 2019

APPROVED:

Co-Major Professor, representing Ocean, Earth, and Atmospheric Sciences

Co-Major Professor, representing Ocean, Earth, and Atmospheric Sciences

Dean of the College of Earth, Ocean and Atmospheric Sciences

Dean of the Graduate School

I understand that my dissertation will become part of the permanent collection of Oregon State University libraries. My signature below authorizes release of my dissertation to any reader upon request.

Jianghui Du, Author

ACKNOWLEDGEMENTS

My research and this dissertation will not come to fruition without the support from my advisors Alan Mix and Brian Haley. Alan has taught me so much in doing research, from coding conceptual models to writing manuscripts for publication. His attention to details, insistence of scientific rigor and open-mindedness have inspired me to become a better scientist. Brian has taught me most of my lab skills, and in his infinite wisdom has goaded me toward better understanding of my research.

I also want to thank the other members on my committee, Andreas Schmittner, Clare Reimers, Staci Simonich and SueAnn Bottoms, for continuous support and guidance that lead to the completion of this dissertation.

The Keck lab has been my research home for the last four years, and I would not have survived the ever-lasting battle against the instruments without the help of my lab fellows. I am especially indebted to Andy Ungerer, Jesse Muratli and April Abbott for teaching me how to operate the instruments.

The stable isotope lab has been my secondary research home, where I am welcomed with desserts rather than acids. June Padman, Jennifer McKay and Andy Ross are the first friends I made when arriving at OSU and they have been sources of mental support ever since.

The QuatTea and OEB groups at CEOAS have helped shape my research ideas and provided mentorship and fellowship.

All my officemates and friends in Corvallis have assisted me through this journey, making my life in a foreign environment much more enjoyable.

To my mother and sister, who have supported without hesitation every single decision I have made in my life, I am forever grateful. How could I ever achieve anything without you?

CONTRIBUTION OF AUTHORS

Chapter 2. Brian Haley and Alan Mix assisted with study design and contributed substantially to the manuscript. Brian Haley also assisted with the Nd isotope analysis.

Chapter 3. Brian Haley and Alan Mix assisted with study design and contributed substantially to the manuscript. Brian Haley assisted with the Nd isotope analysis. Alan Mix assisted with the box model design. Maureen Walczak and Summer Praetorius assisted with the chronology and provided the radiocarbon data.

Chapter 4. Brian Haley and Alan Mix assisted with study design and contributed substantially to the manuscript. Alan Mix and Brian Haley also assisted with the data analysis and box model design.

TABLE OF CONTENTS

Page

TABLE OF CONTENTS (Continued)

Page

TABLE OF CONTENTS (Continued)

Page

TABLE OF CONTENTS (Continued)

Page

TABLE OF CONTENTS (Continued)

Page

LIST OF FIGURES

LIST OF FIGURES (Continued)

Figure Page

LIST OF APPENDIX FIGURES

Figure Page

LIST OF APPENDIX FIGURES (Continued)

Figure Page

LIST OF APPENDIX TABLES

Chapter 1: Introduction

Global Overturning Circulation

The modern Global Overturning Circulation (GOC) consists mainly of two interconnected overturning cells: the Atlantic Meridional Overturning Circulation (AMOC) and Southern Ocean Meridional Overturning Circulation (SOMOC) (Lumpkin & Speer 2007; Marshall & Speer 2012; Talley 2013) (Figure 1.1). AMOC occupies the Atlantic Ocean above ~3000 m. The upper limb of AMOC includes the northward flowing Antarctic Intermediate Water (AAIW) and various mode waters, which feed the production of North Atlantic Deep Water (NADW) in the Nordic-Labrador Seas. SOMOC occupies the abyssal Atlantic and the deep Pacific and Indian Oceans. The lower limb of SOMOC is linked to the production of Antarctic Bottom Water (AABW) around Antarctica, which flows northward into the northern basins. AABW transforms to lighter density deep waters mostly in the Pacific and Indian Oceans as the Pacific Deep Water (PDW) and Indian Deep Water (IDW), as well as in the Atlantic where it converts to NADW. The AMOC and SOMOC cells are intertwined. NADW, the lower limb of AMOC, and PDW and IDW, the upper limb of SOMOC, all return southward toward the surface around Antarctica, driven by westerly induced upwelling. These deep watermasses mix vigorously in the circumpolar circulation. The resulting mixture then feeds the upper limb of AMOC and the lower limb of SOMOC, completing the cycle of GOC.

A separate minor overturning cell exists in the modern North Pacific, linked to the formation of North Pacific Intermediate Water (NPIW) (Talley 2013) (Figure 1.1). Unlike the North Atlantic, there is no deep water formation in the North Pacific today because of low surface salinity (Emile-Geay et al. 2003; Warren 1983).

Role in Global Climate

GOC plays a fundamental role in the global climate system, regulating the movement of fresh water, heat and key biogeochemical compounds (such as carbon dioxide, oxygen and nutrients) among the ocean basins and between the ocean and atmosphere, on timescales ranging from decades to hundreds of thousands of years (Adkins 2013; Broecker 1991; Ganachaud & Wunsch 2000; Lozier et al. 2019; Talley

2013). Modern AMOC introduces a net northward heat flux in the Atlantic, which not only makes the North Atlantic and the surrounding continents warmer compared to elsewhere at similar latitudes, but also forces the Intertropical Convergence Zone to move to the north of the equator (Buckley & Marshall 2016). AMOC is also a principal conduit that links the deep ocean to the atmosphere. For example, through the formation of NADW, oxygen and carbon dioxide dissolved in cold polar surface water are brought to the ocean interior, a process known as ventilation (Sarmiento & Gruber 2013). This makes the North Atlantic a major sink of atmospheric carbon dioxide today (Takahashi et al. 2009). Southern Ocean is another place of deep water formation and therefore also important for ventilating the ocean interior. It is however different from the Atlantic because of the presence of large scale wind driven upwelling, such that the effect of ventilation is zoned: in the upwelling zone deep waters rich in respired carbon are brought to the surface, releasing carbon to the atmosphere, while the deep and intermediate water formation regions on the two sides of the upwelling zone act as a carbon sinks (Gray et al. 2018a).

The climate-GOC interaction is regarded as a leading mechanism explaining global climate changes in the past (Broecker 1998; Curry & Oppo 2005; Duplessy et al. 1988; Mix & Fairbanks 1985). For example, AMOC is sensitive to fresh water forcing in the subpolar North Atlantic, and reduction of AMOC is often cited as the principal cause of Northern Hemisphere cooling events such as the Greenland stadial events (Bond et al. 1997; Bond & Lotti 1995; Broecker 1998). Changes of ocean circulation is also suggested to affect the ocean carbon storage and therefore atmospheric CO_2, thus contributing as a major feedback mechanism in the global carbon cycle (Anderson et al. 2009).

The ongoing global warming due to anthropogenic perturbation is also expected to elicit responses from GOC (Stocker et al. 2013), which would have significant impacts on human society. It is estimated that ~90% of the excess heat in the climate system since the 1970s has been absorbed by the ocean, causing widespread ocean warming that reaches the deepest part of the ocean (Talley et al. 2016). Such anthropogenic warming signals are transmitted from the surface to the

deep ocean mainly through the formation of NADW and AABW (Kostov et al. 2014; Talley et al. 2016). Slowdown of both AMOC and SOMOC in recent decades has been linked to global warming, the effect of which is expected to intensify in the future (Caesar et al. 2018; Talley et al. 2016). Further, carbon sinks associated with the formation of NADW and AAIW are responsible for the ocean's ability of storing of ~30% to 50% of the anthropogenic carbon produced since the industrial revolution (DeVries et al. 2017; Sabine et al. 2004; Talley et al. 2016). The variability of these sinks, however, depends on the climate−GOC feedback and is not well known (DeVries et al. 2017; Landschützer et al. 2015). Understanding the variabilities of GOC and the underlying causes are thus critical if we are to successfully predict climate change in the future.

This aspiration, however, has been hampered by the lack of a consistent documentation of the history of GOC in the recent past. Direct observations of AMOC has only existed since the early 2000s, and considerable more time is necessary for the anthropogenic influence to emerge out of the background of natural variability in the observations (Lozier et al. 2019). And there is no direct observations of SOMOC to date, such that most of our knowledge of its change comes from data inversion using repeated hydrographic lines (Talley et al. 2016). Further, state-of-the-art climate models also differ substantially in their projections of AMOC and SOMOC (Kostov et al. 2014; Meijers 2014), indicating that our understanding of the physics of the circulation remains incomplete.

GOC in the Past

To understand the behavior of GOC on longer timescales and to test implementation of ocean circulation physics in climate models, oceanographers and climatologists often turn to the period since the Last Glacial Maximum (~23,000 to 19,000 years before present) (Masson-Delmotte et al. 2013; Mix et al. 2001; Rahmstorf & Feulner 2013; Schmittner et al. 2011; Waelbroeck et al. 2009). This period saw the last major natural global warming (~3.5^{o}C) predating the current human-induced warming, and an increase of atmospheric CO_2 concentrations (~80

ppm) comparable to that since the industrial revolution (Marcott et al. 2014; Shakun et al. 2012). This period was also marked by centennial to millennial-scale abrupt climate transitions, for example the Heinrich Stadial 1 (HS1, 15,000~17,000 years before present) and the Younger Dryas (YD, 11,500~13,000 years before present) cooling events in the Northern Hemisphere (Shakun et al. 2012). Such abrupt climate change events are hypothesized to be the results of the internal instability of the global climate system, especially that of GOC (Broecker 1998; Shakun et al. 2012), and they are thought to hold clues to the "tipping points" of the global climate system relevant for predicting future climate change (Praetorius & Mix 2014). To establish the history of GOC during these events are thus of great interest, especially because they are also linked to abrupt changes of atmospheric CO_2 concentration (Marcott et al. 2014).

However, reconstructing GOC history since the LGM has been proven challenging. Interpretations of geochemical proxies of ocean circulation often leads to inconsistent conclusions regarding GOC (Curry & Oppo 2005; Gebbie 2014; Lund et al. 2011; McManus et al. 2004; Negre et al. 2010; Oppo et al. 2018; Roberts et al. 2010). Climate models similarly produce conflicting arrays of GOC behaviors (Amrhein et al. 2018; Kurahashi-Nakamura et al. 2017; Menviel et al. 2016; Muglia et al. 2018; Muglia & Schmittner 2015; Otto-Bliesner et al. 2007). One most debated issue is that how much the relative mixing proportions of deep waters produced in the North Atlantic, also known as the Northern Source Water (NSW), and the Southern Ocean, also known as the Southern Source Water (SSW), have changes since the LGM, and previous studies have suggested anywhere between <50% ~ 100% NSW in the deep North Atlantic in the LGM (Amrhein et al. 2018; Duplessy et al. 1988; Gebbie 2014; Kurahashi-Nakamura et al. 2017; Lang et al. 2016; Oppo et al. 2018; Sarnthein et al. 1994). Closely related is the question of depth of the boundary between AMOC and SOMOC, the existing answers to which range from shoaling by ~500 m to deepening by ~500 m (Amrhein et al. 2018; Ferrari et al. 2014; Jansen 2017; Muglia & Schmittner 2015; Otto-Bliesner et al. 2007). In some studies, AMOC and SOMOC are assumed to respond oppositely to climate change, yet in others it is

necessary for them to move in the same direction to explain paleo−circulation records (Menviel et al. 2014, 2016). Studies on the deglacial circulation are also inconclusive. It is unclear that whether AMOC completely ceases in HS1 (McManus et al. 2004), or weakened but still persistent (Bradtmiller et al. 2014). The sign of the change of Pacific circulation during the deglaciation is subject to even greater uncertainty (Broecker et al. 2004, 2008; Davies-Walczak et al. 2014; Lund 2013; Lund et al. 2011; Marchitto et al. 2007; Okazaki et al. 2010; Sikes et al. 2000).

A common cause for such controversies is that interpretations of geochemical proxies often focus on some selected aspects of the circulation while ignoring others. For example, benthic stable carbon isotope ($\delta^{13}C$) is classically interpreted from the perspective of binary NSW−SSW mixing (Oppo & Fairbanks 1987), without considering changes of the preformed $\delta^{13}C$ linked to air-sea exchange (Lynch-Stieglitz et al. 2019; Mix & Fairbanks 1985) and the non-conservative effect due to remineralization (Gebbie 2014); benthic radiocarbon ($\Delta^{14}C$), on the other hand, is often only related to circulation rate while neglecting the effects of watermass mixing and surface reservoir ages (Skinner et al. 2010; Zhao Ning et al. 2018); $^{231}Pa/^{230}Th$ may be affected more by scavenging than circulation strength (Lippold et al. 2012). To resolve ambiguity, it is necessary to analyze how circulation affects tracer distribution from a comprehensive perspective (Gebbie 2014).

Another reason for such controversies is the lack of a global perspective of circulation. Paleoceanography has historically been dominated by studies of the North Atlantic, leading to the thought that most of the climate change events were driven by changes of the North Atlantic circulation. Circulation of the other major ocean basins, most importantly the Southern Ocean and the Pacific Ocean, is understudied. This is problematic for at least two reasons. First, the Pacific has the largest ocean volume and the largest respired carbon reservoir, and it is directly ventilated by deep waters formed in the Southern Ocean, thus making the Pacific-Southern Ocean link critical in regulating the global carbon cycle (Broecker et al. 2004). Second, GOC exists not only because of deep water formation in polar regions of the North Atlantic, but also because of wind-drive upwelling and diffusive transport that brings deep water back

to the surface (Ferrari 2014). Southern Ocean is now known as the key place where deep waters upwell to the surface driven by the westerlies (Marshall & Speer 2012). It has also been shown that diapycnal transformations of dense deep water to lighter density class waters happen mostly in the Pacific (de Lavergne et al. 2017; Talley 2013). That is, watermass transformations in the Southern Ocean and Pacific are essential to the persistence of GOC. Thus, only by analysing global datasets of circulation tracers it is possible to faithfully reconstruct GOC.

Marine Authigenic Neodymium Isotopes

Studying ocean circulation in the past requires "proxies" or "tracers". In this dissertation my discussion is restricted to geochemical proxies of circulation. Ocean circulation is a key factor controlling the distributions of elements and isotopes that have average ocean residence times comparable to the ocean circulation timescales (~100~1,000 years). If such elements and isotopes are preserved in datable archives such as marine sediments, by measuring their global distributions we will be able to infer ocean circulation in the past.

The most commonly used circulation tracers include benthic $\delta^{13}C$, ^{14}C, sedimentary $^{231}Pa/^{230}Th$ and authigenic neodymium (Nd) isotopes ($^{143}Nd/^{144}Nd$). Authigenic neodymium isotopes are the focus of this dissertation for two reasons. First, unlike the other tracers, neodymium isotopes are not sensitive to biological fractionation in normal open ocean conditions, which reduces the compounding factors when used to infer circulation changes (Frank 2002; Goldstein & Hemming 2003). Second, our understanding of the modern marine Nd cycle has changes significantly in recent years, and the interpretive framework of ε_{Nd} in paleoceanography needs to be revised accordingly (Abbott et al. 2015a,b; Haley et al. 2017).

Neodymium isotopic composition is commonly expressed in the ε-notation: $\varepsilon_{Nd} = (^{143}Nd/^{144}Nd_{sample}/^{143}Nd/^{144}Nd_{CHUR} - 1) \times 10^4$, where $^{143}Nd/^{144}Nd_{CHUR} = 0.512638$ (if $^{146}Nd/^{144}Nd$ is normalized to 0.7219) is the Nd isotope composition of the Chondritic Uniform Reservoir, which is representative of that of the Bulk Silicate

Earth (Jacobsen & Wasserburg 1980). ^{143}Nd is a radiogenic isotope produced by the α−decay of ^{147}Sm, the half-life of which is 1.06×10^{11} years (Goldstein & Hemming 2003). Because Nd is more incompatible and therefore more enriched in the crust than Sm, the mantle has a higher Sm/Nd ratio than the crust, which leads to a higher $^{143}Nd/^{144}Nd$ and more positive ε_{Nd} of the mantle than the crust (White 2015). The ε_{Nd} of a rock is a function of the initial Sm/Nd ratio and the age of the rock. For example, the ε_{Nd} of volcanic rocks produced in recent geological history are generally in the range of 0 ε to +10 ε. The ε_{Nd} of continental rocks are generally negative, and it decreases with increasing age. Precambrian continental crusts are among the most unradiogenic (i.e. more negative ε_{Nd}) materials, with ε_{Nd} as low as <−30 ε (Jeandel et al. 2007).

Traditional Paradigm

In the traditional paradigm of explaining the distribution of ε_{Nd} in seawater, it is assumed that Nd is principally introduced to the ocean by river runoff with a small contribution from dissolution of atmospheric dust in the surface ocean (Frank 2002; Goldstein & Hemming 2003; Goldstein & Jacobsen 1987). It is further assumed that the ε_{Nd} of dissolved river water is the same as that of the weathering rocks. Thus, surface seawater ε_{Nd} reflects the geological background of the surrounding continents, and ocean circulation brings such local surface ε_{Nd} signatures to the deep ocean. In this paradigm, NADW is the most negative ε_{Nd} end member (~ −13 ε) in the global deep ocean, because of weathering input from the old surrounding continents, especially that of the Precambrian North American Shield. In contrast, PDW is as the most positive ε_{Nd} end member (~ −4 ε), because of volcanic inputs from the Pacific "ring of fire". The ε_{Nd} of the rest of the global deep water are simply considered a conservative mixture of these two end members (von Blanckenburg 1999), for example the intermediate values of the Southern Ocean waters (~ −8 ε for AAIW and AABW).

To apply ε_{Nd} in paleoceanography, suitable archives are needed. Two major authigenic archives are commonly used: Fe-Mn oxyhydroxides, either as "coatings"

on foraminiferal shells or dispersed in sediments or in the form of manganese nodules; Ca-hydroxy-fluorapatite, such as fish debris (Frank 2002; Goldstein & Hemming 2003; Tachikawa et al. 2017). These archives are assumed to passively record bottom water ε_{Nd}. With the assumption of strict conservativeness and fixed isotopic end members, measurements of authigenic ε_{Nd} down core are used to derive the mixing proportions of deep watermasses, similar to $\delta^{13}C$. For example, more positive ε_{Nd} in the deep Atlantic in the LGM is often cited as evidence of reduced NSW/SSW mixing ratio (Piotrowski et al. 2005; Rutberg et al. 2000a).

Recent advance

Even as the aforementioned paradigm is widely adopted by the paleoceanography community, one fundamental issue of marine Nd cycle remains unresolved and challenges the assumptions adopted in this paradigm. This issue is commonly referred to as the "Nd paradox" (Goldstein & Hemming 2003). In brief, it can be described as the discrepancy between the Nd residence times inferred from Nd concentration versus that of ε_{Nd}. Assuming that river input and atmospheric dust are the main sources of marine Nd, the estimated Nd residence time is much longer than 1000 years, yet the inter-basinal differences of ε_{Nd} implies that the Nd residence time must be shorter than the ocean circulation timescale (~1000 years) otherwise a more homogeneous distribution of ε_{Nd} is expected (Bertram & Elderfield 1993; Jeandel et al. 1995; Tachikawa et al. 2003).

This imbalance of budget indicates significant sources of Nd, apart from the known dissolved river flux and atmospheric input, were not identified. Jeandel and colleagues proposed the "boundary exchange" hypothesis, which suggests that the budget imbalance can be resolved by imposing exchange fluxes of Nd between seawater and sediments on the continental margins, and subsequent modeling studies suggest that the sedimentary Nd source can account for ~90% of the total external Nd sources to the ocean (Arsouze et al. 2007, 2010; Lacan & Jeandel 2005a; Tachikawa et al. 2003). However, "boundary exchange" remains an umbrella term for yet unidentified geochemical processes.

In recent years, new measurements of pore water Nd concentrations and ε_{Nd} suggest a net sedimentary flux of Nd from marine sediments capable of altering bottom water ε_{Nd} (Abbott 2019; Abbott et al. 2015a,b), supporting earlier studies (German & Elderfield 1989; Haley et al. 2004; Haley & Klinkhammer 2003). Crucially, these measurements show that sedimentary Nd flux is not limited to the margins as proposed by the boundary exchange hypothesis, but extend to deep sea sediments. These recent advances therefore require a revision to the global marine Nd budget, such that Nd is introduced to the ocean dominantly at sediment-water interface, rather than at the surface ocean. This revision thus questions the fundamental hypothesis that the traditional interpretations of paleo- ε_{Nd} rest on.

Parallel to the recent seawater and pore water ε_{Nd} studies, process studies on how authigenic phases acquire their ε_{Nd} signatures challenge the assumption that authigenic phases passively record bottom water ε_{Nd}. For example, studies show that both foraminifera and fish debris acquire Nd predominantly after deposition in sediments rather than in the water column (Roberts et al. 2012; Tachikawa et al. 2013, 2014), that is these archives most likely record pore water, rather than seawater ε_{Nd} (Abbott et al. 2016; Martin & Haley 2000; Palmer 1985; Palmer & Elderfield 1985, 1986; Toyoda & Tokonami 1990). Since there is no reason to believe *a priori* that pore water and bottom water should have the same ε_{Nd} (Abbott et al. 2015a), this raises two question: (1) do authigenic phases, which are formed in sediment through interaction with pore water, simply record the bottom water ε_{Nd}, or the diagenesis of authigenic phases supports high Nd concentrations in pore water and therefore controls bottom water ε_{Nd} through benthic flux? (2) Is the difference between the ε_{Nd} of extracted authigenic phases and bottom water due to detrital contamination because of unsuitable extraction methods, as is traditionally assumed, or is this difference created *in situ* in sediments and evidence of the sedimentary source?

Increasing numbers of recently published modern seawater and paleo-authigenic ε_{Nd} data are difficult to be reconciled with the traditional interpretation. For example, whole water column ε_{Nd} from the Bay of Bengal and Panama Basin vary on seasonal timescale, which cannot be explained by watermass mixing but

rather requires rapid changes of Nd sources (Grasse et al. 2017; Yu et al. 2017); paleo-records from the deep North Atlantic show than authigenic phase can acquire ε_{Nd} signatures far exceeding the range of modern seawater, explaining which solely by watermass mixing is difficult (Böhm et al. 2015); it is also shown that in regions of rapidly varying detrital composition, changes of authigenic ε_{Nd} may correlate to detrital ε_{Nd} instead of watermass ε_{Nd} (Blaser et al. 2019). Collectively, recent studies challenge the traditional paradigm that authigenic ε_{Nd} can be largely interpreted from the perspective of conservative watermass mixing.

Dissertation Outline

The motives of this dissertation are twofold. First, I will provide a new interpretive framework of using authigenic ε_{Nd} to study ocean circulation, incorporating the recent advances discussed above. Second, with this new framework, I will analyze new and published authigenic ε_{Nd} records from the global ocean to reconstruct GOC since the LGM, aiming to resolve the inconsistency among tracer reconstructions.

In chapter 2, I examine how authigenic phases in marine sediments acquire their ε_{Nd} signatures, and how this signature is related to that of bottom water, pore water and detrital sediments. The aim is to elucidate what is the effect of sedimentary source on seawater and authigenic ε_{Nd}, which will provide the basis for the new interpretive framework of using ε_{Nd} to reconstruct ocean circulation in paleoceanography. To do so, I first developed a new method of extracting sedimentary authigenic phases for ε_{Nd} analysis that avoids detrital contamination. I tested the method on a collection of core top sediment samples from the Gulf of Alaska (GOA) and assessed sources of leachate Nd, including potential contamination from trace dispersed volcanic ash. I show that authigenic Fe-Mn oxyhydroxide is the dominant phase extracted using this method, and contamination due to detrital sources, including volcanic ash, is negligible. Comparing the extracted core-top authigenic ε_{Nd} to local seawater ε_{Nd} then allows me to establish the link between bottom water and authigenic ε_{Nd}, and the sedimentary influence on both. I

find that the ε_{Nd} of core-top leachates in the GOA is consistently more positive than bottom water. I infer that authigenic phases record pore water ε_{Nd}, and the relationships of ε_{Nd} among bottom waters, pore waters, authigenic phases and detrital sediments are primarily governed by the exposure time of bottom water to sea-floor sediments, rate of exchange across the sediment-water interface and the reactivity and composition of detrital sediments. Consistent with Abbott and colleagues (Abbott 2019; Abbott et al. 2015a,b, 2016), I suggest that sedimentary sources control the distribution of both bottom water and authigenic ε_{Nd}, and propose a new interpretive framework of linking authigenic ε_{Nd} to ocean circulation.

In chapter 3, with the new interpretive framework developed in chapter 2, I reconstruct the Pacific circulation since the LGM using sediment cores from the GOA. High-resolution (~200 yr deglacial sample interval) authigenic ε_{Nd} records were generated at two core sites using the method described in chapter 2. In the new framework benthic exposure time, controlled by circulation rate, is the dominant influence on the distribution of ε_{Nd} in the deep ocean. I therefore compare authigenic ε_{Nd} with the benthic ^{14}C analyzed from the same cores, which allows me to quantitatively reconstruct circulation rate. Using these records, I infer that the abyssal Pacific overturning was weaker than today during the LGM but stronger during HS1 and YD. To reconcile ε_{Nd} and ^{14}C, I suggest that the high ^{14}C age found in the deep Pacific during the deglaciation is attributed to an increase in preformed ^{14}C age of subsurface waters sourced near Antarctica, consistent with movement of aged carbon out of the deep ocean and release of CO_2 to the atmosphere during the abyssal flushing events. The timing of ε_{Nd} changes suggests that deglacial acceleration of Pacific abyssal circulation tracked Southern Hemisphere warming, sea-ice retreat and increase of mean ocean temperature. The inferred magnitude of circulation changes is consistent with deep Pacific flushing as a significant, and perhaps dominant, control of the deglacial rise of atmospheric CO_2.

In chapter 4, I further extend this new interpretive framework globally, and reconstruct the global behavior of GOC since the LGM by analyzing published authigenic ε_{Nd} records from the global ocean basins using Principal Component

Analysis (PCA). I show that the global authigenic ε_{Nd} records are dominantly affected by ocean circulation rather than changes of detrital composition. I then relate the variabilities of global authigenic ε_{Nd} to the different aspects of circulation, including the preformed properties, watermass mixing and circulation rate. I identify two principle components (PCs) in these records. PC1 describes the LGM-Holocene difference. PC2 documents transient deglacial anomalies, focused primarily the HS1 and YD events. I find that PC1 mainly reflects the LGM to Holocene decrease of the preformed ε_{Nd} of deep water produced in the North Atlantic, linked to the shift of the formation location of this watermass. There is also evidence based on the conservative and non-conservative components of ε_{Nd} that GOC strength was overall reduced in the LGM. PC2, on the other hand, indicates that Southern Ocean overturning was stronger during HS1 and YD, causing GOC to strengthen globally, despite that North Atlantic overturning was reduced. I find that the circulation scenario inferred using ε_{Nd} also explains the distribution of other circulation tracers. My results therefore suggest a dominant role of GOC in the increase of atmospheric CO_2 and ocean heat transport since the LGM.

In summary, improved understanding of the modern marine Nd cycle suggests a revision to the global ocean Nd budget. The most important aspect of this revision is to include sedimentary Nd sources from the seafloor. This has implications not only for how deep watermasses acquire their preformed ε_{Nd} but also for the relative contributions of the conservative and non-conservative components of ε_{Nd}. Therefore, the traditional watermass-mixing-only interpretation of authigenic ε_{Nd} needs to be updated. In the new interpretive framework, the diverse effects of circulation on the distribution of ε_{Nd} can be clarified, leading to much higher confidence in circulation reconstruction. With this new framework, I reconstruct the GOC since the LGM, revealing the key climate-GOC link that will help understand the variability of GOC and its role in future climate change.

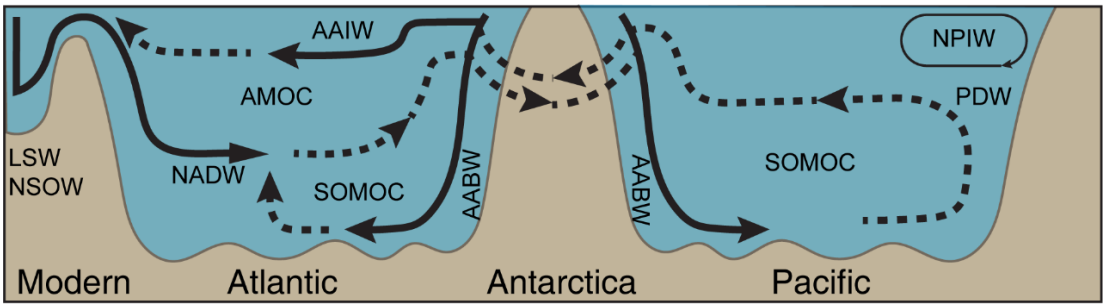

Figure 1.1. Schematics of the modern Global Overturning Circulation.

The schematics is focused on the Atlantic and Pacific Oceans, with emphasis on the connection of the circulation in these two basins through the Southern Ocean. The solid lines with arrows mark major descending watermasses, and the dash lines with arrows mark the return flows. The schematics is produced following Talley (2013).

Chapter 2: Neodymium isotopes in authigenic phases, bottom waters and detrital sediments in the Gulf of Alaska and their implications for paleo-circulation reconstruction

Jianghui Du[1*], Brian. A. Haley[1], Alan. C. Mix[1]

[1]College of Earth, Ocean and Atmospheric Sciences, Oregon State University,

Corvallis, OR 97330, USA. (*Correspondence to: dujia@oregonstate.edu)

Published in *Geochimica et Cosmochimica Acta*

Volume 193 | August 2016 | Pages 14–35

Abstract

The isotopic composition of neodymium (ε_{Nd}) extracted from sedimentary Fe-Mn oxyhydroxide offers potential for reconstructing paleo-circulation, but its application depends on extraction methodology and the mechanisms that relate authigenic ε_{Nd} to bottom water. Here we test methods to extract authigenic ε_{Nd} from Gulf of Alaska (GOA) sediments and assess sources of leachate Nd, including potential contamination from trace dispersed volcanic ash. We show that one dominant phase is extracted via leaching of core-top sediments. Major and trace element geochemistry demonstrate that this phase is authigenic Fe-Mn oxyhydroxide. Contamination of leachate (authigenic) Nd from detrital sources is insignificant (<1%); our empirical results are consistent with established kinetic mineral dissolution rates and theory. Contamination of extracted ε_{Nd} from leaching of volcanic ash is below analytical uncertainty. However, the ε_{Nd} of core-top leachates in the GOA is consistently more radiogenic than bottom water. We infer that authigenic phases record pore water ε_{Nd}, and the relationships of ε_{Nd} among bottom water, pore water, authigenic phases and detrital sediments are primarily governed by the exposure time of bottom water to sea-floor sediments, rate of exchange across the sediment-water interface and the reactivity and composition of detrital sediments. We show that this conceptual model is applicable on the Pacific basin scale and provides a new framework to understand the role of authigenic phases in both modern and paleo-applications including the use of authigenic ε_{Nd} as a paleo-circulation tracer.

Introduction

The isotopic composition of neodymium (ε_{Nd}) of seawater has attracted wide attention in the paleoceanography community as it is considered to be free from complications such as biological fractionation and gas exchange, and therefore can hypothetically be used as a quasi-conservative circulation tracer in the ocean interior (Frank 2002; Goldstein & Hemming 2003). This application of ε_{Nd} builds on an assumption that its heterogeneity in the ocean is inherited from the surrounding continents and persists in water masses. This framework suggests an oceanic

residence time of Nd shorter than the ~1000 yr time scale of global overturning circulation (Goldstein & Hemming 2003; Tachikawa et al. 2003).

Current debates on the oceanic cycle of Nd are centered on two related issues: the sources of marine Nd and the contrasting behaviors of Nd concentration and ε_{Nd} (commonly referred to as the Nd paradox) (Arsouze et al. 2009; Jeandel & Oelkers 2015; Tachikawa et al. 2003). Recent assessments of the oceanic Nd budget suggest atmospheric and dissolved riverine inputs are only minor sources, and to close the budget some "missing" sources are required (Arsouze et al. 2009; Jones et al. 2008; Rempfer et al. 2011; Tachikawa et al. 2003). One study suggested potential contribution from submarine groundwater discharge (Johannesson & Burdige 2007). A recent study of riverine sources showed that although the dissolved Nd flux is small, the amount of Nd released from suspended sediments in river estuaries is globally significant (Rousseau et al. 2015). Lacan and Jeandel (2005a) proposed the "boundary exchange" concept to reconcile the elemental and isotopic budgets of Nd, but this remains an umbrella term that could refer to a suite of unidentified processes. While the original proposition emphasized "exchange", subsequent investigations were more suggestive of a "boundary source" generally limited to the margins (Arsouze et al. 2009; Rempfer et al. 2011; Wilson et al. 2012). Another mechanism proposed to resolve the Nd paradox, reversible scavenging (Siddall et al. 2008), is based on well-established ideas (Bacon & Anderson 1982; Bertram & Elderfield 1993), but awaits validation through better sampling of particulates in the ocean (Jeandel & Oelkers 2015). A different line of work focuses on the influence of pore water and early diagenesis upon the marine Nd cycle (Abbott et al. 2015b; Elderfield & Sholkovitz 1987; Haley et al. 2004; Schacht et al. 2010; Sholkovitz & Elderfield 1988; Sholkovitz et al. 1989, 1992). The effect of benthic flux on bottom water ε_{Nd} distribution was recently quantified in the Northeast Pacific with pore water ε_{Nd} measurements (Abbott et al. 2015a, 2016). One key discovery is that the heterogeneity of sediments in terms of reactivity and isotope composition does play a critical role in the diagenetic and oceanic cycles of Nd (Abbott et al. 2016; Wilson et al. 2013). These works further find, perhaps counterintuitively, that the mobilization

of Nd and other Rare Earth Elements (REEs) during early diagenesis is more favored at greater water depths that are typical of open ocean conditions, and its relationship to the redox cycles of Fe and Mn is complicated (Abbott et al. 2015b,a, 2016; Haley et al. 2004; Haley & Klinkhammer 2003; Schacht et al. 2010). Indeed, while the data are yet spatially limited, there is no mechanistic reason to suggest that the benthic flux is limited to the margins, as might be inferred from the boundary exchange paradigm, and existing data are also not consistent with a surficial sink linked to the presence of Fe-Mn oxides in oxic sediments (Abbott et al. 2016; Haley et al. 2004; Haley & Klinkhammer 2003). Despite such significant advances, sediment-water interaction remains one of the least understood aspects of the oceanic cycle of Nd.

In addition to uncertainties regarding the modern oceanic processes that control Nd concentrations and isotopic compositions in authigenic phases, the application of ε_{Nd} in paleoceanography relies on careful extraction of authigenic ε_{Nd} without contamination. Planktonic foraminifera and fish debris are viewed favorably as authigenic archives because removal of potential contaminating phases is easier than from bulk sediments (Tachikawa et al. 2013, 2014). These archives present practical challenges, however, because they are not present in all areas of the ocean, and their extraction is labor intensive. Retrieving ε_{Nd} signals from authigenic Fe-Mn oxyhydroxide coatings by leaching of bulk sediment offers an advantage that detailed downcore records can be constructed almost anywhere (Böhm et al. 2015; Horikawa et al. 2010; Piotrowski et al. 2004; Rutberg et al. 2000b), but designing suitable leaching procedures that minimize detrital contamination remains challenging. While a few studies suggest leaching with acetic acid (AA) on carbonate rich samples is adequate (Gourlan et al. 2008, 2010), others promote acid-reductive leaching with hydroxylamine hydrochloride (HH) (Bayon et al. 2002; Gutjahr et al. 2007; Martin et al. 2010; Wilson et al. 2013). Few studies have explored systematically the effects of experimental parameters such as reagent concentration, leaching duration, solid/solution ratio on leachate ε_{Nd} and the utility of a decarbonation step (Blaser et al. 2016; Wilson et al. 2013; Wu et al. 2015).

To date, most concern has been focused on designing laboratory procedures to generate authigenic ε_{Nd} records free from detrital contamination. Traditional views assume *a priori* that authigenic phases record bottom water ε_{Nd}; deviations from bottom water signatures are often inferred to reflect problems with the extraction process, particularly in bulk-sediment leaching studies (Elmore et al. 2011; Gutjahr et al. 2008; Huang et al. 2014; Wilson et al. 2013). However, the recently proposed "bottom up" perspective (Abbott et al., 2015b) calls for rethinking of how authigenic ε_{Nd} is related to bottom water. Nearly all the core-top studies in the Pacific Ocean (Vance et al. 2004; Horikawa et al. 2011; Ehlert et al. 2013; Molina-Kescher et al. 2014a) and several others in the Atlantic Ocean (Elmore et al. 2011; Tachikawa et al. 2014) reported ε_{Nd} extracted from foraminifera and fish debris that were different from bottom water, and it seems unreasonable to attribute all these cases to extraction bias, as in some cases of Fe-Mn leachates.

Early on, Palmer (1985) and Palmer and Elderfield (1985) suggested that the diagenetic nature of Fe-Mn oxyhydroxide coatings on foraminiferal tests implied that they register pore water ε_{Nd}. Similarly, Toyoda and Tokonami (1990) concluded that the REEs in biogenic phosphates were dominantly derived from pore water rather than bottom water. While it was well recognized earlier that authigenic phases are actively engaged in the early diagenetic cycle of Nd (Elderfield & Sholkovitz 1987; German & Elderfield 1989; Haley et al. 2004; Sholkovitz & Elderfield 1988; Sholkovitz et al. 1989, 1992), the implications of these findings have rarely entered the discussions on the application of authigenic ε_{Nd} in paleoceanography (Kraft et al. 2013; Tachikawa et al. 2014).

Abbott et al., (2015b) advanced understanding beyond the earlier inferences by showing that dissolved Nd in pore waters had ε_{Nd} that differed from bottom water in the Northeast Pacific. The porewater data on Nd concentrations require a net flux from the sea floor into bottom waters at these sites. Abbott et al. (2016) further found that at their sites bottom water is the least important reservoir in terms of concentration in the early diagenesis of Nd and suggested that trace detrital minerals can significantly influence the authigenic and pore water ε_{Nd} (Abbott et al. 2016).

Similarly, other pore water studies pointed out that the diagenesis of detrital sediments, including volcanic ash, can lead to enrichment of Nd in pore water, which in turn exchanges Nd with authigenic Fe-Mn and phosphate phases (Caetano et al. 2009; Schacht et al. 2010). These findings cast doubt on the traditional interpretation of authigenic ε_{Nd} as a quasi-conservative bottom water tracer and suggest that pore water and detrital sediment are involved in the formation of authigenic ε_{Nd}.

Here we examine the relationships of ε_{Nd} among authigenic phases, bottom waters, and detrital sediments in the Gulf of Alaska (GOA) from the Northeast Pacific (Fig. 2.1a). This is a particularly useful area to test hypotheses about bottom-up control of Nd in the ocean, because it spans the region of the oldest watermasses in the global ocean, for example as reflected in low oxygen content (Fig. 2.1b). Given this high watermass age and the size of the North Pacific, this is an important region for carbon budgets of the global ocean and changes in watermasses here may have global biogeochemical consequences. This poorly understood region also presents some challenges; bulk sediment includes Nd-bearing authigenic and detrital mineral phases with a broad range of reactivities (Abbott et al. 2016; Wilson et al. 2013), and developing a leaching procedure that separates extraction of authigenic Fe-Mn oxyhydroxide from bulk sediment requires distinguishing detrital sediment components, including potentially reactive juvenile volcanic materials, from authigenic components.

We explore rigorously the methodological effects of reagent type, concentration and leaching duration on leachate ε_{Nd} and optimized a combination of experimental parameters to extract Nd from authigenic phases. We test this procedure in a set of core-top and volcanic ash samples to identify the sources of Nd in leachates. We evaluate how detrital contamination may affect leaching results, and provide methods to reliably isolate the uncontaminated ε_{Nd} signature from authigenic Fe-Mn oxyhydroxides in these complex sediments. We find systematic offsets of leachate ε_{Nd} in GOA core-top sediments relative to the ε_{Nd} signature of regional bottom waters. We propose a conceptual model relating authigenic ε_{Nd} to that of bottom water, pore water, and detrital sediment, and show that this model can explain

basin-scale distributions of deep water ε_{Nd} in the Pacific, while a model of conservative watermass mixing cannot. These findings lead to a new framework for the use of authigenic ε_{Nd} as a tracer in paleoceanography that acknowledges the importance of the diagenetic cycle of Nd in the coupled ocean-sediment system (Abbott et al. 2016).

Materials and methods

Sampling

Core-top sediments stored at the Marine Geology Repository of Oregon State University (http://osu-mgr.org/) were sampled for this study (location metadata in Fig. 2.S1). Water depth of these cores ranges from 125 m to 4575 m with about half shallower than 1000 m. Most of the cores, including all but one of the shallower cores, were retrieved by the EW0408 Expedition in 2004. Samples from pristine multicores were taken as close to the sediment interface as possible and were all within the upper 7 cm. The rest of the gravity and piston cores were sampled only for the top 1 cm interval.

All the core-top sediments are described as dark sandy to silty clay. GOA sediments are predominantly lithogenic (>90%) and poor in carbonate (<5%) but may contain traces of biogenic silica and organic matter (Jaeger et al. 2014; Walinsky et al. 2009). The sediments may include discrete volcanic ash layers and minor dispersed volcanic glass to various degrees; most of this ash is sourced from the volcanic centers in the Aleutian Arc and Alaska-Canada Cordillera (Jaeger et al. 2014; Scheidegger et al. 1980). Sedimentation rates are exceptionally high on the GOA margin, 5 mm/yr to 48mm/yr (Walinsky et al. 2009), and even at ~4000 m water depth sedimentation rates are >0.1 mm/yr (Jaeger et al. 2014; Praetorius et al. 2015), suggesting that minor ash input is highly diluted by terrigenous input. No discrete ash layers were found in the upper 20 cm of the cores studied here. Rare (<1%) dispersed volcanic glass was detected in smear slides at two sites (EW0408-25MC at 10 cm and -39MC at 20 cm); no ash was detected in other core-top sediments. All multicore tops sampled here are essentially modern, based on ^{210}Pb

and ^{14}C (Davies et al. 2011; Davies-Walczak et al. 2014; Praetorius et al. 2015; Walinsky et al. 2009). Other core-top samples from archived piston and gravity cores do not have verified ages, but fill out the geographic distribution of sites. However, at each depth range there is at least one verified modern multicore top. Two downcore samples from cores EW0408-85JC and EW0408-87JC, dated using ^{14}C to late glacial time (Davies-Walczak et al. 2014; Praetorius et al. 2015) are also selected.

To further improve our understanding of the effect of volcanic ash on leachate ε_{Nd}, we sampled one ash-bearing sediment interval of core EW0408-66JC, two discrete volcanic glass layers in core EW0408-26JC and two pumice layers in core EW0408-40JC; these latter four are all downcore samples of unknown age, and are referred to as "GOA marine ash layer" samples. Note that none of these samples are pure ash; all contain some ambient sediment. For comparison to a pure ash samples we analyzed *fresh* Mount St. Helens volcanic ash samples collected shortly after the 1980 eruption at four locations in the State of Washington, United States.

Developing leaching tests to extract authigenic ε_{Nd}

We tested various leaching methods on two modern core-top samples (EW0408-84MC and EW0408-88MC), two late-glacial samples (EW0408-85JC and EW0408-87JC, sites correspond to those of EW0408-84MC and -88MC, respectively) and one ash-bearing sample (EW0408-66JC). Collectively, these are referred as "test samples" (Fig. 2.1a). All leach tests started with fresh bulk samples (i.e., no sequential leaching or decarbonation). This choice is made for two reasons: (1) Wilson et al. (2013) showed that it is highly likely a decarbonation step in a sequential leaching procedure could lead to considerable detrital contamination in final leachates; (2) cleaned and uncleaned planktonic foraminiferal ε_{Nd} are typically identical and therefore Nd from the carbonate lattice of fossil shells is insignificant compared to Nd in Fe-Mn coatings (Haley et al. 2005; Palmer 1985; Roberts et al. 2012; Tachikawa et al. 2014). These published results suggest sequential leaching and a decarbonation step will not only lead to loss of authigenic Nd but also increase the risk of contamination, and is not necessary.

For extraction of authigenic components we explored differences between acidic (acetic acid; AA) leaching and acid-reductive (hydroxylamine hydrochloride acidified by acetic acid; HH) leaching. For the AA tests, we made a reagent stock of 3.33 M acetic acid buffered to pH≈4 by sodium acetate. For the HH tests, we made a reagent stock of 0.053 M hydroxylamine hydrochloride, 2.62 M acetic acid and buffered to pH≈4 by sodium hydroxide.

In the AA tests (AA1 to AA3) we fixed the reagent concentration at 10% (v/v of the stock solutions listed above; diluted with Milli-Q® water; MQW, 18.2 Ω) while increasing the leaching duration from 3 hr to 18 hr. We performed two sets of HH tests. In the first experiment (HH1 to HH6) we set the leaching duration to 0.5 hr but increased the reagent concentration from 5% to 50%. In the second experiment (HH7 to HH11), we fixed the HH reagent concentration at 50% and varied the leaching duration from 1 hr to 48 hr. This design illustrates how integrated leaching intensity controlled by either leaching duration or reagent concentration affects leachate ε_{Nd}. All experimental parameters are reported in Table EA2.

For each test, 1 g freeze-dried sediment was rinsed with MQW three times in centrifuge tubes. After supernatant removal, diluted reagent (7 ml in AA tests or 8 ml in HH tests, Table EA2) was added into the tubes, which were then left on a Labquake™ Tube Rotator (Thermo Scientific) for reaction. After waiting for the reaction time specified for each experiment, the samples were centrifuged (4000 rpm, 10 min), supernatant leachates were collected by pipette and filtered through a 0.45 μm nuclepore syringe filters with polyethersulfone membranes, and then were evaporated to dryness. Next, concentrated nitric acid was added to the leachate samples to break down organic compounds. A small aliquot was then extracted for elemental analyses, and the remaining solution was converted to a dominantly chloride solution using 6 M HCl for ion exchange chromatography and isotopic analyses.

For reasons described in the discussion, we applied method HH4 to an array of other core-top samples from the region (Table EA1). Dry weights of some core-top

samples were slightly below 1 g because of limitations of sample availability. In any case, no less than 0.8 g was used and we adjusted the volume of reagent accordingly to fix the solid/reagent ratio at 1 g/8 ml (Wilson et al. 2013). Finally, to evaluate the potential effect of dispersed trace volcanic ash on leachate ε_{Nd}, we applied method HH4 to the Mount St. Helens fresh volcanic ash and GOA marine ash layer samples, and in this case the dry weights of samples were fixed at 1 g.

For bulk sediment analyses, separate samples from the same cores and depths as the leaching tests were freeze dried and then digested using a mixture of HF-HNO_3-HCl in a CEM MARS-6 microwave oven, following our published procedure (Muratli et al. 2012).

Analytical methods

Elemental concentrations

Major elements (Al, Ca, K and Mg, Fe and Mn) and several minor elements (Ba, Co, Cu, V and Sr) were analyzed on a Teledyne Leeman Prodigy ICP-OES at the W.M. Keck Collaboratory for Plasma Spectrometry of Oregon State University. Procedural blanks for these elements were always below method detection limits and 2σ uncertainties were <5% of measured values. Trace elements Cr, Ni, Sc, U, Y, Zn and REEs were analyzed on a Thermo VG ExCell quadrupole ICP-MS in the same laboratory. Samples, standards and blanks were all spiked and normalized with internal standards (^{209}Bi, ^{187}Re and ^{103}Rh). For REEs, procedure blanks were <0.5% and 2σ uncertainty was ~3%. Repeated measurements of digestion standards (PACS-2 and an in house standard) yielded <3% (1σ) external precision for REEs and <6% for all the other elements. All elemental concentrations are reported as total extracted elemental mass normalized to the dry weight of sediment leached (i.e., ng element/g sediment).

Nd and Sr isotopes

Neodymium and Strontium were isolated from other elements in leachates using ion exchange chromatography columns. Neodymium separation employed Ln-

spec^{TM}, following Abbott et al. (2015b). Strontium was purified using Sr-spec^{TM}, following Abbott et al. (2016). Total procedure blanks for Nd and Sr isotope analyses were 0.13±0.07 ng Nd and 6±2 ng Sr, which are negligible (<0.5% for both) relative to sample yields.

Neodymium and Strontium isotopic compositions were analyzed on a *Nu Instruments* MC-ICP-MS in the Keck Collaboratory at Oregon State University. Instrumental mass fractionation was accounted for by normalizing to $^{146}Nd/^{144}Nd$ = 0.7219 and $^{86}Sr/^{88}Sr$ = 0.1194 following exponential laws (O'Nions et al. 1979; Steiger & Jäger 1977). $^{143}Nd/^{144}Nd$ and $^{87}Sr/^{86}Sr$ ratios were then normalized to the accepted values of their respective standards, namely 0.512115 for JNdi-1 and 0.710245 for NBS 987. 2σ uncertainties of the JNdi-1 and NBS 987 standards from repeated analyses were ±0.000018 (n=397) and ±0.000049 (n=671) respectively. In-house standards were used to monitor external precision for $^{143}Nd/^{144}Nd$ and $^{87}Sr/^{86}Sr$ and their long-term 2σ uncertainties were ±0.000019 (n=350) and ±0.000049 (n=461). Neodymium isotope composition was expressed in ε-notation (normalized to the present Chondritic Uniform Reservoir value of 0.512638 (Jacobsen & Wasserburg 1980)). The 2σ external reproducibility in this unit is ±0.37, which is used to create uncertainty bars in the plots.

Results

Nd and Sr in leaching tests and bulk digestions

In the AA tests, the amounts of extracted Nd and the leachate ε_{Nd} are similar for each individual sample (within analytical uncertainty for the latter) (Fig. 2.2, Table EA3). In the HH tests, Nd concentrations increase as extractions become more aggressive, particularly from HH1 to HH4 during which the concentrations more than doubled. Apart from an initial drop of ~1 ε from HH1 to HH3 in EW0408-88MC, leachate ε_{Nd} of all HH tests are essentially constant for each individual sample. Except for HH1 and HH2, AA leaches extract Nd that were 11% to 75% of the HH leaches. The similarity of ε_{Nd} between the AA and HH leachates, with the exception of core-top EW0408-88MC, suggests that a significant amount of Nd that is HH-

extractable is also AA-extractable. This finding is consistent with that of Wilson et al. (2013) that the decarbonation step in sequential leaching procedures is not needed.

In the AA tests, concentrations of Sr do not vary as systematically as those of Nd (Fig. 2.2, Table EA3). In the HH tests, the variations of Sr concentrations are within 20% of the average for all samples except core-top EW0408-88MC, which saw an overall two-fold increase from HH1 to HH6. Further, $^{87}Sr/^{86}Sr$ is essentially constant throughout the tests for each individual sample.

On average, leachates extract ~1% of Nd and ~10% of Sr relative to the total amounts measured from complete digestions of bulk sediments (Fig. 2.2, Table EA3). Bulk sediments have distinctively high ε_{Nd} and low $^{87}Sr/^{86}Sr$ values compared to the leachates. All bulk-sediment ε_{Nd} values are similar (+3.1 to +4.9) and so are bulk $^{87}Sr/^{86}Sr$ (0.70661 to 0.70698) with the exception of a low $^{87}Sr/^{86}Sr$ value of the ash-bearing core EW0408-66JC (0.70571).

Nd and Sr in core-top leachates

We applied the HH4 leaching procedure (0.5 hr, 30% HH, 1g dry sample in 8 ml reagent, pH≈4) on a larger array of core-top samples to assess spatial and water-depth variability of values relative to measured seawater in the GOA (locations in Fig. 2.1a and results in Table EA3). Overall, core-top leachate ε_{Nd} is within the range of –2.0 to +1.5 (Fig. 2.3a). Shallower than 500 m the average value is –0.1 (1σ =0.7, n=10, range from –1.5 to +0.9). At two sites near 700 m, ε_{Nd} is between –1.5 and –1.0. At about 1500 m ε_{Nd} ranges from –1 to 0. At depths greater than 3000 m most samples cluster between –1.5 and –1.0 though two leachates have values as high as +1.0. The ε_{Nd} of core-top leachates are almost always ~2 ε higher (more radiogenic) than GOA seawater at equivalent depths (Haley et al. 2014), although the spatial heterogeneity of seawater ε_{Nd} at depths <200 m makes comparison difficult at shelf depths (Fig. 2.3a). Below 1500 m, leachate ε_{Nd} from piston and gravity core-tops are similar (with the exception of two samples bellow 3000 m) to multicore tops from the same depth range that are verified to be modern, suggesting the vertical distribution described here is a robust feature.

Unlike ε_{Nd}, core-top leachate $^{87}Sr/^{86}Sr$ varies significantly with water depth (Fig. 2.3b). Shallower than 200 m, leachate $^{87}Sr/^{86}Sr$ is in the range of 0.70729 to 0.70905. As depth increases, leachate $^{87}Sr/^{86}Sr$ becomes significantly less variable and it converges to modern seawater value (0.7091792±0.0000021) (Mokadem et al. 2015) at depths greater than 3000 m. Low abundance (<5%) of marine carbonate in GOA sediments makes it possible to correct leachate $^{87}Sr/^{86}Sr$ for contributions of Sr from carbonate dissolution during extraction. We assume that all extracted Ca is from biogenic carbonates (thus the corrections represent maximal offsets from measured leachate values) and then use a Sr concentration of 1200 ppm and modern seawater $^{87}Sr/^{86}Sr$ in marine carbonate to compute the carbonate-free leachate $^{87}Sr/^{86}Sr$ (Fig. 2.3b). Details are presented in the Appendix A. Such corrections make core-top leachate $^{87}Sr/^{86}Sr$ from shallow water sites deviate even more from the known seawater value, but have little effect on the deeper sediment leachate values.

Nd and Sr in ash leachates

Leachates from the four Mount St. Helens fresh ash samples (erupted in 1980) have very similar ε_{Nd} values (+6.2 to +6.4) and the $^{87}Sr/^{86}Sr$ of ash leachates are also in a narrow range (0.70348 to 0.70459), except for one sample from Spokane (0.70608) (Table EA3). Whole-rock digestion of volcanic materials erupted in the same 1980 event yields ε_{Nd} of +5.8 and $^{87}Sr/^{86}Sr$ of 0.703607 (Halliday et al. 1983).

The $^{87}Sr/^{86}Sr$ of the four GOA marine ash layer leachates are very similar to each other (0.70829 to 0.70859), but their ε_{Nd} values differ (–0.6 to +3.1) (Table EA3). Compared to the Mount St. Helens ash samples, these marine ash leachates have much lower ε_{Nd} and higher $^{87}Sr/^{86}Sr$. Note, however, that the marine ash layer samples are not pure ash, but are natural mixtures of ash and ambient sediment.

REEs in leaching tests, bulk digestions, core-top and ash samples

Rare Earth Element patterns normalized to Post-Archean Australian Shale (PAAS) (McLennan 1989) and praseodymium (Pr) are highly consistent across leaching tests and core-top extractions (Fig. 2.4, Table EA3). Leachates are enriched in middle REEs (MREEs) relative to both light REEs (LREEs) and heavy REEs

(HREEs) and except for one core-top sample (Y70-4-56) all the other extractions have negative Ce anomalies. Fully digested GOA bulk sediment is characterized by a flatter yet relatively LREE-depleted pattern (Fig. 2.4a). All the test and core-top leachates and digestions have positive Eu anomalies. Leachates of the dacitic Mount St. Helens ash samples have strong PAAS normalized negative Eu anomalies (Fig. 2.4b). Leachates of GOA marine ash samples (which are mixtures of ash and ambient sediment), however, show positive Eu anomalies and MREE enrichment similar in shape to the GOA core-top leachates (Fig. 2.4b).

Discussions

Insensitivity of leachate ε_{Nd} to experimental parameters and its implication for extracted phases

Within the ranges of tested leaching parameters, ε_{Nd} is insensitive to reagent type, concentration and leaching duration (Fig. 2.2). This consistent behavior of ε_{Nd} contrasts sharply to Nd concentrations, which increase continuously with greater leaching intensity in the HH tests (Fig. 2.2). These data suggest that increasing leaching intensity extracts more Nd of relatively fixed ε_{Nd} from a dominant (plausibly authigenic) phase. The observed decoupling between ε_{Nd} and Nd concentration precludes the possibility that leachate ε_{Nd} represents mixing of two or more phases with distinct ε_{Nd} (for example, authigenic and detrital phases), unless these phases release Nd proportionally during extraction. This proportional release hypothesis would require that the contributing phases have essentially identical reaction kinetics, which is implausible (Wilson et al. 2013).

The consistency of REE patterns (Fig. 2.4) in leaching tests and additional core-top leaches, and their distinct difference from bulk sediment digestions, further support the hypothesis that only one dominant phase was extracted that has a distinct MREE bulge pattern. The relative stability of $^{87}Sr/^{86}Sr$ in leaching tests (Fig. 2.2) also agrees with this hypothesis, although dissolution of carbonates may influence the Sr signal, unlike the Nd (and ε_{Nd}) signals.

We choose the HH4 procedure as our standard method for core-top samples because our test results show this extraction method reflects the least intensive leaching beyond which no change of ε_{Nd} was observed (Fig. 2.2). This choice is arguably arbitrary, but HH4 procedure consistently yields enough Nd for isotopic analysis from ~1 g samples. Further increasing leaching intensity increases the potential risk of contaminating the leachate with other phases (e.g., detrital sediment), although we did not observe any significant changes in leachate ε_{Nd} even with two stronger leach recipes of HH5 and HH6.

Nd bearing phases in sediment

The dominant phase extracted in test and core-top leachates yields ε_{Nd} clearly offset from measured bottom water ε_{Nd} (Fig. 2.3a). To consider whether this offset indicates widespread detrital contamination of leachate Nd, we examine the possible sources of Nd to leachates in sediment. Potential candidates for Nd in the leaches are authigenic Fe-Mn coatings, biogenic materials and detrital sediment. In this study we define detrital sediment as the non-authigenic and non-biogenic fraction of the sediment and in particular refer to the aluminosilicate fraction of the sediment, including both eroded terrestrial materials and volcanic ash.

All the test and core-top leachates have MREE enriched patterns typical of Fe-Mn oxyhydroxide (Gutjahr et al. 2007), suggesting this phase was principally extracted (Fig. 2.4). Biogenic carbonate may harbor REEs but Nd in carbonate lattice is negligible compared with Nd in Fe-Mn coatings (Haley et al. 2005; Palmer 1985; Roberts et al. 2012; Shaw & Wasserburg 1985; Tachikawa et al. 2013, 2014). Given that GOA sediments are poor in carbonates (<5%) (Jaeger et al. 2014; Walinsky et al. 2009), it is unlikely that carbonate contributes significantly to leachate Nd, a suggestion supported by the fact that REE pattern extracted from planktonic carbonate is typically more enriched in HREEs (Freslon et al. 2014; Haley et al. 2005; Molina-Kescher et al. 2014a; Palmer 1985). Biogenic apatite, such as fish debris, also accumulates REEs post-mortem in sediment and is also considered an authigenic archive (Martin & Haley 2000), but there is no visual evidence of its significant

presence in our samples and it is unlikely our weak leaching method can significantly attack apatite (Horikawa et al. 2011; Martin et al. 2010). There are very few studies on REEs and ε_{Nd} associated with other biogenic phases such as opal, organic matter and barite, and they are relatively rare in sediments outside of the fjords in the GOA (Walinsky et al. 2009). Since we do not use the specific reagents that target these biogenic phases (Jones et al. 1994; Martin et al. 1995; Freslon et al. 2014), we do not consider their contribution to leachate Nd to be important. Moreover, organic matter typically has more LREE-enriched (Freslon et al. 2014) and opal more HREE-enriched patterns (Akagi et al. 2011; Xiong et al. 2012) than do our test and core-top leachates, suggesting that these biogenic materials are not significant sources of leached Nd in our samples.

Because the detrital sediment includes Nd-bearing components of different reactivities and distinct isotopic compositions (Abbott et al. 2016; McLennan et al. 1993; Wilson et al. 2013), comparing leachates to bulk sediment digestions gives limited insight into detrital contamination. The same can be said for comparison of leachate to operationally defined "detrital residue" after sequential extractions (Bayon et al. 2002). Separate analysis of the various detrital components may be more insightful, but in practice these detrital components cannot be physically or chemically isolated easily. Instead, we employ geochemical provenance tracers (McLennan et al. 1993) to constrain possible inputs from various detrital end members. This approach assumes that in the leaches, Nd is proportional to its relative concentrations and reactivities in the individual detrital components.

The GOA collects mainly terrestrial sediments from the Alaska-Canada Cordillera with a minor volcanic ash component mostly from the Aleutian arc (Fig. 2.1) (Jaeger et al. 2014; Nokleberg et al. 2000; Plank & Langmuir 1998). The isotopic characteristics of the terranes from Alaska-Canada Cordillera are diverse: the ε_{Nd} and $^{87}Sr/^{86}Sr$ range at least from –25 to +10 and 0.702 to 0.709 respectively (Farmer et al. 1993; Samson et al. 1989, 1990, 1991a,b). Aleutian arc volcanic rock and ash have much narrower distributions of ε_{Nd} and $^{87}Sr/^{86}Sr$, typically within +7 to +9 and 0.702 to 0.704 respectively (Hildreth & Fierstein 2012; Kelemen et al. 2014; Turner et al.

2010). Although the Aleutian arc lavas are mainly basaltic and andesitic (Kelemen et al. 2004, 2014), volcanic ash depositions in the GOA are more evolved and predominantly rhyolitic (Cao & Arculus 1995; Pratt et al. 1973; Scheidegger et al. 1980). Rhyolitic ash is the least reactive of these potential ash sources because of its high acidity (Wolff-Boenisch et al. 2004). Based on ε_{Nd} alone the argument in Section 4.1 precludes volcanic material as the dominant phase directly extracted in our test and core-top leachates.

Finally, it is worth considering the potential effect of "preformed" authigenic Fe-Mn oxyhydroxides that may have been delivered to marine sediments by aeolian particles and river/glacial meltwater sediments (Bayon et al. 2004; Kraft et al. 2013; Poulton & Raiswell 2005). The extremely high sedimentation rate (5 to 48 mm/yr) in the GOA (Walinsky et al. 2009) implies exceptionally high erosion and transport rates (Gulick et al. 2015). GOA sediments are mostly glaciogenic (Jaeger et al. 2014), which typically carry much less preformed phases than river borne sediments (Poulton & Raiswell 2002). The short residence time in very small floodplains, cold temperature and large grain size (Jaeger et al. 2014) are all unfavorable for significant Fe-Mn oxyhydroxide formation during transport (Poulton & Raiswell 2005). Indeed, Mn, Nd (and to some extent Fe) extracted from deeper core-top sediments (>3000 m) are four to ten-fold higher than Mn and Nd extracted from shallower sediments (Table EA3). These data suggest the extracted Fe-Mn phases are formed *in situ* in the marine realm rather than being transported from elsewhere. Moreover, it seems unlikely that preformed Fe-Mn oxyhydroxides could survive the redox cycling during early diagenesis without being converted to marine authigenic phases (Kraft et al. 2013). And if such preformed oxides are resistant to diagenesis, it is then doubtful that they would be mobilized in our mild leaches of 0.5 hr. For these reasons, we assume that we do not need to consider preformed oxides as a distinct reactive phase.

The major and trace element geochemistry of leachates

Elemental distributions in leachates can be used to fingerprint the phases extracted (Gourlan et al. 2010; Gutjahr et al. 2007). Here we compare the major and trace element geochemistry of HH4 leachates, including the five test samples and all the core-top leachates, to that of selected authigenic and detrital end members (Fig. 2.5, GOA geochemical data are reported in Table EA3). Such comparisons are necessarily complicated by possible re-adsorption and non-uniform reaction kinetics during lab extractions (Wilson et al. 2013), so our strategy is to use a multi-faceted approach (leaching tests, major and trace element geochemistry, kinetic mineral dissolution rates, isotope systematics) to derive a conclusion consistent with all observations.

The range of elemental concentrations in potential authigenic end members is constrained by published data from Fe-Mn crusts and nodules, planktonic foraminiferal extractions and published Fe-Mn leachates that are considered to be free from detrital contamination. The implicit assumption, which is borne out by our data compilation, is that the authigenic Fe-Mn phase has a characteristic geochemistry that can be compared with known values elsewhere. We consider not only detrital sediment in the averaged sense (i.e. bulk sediment or operationally defined detrital residue), but also various detrital components of distinct geochemistry and reactivity. Aleutian volcanic products (basaltic and andesitic lavas and rhyolitic and dacitic ashes) will serve as the volcanic detrital end members and the Upper Continental Crust (UCC) will represent the continental sourced detrital materials. The bulk sediments of the GOA, the Aleutian and Alaska subducting sediment composites, the Mid-Ocean Ridge Basalt (MORB) and other sources will be used as detrital end members when necessary. References to these end members are listed in the caption of Fig. 2.5.

Fe-Mn crusts and nodules, uncleaned planktonic foraminifera and published Fe-Mn leachates have similar Al/Nd ratios, on the order of 10^1 to 10^2. Our HH4 leachates are within the range of these values (Fig. 2.5a). The Al/Nd of detrital end members are one to two orders of magnitude higher than all the authigenic phases.

The detrital end members also have low Mn/Fe (<0.1) and Nd/Fe (<0.001). Our HH4 leachates have much higher Mn/Fe and Nd/Fe (Fig. 2.5b), which are unlike detrital components but similar to known authigenic end members. Decarbonated leachates are separated from other authigenic extractions by having Mn/Fe <0.1, suggesting preferential loss of Mn-phases, perhaps Mn-oxides and Mn-carbonates during decarbonation (Roberts et al. 2012; Wilson et al. 2013).

For most elements, ratios to Nd in HH4 leachates are proportional (approximately 1:1) to ratios in authigenic Fe-Mn crusts and nodules (Fig. 2.5c). An exception to this rule is the apparent enrichment of alkali-alkaline earths (Ca, Mg, Sr, and perhaps Ba), K, and U in HH4 leachates. These anomalies reflect additional sources such as carbonate (Ca and Sr), biogenic barite (Ba), sea salts (K and Mg) and authigenic U phases, which have little or no effect on leachate ε_{Nd}.

Enrichment factors, i.e., $\left(\frac{(\text{element/Nd})_{\text{sample}}}{(\text{element/Nd})_{\text{detrital endmember}}}\right)$, of the first series transitional metals in HH4 leachates (normalized to Katmai rhyolitic ash from the Aleutian Arc in Fig. 2.5d and other detrital end members in Fig. 2.S1) show close similarity of leachates to Fe-Mn crusts and nodules (for example, relative enrichment of Mn, Co, Ni, Cu, Zn).

Finally, REE patterns can help to diagnose the underlying geochemical processes, and we examine the indices HREE/LREE ([Yb+Lu]/[Pr+Nd]; PAAS normalized concentrations) and MREE* (2[Tb+Dy]/[Pr+Nd+Yb+Lu]) (Martin et al. 2010; Molina-Kescher et al. 2014a) (Fig. 2.6). Seawater, pore water, Fe-Mn crusts and nodules, planktonic foraminifera, fish debris, published Fe-Mn leachates from wide spatial and temporal ranges, all fall on the same broad trend (dash line). We call this the “authigenic-pore water array.” The existence of this array suggests that the processes fractionating REEs in seawater, pore water and authigenic phases are mechanistically related, possibly reflecting the surface chemistry of authigenic phases and mineral-organic matter-water interactions (Bau et al. 2013; Byrne & Kim 1990; Schijf et al. 2015; Sholkovitz et al. 1994).

In contrast, REE data from detrital sediments and their plausible end member components all fall on a roughly orthogonal trend that we call the “detrital array” (solid lines). This array results from mixing of continental crust and mantle materials. Here mantle materials are represented by MORB and continental crustal materials UCC and PAAS (McLennan 2001) (Fig. 2.6, mixing lines are dotted and solid lines respectively). The trend in the detrital array reflects the partitioning of the REEs during partial melting (McLennan 1989; White 2013): LREEs are less compatible than MREEs and HREEs because of greater ionic radii (with the exceptions of Ce and Eu but they are not included in the MREE* and HREE/LREE indices). As a result, continental crust is more enriched in LREEs relative to the mantle and consequently has lower values of both the MREE* and HREE/LREE indices.

The identification of these two nearly orthogonal trends helps to differentiate the processes responsible for the formation of the phases of interest, i.e., low-temperature aqueous processes for authigenic phases and high-temperature igneous processes for detrital phases. Our HH4 leachates fall within the range of Fe-Mn crusts and nodules and generally follow the trend of the authigenic-pore water array. They certainly do not follow the detrital array trend, and do not form mixing lines toward either the MORB or the UCC/PAAS end members (Fig. 2.6).

From these elemental analyses, we conclude the phase extracted dominantly in HH4 leachates is authigenic Fe-Mn oxyhydroxide, and detrital contamination to leachate Nd is insignificant.

Kinetic mineral dissolution rates

Detrital and authigenic contributions during leaching can be further quantified by considering relative mineral dissolution rates (Table EA4, see the Appendix A). Mineral dissolution mechanisms can be classified as proton-promoted versus ligand-promoted, and for oxyhydroxide reductive versus non-reductive (Brantley 2008; Stone & Morgan 1987; Zinder et al. 1986). Chemical extractions using an acidified reducing reagent applied over a short time interval, such as our HH4 method, should

represent far-from-equilibrium proton-promoted dissolution of silicate minerals and reductive dissolution of Fe-Mn oxyhydroxide (Fig. 2.2), and therefore short-term leaching procedures should be governed by kinetics. Indeed, we found Nd concentrations from HH6 to HH9 tests increase linearly with time (0.5 to 6 hrs), suggesting zero-order kinetics. To estimate Nd extraction from authigenic and silicate minerals we need to know (i) the mineralogy of sediment, (ii) the relative kinetic dissolution rates of these phases under an environmental condition that is similar to our laboratory extractions (pH≈4 and room temperature), (iii) the specific surface area of these minerals and (iv) the relative concentration of Nd in the source minerals.

We report pH-dependent Nd release rate calculations in Fig. 2.7 (details are presented in the Appendix A). Volcanic ash is not included in this calculation because of its rare presence; we discount the potential for ash contamination in Section 4.5. All rates are reported as ng of Nd released from 1 g of mineral/sediment in 0.5 hr to facilitate comparison with our leachate data (Table EA3). We note that interpretation of these estimates is limited to an order-of-magnitude scale, as comparing kinetic mineral dissolution rate measurements with higher precision would requires more data, for example on mineral grain sizes and surface areas, that are beyond the scope of our study (Bandstra & Brantley 2008).

Observed Nd release rates in our HH4 leachates (220 to 2051 ng Nd g^{-1} $0.5hr^{-1}$) fall within the theoretical bounds of reductive dissolution of Fe oxyhydroxide and are very close to the rates previously measured using oxalic acid as reducing agent (Zinder et al. 1986). This finding is consistent with authigenic Fe-Mn oxyhydroxide being the phase extracted dominantly in HH4 leachates. Total Nd release rates from silicate minerals depend on the choice of representative mineral and specific surface area in calculation. Nevertheless, even when choosing silicate minerals of higher reactivity and with generous estimates of specific surface area, detrital Nd release rates (<10 ng Nd g^{-1} $0.5hr^{-1}$ in a pH range of 3.5 to 4.5) from these silicate minerals are two to three orders of magnitude lower than those of authigenic oxyhydroxides or our observed leach values, suggesting they can account for < 1% of total Nd observed in our leachates. Given the ε_{Nd} of GOA bulk sediment is ~+5, these

low levels of detrital contamination should therefore not bias leachate ε_{Nd} by more than +0.05 ε, which is within external analytical precision and thus negligible.

Estimating volcanic ash contamination

Results from leaching volcanic ash samples may provide a more accurate empirical measure of the potential effect of ash contamination on leachate ε_{Nd} than calculations using kinetic dissolution rate can afford. The ε_{Nd} (+6.2 to +6.4) and $^{87}Sr/^{86}Sr$ (0.70348 to 0.70608) of the four Mount St. Helens ash leachates (HH4 method) are very close to bulk digestion/whole rock analyses of materials erupted in the same event (+5.8 to +6.0 for ε_{Nd} and 0.703607 for $^{87}Sr/^{86}Sr$) (Goldstein et al. 1984; Halliday et al. 1983). This provides a well-constrained volcanic end member. These Mount St. Helens ash samples are dacitic, which are more reactive than the rhyolitic ash in GOA sediments (SiO_2 wt% typically>70%) (Cao & Arculus 1995; Pratt et al. 1973; Scheidegger & Kulm 1975) because of low acidity (Wolff-Boenisch et al. 2004). These fresh ash samples are also expected to be much more reactive than the marine dispersed ash in our samples (White & Brantley 2003). Therefore, estimates of volcanic contamination to GOA core-top leachate based on the Mount. St. Helens end member provide an upper limit.

Neodymium extracted from the four fresh Mount. St. Helens ash samples are in the range of 90 to 450 ng/g in 0.5 hr (Table EA3). Since the observed dispersed ash is only of trace amount (<1% wt) in GOA core-top sediments, up to 4.5 ng of Nd might be derived from ash in our core-top leaches extracted from 1 g dry sediment (Fig. 2.7), assuming complete and kinetically unconstrained release and proportional re-adsorption. This estimated value of 4.5 ng of Nd from dispersed ash in 1 g sediment is equivalent to 1% (±0.5%, max=2%) of the total measured Nd in HH4 leachates. If we assume ash ε_{Nd} of +6.9 (Katmai rhyolitic and dacitic ash from Alaska Peninsular(Hildreth & Fierstein 2012), then this ash contribution would bias our core-top leachate ε_{Nd} of about +0.07 ε (±0.04 ε, max=0.15 ε), which is much smaller than our 2σ analytical uncertainty (0.37 ε) and negligible.

Results of leaching the four GOA down-core marine ash layer samples (two volcanic glass layers from EW0408-26JC and two pumice layers from EW0408-40JC, both containing some ambient sediment) further support the robustness of our HH4 method. Though a similar amount of Nd was extracted from these marine ash samples (276 ng/g, 1σ =180; Table EA3), the extracted ε_{Nd} (–0.6 to +3.1) and $^{87}Sr/^{86}Sr$ (0.70829 to 0.70859) are far different from pure volcanic signals, suggesting that ash is not the dominant source of Nd and Sr, even in ash-layer sediments. We infer that authigenic Fe-Mn oxyhydroxide coatings dominate the Nd signal leached, as in our other non-ash layer sediments. Indeed, the REE patterns of these marine ash leachates are very similar to all the other core-top leachates with distinct MREE enrichment pattern (Fig. 2.4b), suggesting the dominance of low-temperature aqueous geochemical processes (Fig. 2.6).

We can also use $^{87}Sr/^{86}Sr$ of these marine ash layer leachates to estimate ash contamination. Though these samples contain little calcium carbonate (total extracted Ca in these leachates are only ~10% of the core-top samples, Table EA3), we still correct their leachate $^{87}Sr/^{86}Sr$ for influence of carbonate dissolution. Such a correction, however, does not decrease leachate $^{87}Sr/^{86}Sr$ more than 0.0005. Using these corrected values, mixing calculations between volcanic ash (0.70371 for Katmai rhyolitic ash) and seawater (0.7091792) show no more than 25% of the non-carbonate Sr measured in these marine ash leachates can be derived from volcanic sources. The relative contribution of volcanic sources to leachate Nd must be even lower, as Fe-Mn coatings are more enriched in Nd than Sr (Gutjahr et al. 2007). We suggest these radiogenic downcore ash layer leachates may represent genuine radiogenic authigenic ε_{Nd} that results from ash diagenesis *in situ*, rather than ash contamination during our lab extractions. This is supported by previous observations that ash dissolution can lead to extreme enrichment of pore water REEs during early digenesis (Schacht et al. 2010).

Similar to the leachates from pure Mount St. Helens ash, the leachates from marine ash layer offer some constraint on volcanic contamination in our GOA core-top leachates. Even if we make a worst-case assumption the GOA core-top samples

contain as much volcanic ash as the four marine ash layer samples, and the contaminating effect to leachate Nd is as high as to leachate Sr, then ash contamination still cannot account for core-top leachate ε_{Nd} that are more radiogenic than –0.5 when the 25% upper limit is used (Fig. 2.3a). Together, we conclude that GOA core-top leachate-bottom water ε_{Nd} differences are not the result of ash contamination.

Thus, our geochemical arguments lead to the conclusion that the dominant Nd bearing phase extracted is authigenic Fe-Mn oxyhydroxide. Detrital contamination, from all the phases considered including ash, is an insignificant source of Nd in GOA HH4 leachates. This implies that the authigenic phases have ε_{Nd} signatures distinct from bottom water (Fig. 2.3a). We conclude that authigenic phases register pore water ε_{Nd}. The following sections explore the consequences of this finding.

Pore water process to explain the decoupling between ε_{Nd} and $^{87}Sr/^{86}Sr$ in core-top leachates

The conclusion above implies that the deviation of core-top authigenic ε_{Nd} from bottom water ε_{Nd} (Fig. 2.3a) must be the results of processes happening *in situ*. We show here that this deviation can be explained by the contribution of the long-term diagenesis of detrital sediment to the *formation* of pore water and authigenic ε_{Nd}. This explanation is consistent with our observation that leachate $^{87}Sr/^{86}Sr$ (corrected for Sr release from carbonate during extraction; Figs. 3b and 8) have seawater-like $^{87}Sr/^{86}Sr$ (core-top samples >3000 m) at the same time that their ε_{Nd} diverges systematically from bottom water values. We refer to this phenomenon as "decoupling".

Because bottom water is far more enriched in Sr over Nd relative to detrital sediments by five orders of magnitude -- for example, 7 ppm Sr (Sarmiento & Gruber 2013) and 4×10^{-6} ppm Nd (Haley et al. 2014), compared to 306 ppm Sr and 19 ppm Nd in GOA bulk sediment -- the $^{87}Sr/^{86}Sr$ signal in pore water is inherited from bottom water and is relatively insensitive to detrital inputs. In contrast to $^{87}Sr/^{86}Sr$, the ε_{Nd} in pore water is highly sensitive to input from sediment diagenesis.

For example, a binary mixing model for pore water $^{87}Sr/^{86}Sr$ and ε_{Nd} between bottom water and detrital sediment, weighted by the composition and reactivity of the sedimentary components (see the Appendix A), shows that the deviation of pore water $^{87}Sr/^{86}Sr$ from the seawater value (0.7091792) would not exceed our 2σ analytical uncertainty (0.000049) until >99.5% of pore water Nd is derived from sediment (Fig. 2.8, green lines). Volcanic materials are typically more reactive than crustal sourced materials (Bayon et al. 2015; Elderfield & Gieskes 1982; Jeandel & Oelkers 2015; Jones et al. 2012; Wilson et al. 2013), but are rare relative to eroded terrigenous material in the GOA. Nevertheless, the reactivity-weighted detrital ε_{Nd} is expected to bias toward volcanic values, so we choose Aleutian basalt and andesite as the reactive end members of detrital sediment to create mixing lines with seawater. Mixing lines between bulk sediment and seawater would lead to virtually the same result. Although this mixing model is quite simple, the GOA deep (>3000 m) core-top leachates fall close to this mixing trend (Figs. 3 and 8), supporting the conclusion that the deviation of authigenic ε_{Nd} from bottom water toward more radiogenic values and the observed ε_{Nd} -$^{87}Sr/^{86}Sr$ decoupling are the results of long-term sediment diagenesis within pore water, at least for this region.

The mixing model can also be used to assess the effects of contamination of ε_{Nd} and $^{87}Sr/^{86}Sr$ during the leaching process. In this case, $^{87}Sr/^{86}Sr$ is most sensitive to contamination effects (Fig. 2.8; vermilion lines and shaded region; two scenarios are chosen to bracket the range of core-top data), because authigenic Fe-Mn oxyhydroxide is more enriched in Nd than Sr relative to ambient detrital sediments (Gutjahr et al. 2007). This trend is orthogonal to the mixing trend that occurs naturally within pore water. Binary mixing between the authigenic phase and Aleutian volcanic products explains the observed range of isotopic values in core-top leachates (Fig. 2.8). Although some contamination from reactive volcanic components may explain the relative low $^{87}Sr/^{86}Sr$ in the core-top leachates, the possible contamination effect on ε_{Nd} is less than analytical precision in all cases except two shallow samples, showing that our HH4 method generally provides robust values of authigenic ε_{Nd}. We note that although some of these data could also fall in

the mixing regions between bulk sediment and authigenic phases, others require the mixing of authigenic phases with volcanic components. Whichever end member is chosen as the source of contamination, the effect on leachate ε_{Nd} is insignificant for most of the samples (in particular the samples >3000 m that have seawater-like $^{87}Sr/^{86}Sr$). We favor the parsimonious argument that laboratory contamination comes primarily from the volcanic components of relatively high reactivity (Wilson et al. 2013), instead from the bulk sediment in the generic sense (which is made of components of distinct reactivity and geochemistry) (Abbott et al. 2016), but emphasize that the effects of this contamination, regardless of the end member chosen, are within analytical precision and thus negligible in our experiments except the two outliers. The more important process in setting the ε_{Nd} of Fe-Mn oxyhydroxides occurs *in situ*, within the porewaters.

A conceptual model relating the ε_{Nd} of authigenic phase to bottom water and detrital sediment

Although with our preferred leaching methods we find that potential contamination effects within the laboratory are very small or negligible, we find that the ε_{Nd} of GOA core-top leachates are systematically higher (more radiogenic) than bottom water (Fig. 2.3a). This is consistent with the findings of Abbott et al. (2015a b) that pore water ε_{Nd} is more radiogenic than bottom water in the Northeast Pacific. Abbott et al. (2016) further suggested that authigenic phases exchange Nd with pore water and that detrital minerals could contribute to the formation of authigenic ε_{Nd} via their long-term influence on pore water ε_{Nd}. Other studies have also shown that mobilization of REEs from detrital sediments, including volcanic ash, during diagenesis is common, and that authigenic Fe-Mn oxyhydroxides and authigenic phosphates are sinks of pore water REEs (Caetano et al. 2009; Chen et al. 2015; Elderfield & Pagett 1986; Elderfield & Sholkovitz 1987; Martin & Haley 2000; Palmer & Elderfield 1985; Rasmussen et al. 1998; Schacht et al. 2010; Soyol-Erdene & Huh 2013; Takahashi et al. 2015; Takebe 2005; Toyoda & Tokonami 1990). Here, we extend the study of Abbott et al., (2015b) and Abbott et al. (2016) to the basin

scale and propose a conceptual model that relates the ε_{Nd} of authigenic phases to pore water, bottom water and detrital sediment (Fig. 2.9).

Traditionally a *diagenetic effect* in a paleoceanographic proxy is referred to as the alteration of an original signal by diagenesis post-burial. In this context previous studies have found minimal *diagenetic alternation* of authigenic ε_{Nd} during late diagenesis, such as the remobilization of Nd in Fe-Mn coatings and the recrystallization of carbonate and apatite after burial (Murphy & Thomas 2010; Palmer & Elderfield 1986). We agree that once authigenic phases are deeply buried their ε_{Nd} are unlikely to be subject to alteration during late diagenesis, mainly because of the extremely high Nd concentration in such phases relative to ambient porewater. However, ε_{Nd} is different from other paleoceanographic tracers in that it is carried in authigenic phases that are the *products* of sediment diagenesis (Abbott et al. 2016; Aller 2014; Berner 1980; Burdige 1993, 2006; Burdige & Gieskes 1983; Canfield 1989; Emerson & Hedges 2003; Froelich et al. 1979; Poulton & Canfield 2005; Poulton & Raiswell 2002; Schulz & Zabel 2006; van der Zee et al. 2003), and therefore the original signal itself is a *diagenetic signal* (Abbott et al. 2016; Palmer 1985; Palmer & Elderfield 1985; Toyoda & Tokonami 1990). We distinguish the *diagenetic formation* of authigenic ε_{Nd} in early diagenesis from its *diagenetic alteration* in late diagenesis.

Pore water can be considered as bottom water altered by sediment diagenesis (Abbott et al. 2016; Schacht et al. 2010). Once bottom water is buried through sedimentation, its ε_{Nd} starts to be modified by relatively slow release of Nd from sedimentary phases (Fig. 2.9). These sedimentary phases do not represent a uniform reservoir of Nd, rather, they include a spectrum of Nd-bearing phases with distinct reactivity and ε_{Nd} (Abbott et al. 2016; Wilson et al. 2013). Unlike our HH4 leaching experiments in which detrital sediment is only in contact with reagent for 30 minutes, detrital sediment may react with pore water on time scales of hundreds to thousands of years. This longer reaction time compensates for slow reaction kinetics, and allows bulk sediment to exert much greater influence on the Nd budget of pore water than it does in the laboratory leaches. Pore water ε_{Nd} depends on a balance of

diffusive/advective exchange with bottom water and relatively slow release of Nd from sediments. As this process is setting the ε_{Nd} signature of pore water, authigenic Fe-Mn oxyhydroxides precipitate out of pore water and hence inherit its ε_{Nd} at the time and depth of precipitation (Fig. 2.9). Once these authigenic coatings are formed, their high concentration of Nd serve to buffer the pore water-bottom water Nd concentration gradient and hence benthic flux (Fig. 2.9) (Abbott et al., 2016)(Abbott et al., 2016)(Abbott et al., 2016)(Abbott et al., 2016)(Abbott et al., 2016).

If there were no benthic flux of Nd with a pore water ε_{Nd} signature, bottom water ε_{Nd} could reflect conservative mixing of the various water mass sources in the deep sea, if reversible scavenging is not important. The net benthic flux of Nd into bottom waters, however, makes ε_{Nd} in bottom waters non-conservative (Fig. 2.9 and 2.10), particularly in the Pacific (Horikawa et al. 2011; Jones et al. 2008). The degree of such modification of bottom water depends on the strength of the benthic source, the integrated exposure time of a water mass to such sources at the sea floor (Abbott et al. 2015a b), and the reactivity and isotopic composition of the detrital sediments (Abbott et al., 2016)(Abbott et al., 2016)(Abbott et al., 2016)(Abbott et al., 2016)(Abbott et al., 2016).

Our finding that authigenic phases, and by implication pore water, have consistently higher ε_{Nd} values than GOA seawater agrees with this model, which explains observations that GOA seawater ε_{Nd} is more radiogenic than expected from conservative mixing between North Pacific Deep Water (NPDW) and North Pacific Intermediate Water (NPIW) at depths > 500m (Fig. 2.3a) (Haley et al., 2014; Abbott et al., 2015 b). We suggest, perhaps in addition to reversible scavenging, the benthic flux of measured radiogenic authigenic ε_{Nd} explains such deviations.

Differences between core-top authigenic and bottom water ε_{Nd} similar to what we documented in the GOA are widespread in the Pacific and are observed in fish debris (Horikawa et al. 2011) and foraminifera (Ehlert et al. 2013; Molina-Kescher et al. 2014a; Vance et al. 2004). Extracted ε_{Nd} is almost always higher than bottom water in these cases, even becoming more radiogenic than the ε_{Nd} of operationally

defined detrital residue (Ehlert et al. 2013). These results agree with the finding of Abbott et al. (2015a b) and Abbott et al., (2016) that pore water ε_{Nd} is always more radiogenic than both bottom water and bulk sediment in the Northeast Pacific. According to our model and based on our GOA study, we attribute these differences to the long-term contribution of more reactive and more radiogenic (mostly volcanic) detrital components (Wilson et al. 2013) to pore water and thus to authigenic ε_{Nd} (Abbott et al. 2016). Even though they may be minor components of the total sediment, their high reactivity relative to bulk sediment increases their influence in pore water (Abbott et al. 2016). We distinguish such diagenetic contributions from laboratory detrital contamination (Fig. 2.8).

We propose that radiogenic benthic flux of Nd is widespread in the Pacific, and that this, rather than surface fluxes or internal cycling, explains the relatively radiogenic nature of deep Pacific seawater ε_{Nd} (Jones et al. 2008). We consider the benthic fluxes to be widespread in the deep sea, and thus separate from previous concepts of boundary exchange (e.g. Arsouze et al. 2009). Here we further show that the benthic flux concept of Abbott et al, (2015b) applies on the basin scale and is consistent with observations of relationships between deep water ε_{Nd} and water mass age. In the deep Pacific, the trend of deep water ε_{Nd} becoming more radiogenic from the Southern Ocean to the North Pacific is paralleled by the aging of watermasses (Fig. 2.10a). We approximate the exposure time proposed in Abbott et al., (2015b) using watermass age based on radiocarbon (Khatiwala et al. 2012). With a box model, we can conduct a simply test of the sensitivity of deep water ε_{Nd} distribution to various magnitudes and isotope compositions of the benthic flux (Fig. 2.10b). Although this box model does not include sinks of Nd, as long as the isotopic composition of the sinks are close to the porewater or bottom water isotopic signature, the sinks would have little impact on the isotopic composition of Nd; the basic relationship of ε_{Nd} vs. age is robust to this model simplification. Model results suggest that, given the ranges of the magnitude (10 to 100 pmol cm^{-2} yr^{-1}) and the isotope composition (–6 to 0 ε_{Nd}) of the benthic flux that are consistent with observations of pore water (Abbott et al. 2015b,a; Haley & Klinkhammer 2003;

Schacht et al. 2010) and authigenic phases (Ehlert et al. 2013; Horikawa et al. 2011; Molina-Kescher et al. 2014a; Vance et al. 2004), deep water ε_{Nd} distribution in the Pacific could indeed be reasonably captured (Fig. 2.10). Clearly, for anything beyond a first-order comparison, multi-component models and future pore water samplings on the abyssal plain would be necessary to improve the model-data fit. Nevertheless, this sensitivity test does indicate this is a reasonable hypothesis. In contrast, a pure conservative mixing model is inconsistent with the data (Fig. 2.10b) (Jones et al. 2008; Rempfer et al. 2011). Reversible scavenging is neglected here, so what is provided here likely overestimates the importance of benthic Nd flux; but the fact that this crude model, with its simplifications, can reasonably capture the distribution of ε_{Nd} in the entire deep Pacific to the first order suggests that benthic flux with pore water ε_{Nd} could be the dominant term in controlling the oceanic distribution of ε_{Nd}.

This conceptual model does not violate findings elsewhere that seawater ε_{Nd} could appear to behave conservatively and core-top authigenic and bottom water ε_{Nd} are similar. For example, in the North Atlantic, a combination of perhaps low benthic fluxes, short exposure times associated with rapid watermass ventilation, and weak detrital reactivity could lead to only slight benthic modification of bottom water ε_{Nd}, (Lambelet et al. 2016). On the other hand, Abbott et al. (2015b) has also shown that bottom water ε_{Nd} could approach pore water because of stronger benthic flux, longer exposure time, or similarity between water mass ε_{Nd} and detrital ε_{Nd}. This suggests that the "authenticity" of authigenic ε_{Nd} as a bottom water signal cannot be validated simply by showing resemblance between authigenic and bottom water ε_{Nd}.

Implication for ε_{Nd} in paleoceanography

Our hypothesis implies that the relevant question for the application of authigenic ε_{Nd} in paleoceanography is not whether authigenic phases and bottom water share similar ε_{Nd}, but what controls the variability of pore water ε_{Nd} in the past. The dynamic interactions between bottom water, pore water, authigenic phases and detrital sediments may seem to complicate the use of ε_{Nd}, but understanding these interactions is essential for recognizing proxy limitations and will likely also lead to

new proxy opportunities. We suggest authigenic ε_{Nd} at a particular site of interest is derived from three processes (Fig. 2.9). Large-scale deep water formation and mixing determine the conservative mixing component of seawater ε_{Nd}. Along the circulation route this conservative component may be modified somewhat by reversible scavenging, but we suggested it is more significantly influenced by benthic fluxes that modify the water mass ε_{Nd} as a function of exposure time before arriving the studied site. Finally, this watermass signal is further modified locally during diagenetic cycling in which the authigenic and pore water ε_{Nd} are created *in situ*.

It is critical to understand the relative importance of these processes to interpret authigenic records in terms of paleoceanography. We suggest on the scale of the Pacific Ocean, local benthic modification is the most important term, for two main reasons: First, the time scale of local benthic process, i.e., early diagenesis, is generally much shorter than changes in watermass circulation (Burdige 2006; Froelich et al. 1979), with a model estimate on the order of 0.2 yr for Nd (Arsouze et al. 2010). Second, the basin scale bottom boundary condition, i.e. core-top sediment composition and reactivity, is relatively invariant on this time scale. In some other cases, such as in the modern Atlantic where the exposure time of bottom water masses to benthic fluxes is small relative to the mixing of different end-member watermasses, the benthic flux "age" effect may not be dominant, but this does not mean it is absent or can be assumed to be irrelevant under different circulation regimes of the past.

The implications for the use of authigenic ε_{Nd} as a paleo-circulation tracer are different under these two scenarios. In the first case, the deviation of authigenic from detrital ε_{Nd} could be used as a proxy for local ventilation rate, i.e. exposure time (Abbott et al., 2015b): fast circulation (low exposure time) may tend to decouple pore water and authigenic ε_{Nd} from the detrital values while leaving the watermass ε_{Nd} signal persistent in pore water and authigenic phases to certain degree; sluggish circulation would homogenize the ε_{Nd} of all these phases. The key challenge, however, is to separate this ventilation effect from any changes in local detrital composition and reactivity. For example, previous studies suggested authigenic ε_{Nd}

could record events of changing sediment composition and were used as proxies for continental weathering, erosion and sediment provenance rather than circulation (Cogez et al. 2015; Le Houedec et al. 2012). Therefore, it is of fundamental importance to measure authigenic and detrital ε_{Nd} concurrently. In the second case, authigenic ε_{Nd} might be used as a quasi-conservative water mass tracer much as it is widely adopted in modern literature, but even in this case it is key to recognize the watermass ε_{Nd} is not simply the result of conservative water mass mixing but the benthic modification along the circulation route needs to be considered, i.e. authigenic ε_{Nd} could be still different from the values expected of conservative mixing. While these are end member cases, in more general situations aspects from both cases could exist. Therefore, understanding the role of sediment-water interaction in the oceanic and diagenetic cycles of Nd is critical in both modern and paleoceanographic applications.

Conclusion

We developed a robust leaching method to extract authigenic ε_{Nd} from bulk sediment and applied it to a set of core-top samples in the GOA. We show that in our experiments one dominant phase is extracted during leaching, and by comparing leachates to selected detrital and authigenic end members using major and trace element signatures, we conclude that the extracted phase is Fe-Mn oxyhydroxide. Detrital contamination of leachate Nd, estimated using kinetic mineral dissolution rate, leaching fresh and marine volcanic ash samples and ε_{Nd} -$^{87}Sr/^{86}Sr$ mass balance calculations, is typically on the order of 1% and does not bias the authigenic ε_{Nd} signal beyond analytical uncertainty; thus, our leaching method accurately reflects the composition of authigenic Fe-Mn oxyhydroxide.

The ε_{Nd} of GOA core-top leachates were consistently higher than bottom water, even though carbonate-corrected $^{87}Sr/^{86}Sr$ of leachate were very close to modern seawater at water depths >3000 m. These observations are reconciled if the authigenic phases record the isotopic values of pore water rather than bottom water.

We proposed a conceptual model to describe the relationship among the leached authigenic phase, pore water, bottom water and detrital sediment, which includes differential reactivity of detrital components, the ε_{Nd} signature of these components, benthic fluxes of Nd, and the time that bottom waters are in contact with the sea floor. This model suggests that on long circulation timescales ε_{Nd} is a non-conservative water mass tracer. We show that this conceptual model can be applied on the Pacific basin scale by simulating the relationship between watermass age and watermass ε_{Nd} in the deep Pacific. In general, different scenarios of parameter combination (benthic flux, detrital composition and reactivity, exposure time etc.) under this new framework can accommodate observations that seawater ε_{Nd} appears to behave conservatively in some regions (for example, the modern Atlantic where benthic exposure times are small relative to the mixing of different watermass end members) and that core-top authigenic and bottom water ε_{Nd} are similar.

Our finding that authigenic ε_{Nd} records porewater rather than bottom water signatures requires a new framework for the use of ε_{Nd} as a circulation tracer in paleoceanography. In particular, we recommend that authigenic and detrital ε_{Nd} should be measured concurrently and the deviation of authigenic from detrital ε_{Nd} can be used as a proxy for local bottom water ventilation rate, if local benthic modification is the dominant factor controlling the formation of authigenic ε_{Nd} and detrital composition and reactivity are time invariant. On the other hand, if the local benthic process is of secondary importance, the traditional quasi-conservative trace approach might be appropriate, bearing in mind that even in this case the watermass ε_{Nd} signal recorded in authigenic phases may not necessarily be the same as expected from conservative water mass mixing, because of the benthic modification along the circulation route.

Acknowledgements

We thank David Graham for donating the Mount St. Helens ash samples. Jesse Muratli was instrumental at the early stage of data collection of this project and offered lab assistance. Andy Ungerer from the W.M. Keck Collaboratory for Plasma

Mass Spectrometry at Oregon State University provided technical supports for the quadrupole ICP-MS and ICP-OES measurements. Discussion with April Abbott improved our understanding of pore water Nd geochemistry. We also appreciate the help from Mysti Weber and Maziet Cheseby in sampling and interpreting smear slide results at the Marine Geology Repository of Oregon State University. We gratefully acknowledge Editor Tina van de Flierdt, David Wilson and two anonymous reviewers for thorough and thoughtful comments that significantly improved our manuscript. This study is funded by NSF grant 1357529 to A.C.M and B.A.H.

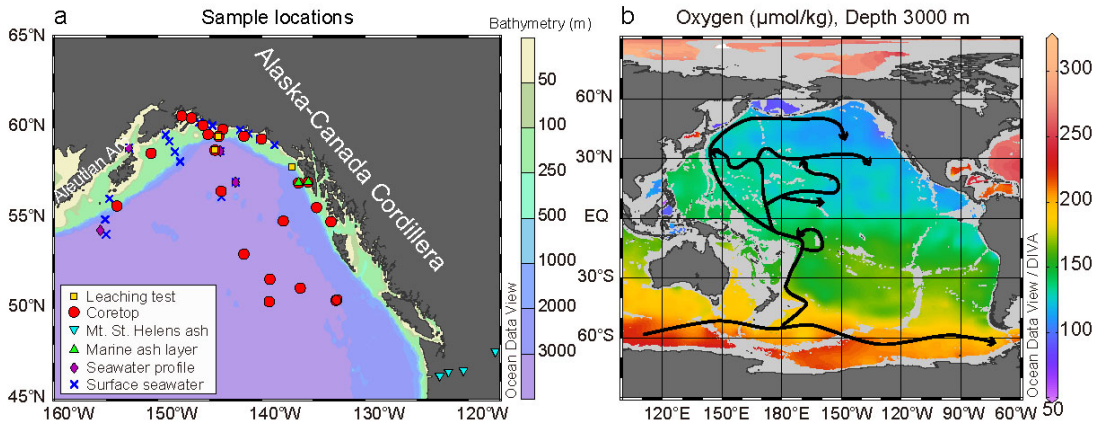

Figure 2.1. Sample locations and hydrography.

(a) Locations of samples, including test samples, core-top samples, marine ash layer samples and Mount St. Helens ash samples. These samples may come from the same core so there is overlap in the map. See Table EA1 for detail sampling information. Locations of the seawater profiles and surface seawater samples in the GOA (Haley et al. 2014) used in Fig. 2.3 are included. (b) Distribution of dissolved oxygen concentration in the Pacific from World Ocean Atlas 2013 database (Garcia et al. 2014) and major Southern Ocean deep water (Lower Circumpolar Deep Water) circulation routes entering the Pacific according to Kawabe and Fujio, (2010). Fig. 2.1b is created using Ocean Data View (Schlitzer 2017).

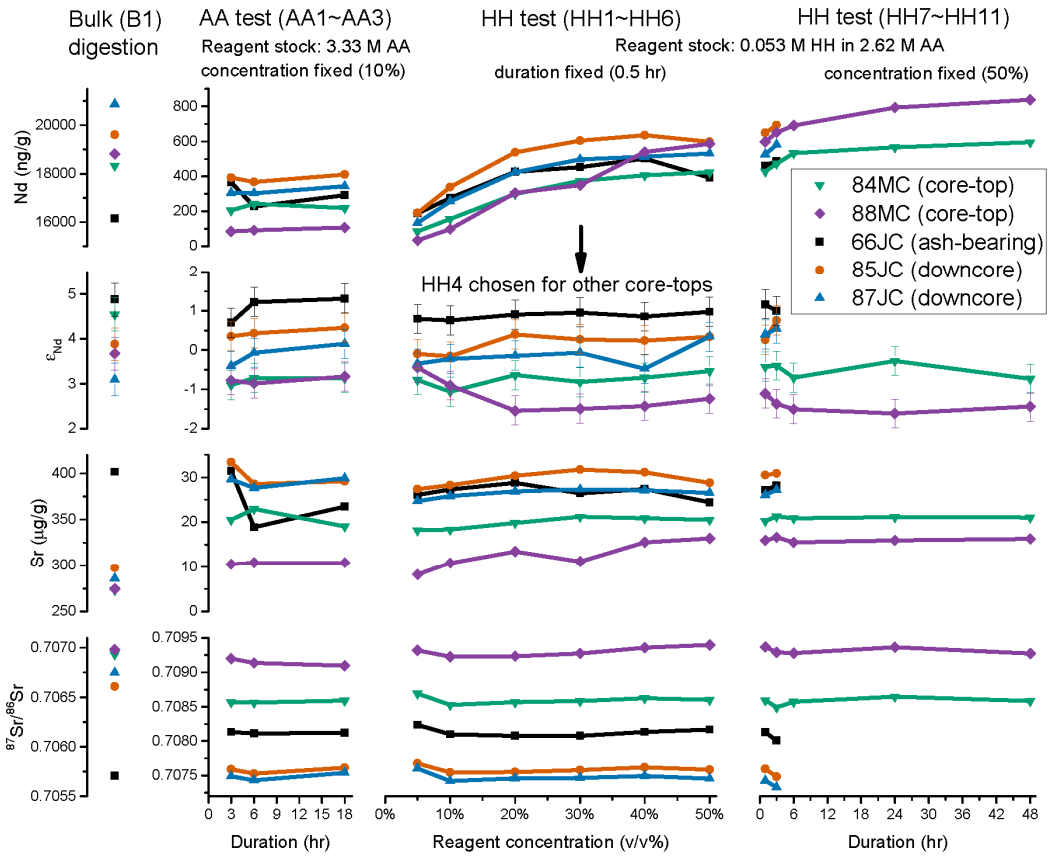

Figure 2.2. Results from leaching tests.

Each datum represents a distinct test, and all tests were done on fresh samples. Bulk digestion (B1) reflects the composition of the total sediment. Partial leaching tests of varying intensity are based on acetic acid (AA) or hydroxylamine hydrochloride (HH). Tests AA1 to AA3 and HH7 to HH11 examine the effect of increasing leach duration with constant reagent concentration. Tests HH1 to HH6 examine the effect of increasing reagent concentration over a fixed time of 30 minutes. Tests HH9 to HH11 were only done on the two modern core-top samples (EW0408-84MC and EW0408-88MC). Elemental concentrations are reported as total extracted elemental mass normalized to dry weight of sediments; note that plot scales for bulk digestions are different from those of leachates. Experimental parameters are reported in Table EA2.

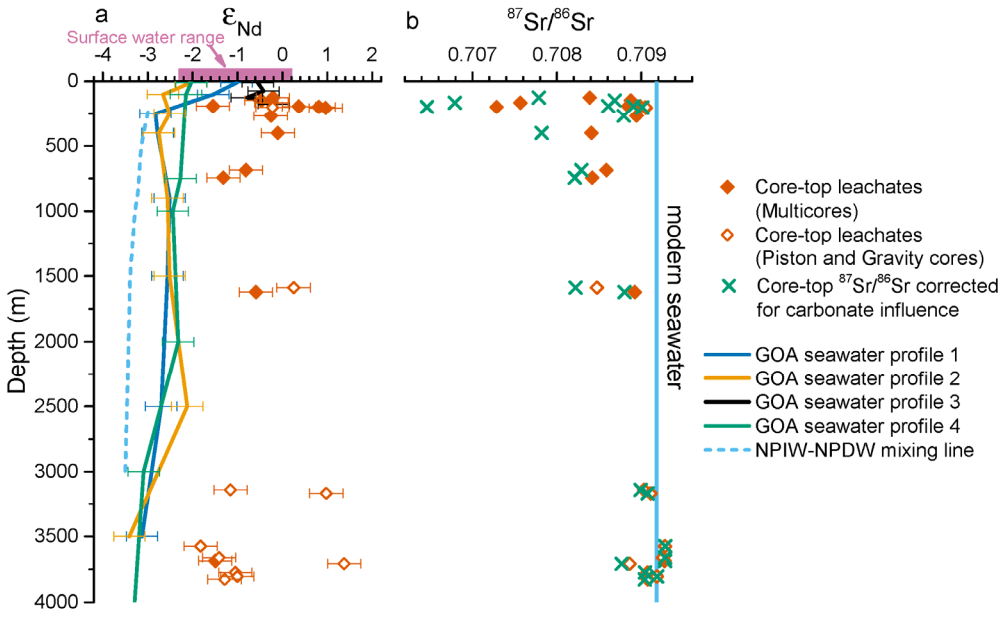

Figure 2.3. (a) ε_{Nd} and (b) $^{87}Sr/^{86}Sr$ of core-top leachates (with analytical uncertainty bars), surface seawater ε_{Nd} (pink bar) and water column ε_{Nd} profiles from the GOA (solid lines with uncertainty) (Haley et al. 2014).

Multicore tops that are verified to be modern are marked by solid diamonds. Piston and gravity core tops that do not have verified ages are marked by hollow diamonds. The similarity of leachate ε_{Nd} between piston and gravity cores and multicores below 1500 m at the same depth range (with the exception of two samples) suggests the vertical distribution is a robust feature. Dashed line is a prediction based on conservative mixing between North Pacific Intermediate Water (NPIW) and North Pacific Deep Water (NPDW) (Abbott et al., 2015b). Modern seawater $^{87}Sr/^{86}Sr$ value of 0.7091792 is from Mokadem et al., (2015). The $^{87}Sr/^{86}Sr$ of core-top leachates corrected for carbonate contributions are also shown as X symbols (see the Appendix A).

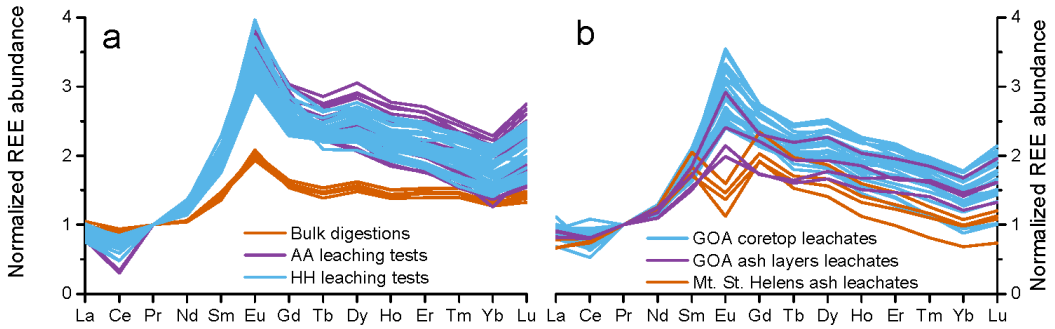

Figure 2.4. PAAS- (McLennan 1989) and Pr-normalized REE patterns of bulk sediments and leachates in this study.

Panel (a) shows AA tests (purple), HH tests (blue) and bulk digestions (vermillion). Panel (b) shows HH4 leaches of GOA core-tops (blue), Mount St. Helens ash leachates (vermillion) and GOA marine ash layer leachates (purple).

Figure 2.5. Major and trace element geochemistry of HH4 leachates compared to authigenic and detrital end members (all elemental concentrations are in mass unit).

(a) Al/Nd ratio (boxes span 25%-75% of the data, whiskers note the entire range of values); (b) Mn/Fe ratio versus Nd/Fe ratio; (c) log10(element/Nd) comparison between HH4 leachates and Fe-Mn crusts and nodules and (d) enrichment factor plot normalized to Katmai rhyolitic volcanic ash from the Aleutian Arc (boxplot setting same as in (a)). Authigenic data represent Fe-Mn crusts and nodules (Hein & Koschinsky 2014; van de Flierdt 2003), planktonic foraminifera (Palmer 1985; Palmer & Elderfield 1985; Roberts et al. 2012; Roberts & Piotrowski 2015) and Fe-Mn leachates (Bayon et al. 2002; Gourlan et al. 2010; Gutjahr et al. 2007, 2010; Martin et al. 2010; Wilson et al. 2013). Detrital data include GOA bulk sediment, UCC (Rudnick & Gao 2014), Aleutian basalt and andesite lavas (Kelemen et al. 2014), Katmai rhyolitic and dacitic volcanic ashes from the Southern Alaska Peninsular (Hildreth & Fierstein 2012; Turner et al. 2010), MORB (Kelemen et al. 2014), Aleutian and Alaska subducting sediment composites as well as the global composite (Plank 2014). The detrital quadrant in (b) contains most of the detrital end members and is defined as $Mn/Fe<0.1$ and $Nd/Fe<0.001$. The uncertainty bars in (c) are created using 1σ standard deviations of the HH4 leachate data and the compiled regional Fe-Mn crust and nodule data from Hein and Koschinsky (2014) respectively. Note that the variability of Fe-Mn crust and nodule data represents regional differences, and the variability on the level of individual samples may be larger.

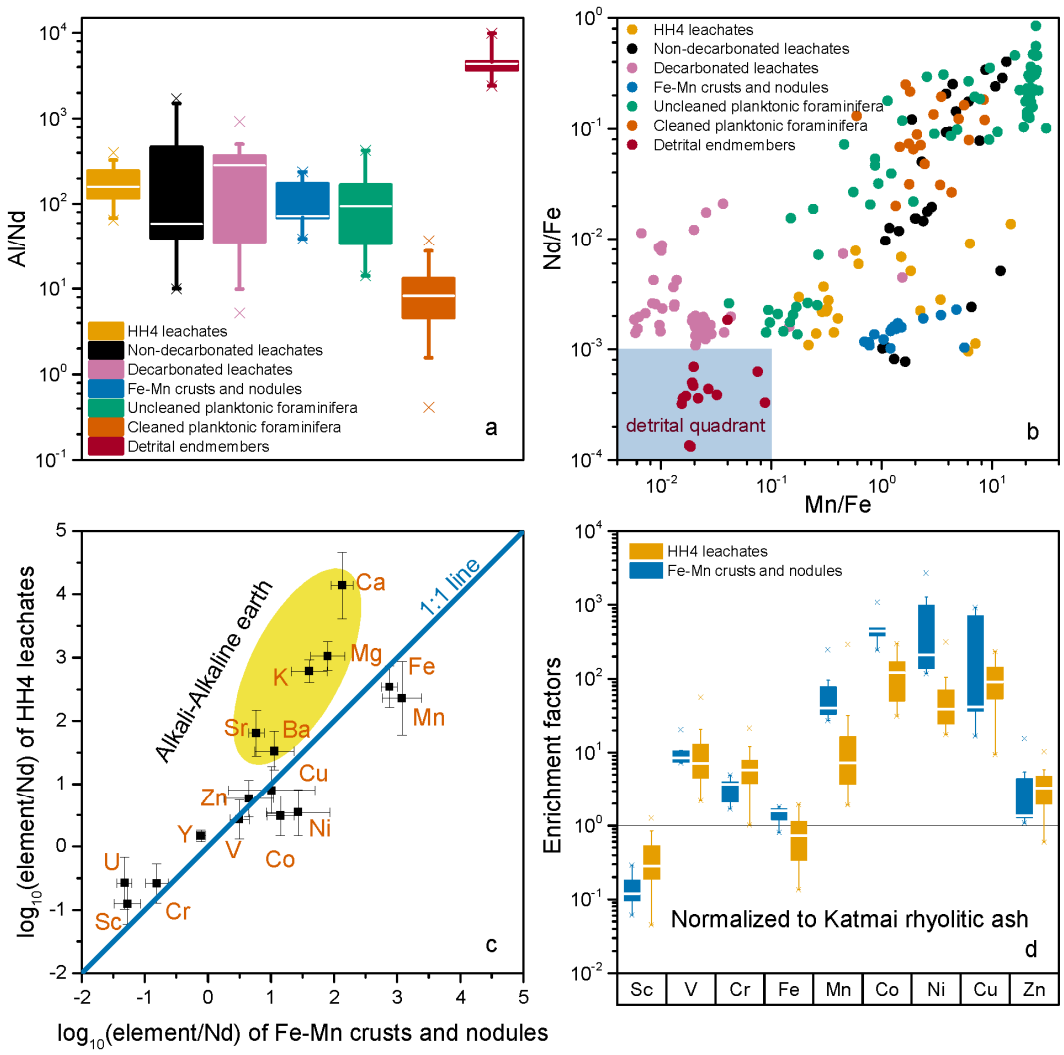

Figure 2.5. Major and trace element geochemistry of HH4 leachates compared to authigenic and detrital end members (all elemental concentrations are in mass unit).

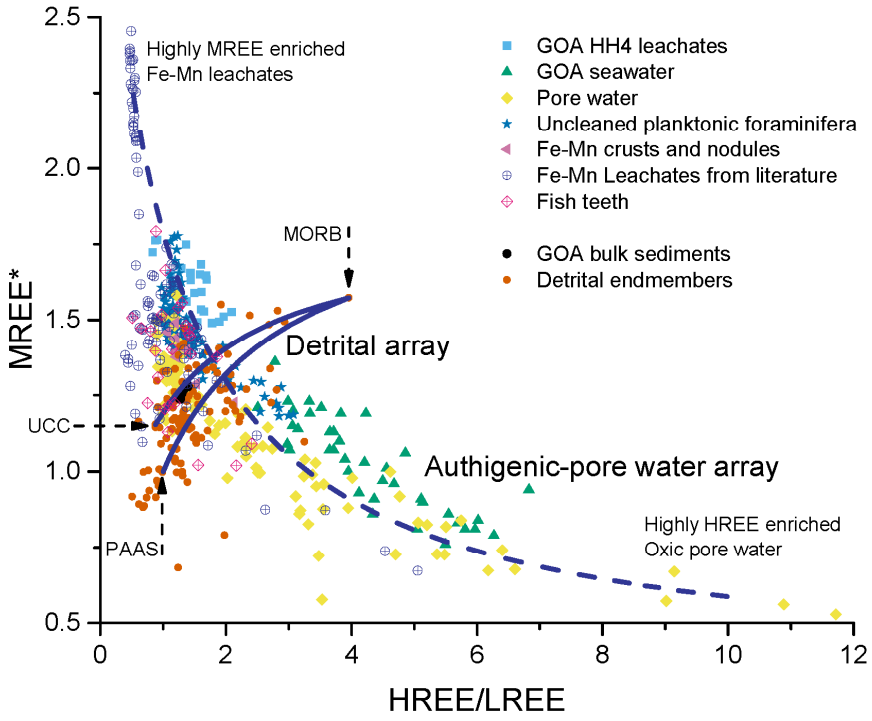

Figure 2.6. HREE/LREE vs. MREE*.

A mixing line between the most MREE enriched leachates (Gutjahr et al. 2010) and the most HREE enriched oxic pore water (Haley et al. 2004) reflects the "authigenic-pore water array" (dashed line). Mixing lines between MORB (Kelemen et al. 2014) and UCC (solid line) (Rudnick & Gao 2014) or PAAS (solid line) reflect the "detrital arrays". Data include those cited in Fig. 2.5 as well as other published values (Bayon et al., 2002; Haley et al., 2004; Bayon et al., 2004; Martin et al., 2010; Kelemen et al., 2014; Plank, 2014; Haley et al., 2014; Molina-Kescher et al., 2014a; Abbott et al., 2015a; Wilson et al., 2013; Cao and Arculus, 1995).

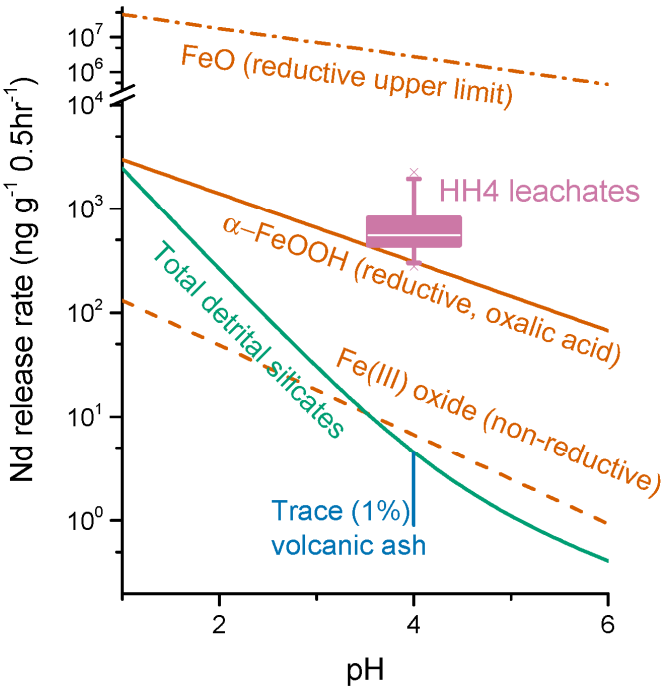

Figure 2.7. Nd release rate measured in GOA HH4 leachates (pH≈4, pink box; box spans 25%-75% of the data, whisker notes the entire range of values) compared with Fe oxyhydroxide and detrital silicate minerals modeled using published kinetic mineral dissolution rates (lines), and pure volcanic ash based on our experiments of leaching fresh Mount St. Helens ash samples.

Reductive dissolution of Fe oxyhydroxide is bounded by dissolution of FeO to the top and proton promoted non-reductive dissolution of Fe(III) oxide to the bottom (Brantley 2008). Reductive dissolution rate of goethite (α-FeOOH) measured in 10^{-3} M oxalic acid is also shown (Zinder et al. 1986). In estimating the amount of Nd released from detrital silicates we consider the bulk mineral composition of GOA sediments and the reactivity of these minerals. Volcanic ash is present at trace level (<1%) in GOA bulk sediments. For Fe oxyhydroxide the results are reported as ng Nd released from 1 g pure minerals in 0.5 hr, while for HH4 leachates, detrital silicates and volcanic ash the units are in ng Nd released from 1 g dry sediment in 0.5 hr. In comparing Nd release rate from HH4 leachates to pure Fe oxyhydroxide minerals we assume the amount of authigenic phases present does not limit the reaction rate, which is supported by the observation that the release of Nd in our HH experiments seems to follow zero-order kinetics (HH6 to HH11, Fig. 2.2). Mn oxyhydroxides are not presented here because relevant inorganic rate measurements are unknown. Details of the calculations are in the Appendix A.

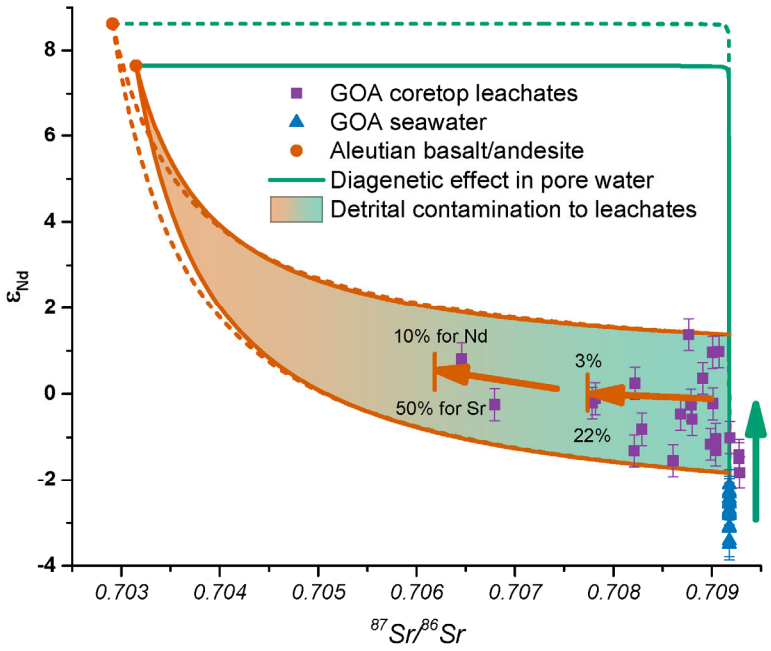

Figure 2.8. The ε_{Nd} -$^{87}Sr/^{86}Sr$ isotopic systems in GOA core-top leachates.

Leachate $^{87}Sr/^{86}Sr$ are corrected for the effect of carbonate dissolution (Fig. 2.3, also see the Appendix A). Green solid and dashed lines are the *in situ* mixing lines between GOA seawater and Aleutian volcanic products, representing the influence of volcanic derived components on pore water and authigenic isotopic compositions happening during sediment diagenesis. The vermilion lines and shaded region indicate the potential effects of mixing between Aleutian volcanic products and authigenic phases in the laboratory during leaching, i.e., this quantifies the effects of contamination on leachate isotopic signatures. The arrows demonstrate the directions of such processes and on the arrow heads we show the percentage volcanic contaminations to leachate Nd and Sr (non-carbonate fraction). For <3 % contamination of the Nd component during leaching, the effect on ε_{Nd} is negligible compared to analytical uncertainties. The geochemistries of the end members are: Sr=445 ppm, Nd=9 ppm, $^{87}Sr/^{86}Sr$=0.70315 and ε_{Nd}=+7.65 for Aleutian basalt; 1035.88 ppm, 20.2 ppm, 0.70291 and +8.62 for Aleutian andesite (Kelemen et al. 2014); and 7 ppm, 4.26 ppb, 0.70918 and –2.7 for GOA seawater (Haley et al. 2014). In creating the vermillion mixing lines, authigenic $^{87}Sr/^{86}Sr$ is taken to be the same as seawater, and two authigenic ε_{Nd} end members (–1.38 and +1.83) are chosen to bracket the core-top leachate data. We use a Sr/Nd ratio of 5.7 for authigenic phases, same as in Fe-Mn crusts and nodules (Hein & Koschinsky 2014).

Figure 2.9. A conceptual model describing the relationship of ε_{Nd} among authigenic phase, pore water, bottom water and detrital sediment.

Water column and pore water ε_{Nd} and Nd concentration profiles are from the HH3000 site in Abbott et al. (2015b). The model is divided into water column, early diagenesis zone and late diagenesis zone. Bottom water is buried and becomes pore water, the isotopic compositions of which will be modified by the diagenesis of detrital sediments and authigenic phases. The detrital sediment comprises components of distinct reactivity and ε_{Nd}, which contribute to pore water Nd differentially. Fe-Mn oxyhydroxide forms in pore water and derives its ε_{Nd} at the time of formation. Once formed, Fe-Mn coatings become the most significant reactive Nd bearing phase in sediment as they have both high Nd concentration and reactivity. Interaction between Fe-Mn coatings and pore water supports a significant benthic flux of Nd, with pore water/authigenic ε_{Nd}. This flux modifies the bottom water ε_{Nd} and tends to shift bottom water ε_{Nd} toward pore water values. The difference between bottom water and pore water/authigenic ε_{Nd} depends on the magnitude of the benthic flux, the integrated time the bottom water is exposed to this flux (Abbott et al., 2015b), the reactivity and composition of detrital sediment. Along the circulation route bottom water ε_{Nd} derived from conservative water mass mixing is continuously modified by the benthic flux, while water-column processes like scavenging and reversible scavenging also affect deep-water ε_{Nd}. Water masses that are not directly in contact with sediment can still feel the benthic influence through lateral and diapycnal mixing. The sink term is not discussed in this study, but we assume it has the same ε_{Nd} as bottom water, while the benthic flux term has the ε_{Nd} of pore water. Once authigenic phases are preserved in the late diagenesis zone, their ε_{Nd} is insensitive to alternation because of high Nd concentration relative to the other solid and dissolved phases.

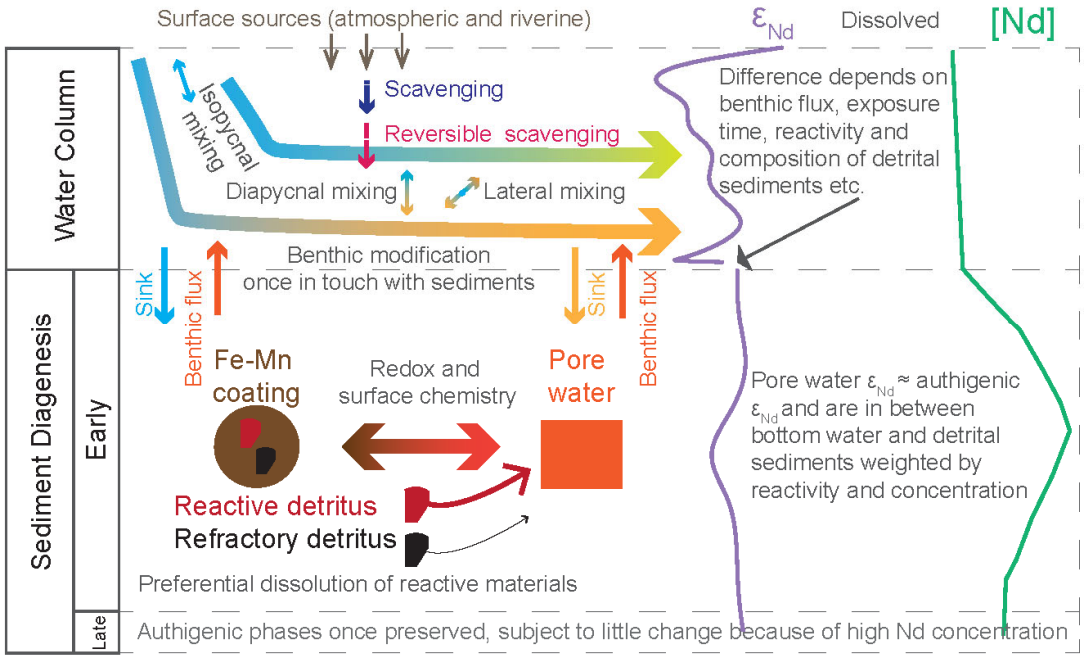

Figure 2.9. A conceptual model describing the relationship of ε_{Nd} among authigenic phase, pore water, bottom water and detrital sediment.

Figure 2.10. The relationship between deep water ε_{Nd} and water mass age.

(a) Contours of radiocarbon-based estimates of deep water mass age from Khatiwala et al., (2012) superimposed on the distribution of seawater ε_{Nd} over the depth range of 2500 m to 4500 m. Data are from references in Lacan et al., (2012) and recent publications (Pahnke et al., 2012; Grasse et al., 2012; Grenier et al., 2013; Jeandel et al., 2013; Ehlert et al., 2013; Amakawa et al., 2013; Haley et al., 2014; Molina-Kescher et al., 2014b; Rickli et al., 2014; Basak et al., 2015; Abbott et al., 2015b). This figure is created using Ocean Data View (Schlitzer 2017). (b) Deep water ε_{Nd} vs. age relationship (blue boxes, boxes span 25%-75% of the data, whiskers note the entire range of values) compared to box model results (solid and dash lines). We assign a watermass age, based on the results from Khatiwala et al., (2012), to each seawater data point and bin the data into 100 yr intervals (blue boxes). The deep Pacific is treated as a single box, the circulation time scale of which is ~1000 yr (Khatiwala et al. 2012). We supply a uniform benthic flux to the box. The magnitude of the flux varies from 10 to 100 pmol cm^{-2} yr^{-1} and the isotope composition of the flux changes from –6 to 0. In this model the starting point of exposure to the benthic flux occurs when the southern sourced deep water enters the Pacific via the Deep Western Boundary Current east of New Zealand. This entering water mass has ε_{Nd} of –9 and Nd concentration of 22 pM (Molina-Kescher et al., 2014) and the age of this water mass relative to surface waters is ~600 yrs (Khatiwala et al., 2012). Seawater ε_{Nd} expected from conservative water mass mixing only are also shown (purple boxes). We use the watermass decomposition product of Khatiwala et al., (2012), which gives the volumetric makeup of a deep ocean point computed using endmembers including Antarctic Bottom Water (AABW), North Atlantic Deep Water (NADW), Antarctic Intermediate Water (AAIW), North Pacific Intermediate Water (NPIW) and other surface watermasses. The end member seawater ε_{Nd} data are chosen to be compatible with this set of watermass mixing ratios. All relevant data are presented in Table EA5 in the Appendix A. This model does not take into account reversible scavenging.

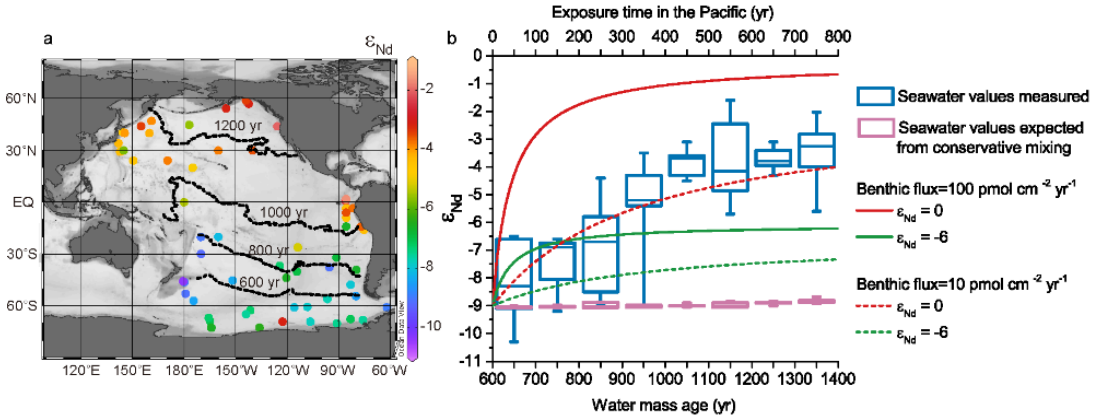

Figure 2.10. The relationship between deep water εNd and water mass age.

Chapter 3: Flushing of the deep Pacific Ocean and the deglacial rise of atmospheric CO_2 concentrations

Jianghui Du[1]*, Brian A. Haley[1], Alan C. Mix[1], Maureen H. Walczak[1], Summer K. Praetorius[2]

[1]College of Earth, Ocean and Atmospheric Sciences, Oregon State University, 104 CEOAS Administration Building, Corvallis, OR 97331, USA.

[2]United State Geological Survey, Menlo Park, CA 94025, USA.

Published in Nature Geoscience

Volume 11 | October 2018 | Pages 749–755

Abstract

During the last deglaciation (19,000 – 9,000 years ago) atmospheric CO_2 increased by ~80 ppm. Understanding the mechanisms responsible for this change is a central theme of paleoclimatology, relevant for predicting future CO_2 transfers in a warming world. Deglacial CO_2 rise hypothetically tapped an accumulated deep Pacific carbon reservoir, but the processes remain elusive as they are under-constrained by existing tracers. Here we report high-resolution authigenic neodymium isotope data in North Pacific sediment cores and infer abyssal Pacific overturning weaker than today during the Last Glacial Maximum but intermittently stronger during steps of deglacial CO_2 rise. Radiocarbon evidence suggestive of relatively "old" deglacial deep Pacific water is reinterpreted here as an increase in preformed ^{14}C age of subsurface waters sourced near Antarctica, consistent with movement of aged carbon out of the deep ocean and release of CO_2 to the atmosphere during the abyssal flushing events. The timing of neodymium isotope changes suggests that deglacial acceleration of Pacific abyssal circulation tracked Southern Hemisphere warming, sea-ice retreat and increase of mean ocean temperature. The inferred magnitude of circulation changes is consistent with deep Pacific flushing as a significant, and perhaps dominant, control of the deglacial rise of atmospheric CO_2.

Introduction

What role did abyssal circulation play in releasing carbon from the deep ocean to the atmosphere during the last deglaciation? Changes of watermass boundaries have been reported based on stable isotopes(Curry & Oppo 2005; Sikes et al. 2017), but paleo-watermass geometry does not necessarily constrain circulation rates(Jansen & Nadeau 2016; Wunsch 2003). Radiocarbon is similarly inconclusive about rates(Marchitto et al. 2007; Broecker et al. 2007; Okazaki et al. 2010; Burke & Robinson 2012; Davies-Walczak et al. 2014; Rose et al. 2010; Cook & Keigwin 2015; Lund et al. 2011). At face value, the presence of ^{14}C-deficient deep waters during the deglaciation may suggest slow abyssal circulation(Lund et al. 2011; Sikes et al. 2016) and argues against carbon release from the deep Pacific. The use of ^{14}C as a circulation rate tracer, however, is complicated by the influence of preformed ^{14}C

age(Wunsch 2003), which depends on air-sea carbon isotope exchange that has a much longer equilibration time-scale than gas exchange (years versus months)(Jones et al. 2014). In modern deep Pacific, the preformed age of Southern Ocean source water accounts for nearly half of the apparent watermass ^{14}C age (Koeve et al. 2015) (i.e., the circulation age is much less than the ^{14}C age) and it likely changed during the deglaciation (Sarnthein et al. 2015; Sikes et al. 2016; Skinner et al. 2010).

The neodymium isotope composition (ε_{Nd}) of authigenic phases in marine sediments offers an independent constraint on Pacific circulation rates. We adopt a model in which the ε_{Nd} and the Nd budgets of the Pacific are significantly influenced by benthic fluxes(Lacan & Jeandel 2005a; Abbott et al. 2015a; Du et al. 2016; Haley et al. 2017) (at all depths, but primarily from >3000 m because of hypsometry, Methods, Fig. 3.S1). On the time-scales of Pacific mixing, under this premise spatial and temporal changes in ε_{Nd} are modulated mostly by the non-conservative effect of sediment exposure time as a function of bottom water residence time(Abbott et al. 2015a; Du et al. 2016; Haley et al. 2017) (Methods). Such a model for modern deep Pacific ε_{Nd} is supported by the strong correlation between core-top authigenic ε_{Nd} and circulation age(Gebbie & Huybers 2012) (Fig. 3.1, Fig. 3.S2).

We propose that to a first order the Pacific benthic Nd flux is approximately constant since the Last Glacial Maximum (LGM) because over this timespan (1) deep-sea sediment provenance changed little on the basinal scale and (2) benthic Nd flux is insensitive to changes in diagenetic redox regimes (Appendix B, Fig. 3.S1). A consequence of this supposition is that temporal changes in authigenic ε_{Nd} in Pacific sediment cores far from the watermass source would be most strongly influenced by the abyssal circulation rate, wherein longer integrated sediment exposure time yields more radiogenic (higher) ε_{Nd}(Abbott et al. 2015a; Du et al. 2016).

Results

Here we reconstruct deglacial Pacific circulation using two new, high-resolution (~200-year deglacial sample interval) authigenic ε_{Nd} records from the Gulf of Alaska (Fig. 3.1). Deeper core EW0408-87JC and its reoccupation IODP Site

U1418 (58.8ºN, 144.5ºW, 3680 m) underlie Pacific Deep Water (PDW), the "oldest", most carbon-rich and for ε_{Nd} the most radiogenic watermass in the ocean today. This site is ideally located to record the integrated exposure time associated with the transit of Antarctic Bottom Water (AABW) across the full meridional span of the Pacific from south to north. Shallower core EW0408-85TC/JC and co-located IODP Site U1419 (59.6ºN, 144.2ºW, 682 m) underlie North Pacific Intermediate Water (NPIW) at a depth less sensitive to abyssal overturning but potentially sensitive to interior stratification and formation of local North Pacific watermasses.

We generated authigenic ε_{Nd} records by leaching non-decarbonated bulk sediments (Methods, Fig. 3.S3), and compared these data to the benthic-planktonic ^{14}C age differences analyzed from the same cores(Davies-Walczak et al. 2014) (Methods). Through a twin-tracer approach, we constrain abyssal circulation rate using ε_{Nd}, and deconvolve the preformed component of ^{14}C age from watermass age (Methods, Appendix B). Because the adjustment time-scales of both tracers are comparable to the time-scales of deglacial climate change, understanding their temporal evolution necessitates a transient modeling approach (Wunsch 2003), which we employ here to constrain circulation history, and by comparison to sensitivity tests with detailed biogeochemical climate models to discuss its implications for the carbon cycle.

Discussions

Deglacial Evolution of North Pacific ε_{Nd}

Values of ε_{Nd} at the deep site were higher during the LGM than today (Fig. 3.2b), suggesting reduced AABW transport into the Pacific in agreement with some model simulations(Menviel et al. 2016). This sluggish circulation would have allowed accumulation of respired carbon in the glacial deep Pacific(Sikes et al. 2017).

Deglacial decrease of our deep site ε_{Nd} (Fig. 3.2b) can be explained by faster overturning (less benthic exposure time). The change in ε_{Nd} near 19 ka coincides with the initial deglacial warming of West Antarctica(Cuffey et al. 2016), reduction of Antarctic sea-ice (indicated by decreasing sea-salt sodium concentration)(WAIS

Divide Project Members 2013), and the first significant postglacial sea-level rise(Clark et al. 2004), but predates the sustained warming of East Antarctica(Parrenin et al. 2013) and the rapid atmospheric CO_2 increase(Marcott et al. 2014) (Fig. 3.2). After this early change, further ε_{Nd} decrease corresponds to steps of atmospheric CO_2 rise between 18-14.5 ka and 13-11.5 ka, during which times sea-ice retreated and temperature increased synchronously in West and East Antarctica together with the global ocean(Bereiter et al. 2018). These intervals also saw negative atmospheric $\delta^{13}C$ excursions(Bauska et al. 2016; Schmitt et al. 2012) and reduced Southern Ocean stratification(Anderson et al. 2009; Basak et al. 2018; Burke & Robinson 2012; Sikes et al. 2016, 2017; Skinner et al. 2010) (Fig. 3.2d, e). All these signals are consistent with the interpretation of North Pacific ε_{Nd} in which accelerated abyssal Pacific circulation was driven mainly by Southern Ocean processes.

Intermediate-depth site EW0408-85TC/JC/U1419 recorded relatively constant ε_{Nd} from the LGM until ~14 ka, then it covaried with the deep record between 14-10 ka (Fig. 3.2a). In this interval, changes in the intermediate-depth record seemingly precede those of the deep record. This difference in timing can be explained by the shorter transient response time of the smaller intermediate-depth Nd reservoir relative to the deep reservoir (see Transient Simulations below). Similar modern and LGM ε_{Nd} values at intermediate-depth support hypotheses that glacial NPIW circulation was similar to today(Menviel et al. 2016). Together deep and intermediate-depth records suggest deglacial acceleration of Pacific circulation and collapse of glacial stratification likely progressed from deep to shallow(Sikes et al. 2017).

Transient Simulations

We quantify plausible changes in circulation from these data using a six-box model of the Pacific, starting with modern geostrophic flows well-constrained by hydrographic data(Talley 2008, 2013) (Fig. 3.S4). We simulate deglacial ε_{Nd} and apparent (^{14}C) watermass age by hypothetically varying AABW transport scaled to Antarctic climate records, and adjust mixing between NPIW and PDW and the preformed age of AABW (Methods, Appendix B). Acknowledging the limitations of

box models, we gain quantitative insight into plausible circulation rate changes from these relatively simple perturbations.

The deglacial North Pacific deep ε_{Nd} observations are consistent with acceleration of abyssal circulation produced by scaling AABW transport to the rate change of atmospheric CO_2 (Fig. 2c, 3a, c), implying that whatever processes responsible for circulation changes can also plausibly relate to CO_2 changes. Mechanistically, scaling the transport to the rates of Antarctic warming or sea-ice retreat yields similarly reasonable solutions (Fig. 3.4, Appendix B). For example, the 19-ka ε_{Nd} event found at our deep site can be explained if circulation rate is scaled to early sea-ice retreat rate (as documented by ice core sodium) and warming in West Antarctica. We speculate that this first acceleration of abyssal Pacific circulation, although linked to Antarctic climate events, may have occurred in a heavy ice-cover regime that was not yet amenable to substantial CO_2 venting.

In our box model, AABW transport into the Pacific changes by a factor of three, from ~8 Sv (1 Sv = 10^6 m^3 sec^{-1}) during the LGM, to ~20-25 Sv during the deglacial intervals of rapidly rising atmospheric CO_2, followed by relaxation to the modern value of ~14 Sv(Talley 2013) (Fig. 3.3a, Fig. 3.S5). By comparing these results to carbon-cycle sensitivities from more comprehensive models, we can estimate plausible impacts of our inferred deglacial abyssal Pacific circulation changes on atmospheric CO_2 and its $\delta^{13}C$. Adopting model sensitivities of 1.5~3.4 ppm/Sv(Lauderdale et al. 2017; Menviel et al. 2014) for atmospheric pCO_2 and -0.0069‰/Sv(Menviel et al.) for atmospheric $\delta^{13}C$ to changes of AABW transport, a ~12-17 Sv increase of AABW transport in the early deglaciation could result in ~20-50 ppm increase of pCO_2 and ~0.08-0.12‰ decrease of $\delta^{13}C$. The ~9 Sv increase in the late deglaciation could result in ~15-30 ppm increase of pCO_2 and ~0.06 ‰ decrease of $\delta^{13}C$. These estimates are comparable to the observed stepwise changes of ~50 ppm and ~30 ppm increase of pCO_2 and ~0.3‰ and ~0.1‰ decrease of $\delta^{13}C$ in these intervals(Bauska et al. 2016; Marcott et al. 2014; Schmitt et al. 2012) respectively (Fig. 3.2c, d), suggesting that acceleration of the abyssal Pacific

circulation rate may be an important, and perhaps dominant, control of deglacial atmospheric CO_2 rise.

In the context of these abyssal circulate rate changes, the intermediate-depth ε_{Nd} record can be simulated by varying NPIW-PDW exchange (related to subsurface stratification and mixing), wherein progressively upward de-stratification started in the early stage of the Antarctic warming intervals (Fig. 3.3e, g, Fig. 3.S5). The strong NPIW-PDW exchange required in the model at ~17.5 ka and ~12.5 ka reflects weaker intermediate-to-deep stratification than today, implying easier access of carbon from the deep ocean reservoir to the surface and the potential for some CO_2 venting in the North Pacific(Davies-Walczak et al. 2014; Gray et al. 2018b). Differences in our model transient responses of ε_{Nd} and ^{14}C age in the intermediate and deep boxes to the same physical events (Fig. 3.3) highlight that tracers with different geochemistries need not respond "in-phase" with each other but are fundamentally mediated by tracer residence times at various depths.

Superficially, inferred deglacial acceleration of abyssal Pacific circulation seems to contradict discoveries of ^{14}C-deficient deep watermasses in the North Pacific(Lund et al. 2011) (Fig. 3.3d). Our simulations, however, can reproduce the observed apparently "old" deglacial watermass ages by increasing the preformed ^{14}C age of southern-source waters at times of increasing AABW transport (Fig. 3.3b, Fig. 3.S6). This increase in preformed ^{14}C age (by 1000 years) would have made the ^{14}C age (with respect to the atmosphere) of Antarctic surface water approach, but not exceed, that of the deep Pacific, implying efficient mixing of PDW into circumpolar regions(Sikes et al. 2017) and inefficient isotopic gas exchange. In our model, changes of preformed age dominate over that of circulation rate in deep Pacific ^{14}C records (Fig. 3.3d).

Greater deglacial preformed ^{14}C ages of Southern Ocean watermasses may result from weaker stratification and increasing upwelling around Antarctica(Anderson et al. 2009). Inefficient carbon isotopic equilibration is reasonable given ice-strewn waters as sea-ice retreated and excess CO_2 vented to the

atmosphere. Reconstructions of deglacial preformed ^{14}C age in the AABW formation region do not exist yet, but a recent global data synthesis suggests changes of deglacial Southern Ocean surface preformed age are necessary to explain the distribution of benthic ^{14}C in the ocean interior(Zhao Ning et al. 2018). A subantarctic record(Skinner et al. 2010) (MD07-3076, 44°4.46'S, South Atlantic) shows pronounced increases of surface reservoir age of magnitudes (~1000 years) and timing similar to our model prediction. High apparent deglacial reservoir ages were also found in Eastern Equatorial Pacific(de la Fuente et al. 2015) and South Pacific(Rose et al. 2010), implying that redistribution of carbon in shallow subsurface mode waters sourced from the Southern Ocean propagated high preformed ^{14}C to lower latitude upwelling regions where some CO_2 could have vented during the deglaciation(Martínez-Botí et al. 2015).

In the North Pacific, deep-to-intermediate gradient of benthic ^{14}C reservoir age was smaller than today during our inferred NPIW-PDW mixing events (Fig. 3.3f), even as apparent ^{14}C watermass ages at both depths increased (Fig. 3.3d, h). This too reflects changes in preformed ^{14}C in the interior Pacific: the deep "old" ^{14}C age signal reached intermediate-depth as abyssal stratification weakened during the deglaciation.

Alternative hypotheses

Changes in preformed ε_{Nd} values in Southern Ocean source waters alone cannot explain our North Pacific data, because, unlike ^{14}C, the effect of preformed properties on deep-sea ε_{Nd} is limited(Abbott et al. 2015a; Du et al. 2016; Haley et al. 2017) (Methods, Appendix B). In our model we prescribe the preformed ε_{Nd} using published South Ocean records as boundary conditions (Methods, Appendix B, Fig. 3.S7). The model result therefore accounts for available ε_{Nd} data from both the Southern Ocean (dominated by mixing) and North Pacific (dominated by benthic exposure time after the long abyssal transit).

Production of North Pacific intermediate or Deep Water also cannot explain our North Pacific observations, with the possible exception of a short interval (16~17

ka) when benthic-planktonic age differences became smaller than today at our intermediate-depth site(Davies-Walczak et al. 2014; Okazaki et al. 2010; Rae et al. 2014) (Fig. 3.3h, Appendix B). Even in this case benthic ^{14}C precludes a northern-sourced watermass reaching the deep ocean (>2700 m, depth of W8709A-13PC): not only the deep site benthic-planktonic ^{14}C age differences remained higher than today but also the deep-to-intermediate depth benthic ^{14}C gradient increased during this interval (Fig. 3.3d, f, Fig. 3.S8). Thus, if an intermediate watermass formed in the Sea of Okhotsk and Bering Sea (as it does today), its effects were small; the ε_{Nd} provide no evidence for such a watermass in the Northeast Pacific (Appendix B).

Theoretical arguments suggest that Southern Ocean surface buoyancy forcing can directly regulate stratification in the ocean interior(Jansen & Nadeau 2016), even in the North Pacific. As such, it is not necessary to invoke local deep-water formation to explain the collapse of intermediate-to-deep stratification suggested by our data and simulations. Rather, the strong correlation between our deep records and Antarctic climate can be readily reconciled if Antarctic forcings were a significant factor controlling the subsurface watermass properties of the North Pacific.

Finally, the ε_{Nd} data are inconsistent with hypotheses that changes of the Atlantic Meridional Circulation (AMOC) controlled properties of the deep Pacific during the deglaciation (Appendix B, Fig. 3.S7). Reduction of low-ε_{Nd} North Atlantic Deep Water (NADW) should lead to an increase of deep Pacific ε_{Nd}(Friedrich et al. 2014), yet during the intervals of weakest AMOC(McManus et al. 2004) (14.5-17.5 ka and 11.5-12.5 ka) both deep North Pacific and Southern Ocean(Basak et al. 2018) ε_{Nd} decreased.

Conclusion

A Search for Mechanisms and Future Implications

Our data and model simulations lead to a conceptual understanding of the deep Pacific circulation and the deglacial flushing of its carbon reservoir via abyssal overturning from the south(Talley 2013) (Fig. 3.5). Although our data do not fully constrain the watermass transformation processes around Antarctica, they provide key

constraints regarding the scale and timing of changes in the abyssal overturning cell and the extent of gas-isotope exchange required to explain the ^{14}C signal in ocean interior.

A likely candidate mechanism is found in Antarctic sea-ice, which controls both buoyancy flux(Jansen & Nadeau 2016; Marzocchi & Jansen 2017) and gas exchange(Jones et al. 2014; Loose et al. 2014). Most model simulations generate expanded sea-ice during glacial times and relate sea-ice area to buoyancy loss and increased abyssal stratification(Jansen & Nadeau 2016; Marzocchi & Jansen 2017), but the effects of sea-ice on gas exchange and isotopic equilibration remain poorly known(Loose et al. 2014). During the deglaciation, sea-ice breakup and transport in a divergent wind field during warming events may create a net freshwater export to subpolar latitudes important for watermass transformation(Abernathey et al. 2016). The intensity and position of Southern Hemisphere westerlies also play roles in northward transport of near-surface waters, southward return flow of PDW to the Antarctic, and the upwelling of deep water to the surface(Anderson et al. 2009). In addition, accumulation of geothermal heat(Adkins et al. 2005) may have added buoyancy to the ocean interior due to both sluggish glacial circulation and an increase of deglacial hydrothermal activity(Lund et al. 2016). Further exploration of possible mechanisms will be informed by the strong constraint on changing circulation rates provided by our North Pacific ε_{Nd} data.

The deglacial changes in abyssal circulation suggested here can be envisioned as a transition from a predominantly haline stratified glacial mode to a weakly thermal stratified modern mode(Adkins et al. 2002; Zahn & Mix 1991) (Fig. 3.5), which likely implies points of instability. This appears to happen in two main steps in the deep Pacific, both in the north (this study) and south(Sikes et al. 2017), coincident with Antarctic warming and CO_2 rise. Steps in the deep Atlantic occurred later during the Bølling-Allerød and early Holocene warming periods(Roberts et al. 2016), and are not aligned with CO_2 increase. The abyssal Pacific circulation, forced from the south, is more likely to have tapped the larger deep ocean carbon reservoir, and appears to be a key to deglacial CO_2 rise.

At present, the deep Pacific still retains a substantial carbon reservoir, and future transfer of carbon from this reservoir to the atmosphere via the Southern Ocean is conceivable. Projections of future circulation have so far focused mainly on changes forced by meltwater in the North Atlantic. Our reconstructions of Pacific overturning in the past motivate additional focus on the Southern Ocean and the Pacific abyssal circulation, for which there is no consensus in models even as to the sign of potential future changes(Meijers 2014).

Methods

Neodymium isotopes

The authigenic ε_{Nd} records were generated using the "HH4" method described previously(Du et al. 2016) wherein non-decarbonated bulk sediments were reductively leached to extract Nd from authigenic Fe-Mn oxyhydroxides. This method was extensively tested on a large array of core-top and volcanic ash samples to show that it can faithfully extract authigenic components with negligible contamination from lithogenic phases, including volcanic ash(Du et al. 2016). Decarbonation was abandoned as it likely leads to lithogenic contamination(Blaser et al. 2016; Howe et al.; Molina-Kescher et al. 2014a; Tachikawa et al. 2017; Wilson et al. 2013; Wu et al. 2015). The validity of our leaching method is shown using various geochemical tools(Du et al. 2016) (Fig. 3.S3). Untreated sediments for about half of the samples were also digested using a CEM MARS-6 microwave following our published methodolgy(Muratli et al. 2012) for analysis of bulk sediment ε_{Nd}, which reflects the ε_{Nd} of lithogenic sources that dominate the bulk sediment Nd budget.

Nd isotope analysis was done on a *Nu Instruments* MC-ICP-MS in the W.M. Keck Collaboratory for Plasma Spectrometry at Oregon State University(Abbott et al. 2015a; Du et al. 2016). Mass bias was corrected by normalizing to $^{146}Nd/^{144}Nd=0.7219$ using an exponential law(O'Nions et al. 1979). Samples were bracketed by the JNdi-1 standard(Tanaka et al. 2000) and an in-house standard. Instrumental drift was corrected by normalizing the JNdi-1 analyses to their accepted $^{143}Nd/^{144}Nd$ ratio (0.512115(Tanaka et al. 2000)). The 2σ $^{143}Nd/^{144}Nd$ uncertainty of

JNdi-1 standard was 10 ppm (n=278). The 2σ external uncertainty of the in-house standard was 15 ppm (n=274), i.e. ±0.29 ε-unit, which is adopted for uncertainty bars in the figures. Total procedure blanks for Nd isotope analyses of the leachates and digests were 53±52 pg (n=19); i.e., <0.1% of the sample yields. Total sediment digest repeats of two USGS reference materials AGV-1 and BHVO-2 for the $^{143}Nd/^{144}Nd$ ratio were 0.512793±0.000018 (2σ, n=10) and 0.512985±0.000024 (2σ, n=9), both in excellent agreement with published values of 0.512791±0.000013 (2σ) and 0.512984±0.000011 (2σ) respectively(Weis et al. 2006).

Radiocarbon and chronology

The age models of EW0408-85TC/JC and EW0408-87JC were published before and created using planktonic foraminiferal dates and reservoir ages constrained by tephrochronology and correlation(Davies-Walczak et al. 2014; Praetorius et al. 2015; Praetorius & Mix 2014). The sample ages are calculated using Bchron(Haslett & Parnell 2008) taking into account sample thickness rather than interpolating calibrated ^{14}C dates. Radiocarbon based age models of U1419 and U1418 are provided by Mix et al. (*in preparation*) and Walczak et al., (*in preparation*). The age models of these two sites are created using planktonic ^{14}C dates of exceptionally high density: 71 dates from EW0408-85TC/JC/U1419 and 33 dates from EW0408-87JC/U1418 in the last 22 ka. Comparison to tephrochronology suggests negligible changes in surface-ocean reservoir in this region(Praetorius & Mix 2014) and this lends high confidence in our age models. Benthic ^{14}C record of EW0408-85TC/JC was reported previously(Davies-Walczak et al. 2014). Benthic ^{14}C records of EW0408-87JC and U1419 are provided by Praetorius et al., (*under review*) and Walczak et al., (*in preparation*) respectively.

Benthic ^{14}C record from core W8709A-13PC (42.1ºN, 125.8ºW, 2710 m) on the Gorda Ridge, Northeast Pacific, complements the deep record of EW0408-87JC, which extends only to ~17 ka. During the deglaciation these two records covary (Fig. 3.3d). Here we use only the new ^{14}C dates from core W8709A-13PC generated at the W. M. Keck Carbon Cycle Accelerator Mass Spectrometry Laboratory at the

University of California, Irvine(Lund et al. 2011). Earlier published data from this core are not included because they came from various laboratories; some of the earlier dates are inconsistent with or have larger uncertainties than the newer high-quality data. The original age model of W8709A-13PC was created using planktonic dates and a reservoir correction of 730±200 year(Lund et al. 2011). For internal consistency, we use Bchron(Haslett & Parnell 2008) to generate Bayesian age models with both the original reservoir correction and a correction of 870±80 year (i.e. ΔR=470±80 year) for our Gulf of Alaska cores(Davies-Walczak et al. 2014). The median ages of these two models only differ by ~150 year (i.e., the difference in the reservoir age) and do not affect our interpretations. In the figures we show the age model created using the tephra-calibrated reservoir corrections from the Gulf of Alaska.

The ε_{Nd}-^{14}C age twin-tracer approach

The distribution of a tracer in the ocean is controlled not only by circulation (mixing, circulation rate) but also the preformed properties of the source waters and its interior sources and sinks. In modern deep Pacific, nearly half of the ^{14}C watermass age is attributed to preformed age (equivalent to surface reservoir age at the surface ocean), while circulation age (also known as ventilation age, ideal age etc.) accounts for the other half(Gebbie & Huybers 2012; Koeve et al. 2015). The large influence of preformed age reflects inefficient ^{14}C exchange in surface waters around Antarctic (Appendix B)(Jones et al. 2014). Benthic ^{14}C age therefore can be used as a tracer of circulation rate only if the preformed age remained constant in the past or is independently known.

Unlike ^{14}C, surficial sources (atmospheric and riverine) are minor in the marine Nd budget(Abbott et al. 2015b; Arsouze et al. 2009; Rempfer et al. 2011; Tachikawa et al. 2003), which is dominated by benthic flux from deep sea (>3000 m) sediments (Appendix B, Fig. 3.S1). Consequently, deep sea ε_{Nd} is not sensitive to its preformed properties but sensitive to changes in abyssal circulation rate, which controls the exposure time of deep water to benthic flux(Abbott et al. 2015a; Du et al.

2016; Haley et al. 2017). Modern Pacific overturning circulation is dominated by the abyssal AABW cell(Talley 2013): it is the most dense major watermass in the ocean, and it spreads northward in the Pacific attached to the abyssal seafloor. Consequently, its ε_{Nd} is most susceptible to benthic modification(Haley et al. 2017), making ε_{Nd} an ideal tracer to study the lower branch of the Global Overturning Circulation. This connection is strong also because watermass transformation in this lower branch happens mostly along the benthic boundaries due to bottom enhanced mixing: abyssal circulation in the Pacific thus reflects basin shape, and its basic structure is stable(de Lavergne et al. 2015, 2017; Ferrari et al. 2016) and benthic sources of Nd diffuse into the ocean interior efficiently(Abbott et al. 2015a; Haley et al. 2017).

In the deep Pacific, the benthic flux has more positive ε_{Nd} than the incoming source waters from the Southern Ocean(Abbott et al. 2015a; Du et al. 2016). We therefore expect the watermass ε_{Nd} to become more positive as it ages and its exposure time to the flux increases(Abbott et al. 2015a; Du et al. 2016). This predicted benthic flux effect is demonstrated in the strong correlation between modern core-top authigenic and seawater ε_{Nd} and ^{14}C based circulation age(Gebbie & Huybers 2012) (Fig. 3.S2). Our bottom-up interpretation of authigenic ε_{Nd} originates from the improved understanding of marine Nd budget in recent years(Abbott et al. 2015a,b, 2016; Arsouze et al. 2009; Du et al. 2016; Haley et al. 2017; Lacan & Jeandel 2005a; Rempfer et al. 2011; Tachikawa et al. 2003). An alternate interpretation of authigenic ε_{Nd} as a tracer for conservative watermass mixing assumes (1) dissolved Nd is predominantly introduced to the ocean at the surface; (2) authigenic phases passively inherit bottom water ε_{Nd} signatures; (3) preformed watermass end-member ε_{Nd} are time-invariant, all of which have been questioned(Abbott et al. 2015a,b; Arsouze et al. 2009; Du et al. 2016; Howe et al. 2016c; Jones et al. 2008; Lacan & Jeandel 2005a; Rempfer et al. 2011; Roberts & Piotrowski 2015; Tachikawa et al. 2003). The bottom-up interpretation explains the distributions of not only bottom water ε_{Nd}, but also that of authigenic phases(Abbott et al. 2015a,b, 2016; Du et al. 2016; Haley et al. 2017). Under this framework the

authigenic and bottom water ε_{Nd} need not be the same, as seen in the consistent offset between them in the Pacific (Fig. 3.S2).

In our ε_{Nd}-^{14}C age twin-tracer approach, deep ocean ε_{Nd} is used to constrain abyssal circulation rate because of its high sensitivity to this parameter. The inferred circulation rate information is then used to isolate the preformed age component of the deep ocean ^{14}C. In doing so we also test whether the observed changes in deep ε_{Nd} and ^{14}C age were caused by far field (i.e. Southern Ocean) or local (i.e. North Pacific) factors. This test is aided by considering also the intermediate-depth ε_{Nd} and ^{14}C age, the changes of which are either caused by variations in local intermediate/deep water formation or mixing with the deep ocean. Overall, we seek a physical explanation of deglacial Pacific circulation (circulation rate and mixing) that is consistent with ε_{Nd} and ^{14}C age at both intermediate and deep sites in the North Pacific.

Box model

Our twin-tracer approach is quantified by transiently modeling these two tracers in the Pacific during the deglaciation using a six-box model. Transient modeling is necessary as neither circulation nor tracer distributions are expected to be under steady state during the deglaciation considering the abrupt climate changes. The model was based on the box inverse model of Talley(Talley 2003, 2008, 2013), wherein zonal averages of meridional transports at different density layers across 28°S and 24°N were computed using hydrographic data. We merged the density layers into six boxes and defined these boxes with depth. The configuration of these boxes is presented in Figure 3.S4. The governing equation of ε_{Nd} in each box is (Appendix B)

$$\frac{d\varepsilon_{Nd}}{dt} = \frac{1}{\tau_{Nd}}\varepsilon_{Nd}^{B} + \frac{1}{\tau_{w}}\sum m^{i}\varepsilon_{Nd}^{i} - (\frac{1}{\tau_{Nd}} + \frac{1}{\tau_{w}})\varepsilon_{Nd} \quad , (1)$$

where τ_w and τ_{Nd} are the residence times of water (with respect to watermass transport) and Nd (with respect to benthic flux) in the box respectively; ε_{Nd}^{B} is the isotope composition of the benthic source; m^i and ε_{Nd}^{i} are the concentration weighted

mixing ratio and isotope composition of the i^{th} source water of the box, representing the conservative mixing of the preformed values. In the box model context local water residence time is equivalent to benthic exposure time(Abbott et al. 2015a) and circulation age(Gebbie & Huybers 2012). Here we have ignored surficial (atmospheric and riverine) sources of Nd as they are negligible in the Pacific Nd budget (Appendix B).

$$\text{At steady state, } \varepsilon_{Nd} = \frac{\tau_w}{\tau_{Nd}+\tau_w}\varepsilon_{Nd}^{B} + \frac{\tau_{Nd}}{\tau_{Nd}+\tau_w}\sum m^i \varepsilon_{Nd}^{i} \text{ , i.e. } \varepsilon_{Nd} \text{ of the box}$$

equals the weighted average of the benthic source (non-conservative) and preformed (conservative) terms, and the weighing factor is controlled by the ratio τ_w/τ_{Nd}. This means the expression of the benthic source is modulated by circulation rate that controls τ_w, assuming τ_{Nd} is constant as we expect during the deglaciation (Appendix B). In the Pacific τ_{Nd} (~400 year, Appendix B) is much shorter than τ_w (~1000 year)(Gebbie & Huybers 2012; Koeve et al. 2015), and consequently the benthic source term dominates, explaining the strong correlation between circulation age and ε_{Nd} (Fig. 3.1c, Fig. 3.2Sa). This contrasts with the modern North Atlantic where τ_{Nd} is longer than τ_w (~200 year)(Gebbie & Huybers 2012; Koeve et al. 2015) and where the major deep watermass NADW is largely isolated from abyssal seafloor by the underlying AABW, leading to quasi-conservative behaviors of ε_{Nd}(Haley et al. 2017; Lambelet et al. 2016). The dominance of the benthic flux does not negate the considerable contribution of preformed component to the Pacific Nd budget, and our interpretation of ε_{Nd} therefore rests on the interplay of these two components which is mediated by circulation rate (Appendix B).

Because of the differences between authigenic and bottom water ε_{Nd} (Fig. 3.S2b) and between regional and box mean seawater ε_{Nd}, authigenic ε_{Nd} from an individual site may be offset from the box mean seawater ε_{Nd}. Based on our previous survey of the authigenic and seawater ε_{Nd} in the Gulf of Alaska(Du et al. 2016), we adopt an empirical constant that the authigenic ε_{Nd} at our two sites are both +2.8 ε higher than the mean seawater ε_{Nd} of the NPIW and PDW boxes. Therefore, simulated seawater results are converted to equivalent authigenic ε_{Nd} using this

constant offset. We note that our interpretations, and the model we generate, rely only on relative changes in ε_{Nd}. The model can be run with either constant (default) or dynamic Nd concentrations (Appendix B).

In modeling watermass ^{14}C age, we follow the approach of decomposing it to preformed and circulation age components(Gebbie & Huybers 2012; Koeve et al. 2015) (Appendix B). The governing equation of the watermass age a in each box is

$$\frac{da}{dt} = \frac{1}{\tau_w}\sum m^i a^i + 1 - \frac{1}{\tau_w} a, \quad (2)$$

where m^i and a^i are the mixing ratio and age of the i^{th} source water of the box, representing conservative mixing of the preformed ages; the term *1* indicates aging of the watermass by 1 unit of time per unit time step, i.e. the interior source term. At steady state $a = \sum m^i a^i + \tau_w$. Unlike ε_{Nd}, the preformed and the circulation age terms are equally weighted, i.e., the watermass age is sensitive to both components. This leads to the possibility that the observed changes in apparent watermass ^{14}C age may not reflect changes in circulation rate alone.

The differences between the modeled watermass ages of the NPIW and PDW boxes and the North Pacific surface reservoir age can be directly compared to the benthic-planktonic ^{14}C age differences in our records. Here we assume little or no change in the surface-ocean reservoir age at our North Pacific sites. Based on correlation and tephrochronology, near-surface reservoir ages are constrained to be relatively constant (within a few hundred years) in this region during the deglacial interval(Praetorius et al. 2016; Praetorius & Mix 2014).

The model is first configured to describe modern distributions of ε_{Nd} and watermass age in the Pacific (Appendix B). We estimated benthic sources and sinks in each box using modern observations of seawater and authigenic ε_{Nd}. In the model seafloor area, including that from the continental shelf and slope and the abyssal plain, exposed in each box is estimated using hypsometric curves(Menard & Smith 1966) (Appendix B, Fig. 3.S1 and Table 3.S2).

Transient simulations

In our simulations we assume that benthic flux is constant, which is equivalent in assuming τ_{Nd} is constant (Appendix B). Our estimates show that the Pacific Nd budget is dominated by benthic flux from deep sea sediments (>3000 m) because most of the seafloor area is concentrated below this depth (Appendix B, Fig. 3.S1). This suggests that the basinal benthic flux should be stable on the time scale of glacial-interglacial cycles, as large-scale deep-sea sediment provenance is primarily controlled by tectonic activities operating on much longer time scales(Dunlea et al.; McLennan et al. 1993; Ziegler et al. 2007). We further show in the Appendix B that deglacial changes in surficial fluxes of Nd (dust and freshwater/meltwater fluxes) do not significantly affect the Pacific Nd budget, and benthic flux is also not sensitive to sediment redox state (Fig. 3.S1) and sedimentation rate. Instead, changes in Southern Ocean watermass transport is the most likely candidate to explain our ε_{Nd} records.

Under this framework, the ε_{Nd} and watermass age of the North Pacific boxes will change in response to forcings specified on the deep Southern Ocean boundary (controlling the influx of Southern Ocean deep waters), the North Pacific surface boundary (controlling local formation of intermediate and potentially deep water) and the NPIW-PDW boundary (controlling vertical mixing) (Fig. 3.S4). All the parameters associated with the AAIW box are fixed, as they have limited effect on the North Pacific boxes.

In the deglacial simulations reported in Figure 3.3 we identify three adjustable parameters: the scaling factor applied to the transports associated with AABW, i.e. F2, F3 and F4 (Fig. 3.S4); the scaling factor applied to the PDW-NPIW exchange flux, i.e. F6; the preformed age anomaly of AABW specified at the southern boundary. We multiply the water fluxes by their respective scaling factors in model simulations. The preformed age anomaly at the 28°S boundary is assumed to be the same as at the AABW surface formation region, and the implemented preformed age boundary condition is the modern boundary condition of 1600 years plus this anomaly (Appendix B). In these simulations Nd concentrations in each box are fixed.

The ε_{Nd} at the southern boundaries are specified based on paleo-reconstructions in the South Pacific(Basak et al. 2018; Elderfield et al. 2012; Hu et al. 2016a; Molina-Kescher et al. 2016; Noble et al. 2013): preformed ε_{Nd} of AABW and AAIW are 1.8 ε and 1 ε higher in the LGM respectively and then decrease to their modern values linearly from 17.5 to 11 ka (Appendix B, Fig. 3.S7).

We first carried out LGM steady state simulations to generate initial values for the deglacial transient simulations. In the sensitivity tests described later (Appendix B), we adjusted the three parameters to fit the LGM solution to our observations. The chosen parameters are a scaling factor of 0.55 applied to the AABW transports; a scaling factor of 0.6 applied to PDW-NPIW exchange; and an AABW preformed age anomaly of -400 years (Fig. 3.S5, 3.S6).

In the deglacial transient simulations, we first adjusted the AABW transport, which was scaled to the rate change of atmospheric CO_2, to explain our deep North Pacific ε_{Nd} record. The rationale is that if changes in AABW transport can explain changes of atmospheric CO_2 then it should also explain our ε_{Nd} record. We then adjusted the preformed age of AABW such that together with the inferred AABW transport the deep watermass age record was explained. Next, we adjusted the NPIW-PDW exchange flux to explain the intermediate-depth benthic age record. Once these parameters are specified, modeled intermediate-depth ε_{Nd} should also fit our observation if our physical explanation is valid, and this serves as an independent check on the model. The deglacial time series of these parameters and model results are shown in Figure 3.3. In these simulations we did not seek exact fits to our data but aimed to explain the main events in the data. Therefore, we used simple square wave schemes for the preformed age of AABW and NPIW-PDW mixing parameters. These simulations that best represent our data are called “standard simulations” and plotted using solid lines in Figure 3.3.

Sensitivity tests

In Figure 3.3 we also show a few model sensitivity tests that are indicated using dashed lines. In Fig. 3.3d we show experiments with fixed preformed age and

fixed circulation rate, i.e. constant AABW preformed age and transport respectively. In Fig. 3.3h we show an experiment with fixed NPIW-PDW exchange. These tests differ from the standard simulation in that only the tested parameters were changed. To run these tests, LGM steady state solutions were first found that also differ from the standard case only in the tested parameters. Extra simulations in which we scaled the AABW transport to other Antarctic forcings are reported in Figure 3.4 (Appendix B). These simulations are the same as the "standard simulations" except the scaling factor applied to AABW transport.

In the Appendix B we also use sensitivity tests to (1) find the optimal combination of the parameters for the LGM steady state solution that was used to initialize the deglacial transient simulations (Fig. 3.S5); (2) show that the uncertainty in the preformed age of AABW during the LGM does not affect our deglacial transient simulations (Fig. 3.S6); (3) show that our deep North Pacific ε_{Nd} record cannot be explained by changes in the preformed ε_{Nd} of AABW that might be related to changes in North Atlantic Deep Water formation (Fig. 3.S7); (3) show that our data are inconsistent with enhanced formation of NPIW or formation of local deep water in the subpolar Northeast Pacific (with the exception of the short interval 16-17 ka), even when plausible changes of the North Pacific surface preformed ε_{Nd} and age are considered (Fig. 3.S9); (10) show that whether fixing Nd concentrations or simulating them dynamically has little influence on the simulated ε_{Nd} (Fig. 3.S10).

Acknowledgements

We thank Jesse Muratli for assistance with bulk sediment digestion and Andy Ungerer for assistance with elemental and isotope analyses in the W.M. Keck Collaboratory for Plasma Spectrometry at Oregon State University. We thank the OSU Marine and Geology Repository and the International Ocean Discover Program for providing sediment samples. IODP-U1418 samples were provided by Christina Belanger. This study was supported by NSF grant MGG-1357529 (A.C.M and B.A.H).

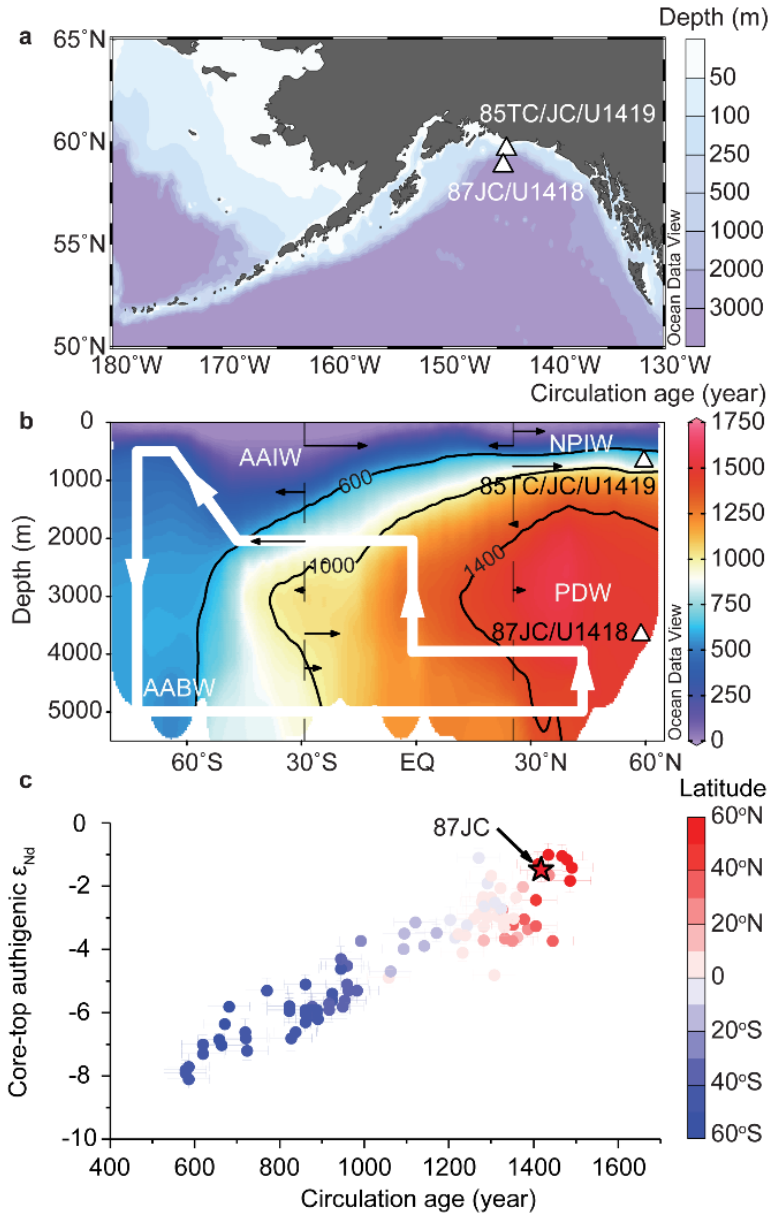

Figure 3.1. Study sites and Pacific circulation.

a, Location of the intermediate-depth (EW0408-85TC/JC/U1419) and the deep (EW0408-87JC/U1418) sites in the Gulf of Alaska. **b,** A meridional (138ºW) section of circulation age in the Pacific(Gebbie & Huybers 2012). Solid small arrows indicate modern water transport across the 28ºS and 24ºN hydrographic sections and thick arrows show the schematic abyssal circulation(Talley 2008). **c,** Relationship between Pacific core-top authigenic ε_{Nd} (>2500 m, Fig. 3.S2, with 2σ analytical uncertainty) and circulation age (1σ=50 year)(Gebbie & Huybers 2012). The star symbol is Site EW0408-87JC.

Figure 3.2. Deglacial North Pacific ε_{Nd} compared to global climate records.

Authigenic ε_{Nd} from site EW0408-85TC/JC/U1419 (**a**) and site EW0408-87JC/U1418 (**b**). Error bars in **a** and **b** indicate long term 2σ (0.29 ε) external reproducibility (Methods). **c**, Ice core CO_2 and its rate of change(Marcott et al. 2014; Bereiter et al. 2015). **d**, $\delta^{13}C$ of atmospheric CO_2(Bauska et al. 2016; Schmitt et al. 2012). **e**, Southern Ocean opal flux from core TN057-13PC4(Anderson et al. 2009). **f**, Temperature anomalies from West (WAIS Divide)(Cuffey et al. 2016) and East (EAT)(Parrenin et al. 2013) Antarctica, and sea salt sodium concentration (ssNa, 50-year median value, a proxy for sea-ice) from WAIS Divide(WAIS Divide Project Members 2013). **g,** Mean ocean temperature anomaly with 1σ uncertainty(Bereiter et al. 2018). **h,** North Atlantic $^{231}Pa/^{230}Th$ records with 1σ uncertainty(Böhm et al. 2015; McManus et al. 2004). The blue shaded interval marks the early deglacial increase of temperature and decrease of sea-ice in West Antarctica. The yellow shaded intervals mark the synchronous increase of atmospheric CO_2, decrease of sea-ice and increase of temperature in both West and East Antarctica, and rise of global ocean mean temperature.

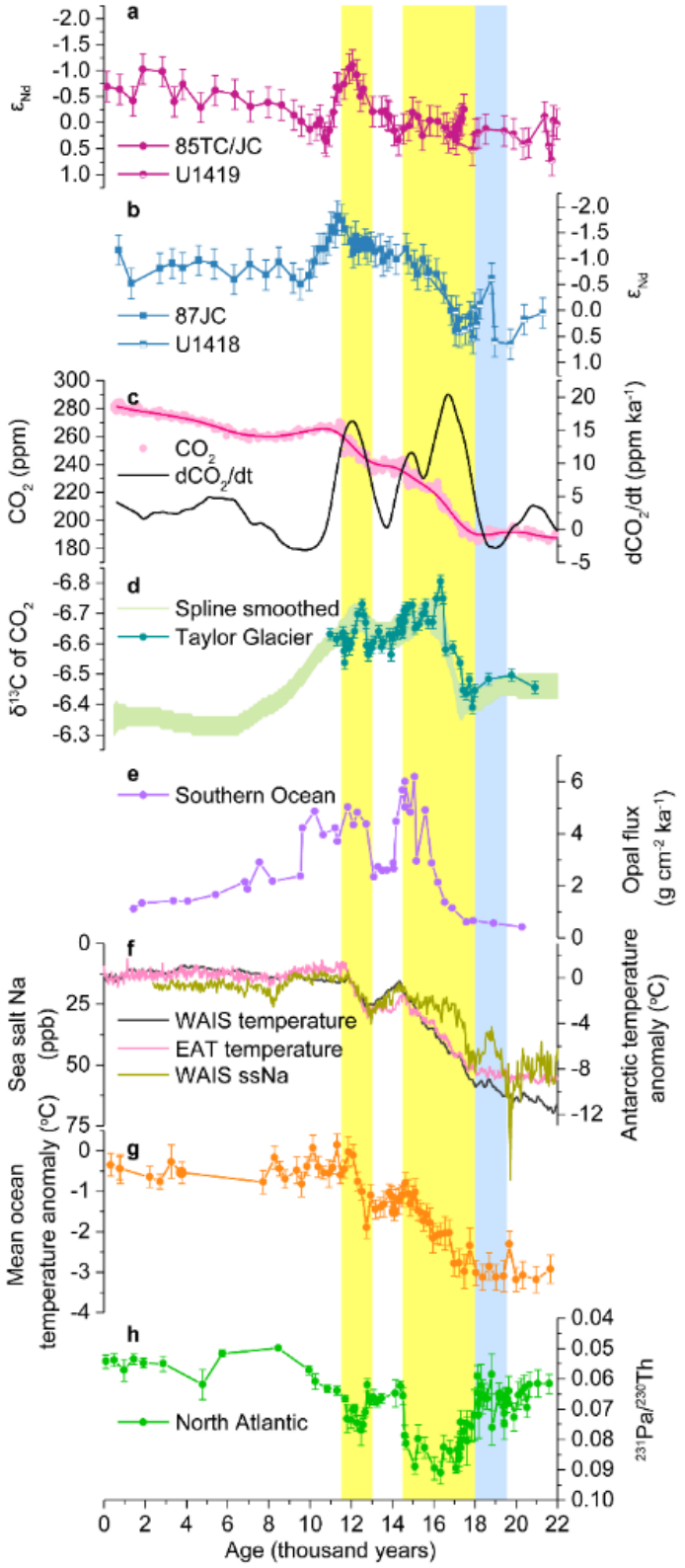

Figure 3.2. Deglacial North Pacific ε_{Nd} compared to global climate records.

Figure 3.3. Transient simulations of North Pacific circulation tracers.

a, AABW transport scaled to the rate change of atmospheric CO_2. b, The preformed ^{14}C age of AABW. c, Modeled and measured ε_{Nd} at deep site EW0408-87JC/U1418. d, Modeled and measured benthic-planktonic age differences at deep site EW0408-87JC and W8709A-13PC(Lund et al. 2011) (Methods). Error bars are 1σ analytical uncertainties. e, PDW-NPIW exchange. f, Benthic ^{14}C age gradients between NPIW (EW0408-85TC/JC/U1419(Davies-Walczak et al. 2014)) and PDW (EW0408-87JC and W8709A-13PC(Lund et al. 2011)) boxes (95% confidence intervals include uncertainties of both age models and ^{14}C measurements), compared to the model output. The dash line indicates the modern gradient(Key et al. 2004). g and h, same as c and d respectively but for the intermediate-depth site EW0408-85TC/JC/U1419. The standard simulations are plotted using solid lines. Dashed lines indicate model sensitivity tests (Methods). The color shaded intervals are the same as in Figure 3.2.

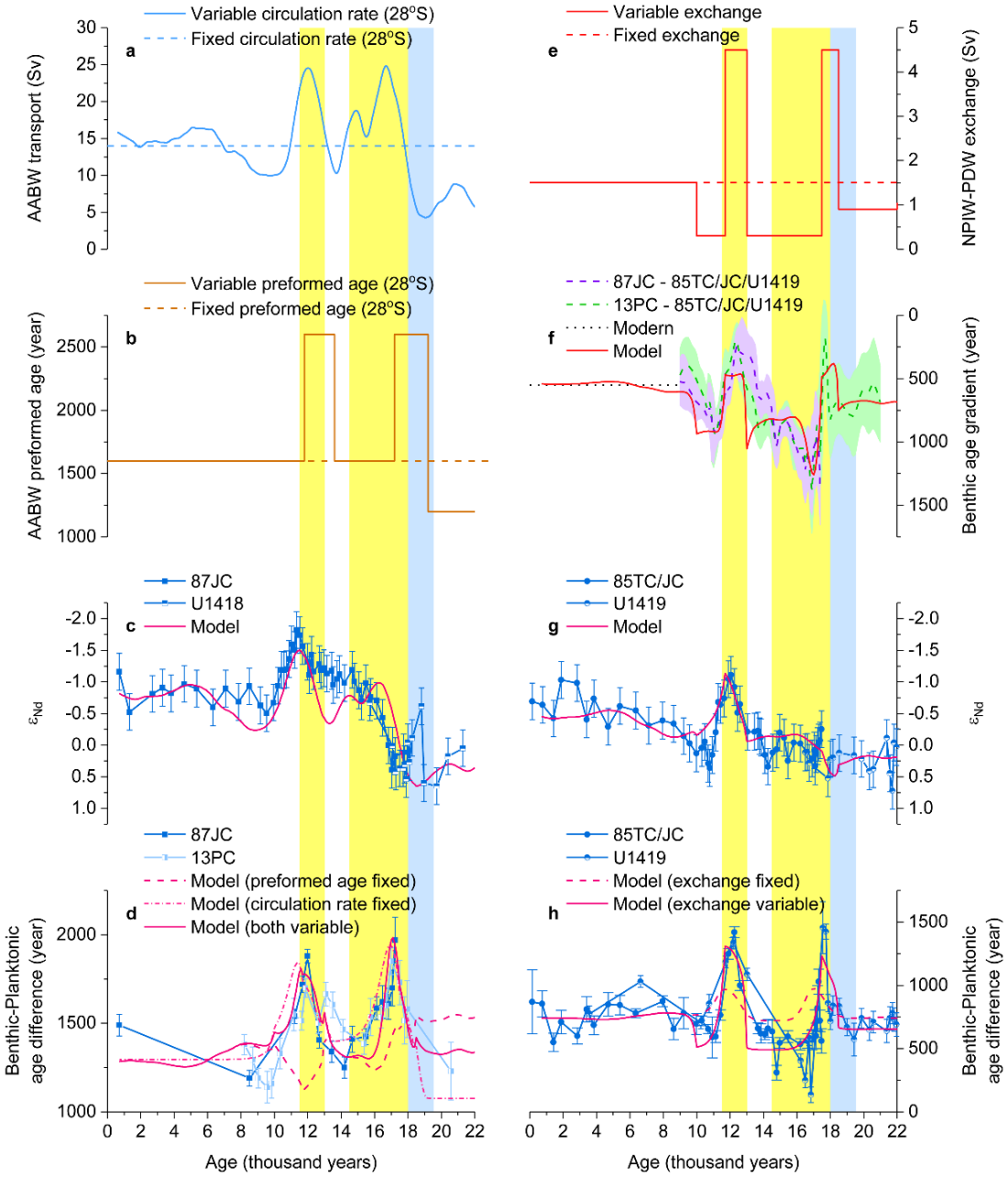

Figure 3.3. Transient simulations of North Pacific circulation tracers.

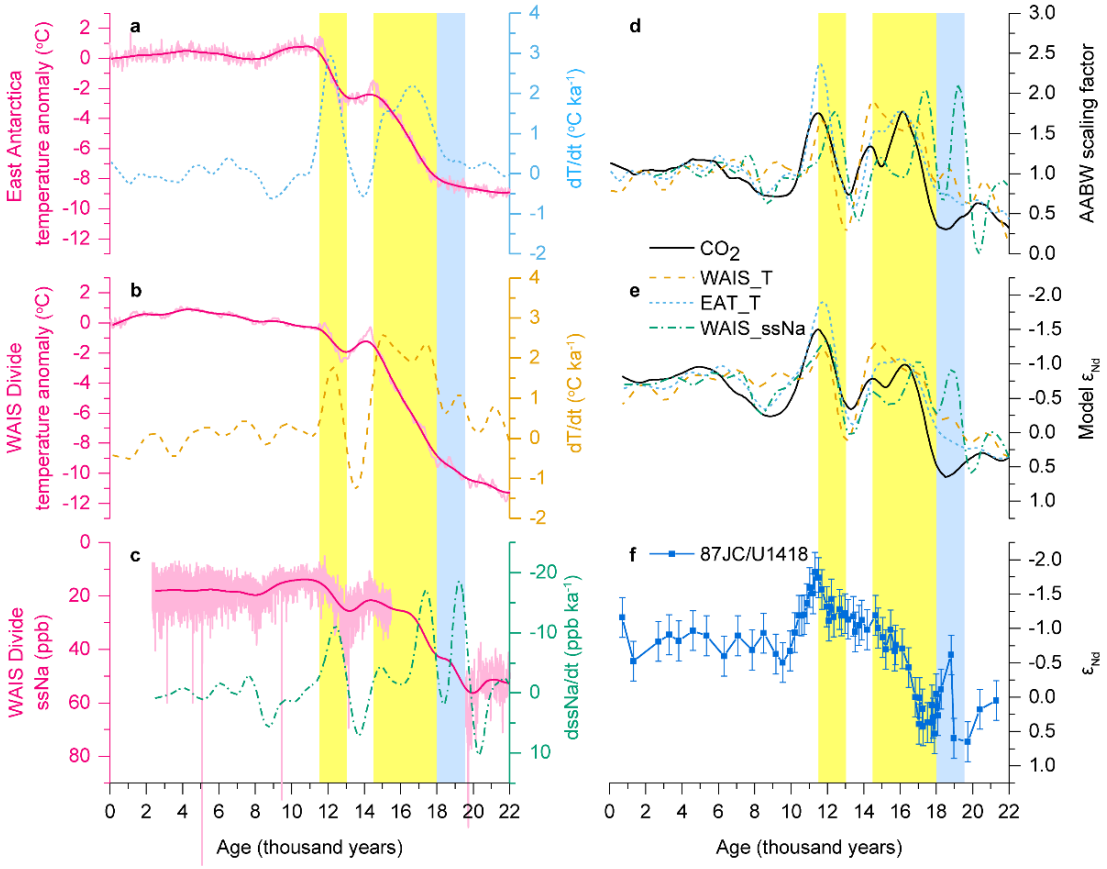

Figure 3.4. Transient simulations using Antarctic climate forcings.

The forcings include East Antarctic temperature(Parrenin et al. 2013) in **a** (EAT_T in **d** and **e**), West Antarctic temperature(Cuffey et al. 2016) in **b** (WAIS_T in **d** and **e**) and sea-ice (sea salt Na)(WAIS Divide Project Members 2013) in **c** (WAIS_ssNa in **d** and **e**). We smoothed the original high-resolution records by averaging over 250-year windows and computed the derivatives using nonparametric kernel regression with a bandwidth of 1000 year. We then scaled the AABW transport to the z-scores of the derivatives (**d**), which were used to model deep North Pacific ε_{Nd} (**e**) and compared to our record (**f**). The scaling is with respect to the modern transport (14 Sv). The simulation reported in Figure 3.3c is also shown in **d** and **e** (labeled "CO_2"). The color shaded intervals are the same as in Figure 3.2.

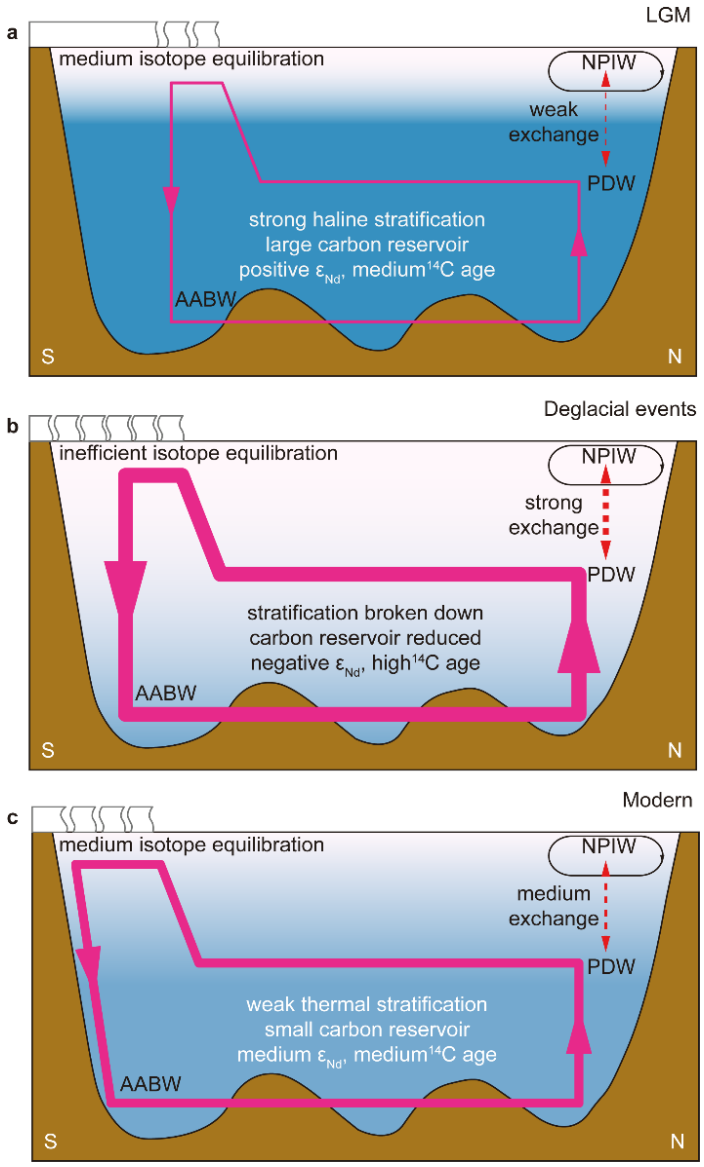

Figure 3.5. Conceptual models of LGM to Holocene circulation evolution in the Pacific.

a, LGM. Strong haline stratification and sluggish deep circulation. Pacific-wide deep carbon reservoir developed. **b**, Deglacial flushing events. Strong overturning and weak deep stratification. Deep carbon reservoir is released to the atmosphere and reached intermediate-depth. Preformed ages were high. **c**, Modern. Weak thermal stratification, moderate overturning and intermediate preformed ages. The circulation strength is indicated by the thickness of the overturning cell, and the interior stratification is represented using NPIW-PDW exchange (i.e. weak exchange is equivalent to stronger stratification) and the gradient of color shading.

Chapter 4: Evolution of the Global Overturning Circulation since the Last Glacial Maximum

Jianghui Du[1*], Brian. A. Haley[1], Alan. C. Mix[1]

[1]College of Earth, Ocean and Atmospheric Sciences, Oregon State University,

Corvallis, OR 97330, USA. (*Correspondence to: dujia@oregonstate.edu)

Abstract

The Global Overturning Circulation (GOC) is linked to climate change on glacial-interglacial, multi-millennial, and perhaps shorter timescales. The future of GOC behavior is difficult to predict, but will certainly feedback with long-term changes that may be triggered by human influence. Our understanding of past climate-GOC linkages remains hindered by apparent conflicts among proxy measures of circulation. Here we reconstruct past changes of GOC patterns and rates since the Last Glacial Maximum (LGM) based on a global synthesis of marine neodymium isotope records, reconciled with other circulation tracers. We show that during the LGM, the source region of North Atlantic overturning shifted and the overall strength of GOC was reduced, even though the relative proportions of northern and southern sourced watermasses were similar to today. Driven by vigorous Southern Ocean overturning, GOC strengthened as atmospheric CO_2 and deep ocean temperature rose during the northern-hemisphere stadial events that punctuated deglacial warming and suppressed North Atlantic overturning. GOC is thus sensitive to climate change, globally interconnected via the Southern Ocean, and its variability affects atmospheric CO_2 and the ocean heat budget.

The Global Overturning Circulation (GOC) is responsible for the transport of carbon and heat among the ocean basins and between the ocean and the atmosphere. GOC can be conceptualized primarily as two connected overturning cells(Talley 2013). The upper cell is linked to the formation of North Atlantic Deep Water (NADW) and the Atlantic Meridional Overturning Circulation (AMOC). The lower cell is associated with the production of Antarctic Bottom Water (AABW) which occupies the deeper parts of the abyssal ocean, and is referred to as the Southern Ocean Meridional Overturning Circulation (SOMOC). These two major cells are interconnected via upwelling in the Southern Ocean where deep waters, including NADW, are mixed together in the circumpolar circulation. Part of the resultant mixture contributes to AABW formation, which circulates northward above the seafloor and returns at mid-depth (for example, as Pacific Deep Water; PDW): the rest converts to less dense watermasses transported northward at intermediate and

shallower depths, eventually contributing to the production of NADW and other minor watermasses. In paleoceanography, the two principal deep watermasses are commonly referred to as Northern and Southern Source Waters (NSW and SSW), because they likely had different properties in the past.

That GOC influences the global carbon cycle and heat transport is a leading tenet in paleoclimatology(Shakun et al. 2012). However, despite decades of research, a globally consistent description of GOC history remains elusive. For example, climate models produce a conflicting array of AMOC behaviors during the Last Glacial Maximum (LGM, ~21 ka), and proxy data are also inconclusive regarding AMOC changes(Oppo et al. 2018; Gebbie 2014; Muglia et al. 2018; Menviel et al. 2016; Muglia & Schmittner 2015; Otto-Bliesner et al. 2007). The evolution of SOMOC is even more ambiguous and poorly known, which is problematic for studying the global carbon cycle because SOMOC ventilates the bulk of the deep Pacific, volumetrically the largest watermass and carbon reservoir that is exchangeable with the atmosphere. Analyzing GOC from a global perspective is essential because the AMOC and SOMOC cells are intertwined: the properties of SSW cannot evolve independently of those of NSW and *vice versa*, and circulation scenarios inferred based on Atlantic data must also satisfy the constraints imposed by data from the other ocean basins.

Marine neodymium isotope records

Here we use the radiogenic neodymium (Nd) isotopes (the $^{143}Nd/^{144}Nd$ ratio) of marine authigenic phases from the global ocean basins to examine the history of GOC since the LGM. Here the $^{143}Nd/^{144}Nd$ ratio is expressed as $\varepsilon_{Nd} = \left(\frac{(^{143}Nd/^{144}Nd)}{(^{143}Nd/^{144}Nd)_{CHUR}} - 1\right) \times 10^4$ in terms of its deviation from that of the chondritic uniform reservoir (CHUR). Neodymium isotopes are a powerful proxy for ocean circulation(Goldstein & Hemming 2003; van de Flierdt et al. 2016), but recent developments in the understanding of the modern marine Nd cycle calls for a revision to the interpretive framework of using ε_{Nd} as a paleo-circulation tracer, in which authigenic ε_{Nd} is previously presumed to act primarily as a conservative mixing tracer

of watermasses with fixed preformed properties(Du et al. 2016; Haley et al. 2017; Du et al. 2018; Abbott et al. 2015a,b; Lacan & Jeandel 2005a; Tachikawa et al. 2003). Building upon recent studies of benthic processes, we rework the modern global ocean Nd-ε_{Nd} budget using a geostrophically constrained box model, and close the budget through imposing a net isotopic flux from deep-sea detrital sediments as the dominant external source of marine Nd(Abbott et al. 2015b; Du et al. 2018) (Methods, Fig. 4.S1, Table 4.S1). Sedimentary sources affect the preformed ε_{Nd} of deep watermasses and also introduce a non-conservative ε_{Nd} component(Abbott et al. 2015a; Du et al. 2016, 2018; Haley et al. 2017; Lacan & Jeandel 2005a,b; van de Flierdt et al. 2016).

With this new conceptual and model framework, we deconvolve authigenic ε_{Nd} into three components (Methods): the preformed ε_{Nd} of watermasses inherited from detrital sources at the locations of deep water formation; the conservative mixing of the watermasses with distinct preformed ε_{Nd}; and the non-conservative effect as a function of benthic exposure time (controlled by circulation rate) and detrital composition (which controls the isotopic signature of the benthic source)(Du et al. 2018). The relative contributions of the three components are expected to change in the past, since they are linked to the different aspects of circulation that may evolve independently(Du et al. 2018). Thus, decomposing authigenic ε_{Nd} and identifying the respective mechanisms are essential for circulation reconstruction(Du et al. 2018). Here we synthesize and resolve the spatial-temporal modes of global and regional authigenic ε_{Nd} variability in 64 time-series records spanning the last 22,000 years (Table 1) using principal component analysis (PCA) based on covariance (Methods). Loadings (spatial patterns) of each orthogonal component are scaled to represent the component variance in the original records. PCA resolves significant orthogonal patterns of variation common to the full array of records, and excludes uncorrelated noise or local anomalies relative to the large-scale patterns.

Results

Two principal components (PCs) explain ~92% of the total variance (PC1 and PC2 contribute ~86% and ~6% respectively) (Fig. 4.1). PC1 describes the LGM-Holocene difference, with a relatively smooth temporal transition during the deglacial interval. PC2 documents transient deglacial anomalies, focused primarily near ~16 ka and ~12 ka, apparently coeval with Heinrich Stadial 1 (HS1) and Younger Dryas (YD) events, respectively. Because of the low temporal resolution in some records and a relatively low fraction of variance ascribed to PC2, its spatial pattern is less clear than that of the more dominant PC1. Nevertheless, distinct regional patterns of PC2 are apparent.

Based on the PCA results and the understanding of changes of detrital sources to the ocean since the LGM using a global detrital ε_{Nd} dataset (Methods), we identified authigenic ε_{Nd} records that are potentially affected by the variability of local detrital composition and input (Appendix C). Circulation information can still be gained from these records, but any inference based on them must also consider the local detrital influence.

Discussions

LGM Circulation

Positive PC1 loadings reflect more positive ε_{Nd} during the LGM (Fig. 4.1, 4.2). PC1 loadings are almost always positive at deep sites (>1500 m), but often close to zero at intermediate depths (500~1500 m). The most positive PC1 loadings occur in the North Atlantic north of 40^{o}N at all depths. Here, glacial ε_{Nd} values are higher than interglacial values by ~5 ε. A clear pattern can be traced throughout the global deep ocean, wherein the glacial increase of ε_{Nd} lessens moving from the North Atlantic to the Southern Ocean, and continues to decline into the Pacific and Indian Ocean. Slightly negative PC1 loadings are found at intermediate-depth Atlantic sites south of 40^{o}N, reflecting slightly more negative (< ~0.5 ε) ε_{Nd} in glacial relative to interglacial intervals.

The spatial pattern of PC1 can be explained by an increase of the preformed ε_{Nd} of glacial NSW and the global propagation of this perturbation downstream from

the North Atlantic (Fig. 4.1, 4.2). The gradual reduction of the magnitude of the perturbation farther from its place of origin reflects diminishing NSW contribution and the fact that the Nd residence time (300~600 years) in the ocean is shorter than that of global circulation (~1000 years), which limits the expression of the preformed effect as deep waters age(Du et al. 2018). The spatial pattern of PC1 rejects an alternate hypothesis that the AMOC and SOMOC cells were disconnected in the LGM(Ferrari et al. 2014). Rather, the NSW perturbation also changed the preformed ε_{Nd} of SSW, which subsequently transmitted the signal to the deep Pacific and Indian Ocean, implying that NSW contributed to SSW production in the LGM as it does today(Talley 2013).

A change of the preformed ε_{Nd} suggests that the location of NSW formation differed in the LGM relative to today. Labrador Sea Water (LSW) formation and Deep Western Boundary Current (DWBC) were not prevalent in the Labrador Basin in the LGM(Fagel et al. 1999; Hillaire-Marcel et al. 2001), resulting in reduced contribution of low-ε_{Nd} Precambrian detrital materials (<–25 ε) to the preformed ε_{Nd} of NSW(Arsouze et al. 2008; Lacan & Jeandel 2005b). Further, in the LGM, the export of Nordic Sea Overflow Water (NSOW) appears negligible(Thornalley et al. 2015); the deep water ε_{Nd} in the Nordic Seas was even more negative than today(Struve et al. 2019), suggesting limited effect of NSOW on the net preformed ε_{Nd} of glacial NSW. These inferences are consistent with climate model simulations in which glacial winter sea ice extended southward to Iceland (Fig. 4.3), thereby limiting ocean-to-atmosphere heat loss and deep water convection in the Nordic and Labrador Seas(Otto-Bliesner et al. 2007) (Fig. 4.S2). Paleo-proxies and climate models are consistent with a glacial shift of the principal NSW formation region to south of Iceland(Otto-Bliesner et al. 2007; Sarnthein et al. 1994; Waelbroeck et al. 2009). We suggest that a more positive preformed ε_{Nd} of NSW was acquired in the LGM at the more southerly source regions because of proportionately higher influence of the Icelandic (>0 ε) and Phanerozoic (~ –11 ε) Nd sources at the expense of the Precambrian sources (Fig. 4.3).

In a suite of box model sensitivity tests, we show that the observed glacial change of global authigenic ε_{Nd} can be simulated by increasing the preformed ε_{Nd} of NSW, but *not* by changing the preformed ε_{Nd} of SSW *nor* reducing NSW contribution (Methods, Fig. 4.S3). This global view rejects explanations based only on Atlantic data that suggest more positive authigenic ε_{Nd} in the glacial deep Atlantic was the result of reducing NSW versus SSW mixing ratios(Roberts et al. 2010). Building on the sensitivity results, a transient simulation in which we scaled the preformed ε_{Nd} of NSW to PC1 can explain the observed global PC1 pattern and glacial-interglacial variations of authigenic ε_{Nd} (Methods, Fig. 4.S4). Our results are consistent with high sensitivity of the preformed ε_{Nd} of NSW to the location and pathway of deep water formation(Lacan & Jeandel 2005b) (Fig. 4.3).

Within the Atlantic, the PC1 pattern is strongest mainly at depths >2500 m, suggesting limits to the proposed shoaling of AMOC(Curry & Oppo 2005; Gebbie 2014; Keigwin & Swift 2017; Oppo et al. 2018). Because the Drake Passage does not admit net meridional geostrophic flow on constant density surfaces, if the glacial NSW becomes shallower than the sill depth (~2000 m), it would not significantly contribute to SSW production south of the Drake Passage as it does today(Sikes et al. 2017; Talley 2013). In this case, perturbation to the preformed ε_{Nd} of NSW in the LGM should be limited to the Atlantic and not propagated into the Pacific Ocean, contradicting the observed PC1 pattern and related changes of authigenic ε_{Nd} (Fig. 4.2).

Glacial NSW contribution can be quantified using the ε_{Nd} perturbation associated with PC1. This perturbation method is preferred to the classic two-end-member mixing method(Howe et al. 2016a), because perturbation corrects for preformed end-members that vary through time. At depths >2500 m and between the equator and 40°S, the magnitude of glacial ε_{Nd} perturbation is ~2.5 ε (Fig. 4.2). This is about half of the perturbation (~5 ε) in the subpolar North Atlantic, implying ~50% contribution of glacial NSW, similar to modern NADW(Gebbie & Huybers 2010) but shifted to greater depths. This LGM perturbation decreases to ~1 ε in the deep Pacific, consistent with ~20% contribution of NSW to the Pacific, similar to modern

estimates(Gebbie & Huybers 2010). Thus, once the preformed effect is removed, authigenic ε_{Nd} evidence suggests little or no change of NSW:SSW ratio in the glacial deep Atlantic and Pacific relative to the Holocene(Gebbie 2014), consistent with the view that PC1 is mainly driven by changes in the preformed ε_{Nd} of NSW, rather than major changes in the watermass mixing ratios.

Although the pattern of LGM circulation was similar to today, the conservative and non-conservative components of authigenic ε_{Nd} do require reduction of GOC rate. Negative PC1 loadings and lower glacial ε_{Nd} at intermediate-depths in the Atlantic, along with increased preformed ε_{Nd} of SSW, indicate weaker penetration of glacial Antarctic Intermediate Water (AAIW) (Fig. 4.2), implying that the upper limb return flow of AMOC was reduced in the LGM(Oppo et al. 2018). The greater heterogeneity of glacial authigenic ε_{Nd} in the subpolar North Atlantic is consistent with an increase of water residence time (τ_w) in the deep Atlantic in the LGM (Fig. 4.S5). That is, a slowing of AMOC would increase benthic exposure time, allowing the heterogeneity of distinct regional detrital sources to become more fully expressed in authigenic ε_{Nd}(Du et al. 2016). Similarly, reduction of SOMOC in the LGM can be inferred from the deep North Pacific authigenic ε_{Nd}; increasing non-conservative effect of authigenic ε_{Nd} in the North Pacific is consistent with abyssal flows reduced by about 50% in the LGM(Du et al. 2018). Taking into account our inference that the NSW:SSW ratio was not significantly altered, our global analysis supports a circulation scenario of both glacially weaker AMOC *and* SOMOC by roughly half(Menviel et al. 2016).

Deglacial Circulation

Positive PC2 loadings, reflecting positive ε_{Nd} excursions during HS1 and the YD (Fig. 4.1, 2), reveal a significant deglacial pattern of ε_{Nd} variability. In many, but not all, areas the deglacial anomaly pattern is masked in visual inspection by the dominant glacial-interglacial variability of PC1, but is detected in multivariate statistical decomposition as we have done here.

In the subpolar North Atlantic, PC2 loadings point to regions of heterogenous detrital imprint during Heinrich Events (HEs) (Methods, Appendix C). Such strong imprints (high loadings) and increasing heterogeneity is consistent with longer benthic exposure time and thus weaker AMOC during HEs(Blaser et al. 2019).

At intermediate-depth in the Atlantic (30°S~30°N, 500~1500 m), strong *negative* PC2 loadings and *negative* ε_{Nd} excursions (~1 ε) in regions that lack local detrital variability are consistent with reduction of the return flow feeding NSW production during HS1 and YD(Huang et al. 2014), even more so than the LGM (Fig. 4.2).

The contrasting patterns of PC2 loadings between the deep North Atlantic and North Pacific (Fig. 4.2, 4.4) indicate stronger SOMOC during HS1 and YD. In these intervals, the PC2 components of ε_{Nd} in the deep North Atlantic and North Pacific converged toward Southern Ocean values (Fig. 4.4). This convergence suggests a greater contribution of the conservative component to authigenic ε_{Nd} relative to the non-conservative component(Du et al. 2018), implying reduced τ_w (*i.e.*, faster overturning) globally in the deep ocean during HS1 and YD. In the deep Southern Ocean, the PC2 loadings are close to zero and the PC2 components of ε_{Nd} changed little during the deglaciation (Fig. 4.4). This muted signal is consistent with more effective homogenization of global deep waters through vigorous SOMOC.

To examine this inference quantitatively, we performed a transient box model simulation (Methods), in which we increased SOMOC transport (SSW production) during HS1 and YD via scaling to PC2 but kept AMOC (NSW production) constant (Fig. 4.4). This simulation captured the Atlantic-Pacific convergence of ε_{Nd} in these intervals. In contrast, an alternative simulation with reduced AMOC but constant SOMOC in these intervals led to Atlantic-Pacific divergence (Fig. 4.S6). Thus, smaller global deep water τ_w during HS1 and YD required to explain the authigenic ε_{Nd} data implies that the effects of strengthening SOMOC overcome those of reducing AMOC, the former being globally dominant while the latter being limited to North Atlantic at shallow-to-intermediate depth (Fig. 4.2).

We therefore conclude that PC1 mainly reflects the change of the preformed ε_{Nd} of NSW while PC2 largely indicates the variation of SOMOC. This conclusion is borne out in a final simulation in which we used both the SOMOC scaling and accounted for NSW preformed ε_{Nd} changes (Fig. 4.S4). The results reasonably reproduce the global authigenic ε_{Nd} variability on both glacial-interglacial and millennial timescales, supporting our mechanistic interpretations of the statistical decompositions.

Implications for LGM climate

Our ε_{Nd}-based inference that the LGM NSW fractional contribution to deep ocean watermasses was similar to today can be reconciled with benthic $\delta^{13}C$ data(Curry & Oppo 2005), *if* the non-conservative component of $\delta^{13}C$ due to remineralization increased, and/or *if* the preformed $\delta^{13}C$ of SSW and/or NSW decreased in the LGM(Gebbie 2014; Mix & Fairbanks 1985; Howe et al. 2016a). Carbonate system parameters suggest greater accumulation of remineralized carbon in the glacial deep ocean(Rae et al. 2018), and inverse methods suggest lower preformed $\delta^{13}C$ of glacial SSW(Gebbie 2014; Oppo et al. 2018). A two-layer structure of glacial NSWs is possible, with a high preformed $\delta^{13}C$ intermediate-depth NSW formed through open-ocean convection with strong air-sea gas exchange, and a low preformed $\delta^{13}C$ bottom NSW formed under sea ice with limited air-sea gas exchange(Howe et al. 2016a; Keigwin & Swift 2017; Mix & Fairbanks 1985) (Fig. 4.5). This ε_{Nd}-$\delta^{13}C$ comparison speaks to the importance of the multi-proxy approach to circulation reconstruction, taking advantage of the differing mechanisms that set the preformed properties of circulation tracers.

Reduced GOC rate in the LGM required by authigenic ε_{Nd} is consistent with an estimate of global ocean τ_w ~700 years longer than today based on benthic radiocarbon(Skinner et al. 2017). If preformed properties, as we inferred from PC1, dominate the glacial-interglacial changes of authigenic ε_{Nd} (Fig. 4.1, 4.2), then more extreme increases of glacial τ_w can be ruled out(Du et al. 2018). Substantially longer τ_w would force authigenic ε_{Nd} to converge toward regional detrital signatures as the

non-conservative effect becomes dominant(Abbott et al. 2015a; Du et al. 2018), which is inconsistent with observations (Fig. 4.1, 4.2, 4.4).

The glacial GOC scenario based on ε_{Nd} has important implication for understanding reduced atmospheric CO_2 in the LGM relative to Holocene values. That the glacial NSW proportion was roughly equivalent to today rules out hypotheses invoking higher efficiency of the glacial biological pump related to increasing ventilation by NSW(Kwon et al. 2012). Instead, with support from general circulation-biogeochemical model simulations(Menviel et al. 2016; Muglia et al. 2018), we infer that the overall sluggish GOC, including both AMOC and SOMOC cells (Fig. 4.5), drove increased carbon sequestration in the glacial deep ocean.

Implications for the deglacial climate

Our synthesis of global ε_{Nd} patterns of variation resolve a face-value disparity between deglacial records of authigenic ε_{Nd} and sedimentary $^{231}Pa/^{230}Th$ in the deep North Atlantic (Fig. 4.4). Previous studies inferred little change of deep North Atlantic circulation from LGM to HS1 based on visual inspection of authigenic ε_{Nd} time-series or time-slice reconstructions(Howe et al. 2018; Roberts et al. 2010). Our global multivariate decomposition shows that the PC1 (preformed) and PC2 (mixing proportion) contributions to authigenic ε_{Nd} acted in opposite directions in the deep North Atlantic at that time, thus masking changes in circulation based on visual inspection (Fig. 4.S7). Once the preformed component (PC1) is removed, the PC2 component of ε_{Nd} does indeed track $^{231}Pa/^{230}Th$ in the deep North Atlantic, revealing that changes of overturning strength and watermass mixing are coupled during the deglaciation (Fig. 4.2, 4.4).

Authigenic ε_{Nd} and sedimentary $^{231}Pa/^{230}Th$ in the deep North Atlantic are both consistent with the scenario of weaker AMOC and stronger SOMOC during HS1 and YD. While the overall increase of $^{231}Pa/^{230}Th$ in the deep North Atlantic during these stadial intervals could be explained by reduced AMOC(Ng et al. 2018), the excess ^{231}Pa (exceeding the production ratio of 0.093) cannot. Such excess is found in some deep North Atlantic sites during HS1 and YD, and is unrelated to opal

scavenging(Ng et al. 2018) (Fig. 4.4). Cessation of NSW export during these stadial events is not supported by ε_{Nd} (Fig. 4.4), and complete collapse of AMOC would at most cause $^{231}Pa/^{230}Th$ to increase to its production ratio. Instead, stronger SOMOC as indicated by ε_{Nd} provides a net source of ^{231}Pa to the deep North Atlantic, and can explain the previously enigmatic excess ^{231}Pa in that region.

During HS1 and YD, in spite of diminished AMOC, global deep and bottom water τ_w decreased because of stronger SOMOC (Fig. 4.4, 4.5). This inference is consistent with ^{14}C data, which show that the deep North Atlantic had as large a ^{14}C offset (~–250%) from the atmosphere as the Southern Ocean during HS1(Robinson et al. 2005). This scenario of fast overturning of a SSW with high apparent ^{14}C age during HS1 and YD also fits the North Pacific ^{14}C data(Du et al. 2018). The high apparent ^{14}C reservoir age in the deep ocean during these intervals should thus be attributed to high preformed ^{14}C age, driven by mixing of old PDW into the Southern Ocean and incomplete gas-isotope exchange as excess CO_2 was released to the atmosphere(Du et al. 2018). Further supporting evidence comes from benthic $\delta^{13}C$. During HS1, the benthic $\delta^{13}C$ at depths >3,000 m in the South Pacific and South Atlantic were similar (~0 ‰), eliminating the strong inter-ocean gradients seen both in the LGM and Holocene(Sikes et al. 2017). Analogous to ^{14}C, this Atlantic-Pacific convergence of $\delta^{13}C$ in HS1 occurred when Atlantic $\delta^{13}C$ was becoming more negative(Lund et al. 2015). This pattern implicates changes of the preformed $\delta^{13}C$ as a significant driver of evolving deglacial benthic $\delta^{13}C$(Lynch-Stieglitz et al. 2019; Mix & Fairbanks 1985), the effect of which was large enough to mask other components of benthic $\delta^{13}C$ based on visual inspection.

The acceleration of SOMOC during HS1 and YD for the most part aligns with steps of rapid deglacial rise of atmospheric CO_2 concentration(Du et al. 2018; Marcott et al. 2014; Shakun et al. 2012) (Fig. 4.4). Increasing carbon storage in the mid-depth Atlantic during these stadial events precludes reduction of AMOC as a prime driver of atmospheric CO_2 rise(Lacerra et al. 2017). Release of excess CO_2 due to SOMOC is a more likely driver(Anderson et al. 2009). Our global ε_{Nd} synthesis, and decomposition of preformed, conservative, and non-conservative influences on

this tracer, demonstrates that large-scale GOC changes could have readily generated these Southern Ocean biogeochemical observations. Authigenic ε_{Nd} evidence of deglacial strengthening of SOMOC can explain observed deglacial decreases of the $\delta^{13}C$ of CO_2 in the atmosphere(Bauska et al. 2016; Du et al. 2018; Schmitt et al. 2012) (Fig. 4.4, 4.5). The SOMOC scaling used in our box model, which can reproduce deep ocean authigenic ε_{Nd} records in both the Atlantic and Pacific (Fig. 4.4), is similar to the one used in an Earth System Model that simulates atmospheric rise of CO_2 during HS1(Menviel et al. 2018). Authigenic ε_{Nd} therefore suggests a dominant role of SOMOC in the deglacial rise of atmospheric CO_2 concentration(Du et al. 2018).

Inferred change of SOMOC may also explain the evolution of global ocean heat budget during the deglaciation. Mean Ocean Temperature (MOT)(Bereiter et al. 2018), volumetrically weighted toward the deep ocean, increased rapidly during HS1 and YD (Fig. 4.4). With reduced AMOC in these intervals, stronger SOMOC is needed to efficiently bring heat from the surface to the global deep ocean. Our ε_{Nd}-based inference that a greater volume of the global deep ocean was ventilated by SOMOC during these intervals explains why MOT is highly correlated to Antarctic and Southern Ocean surface temperature(Bereiter et al. 2018). We infer that SOMOC sustained warming during the last deglaciation, through its influence on both atmospheric CO_2 and ocean heat transport(Shakun et al. 2012).

By taking into account the time-evolving components, we are able to reconcile the various ocean circulation tracers. The resulting reconstruction implicates a major role of GOC variability in global climate change since the LGM.

Methods

Box model and the modern global ocean Nd-ε_{Nd} budget

The box model has four ocean boxes: Atlantic, Pacific, Indian and Southern Ocean, which is separated from the other basins at 30°S. It is a global extension of the previous Pacific only model(Du et al. 2018). We choose not to divide the ocean basins into smaller boxes because: (1) greater numbers of boxes lead to greater

degrees of freedom, which are more difficult to constrain with existing data; (2) our study focuses on the global scale inter-basin differences rather than intra-basin variability; (3) the deep ocean is volumetrically dominant in the budget. The physical circulation of the model follows Talley's box geostrophic inverse models, which has the "figure 8" pattern of modern GOC(Talley 2013) (Fig. 4.S1). Model set up can be found in Appendix C as well as ref.(Du et al. 2018).

It has long been recognized that dust and dissolved river Nd fluxes are too small to close the modern marine Nd-ε_{Nd} budget, and some "missing" *external* sources are required(Abbott et al. 2015b; Arsouze et al. 2009; Du et al. 2018; Tachikawa et al. 2003). Most recent studies point to sedimentary flux as this missing source(Abbott et al. 2015b; Arsouze et al. 2009; Du et al. 2018; Haley et al. 2017; Lacan & Jeandel 2005a; Tachikawa et al. 2003). The key constraint on this missing source is the global residence time of Nd (τ_{Nd}, with respect to the scavenging sink), and recent estimates converge to a τ_{Nd} range of 300 to 600 years(Abbott et al. 2015b; Arsouze et al. 2009; Du et al. 2018; Rempfer et al. 2011; Tachikawa et al. 2003). Adopting this τ_{Nd} constraint, the "best-fit" missing source according to our model sensitivity test is 20 to 30 pmol cm^{-2} yr^{-1} (Fig. 4.S1). This required missing source is quantitatively similar to current estimates of the benthic Nd flux based on pore-water measurements(Abbott et al. 2015b; Du et al. 2018; Haley et al. 2004; Haley & Klinkhammer 2003), which have an arithmetic mean of 13 pmol cm^{-2} yr^{-1} and seafloor area weighted mean of 26 pmol cm^{-2} yr^{-1}, suggesting that the sedimentary source could complete the global Nd-ε_{Nd} budget(Abbott et al. 2015b; Du et al. 2018). Here we assume that the missing source is due to a benthic sedimentary flux, but we emphasize that any conclusion derived from our box model is valid as long as some missing source exist, which, again, is required by the global Nd-ε_{Nd} data(Du et al. 2018; Tachikawa et al. 2003; Arsouze et al. 2009; Rempfer et al. 2011; Abbott et al. 2015b; Behrens et al. 2018), regardless the exact mechanisms that introduce this source.

We therefore use a globally uniform benthic Nd flux of 25 pmol cm^{-2} yr^{-1}, in addition to the well-constrained surface fluxes, to derive the modern Nd-ε_{Nd} budgets

of the ocean boxes (Extended Data Table 1). Globally, surficial sources (dust and dissolved river fluxes) and benthic flux account for ~5% and ~95% of the *external* Nd source fluxes, in agreement with recent estimates(Abbott et al. 2015b; Arsouze et al. 2009; Du et al. 2018; Rempfer et al. 2011; Tachikawa et al. 2003). When considering the redistribution of Nd within the ocean due to watermass transport, we find that globally surficial sources only account for ~2%, transport accounts for ~56%, and benthic sources accounts for ~42% of the total fluxes (*i.e.*, *external* sources plus *internal* fluxes due to transport).

In our budget analysis (Extended Data Table 1), the modern Atlantic requires a sedimentary source with ε_{Nd} more negative than basinal mean seawater (–17 ε for benthic source versus –12 ε for seawater) while the opposite is true for the Pacific (–2 ε for benthic source versus –4 ε for seawater). This contrast has been shown previously budget analysis(Tachikawa et al. 2003). In the Atlantic, such a negative ε_{Nd} benthic source can readily come from sediments in the Labrador Basin(Lacan & Jeandel 2005b), where a high fraction of the detrital sediments is derived from Precambrian materials in the Canadian Shield. There is a clear potential behind this negative ε_{Nd} detrital source in setting the modern seawater ε_{Nd} in the Atlantic through its influence on the preformed ε_{Nd} of NADW(Lacan & Jeandel 2005b). In the Pacific, the volcanic fraction within detrital sediments offers a high ε_{Nd} benthic source, consistent with pore water and authigenic studies(Abbott et al. 2015a; Du et al. 2016). This basin-scale Atlantic-Pacific contrast in detrital influence is consistent with our understanding of detrital reactivity in these two ocean basins based on recent sediment leaching studies(Blaser et al. 2016, 2019; Du et al. 2016).

The three components of seawater and authigenic ε_{Nd}

The preformed ε_{Nd} indicates the formation location of deep watermasses. For example, the modern preformed ε_{Nd} (~ –13 ε) of NADW is set by a blend of detrital sources surrounding the North Atlantic(Fagel et al. 1999; Lacan & Jeandel 2005b; van de Flierdt et al. 2016): Precambrian crusts from central North America and Greenland ($\varepsilon_{Nd} < -25$); Phanerozoic crusts from North and West Europe, North

Africa, East Greenland and Northeast America ($\varepsilon_{Nd} \sim -11$); and Icelandic basalt ($\varepsilon_{Nd} > 0$). NADW inherits a weighted average of these detrital signatures partially via its precursor watermasses: Labrador Sea Water (LSW, ~–14 ε) carries the Precambrian influence, Nordic Sea Overflow Water (NSOW, ~–8 ε) imparts the Icelandic source, and Mediterranean Overflow Water (MOW, ~–9 ε) conveys the Phanerozoic signature. The initial preformed ε_{Nd} resulting from mixing these precursor watermasses is further modified by boundary exchange with extremely negative ε_{Nd} sediments of Precambrian origin along the pathway of the Deep Western Boundary Current (DWBC) in the Labrador Basin(Lacan & Jeandel 2005b). This boundary exchange is borne out in our analysis of the modern Atlantic Nd-ε_{Nd} budget as seen in the requirement of a local sedimentary source with ε_{Nd} more negative than seawater (Extended Data Table 1). Changes of the preformed ε_{Nd} of NSW are to be expected if the formation mode, location and pathway of NSW were different in the past.

Once acquired, the distinct preformed ε_{Nd} of the source waters propagates into the ocean interior through GOC. In the Atlantic, where watermass residence times are relatively short, the modern distribution of intermediate and deep water ε_{Nd} can be inferred from the mixing ratio of NSW and SSW, based on their observed preformed ε_{Nd} values (~–13 and ~–8 respectively)(van de Flierdt et al. 2016). Interpreting paleo-ε_{Nd} from the perspective of conservative mixing, however, requires independent knowledge of the temporal evolution of the preformed ε_{Nd} values *and* the water mass residence times that control non-conservation(Du et al. 2018).

The non-conservative effect of ε_{Nd} is a function of benthic exposure time and detrital sediment composition, and over time this transforms seawater and authigenic ε_{Nd} towards dynamic equilibrium with local detrital ε_{Nd}(Du et al. 2016, 2018; Wilson et al. 2013). For example, the deep Pacific circulates slowly, so modern PDW (~–4 ε) acquires its relatively positive ε_{Nd} signature because of prolonged exposure to volcanic (>0 ε) sedimentary materials abundant in the Pacific(Du et al. 2016), as seen in the derived modern Pacific Nd-ε_{Nd} budget (Extended Data Table 1).

The relative impacts of the non-conservative versus conservative component of ε_{Nd} are controlled by τ_w/τ_{Nd}, the ratio of steady-state residence time of deep water (with respect to watermass transport within a basin) to the residence time of Nd (with respect to scavenging sink)(Abbott et al. 2015a; Du et al. 2018). The steady state ε_{Nd} of an ocean box is the weighted average of two terms (ignoring the minor surficial sources)(Du et al. 2018):

$$\varepsilon_{Nd} = \frac{\tau_w}{\tau_{Nd} + \tau_w} \varepsilon_{Nd}^B + \frac{\tau_{Nd}}{\tau_{Nd} + \tau_w} \sum m^i \varepsilon_{Nd}^i \ .$$

The first term is the non-conservative term reflecting benthic input (ε_{Nd}^B is the isotope composition of the benthic source). The second term is the conservative term reflecting the mixing of source waters of distinct preformed properties (m^i and ε_{Nd}^i are the mixing ratios and isotope compositions of the source waters). Thus, greater τ_w/τ_{Nd} indicates stronger expression of the benthic influence.

Today, a τ_{Nd} of 300 to 600 years(Abbott et al. 2015b; Arsouze et al. 2009; Du et al. 2018; Rempfer et al. 2011; Tachikawa et al. 2003) implies greater conservative mixing effect in the Atlantic (where $\tau_w/\tau_{Nd} < 1$) but greater non-conservative effect in the Pacific (where $\tau_w/\tau_{Nd} > 1$)(Du et al. 2018). This is seen in our budget analysis in which transport (*i.e.* conservative component) is the dominant term controlling the Atlantic Nd-ε_{Nd} budget, while sedimentary flux (*i.e.* non-conservative component) is the dominant term controlling the Pacific Nd-ε_{Nd} budget (Extended Data Table 1). Globally, the conservative component slightly exceeds the non-conservative component in the contribution to the modern Nd-ε_{Nd} budget (Extended Data Table 1). This is consistent with the "quasi-conservative" nature of ε_{Nd} in the modern ocean(Goldstein & Hemming 2003; van de Flierdt et al. 2016), and emphasizes that both the conservative and non-conservative components are needed to explain the distributions of modern Nd and ε_{Nd}(Abbott et al. 2015a; Du et al. 2018; Haley et al. 2017). Past changes in ocean circulation may result in different τ_w, and consequently the relative contributions of these two components may vary. By constraining and correcting for the preformed and conservative components, the non-conservative

component of authigenic ε_{Nd} can be isolated, allowing reconstruction of circulation rate through its link to benthic exposure time(Abbott et al. 2015a; Du et al. 2018).

The implication is that the degree of heterogeneity of seawater and authigenic ε_{Nd} is likely to be a proxy for τ_w. The distribution of detrital source ε_{Nd} is heterogenous globally, which effectively sets the "blue print" for seawater and authigenic ε_{Nd}. The role of circulation is to destroy this heterogeneity: slower abyssal circulation (greater τ_w/τ_{Nd}) will force Atlantic and Pacific seawater and authigenic ε_{Nd} to diverge from each other as watermasses ε_{Nd} in each basin converges to local detrital ε_{Nd}, because the non-conservative effect manifests more strongly. Conversely, faster abyssal circulation (smaller τ_w/τ_{Nd}) would cause ε_{Nd} in seawater and authigenic phases to be more similar in the two basins, because conservative mixing becomes dominant relative to benthic fluxes.

Global ε_{Nd} data collection

We compiled published authigenic ε_{Nd} records since the LGM, *i.e.*, data with numerical ages younger than 22 ka, or were reported as Holocene or LGM time-slices. The authigenic data were generated from archives including foraminifera, fish debris, coral and dispersed sedimentary Fe-Mn oxyhydroxides. Strong evidence has emerged in recent years that these archives record a transition between bottom water and pore water ε_{Nd}(Abbott et al. 2015a, 2016; Blaser et al. 2016; Du et al. 2016; Roberts et al. 2012; Struve et al. 2017; Tachikawa et al. 2014; Toyoda & Tokonami 1990). We did not include the published sedimentary leach ε_{Nd} records that do not agree consistently with foraminifera and/or fish debris ε_{Nd} data from the same site. We did not use any core-top authigenic ε_{Nd} data that have no age constraints. Site information is reported in Table 4.S1. Data from the same site generated using various archives and from different studies were averaged to create the time-series and time-slice data used in this study (Appendix C). In summary, there are 64 stations with time-series records spanning the deglaciation (10~19 ka), 260 stations with Holocene time-slice records and 144 stations with LGM time-slice records in this authigenic dataset.

We also compiled published modern seawater ε_{Nd} data and detrital sediment ε_{Nd} data since the LGM. The seawater dataset use here is built upon existing compilations(Lacan et al. 2012; Tachikawa et al. 2017; van de Flierdt et al. 2016), which is used to derived the modern global ocean Nd-ε_{Nd} budget. The detrital sediment ε_{Nd} dataset includes data generated using various methods (bulk sediment digests, operationally defined detrital residual digests and specific size fraction digest) (Appendix C). The detrital ε_{Nd} data help to identify influences of local detrital variability on authigenic ε_{Nd} records (Appendix C).

Data gridding

We performed variational analysis(Barth et al. 2014) to generate the 2-D gridded data used in the plots. To create the gridded data for the latitude-depth section plots in Figure 4.2, we used a signal-to-noise ratio of 10, a fixed correlation length scale of 30^o for latitude and a variable correlation length scale for depth, increasing as an error function of depth from 100 m at 500 m to 1000 m below 2000 m. To create the gridded data for the longitude-latitude plots in Figure 4.3, we used a signal-to-noise ratio of 10, a fixed correlation length scale of 15^o for latitude and 30^o for longitude.

Principal component analysis

The authigenic ε_{Nd} time-series records were first binned into 500-year intervals between 0 and 22 ka. The binned data form a matrix where each column represented a site and each row an age bin. No single record had enough resolution and age range to fill all bins, and missing values in the data matrix need to be filled. Instead of using interpolation/extrapolation, we performed PCA missing data imputation using a regularized iterative algorithm(Josse & Husson 2016). The advantage is that the missing data are estimated using the correlation structure of the entire dataset. Thus, no artificial variance is introduced as is prone with interpolation/extrapolation methods. We then performed covariance-based PCA on the completed dataset, such that the resulting loadings are scaled to the variance in the authigenic ε_{Nd} records. Finally, we decomposed the completed authigenic ε_{Nd} records

into its constituent PCs. This is necessary because the PCs only summarize the "common" signals shared by authigenic ε_{Nd} records in variance units. Decomposition recreates the authigenic ε_{Nd} records using the PC time-series and their respective loadings at each site, thus putting these "common" signals back into each individual ε_{Nd} record(Lê et al. 2008). Decomposed authigenic ε_{Nd} records at each individual site are show in Table 4.S2. To estimate uncertainties, we created 10,000 synthetic data matrices with missing data by adding Gaussian white noise with an 1σ of 0.2 ε to the original data matrix (the raw data matrix after binning and before PCA). We applied a fixed uncertainty (2σ=0.4), because not all studies reported the long-term external 2σ uncertainty of ε_{Nd} analysis. Our assumed uncertainty is conservative relative to typical 2σ analytical uncertainties (0.2~0.3) of modern MC-ICP-MS and TIMS. The synthetic data matrices with missing values were then subjected to the imputation and PCA procedures described above, and the results, *i.e.*, PC time-series and their respective loadings at each site, were summarized using median values and 95% confidence intervals (CIs).

Influences of the local detrital variability on authigenic ε_{Nd} records

Seawater and authigenic ε_{Nd} may respond over time to changes of local detrital sediment composition and input(Blaser et al. 2019; Du et al. 2016; Struve et al. 2019; Wilson et al. 2013), in addition to circulation change. To identify such local influences, we examined the regionally resolved records of detrital ε_{Nd} since the LGM (Appendix C). In most areas, detrital ε_{Nd} changes little; in these places, changes in authigenic ε_{Nd} appear to have simple responses to changes in bottom water ε_{Nd}. On the other hand, authigenic ε_{Nd} tracks detrital variability in three regions.

In the Equatorial Pacific, authigenic ε_{Nd} coevolved with detrital composition on glacial-interglacial timescales(Hu & Piotrowski 2018; Xie & Marcantonio 2012). Using the Equatorial Pacific records Hu and Piotrowski argued that the deep Pacific circulation strengthened during the LGM(Hu & Piotrowski 2018). However, our global analysis shows that the Equatorial Pacific authigenic ε_{Nd} records are neither consistent with the global trend nor with records from the rest of the Pacific

(Appendix C). We show that these authigenic ε_{Nd} records can be corrected to remove the influence of local detrital variability, and once corrected they become fully consistent with the global data, indicating that these records received combined circulation-detrital influences.

In the subpolar North Atlantic, authigenic ε_{Nd} covaried with millennial-timescale changes of detrital composition that reflect intermittent inputs of ice-rafted continental materials, the so-called Heinrich Events (HEs) defined by detrital Heinrich Layers (HLs)(Blaser et al. 2019) (Appendix C). An extreme case of HEs detrital imprint has previously been documented in the center of the IRD belt where authigenic ε_{Nd} is completely overprinted by detrital ε_{Nd}(Blaser et al. 2019). Our results show that HEs detrital imprint on authigenic ε_{Nd} is somewhat more widespread to the periphery of the IRD belt, but often subtler such that detection is aided by multivariate decomposition methods as done here using PCA.

In the North Indian Ocean, especially in the Bay of Bengal, authigenic ε_{Nd} changes correlate to changing terrestrial input linked to Indian Monsoon activity on both glacial-interglacial and millennial timescales(Burton & Vance 2000). Evaluating authigenic ε_{Nd} from this region in the global ocean context indicates that authigenic ε_{Nd} here recorded a mixed ocean-terrestrial signal (Appendix C).

Because authigenic ε_{Nd} records from these three regions were generated mostly using fish debris and foraminifera archives, the suggested detrital influence must reflect *in situ* sedimentary processes, in addition to watermass effects. To remain unbiased, we keep these records in our global analysis and examine them in detail in Appendix C. Analyzing authigenic and detrital ε_{Nd} records together and under a global context therefore improves confidence in GOC reconstructions.

LGM surface buoyancy flux in the subpolar North Atlantic

PMIP3 model(Meinshausen et al. 2011) outputs were retrieved from the open-access Earth System Grid Federation portal (https://esgf-node.llnl.gov/projects/esgf-llnl/). Eight models reported LGM simulations, but the variables necessary to

calculate the desired quantities were not always archived online. Here we focus on the multi-model median values of average winter (January-February-March) sea ice fraction (8 models), buoyancy flux (6 models) and sea surface temperature (6 models). Model outputs on the native grids were regridded on to a 1° by 1° rectilinear grid to calculate multi-model median values using the Earth System Modeling Framework regridding package of the NCAR Command Language(Brown et al. 2018). Total buoyancy flux and its thermal component was calculated following ref.(Marshall & Plumb 2008). The data are shown as anomalies with respect to the preindustrial control (Fig. 4.S2).

Box model sensitivity tests

We performed four sensitivity tests (Fig. 4.S3) split into two categories: two tests that illustrate how ε_{Nd} responds to changes in circulation rate and watermass mixing ratio, and two tests that illustrate how ε_{Nd} responds to changes in preformed ε_{Nd} of the end-members, as follows: "NSW/4", reducing NSW production (*F1* in Fig. 4.S1) by 4-fold; SSW*4", increasing SSW production (*F2, F4* and *F6* in Fig. 4.S1) by 4-fold; “NSW_pref+5”, increasing the NSW preformed ε_{Nd} by 5 ε; “SSW_pref+5”, increasing the SSW preformed ε_{Nd} by 5 ε. Both “NSW/4” and “SSW*4” result in reduction of the NSW mixing ratio. Our box model cannot resolve the local processes that set the preformed ε_{Nd} at the locations of deep water formation(Lacan & Jeandel 2005b). Instead, we implement this change via the sedimentary source ε_{Nd}, which has the same effect in the box model(Du et al. 2018). These simulations all started with the modern condition, and the forcings described above were applied for 1000 years, by which time new steady-state was established. All other parameters remain the same as the modern case.

Box model transient simulations

We use transient simulations to find plausible physical mechanisms underlying the two PCs (Fig. 4.4), informed by the sensitivity results (Fig. 4.S3).

We first performed a transient simulation (“NSW_pref” in Fig. 4.S4) to test how well the PC1 pattern can be explained by varying the preformed ε_{Nd} of NSW. In

this simulation, we scaled the preformed ε_{Nd} of NSW to PC1. As discussed above, this was done by varying the Atlantic sedimentary source ε_{Nd}, wherein the LGM NSW preformed ε_{Nd} was increased by +5 ε relative to the Holocene, matching the observed increase of authigenic ε_{Nd} in the subpolar North Atlantic (Fig. 4.2) and supported by the sensitivity tests (Fig. 4.S3). We then varied the NSW preformed ε_{Nd} anomaly (with respect to the Holocene) over the last 22 ka by linearly scaling it to PC1. We hypothesize that this change of preformed ε_{Nd} results from a shift of the location of NSW formation to south of Iceland such that the influence of highly negative ε_{Nd} (<–25 ε) Precambrian detrital sediments in the Labrador Basin was reduced (Fig. 4.3). All the other parameters in this simulation were held constant as in the modern case.

We then performed another set of transient simulations to test our hypothesis that the PC2 pattern is associated with deglacial change of SSW production rate (SOMOC transport) but *not* NSW production rate (AMOC transport) (Extended Data Fig. 4.6).

In "SOMOC+", we scaled SOMOC transport to PC2. In this scaling, we reduced LGM SOMOC transport (SSW production) to the deep Atlantic, Pacific and Indian Oceans by half relative to the Holocene. We then prescribed SOMOC transport (with respect to the Holocene) over the last 22 ka by linearly scaling it to PC2. The choice of SOMOC scaling is chosen based on our previous study in the Pacific(Du et al. 2018), and is similar to the scaling used in an Earth System Model to simulate deglacial change of atmospheric CO_2 concentration(Menviel et al. 2018). This scaling reflects our interpretation that PC2 indicates strengthening of SOMOC during HS1 and YD, as shown in the sensitivity tests. All the other parameters, including AMOC transport, were held constant as in the modern case.

In "AMOC−", we scaled AMOC transport to North Atlantic records of $^{231}Pa/^{230}Th$, which is a proxy for AMOC strength(Ng et al. 2018). We used the North Atlantic $^{231}Pa/^{230}Th$ compilation in ref.(Ng et al. 2018). We smoothed the data using Loess regression and extract the median $^{231}Pa/^{230}Th$ time-series in the last 22 kyr (Fig.

4.4). In this simulation, we reduced LGM AMOC transport to half of the Holocene, as suggested in the main text. We then scaled AMOC transport over the last 22 ka linearly to the median $^{231}Pa/^{230}Th$ time-series. Any resulting negative scaling factor was cut off at zero, which occurs at HS1. As such, this is an extreme scenario of AMOC variability during the deglaciation, wherein AMOC entirely ceased in HS1. All the other parameters, including SOMOC transport (SSW production), were held constant as in the modern case.

In "SOMOC+ AMOC−", we used both the SOMOC and AMOC scaling factors discussed above to examine the composite effect of these two varaiables. All the other parameters were held constant as in the modern case.

Finally, we performed a simulation ("NSW_pref+SOMOC" in Extended Data Fig. 4.4) adopting both the PC1 and PC2 related mechanisms, *i.e.*, using both the preformed ε_{Nd} anomaly of NSW in "NSW_pref" and SOMOC scaling factors in "SOMOC+". All the other parameters were held constant as in the modern case.

Acknowledgements

Funding for this study was provided by National Science Foundation Grant #1502754 to A.C.M. and #1357529 to A.C.M and B.A.H.

Author contributions: J.D., B.A.H. and A.C.M designed this study. J.D. led the effort of data collection, analysis and modeling. B.A.H. and A.C.M. contributed to data analysis, modeling and interpretation. J.D. wrote the initial manuscript with significant contributions from B.A.H. and A.C.M.

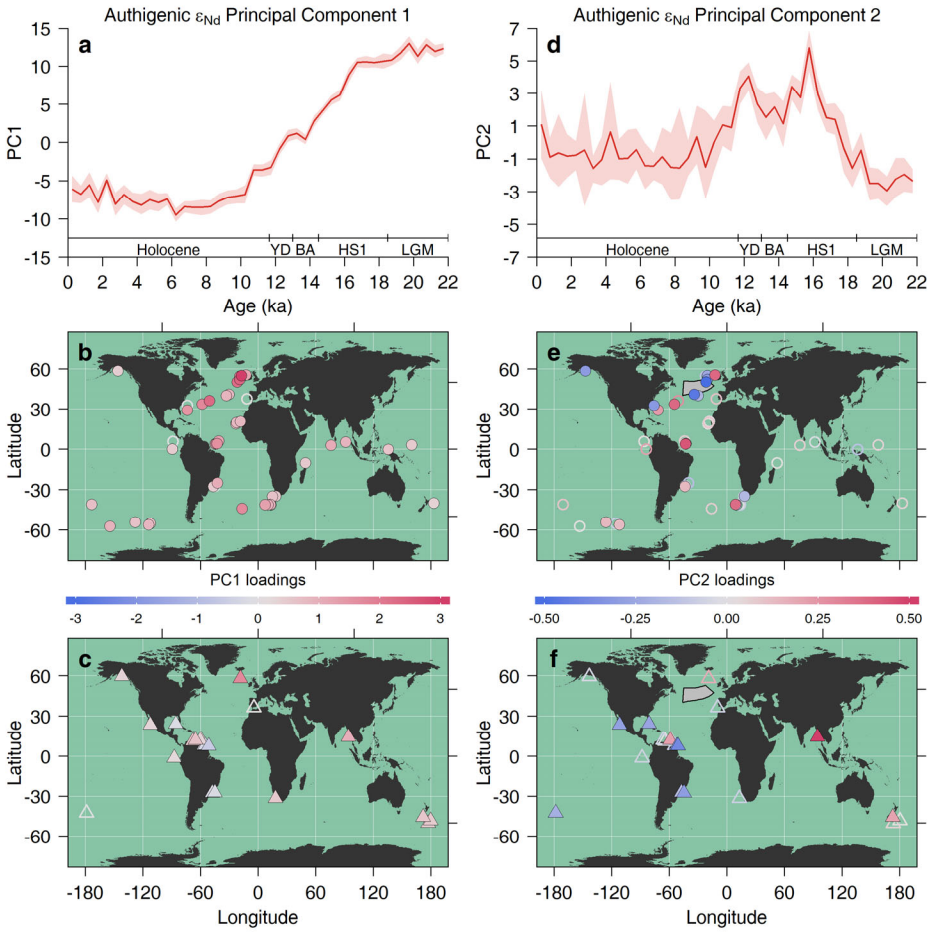

Figure 4.1. Principal components (PCs) of global authigenic ε_{Nd} data since the LGM.

a, PC1 time-series (shading is 95% confidence interval/CI). b, PC1 loadings at deep sites (circles, >1500 m). c, PC1 loadings at intermediate-depth sites (triangles, 500~1500 m). d to f Same as a to c but for PC2. The absolute value of the loadings is proportional to variance of each component in authigenic ε_{Nd} records. Filled symbols indicate loadings that are significantly different from zero (95% CI); open symbols are not significantly different from zero. The grey shaded area in the North Atlantic in e and f is the ice-rafted-debris (IRD) belt associated with HEs(Hemming 2004).

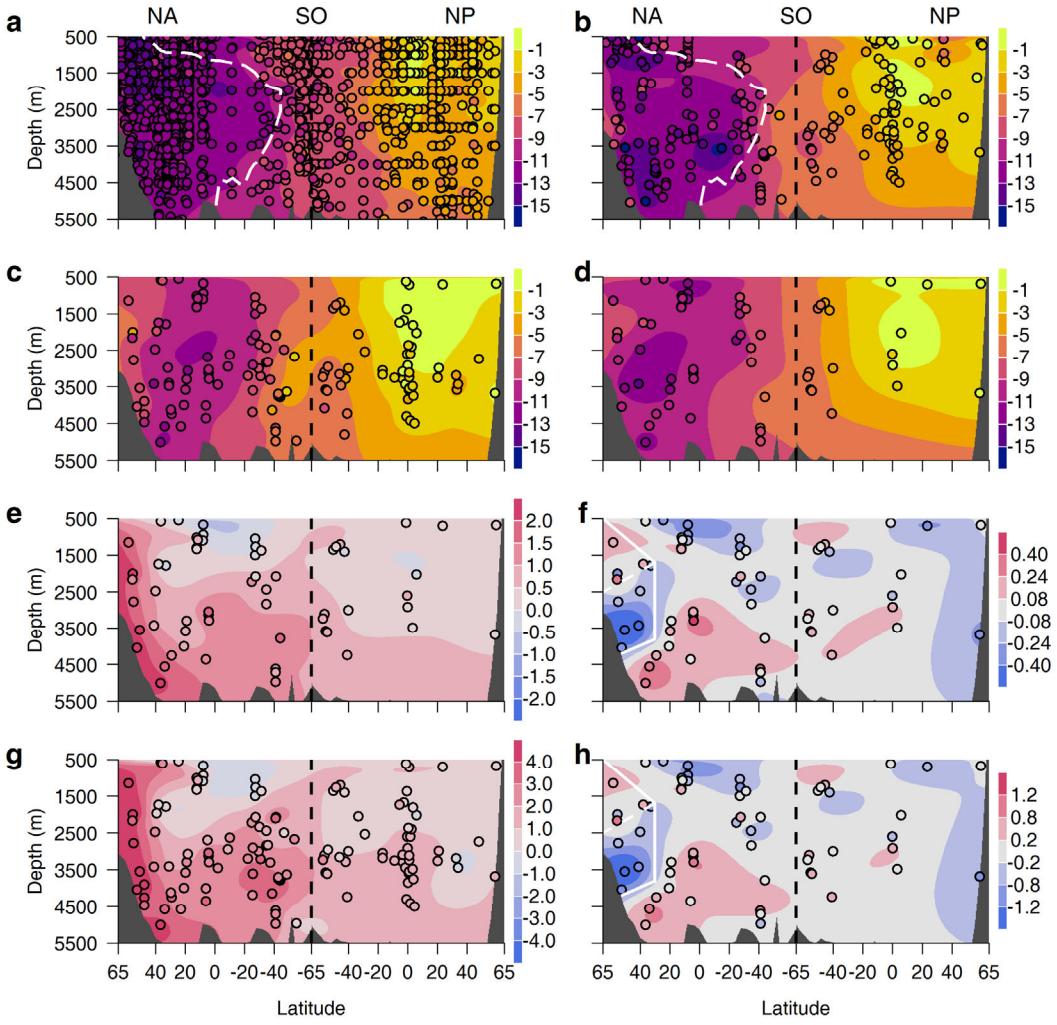

Figure 4.2. Atlantic-Pacific Ocean data sections.

a, Modern seawater ε_{Nd}. b, Holocene authigenic ε_{Nd}. c, LGM authigenic ε_{Nd}. d, HS1 authigenic ε_{Nd}. e, PC1 loadings. f, PC2 loadings. g, PC1 reconstructed LGM-Holocene authigenic ε_{Nd} difference. h, PC2 reconstructed HS1-LGM authigenic ε_{Nd} difference. The Atlantic and Pacific sections are joined at 65°S in the Southern Ocean (SO) indicated by the black dash line. North Atlantic (NA) is to the left and North Pacific (NP) to the right. In a and b, the white dash line indicates the modern 50% NSW volume fraction(Gebbie & Huybers 2010). In f and h, the white solid line separates the regions affected by detrital imprint on authigenic ε_{Nd} during HEs around the IRD belt in Figure 4.1, and the white dash line further divides this region based on detrital sources (Appendix C). For data source and gridding see Methods.

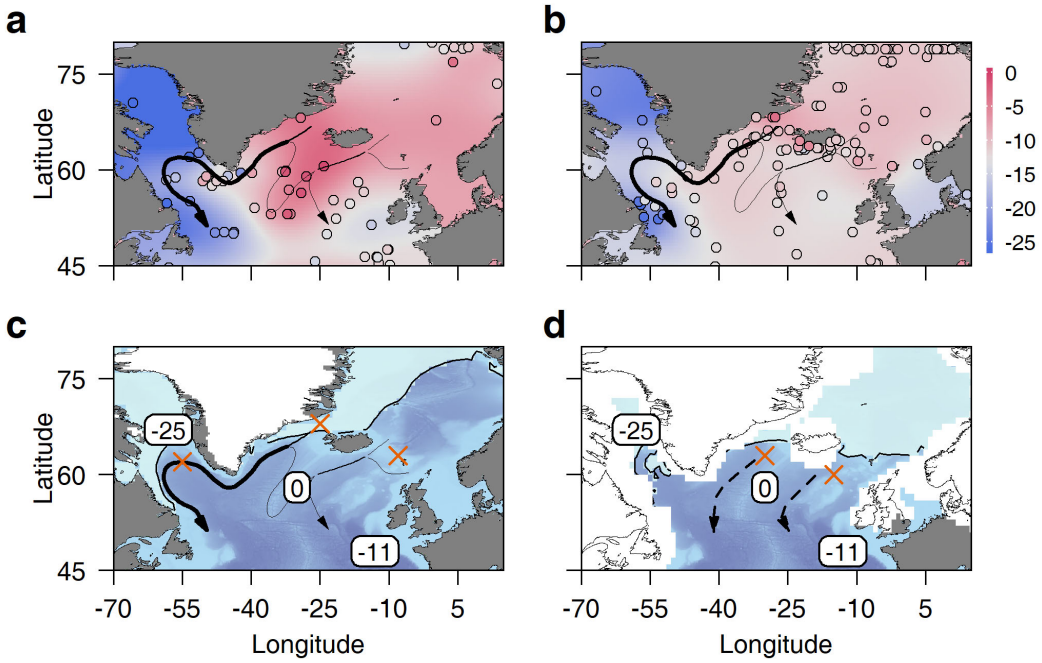

Figure 4.3. Influence of the detrital Nd sources on the preformed ε_{Nd} of NSW, and its relation to the formation location of NSW in the subpolar North Atlantic.

a, Core-top detrital ε_{Nd}. b, Modern *bottom* water (defined as within 500 m of seafloor) ε_{Nd}. Red (blue) color indicates more positive (negative) ε_{Nd} than the preformed ε_{Nd} (~–13) of modern NADW exported to the subtropics(van de Flierdt et al. 2016). c, Modern and d, Hypothetical LGM deep circulation in the subpolar North Atlantic. Black solid lines in a to c indicate modern circulation pathways the widths of which are schematically scaled to transport(Daniault et al. 2016). Black dash lines in d indicate hypothetical LGM circulation pathways inferred from ε_{Nd}. Distributions of ice sheet/shelf (white pixels) and 50% winter sea ice fraction coverage (cyan pixels with black borders) during the pre-industrial in c and LGM in d are from the Paleoclimate Modelling Intercomparison Project Phase III (PMIP3) results (Methods). The numbers in white background in c and d indicate the ε_{Nd} of the three main detrital sources in a (Methods). The "X" symbols in c and d mark modern(Lacan & Jeandel 2005b) and hypothetical LGM boundary exchange sites that affect the preformed ε_{Nd} of NSW.

Figure 4.4. Observed and simulated deglacial authigenic ε_{Nd} records compared to global climate proxies.

a, Multiplication factor (with respect to the Holocene mean and scaled to PC2) applied to SOMOC transport in the transient simulation. b, Model results (solid lines) compared to the PC2 components (ribbons with 95% CIs) of representative authigenic ε_{Nd} records. The records are from North Pacific site EW0408-87JC (58.8°N, 144.5°W, 3,680 m)(Du et al. 2018), Southern Ocean site PS75/073_2 (57.2°S, 151.6°W, 3,234 m)(Basak et al. 2018) and North Atlantic site OCE326_GGC6 (33.7°N, 57.6°W, 4,543 m)(Roberts et al. 2010). The mean ε_{Nd} offset between each individual site and the ocean box average is removed to facilitate data-model comparison. c, $^{231}Pa/^{230}Th$ records from the North Atlantic(Ng et al. 2018) (dots indicate raw data with 2σ error bars; ribbon indicates Loess 95% CI). 0.093 (dotted line) is the production ratio. d, Ice core CO_2 (blue dots with 1σ error bars)(Marcott et al. 2014) and noble gas derived Mean Ocean Temperature (MOT) anomaly (red ribbon with 1σ CI)(Bereiter et al. 2018). e, Ice core $\delta^{13}C$-CO_2 from the high resolution Taylor Glacier record (blue dots with 1σ error bars)(Bauska et al. 2016) and a previous spline-smoothed compilation (blue ribbon with 1σ CI)(Schmitt et al. 2012), together with the rate change of MOT ($dMOT/dt$) estimated using nonparametric kernel regression smoothing with a bandwidth of 1.5 kyr (red ribbon with 1σ CI).

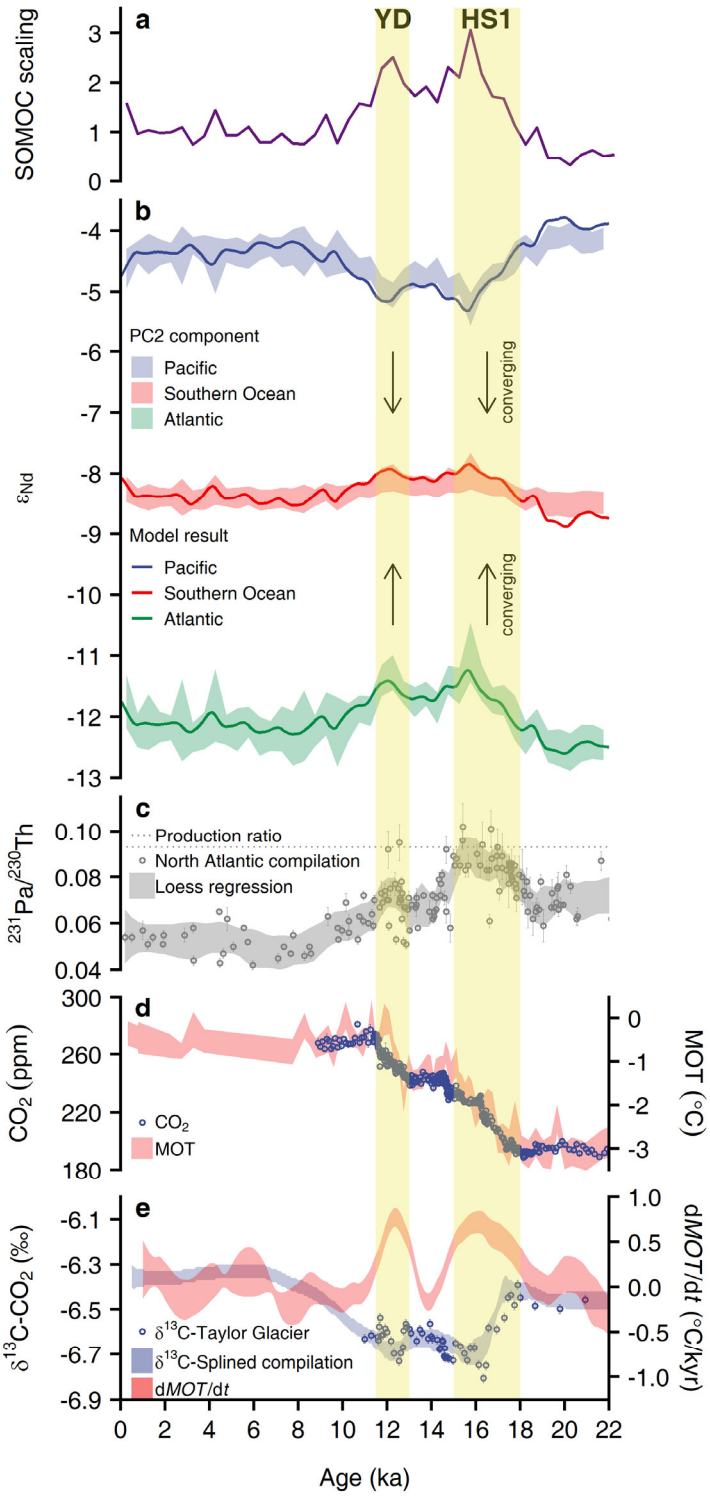

Figure 4.4. Observed and simulated deglacial authigenic ε_{Nd} records compared to global climate proxies.

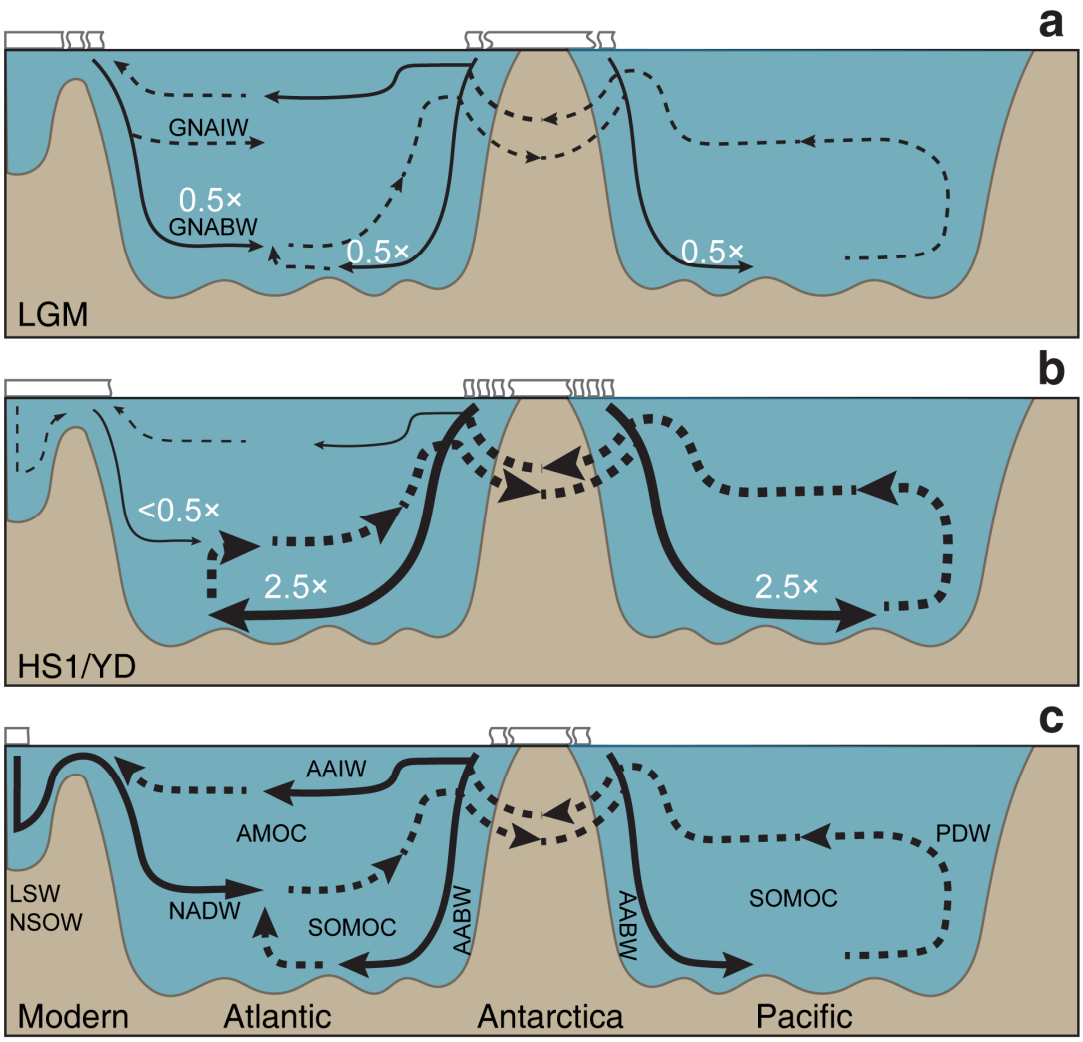

Figure 4.5. Schematics of ocean circulation in the LGM (a), HS1 and YD (b), and today (c).

The modern scheme is based on ref.(Talley 2013), in which the Atlantic and Pacific branches of SOMOC are interconnected around Antarctica. The solid lines with arrows mark major descending watermasses, and the dash lines with arrows mark the return flows or hypothetical watermasses. Note inferred Glacial North Atlantic Intermediate and Bottom Water (GNAIW and GNABW). For schematics LSW and NSOW appear together but separated from the North Atlantic basin. The thickness of the lines indicates hypothetical transport strength. The white numbers in a and b indicate inferred scaling of the circulation strength relative to the modern case in c (i.e., "2.5×" means 2.5 times of today) (Fig. 4.4). The white blocks on top indicate continental and sea ice/shelf.

Chapter 5: Conclusions

Summary

In this dissertation I revisit the application of marine authigenic ε_{Nd} as a tracer of ocean circulation in the past. Incorporating the recent advances in understanding the modern marine Nd cycle, I propose a new framework of using authigenic ε_{Nd} in paleoceanography. With this new framework, I reconstruct the Global Overturning Circulation (GOC) since the Last Glacial Maximum (LGM).

I first developed a leaching method to reliably extract marine authigenic Fe-Mn oxyhydroxide from bulk sediments. This method was tested on a suite of core top and volcanic ash samples from the Gulf of Alaska (GOA). I used geochemical tools, including trace elemental compositions and Sr-Nd isotopes to identify the phases extracted using this method. I showed that the dominant phases extracted was Fe-Mn oxyhydroxide, while contamination due to leaching detrital sediments and dispersed volcanic ash is negligible. However, when compared to seawater ε_{Nd} profiles from the same region, I found that the ε_{Nd} of authigenic phases and bottom water were different. This challenges the traditionally assumption that authigenic phases should passively record bottom water ε_{Nd}. Instead, I show that this difference is evidence of sedimentary sources of Nd. Building on the recent works on pore water and authigenic phase ε_{Nd}, I created a conceptual model that explains how authigenic phases acquire their ε_{Nd} signatures, in which the interactions between bottom water, pore water, authigenic phases and detrital sediments, mediated by early diagenesis, is required to fully understand what authigenic ε_{Nd} means. This conceptual model considers the non-conservative effect on authigenic ε_{Nd}, which is a function of both benthic exposure time and detrital sediment composition. I show that this conceptual model can be applied to the distributions of seawater and authigenic ε_{Nd} in the Pacific.

With this new conceptual model, I reconstructed the Pacific circulation since the LGM. I generated two new high resolution authigenic ε_{Nd} records using cores from the intermediate and abyssal depths of the GOA using the new method I developed. The ε_{Nd} records were complemented with benthic ^{14}C records from the same sites. Because the non-conservative effects dominate the distribution of ε_{Nd},

which is modified by benthic exposure time, I was able to reconstruct quantitatively the Pacific circulation rate together with benthic ^{14}C. This reconstruction was aided by including other published records from the South Pacific using a box model. I found that the Pacific abyssal circulation was weakened by ~half in the LGM, because of reduced Southern Ocean overturning. During the deglacial Northern Hemisphere stadial events, transport of deep waters from the Southern Ocean into the Pacific increases by ~2-fold. The reconstruction of the Pacific circulation leads to the conclusion that variability of the abyssal overturning was likely responsible for changes of atmospheric CO_2 since the LGM.

Finally, I synthesized the global marine authigenic ε_{Nd} records since the LGM under the new conceptual framework. Using Principal Component Analysis (PCA), I identified the global and inter-basinal scale modes of ε_{Nd} variability. I found that the global ε_{Nd} data can be explained by two major Principal Components (PCs). PC1 explains mainly the glacial-interglacial variations, such that the global deep ocean ε_{Nd} was more positive in the LGM than the Holocene, the magnitude of change was greater in the Atlantic and smaller in the Southern and Pacific Oceans. I suggest that PC1 can be explained by an increase of the preformed ε_{Nd} of the Northern Source Water because the principal location of deep water formation shifted toward south of Iceland, where a more positive preformed ε_{Nd} was acquired through boundary exchange with sediments that have higher ε_{Nd}. PC2 is dominated by the deglacial millennial scale changes coeval with Heinrich Stadial 1 and the Younger Dryas events. During these events, deep North Atlantic and North Pacific ε_{Nd} converged, suggesting vigorous Southern Ocean overturning overcame the reduction of North Atlantic overturning. These inferences were tested using a global box model. The inferred circulation change correlates to changes of atmospheric CO_2 and ocean heat transport, suggesting a major role of GOC in the global climate system

Future Perspectives

Studying the ocean in the past is key to understanding the role of the ocean in Earth's climate because modern observations of the ocean are often too short. Our

ability to reconstruct past ocean changes rests on our understanding of the geochemical processes regulating the distribution of the tracers used for such reconstructions. With increasing analytical capacity and ever-expanding observational database, our understanding of the cycling of trace metals, among the most common circulation tracers, is evolving rapidly. Application of these tracers in paleoceanography therefore needs to be continuously updated.

Despite the recent advances, our knowledge of the modern marine Nd cycle is still limited (Abbott et al. 2016; Haley et al. 2017). The most urgent need at this moment is to study the processes happening at the sediment-water interface and how they affect the distributions of the ε_{Nd} of bottom water, pore water and authigenic phases. At the minimum, we need to increase the number of benthic flux and pore water ε_{Nd} measurements considerably. The major issue to address is what environmental factors control the magnitude and ε_{Nd} of benthic Nd flux (Abbott et al. 2015b). Lab experiments is also necessary to understand the reactivity of detrital sediments (Abbott et al. 2016; Blaser et al. 2016; Wilson et al. 2013), which are clearly involved in setting up the sedimentary Nd source. The implication of detrital sediments being reactive is profound, since it affects the cycling of all trace metals and isotopes in the ocean-sediment system.

Historically, studies of past ocean circulation often focus on reconstructing the watermass mixing ratio, especially the relative contributions of deep waters produced in the North Atlantic versus Southern Ocean. However, watermass mixing is not the sole, and often not the most important, aspect of the ocean circulation that affects tracer distribution. The surface and bottom boundary conditions of the ocean, which set the preformed properties of the tracers, and the circulation rate, which controls the relative influence of the conservative and non-conservative effects, are also critical in interpreting paleo-circulation tracers. Because circulation affects tracer distributions in non-unique ways, using tracers to reconstruct circulation requires decomposition (Gebbie 2014; Khatiwala et al. 2012), that is, separating the tracer into the components linked to the different aspects of the circulation. Future studies need to consider reinterpreting existing tracer records under such a framework.

The Atlantic-only paradigm has dominated paleoceanography since the beginning. Undoubtedly, formation of NADW is important, but to neglect the role of the other ocean basins and watermasses may miss the "bigger pictures" of ocean circulation change in the past. Increasingly, watermass transformation in the Pacific and Indian Ocean that converts dense deep water to lighter waters, which appears to happen mostly through the benthic boundary layer, is seen as crutial in sustaining the GOC (de Lavergne et al. 2015, 2017; Ferrari 2014; Ferrari et al. 2016; Mashayek et al. 2017; Talley 2013). And it is linked to Southern Ocean overturning, our understanding of which remains incomplete. Increasing our attention to these basins is necessary for a wholistic understanding of the GOC.

Bibliography

Abbott AN. 2019. A benthic flux from calcareous sediments results in non-conservative neodymium behavior during lateral transport: A study from the Tasman Sea. *Geology*. 47(4):363–66

Abbott AN, Haley BA, McManus J. 2015a. Bottoms up: Sedimentary control of the deep North Pacific Ocean's εNd signature. *Geology*. 43(11):1035–1035

Abbott AN, Haley BA, McManus J. 2016. The impact of sedimentary coatings on the diagenetic Nd flux. *Earth and Planetary Science Letters*. 449:217–27

Abbott AN, Haley BA, McManus J, Reimers CE. 2015b. The sedimentary flux of dissolved rare earth elements to the ocean. *Geochimica et Cosmochimica Acta*. 154:186–200

Abe-Ouchi A, Saito F, Kageyama M, Braconnot P, Harrison SP, et al. 2015. Ice-sheet configuration in the CMIP5/PMIP3 Last Glacial Maximum experiments. *Geoscientific Model Development*. 8(11):3621–37

Abernathey RP, Cerovecki I, Holland PR, Newsom E, Mazloff M, Talley LD. 2016. Water-mass transformation by sea ice in the upper branch of the Southern Ocean overturning. *Nature Geoscience*. 9(8):596–601

Adkins JF. 2013. The role of deep ocean circulation in setting glacial climates. *Paleoceanography*. 28(3):539–61

Adkins JF, Ingersoll AP, Pasquero C. 2005. Rapid climate change and conditional instability of the glacial deep ocean from the thermobaric effect and geothermal heating. *Quaternary Science Reviews*. 24(5–6):581–94

Adkins JF, McIntyre K, Schrag DP. 2002. The Salinity, Temperature, and δ18O of the Glacial Deep Ocean. *Science*. 298(5599):1769–73

Akagi T, Fu F, Hongo Y, Takahashi K. 2011. Composition of rare earth elements in settling particles collected in the highly productive North Pacific Ocean and Bering Sea: Implications for siliceous-matter dissolution kinetics and formation of two REE-enriched phases. *Geochim. Cosmochim. Acta*. 75(17):4857–76

Alekseyev VA. 2007. Equations for the dissolution reaction rates of montmorillonite, illite, and chlorite. *Geochem. Int.* 45(8):770–80

Aller RC. 2014. 8.11 - Sedimentary Diagenesis, Depositional Environments, and Benthic Fluxes A2 - Holland, Heinrich D. In *Treatise on Geochemistry (Second Edition)*, ed. KK Turekian, pp. 293–334. Oxford: Elsevier

Amakawa. 2004. Nd concentration and isotopic composition distributions in surface waters of Northwest Pacific Ocean and its adjacent seas. *Geochemical Journal*. 38:493–504

Amakawa H, Nozaki Y, Alibo DS, Zhang J, Fukugawa K, Nagai H. 2004. Neodymium isotopic variations in Northwest Pacific waters. *Geochimica et Cosmochimica Acta*. 68(4):715–27

Amakawa H, Sasaki K, Ebihara M. 2009. Nd isotopic composition in the central North Pacific. *Geochimica et Cosmochimica Acta*. 73(16):4705–19

Amakawa H, Tazoe H, Obata H, Gamo T, Sano Y, Chuan-Chou S. 2013. Neodymium isotopic composition and concentration in the Southwest Pacific Ocean. *Geochem. J.* 47(4):409–22

Amante C, Eakins BW. 2009. ETOPO1 arc-minute global relief model : procedures, data sources and analysis

Amrhein DE, Wunsch C, Marchal O, Forget G. 2018. A Global Glacial Ocean State Estimate Constrained by Upper-Ocean Temperature Proxies. *J. Climate*. 31(19):8059–79

Anderson RF, Ali S, Bradtmiller LI, Nielsen SHH, Fleisher MQ, et al. 2009. Wind-Driven Upwelling in the Southern Ocean and the Deglacial Rise in Atmospheric CO2. *Science*. 323(5920):1443–48

Arsouze T, Dutay J-C, Kageyama M, Lacan F, Alkama R, et al. 2008. A modeling sensitivity study of the influence of the Atlantic meridional overturning circulation on neodymium isotopic composition at the Last Glacial Maximum. *Clim. Past*. 4(3):191–203

Arsouze T, Dutay J-C, Lacan F, Jeandel C. 2007. Modeling the neodymium isotopic composition with a global ocean circulation model. *Chemical Geology*. 239(1–2):165–77

Arsouze T, Dutay J-C, Lacan F, Jeandel C. 2009. Reconstructing the Nd oceanic cycle using a coupled dynamical – biogeochemical model. *Biogeosciences*. 6(12):2829–46

Arsouze T, Treguier AM, Peronne S, Dutay J-C, Lacan F, Jeandel C. 2010. Modeling the Nd isotopic composition in the North Atlantic basin using an eddy-permitting model. *Ocean Sci.* 6(3):789–97

Asahara Y, Takeuchi F, Nagashima K, Harada N, Yamamoto K, et al. 2012. Provenance of terrigenous detritus of the surface sediments in the Bering and Chukchi Seas as derived from Sr and Nd isotopes: Implications for recent climate change in the Arctic regions. *Deep Sea Research Part II: Topical Studies in Oceanography*. 61–64:155–71

Bacon MP, Anderson RF. 1982. Distribution of thorium isotopes between dissolved and particulate forms in the deep sea. *J. Geophys. Res.* 87(C3):2045–56

Balbas AM, Barth AM, Clark PU, Clark J, Caffee M, et al. 2017. 10Be dating of late Pleistocene megafloods and Cordilleran Ice Sheet retreat in the northwestern United States. *Geology*. 45(7):583–86

Bandstra JZ, Brantley SL. 2008. Data Fitting Techniques with Applications to Mineral Dissolution Kinetics. In *Kinetics of Water-Rock Interaction*, eds. SL Brantley, JD Kubicki, AF White, pp. 211–57. Springer New York

Barth A, Beckers J-M, Troupin C, Alvera-Azcárate A, Vandenbulcke L. 2014. divand-1.0: n-dimensional variational data analysis for ocean observations. *Geosci. Model Dev.* 7(1):225–41

Basak C, Fröllje H, Lamy F, Gersonde R, Benz V, et al. 2018. Breakup of last glacial deep stratification in the South Pacific. *Science*. 359(6378):900–904

Basak C, Martin EE, Horikawa K, Marchitto TM. 2010. Southern Ocean source of 14C-depleted carbon in the North Pacific Ocean during the last deglaciation. *Nature Geosci*. 3(11):770–73

Basak C, Pahnke K, Frank M, Lamy F, Gersonde R. 2015. Neodymium isotopic characterization of Ross Sea Bottom Water and its advection through the southern South Pacific. *Earth and Planetary Science Letters*. 419:211–21

Bau M, Tepe N, Mohwinkel D. 2013. Siderophore-promoted transfer of rare earth elements and iron from volcanic ash into glacial meltwater, river and ocean water. *Earth and Planetary Science Letters*. 364:30–36

Bauska TK, Baggenstos D, Brook EJ, Mix AC, Marcott SA, et al. 2016. Carbon isotopes characterize rapid changes in atmospheric carbon dioxide during the last deglaciation. *Proceedings of the National Academy of Sciences*. 113(13):3465–70

Bayon G, German CR, Boella RM, Milton JA, Taylor RN, Nesbitt RW. 2002. An improved method for extracting marine sediment fractions and its application to Sr and Nd isotopic analysis. *Chemical Geology*. 187(3–4):179–99

Bayon G, German CR, Burton KW, Nesbitt RW, Rogers N. 2004. Sedimentary Fe–Mn oxyhydroxides as paleoceanographic archives and the role of aeolian flux in regulating oceanic dissolved REE. *Earth and Planetary Science Letters*. 224(3–4):477–92

Bayon G, Toucanne S, Skonieczny C, André L, Bermell S, et al. 2015. Rare earth elements and neodymium isotopes in world river sediments revisited. *Geochimica et Cosmochimica Acta*. 170:17–38

Behrenfeld MJ, Falkowski PG. 1997. Photosynthetic rates derived from satellite-based chlorophyll concentration. *Limnol. Oceanogr.* 42(1):1–20

Behrens MK, Pahnke K, Schnetger B, Brumsack H-J. 2018. Sources and processes affecting the distribution of dissolved Nd isotopes and concentrations in the West Pacific. *Geochimica et Cosmochimica Acta*. 222:508–34

Bereiter B, Eggleston S, Schmitt J, Nehrbass-Ahles C, Stocker TF, et al. 2015. Revision of the EPICA Dome C CO2 record from 800 to 600 kyr before present. *Geophysical Research Letters*. 42(2):542–49

Bereiter B, Shackleton S, Baggenstos D, Kawamura K, Severinghaus J. 2018. Mean global ocean temperatures during the last glacial transition. *Nature*. 553(7686):39

Berelson W. 2001. The Flux of Particulate Organic Carbon Into the Ocean Interior: A Comparison of Four U.S. JGOFS Regional Studies. *Oceanography*. 14(4):59–67

Berner RA. 1980. *Early Diagenesis: A Theoretical Approach*. Princeton University Press

Bertram CJ, Elderfield H. 1993. The geochemical balance of the rare earth elements and neodymium isotopes in the oceans. *Geochimica et Cosmochimica Acta*. 57(9):1957–86

Blaser P, Lippold J, Gutjahr M, Frank N, Link JM, Frank M. 2016. Extracting foraminiferal seawater Nd isotope signatures from bulk deep sea sediment by chemical leaching. *Chemical Geology*. 439:189–204

Blaser P, Pöppelmeier F, Schulz H, Gutjahr M, Frank M, et al. 2019. The resilience and sensitivity of Northeast Atlantic deep water εNd to overprinting by detrital fluxes over the past 30,000 years. *Geochimica et Cosmochimica Acta*. 245:79–97

Bode GW. 1973. Appendix VI: Carbon and Carbonate Analyses, Leg 18. In *Initial Reports of the Deep Sea Drilling Project*, Vol. 18, eds. LVD Kulm, R von Huene, pp. 1069–76. Washington, D.C.: U.S. Govt. Printing Office

Böhm E, Lippold J, Gutjahr M, Frank M, Blaser P, et al. 2015. Strong and deep Atlantic meridional overturning circulation during the last glacial cycle. *Nature*. 517(7532):73–76

Bond G, Showers W, Cheseby M, Lotti R, Almasi P, et al. 1997. A Pervasive Millennial-Scale Cycle in North Atlantic Holocene and Glacial Climates. *Science*. 278(5341):1257–66

Bond GC, Lotti R. 1995. Iceberg Discharges Into the North Atlantic on Millennial Time Scales During the Last Glaciation. *Science*. 267(5200):1005–10

Boudreau BP. 1997. *Diagenetic Models and Their Implementation: Modelling Transport and Reactions in Aquatic Sediments*

Bradtmiller LI, McManus JF, Robinson LF. 2014. $^{231}Pa/^{230}Th$ evidence for a weakened but persistent Atlantic meridional overturning circulation during Heinrich Stadial 1. *Nature Communications*. 5:5817

Brady EC, Otto-Bliesner BL, Kay JE, Rosenbloom N. 2012. Sensitivity to Glacial Forcing in the CCSM4. *Journal of Climate*. 26(6):1901–25

Brantley SL. 2008. Kinetics of Mineral Dissolution. In *Kinetics of Water-Rock Interaction*, pp. 151–210. Springer, New York, NY

Brantley SL, Mellott NP. 2000. Surface area and porosity of primary silicate minerals. *American Mineralogist*. 85(11–12):1767–83

Brantley SL, Olsen AA. 2014. Reaction Kinetics of Primary Rock-Forming Minerals under Ambient Conditions. In *Treatise on Geochemistry (Second Edition)*, eds. HD Holland, KK Turekian, pp. 69–113. Oxford: Elsevier

Broecker W, Barker S, Clark E, Hajdas I, Bonani G, Stott L. 2004. Ventilation of the Glacial Deep Pacific Ocean. *Science*. 306(5699):1169–72

Broecker W, Clark E, Barker S. 2008. Near constancy of the Pacific Ocean surface to mid-depth radiocarbon-age difference over the last 20 kyr. *Earth and Planetary Science Letters*. 274(3–4):322–26

Broecker W, Clark E, Barker S, Hajdas I, Bonani G, Moreno E. 2007. Radiocarbon age of late glacial deep water from the equatorial Pacific. *Paleoceanography*. 22(2):PA2206

Broecker WS. 1991. The Great Ocean Conveyor. *Oceanography*. 4(2):79–89

Broecker WS. 1998. Paleocean circulation during the Last Deglaciation: A bipolar seesaw? *Paleoceanography*. 13(2):119–21

Brown D, Brownrigg R, Haley M, Huang W. 2018. The NCAR Command Language (Version 6.5.0) [Software]. *Boulder, Colorado: UCAR/NCAR/CISL/TDD*

Buckley MW, Marshall J. 2016. Observations, inferences, and mechanisms of the Atlantic Meridional Overturning Circulation: A review. *Reviews of Geophysics*. 54(1):5–63

Burdige DJ. 1993. The biogeochemistry of manganese and iron reduction in marine sediments. *Earth-Science Reviews*. 35(3):249–84

Burdige DJ. 2006. *Geochemistry of Marine Sediments*. Princeton University Press

Burdige DJ, Gieskes JM. 1983. A pore water/solid phase diagenetic model for manganese in marine sediments. *Am J Sci*. 283(1):29–47

Burke A, Robinson LF. 2012. The Southern Ocean's Role in Carbon Exchange During the Last Deglaciation. *Science*. 335(6068):557–61

Burton KW, Vance D. 2000. Glacial–interglacial variations in the neodymium isotope composition of seawater in the Bay of Bengal recorded by planktonic foraminifera. *Earth and Planetary Science Letters*. 176(3–4):425–41

Byrne RH, Kim K-H. 1990. Rare earth element scavenging in seawater. *Geochimica et Cosmochimica Acta*. 54(10):2645–56

Caesar L, Rahmstorf S, Robinson A, Feulner G, Saba V. 2018. Observed fingerprint of a weakening Atlantic Ocean overturning circulation. *Nature*. 556(7700):191–96

Caetano M, Prego R, Vale C, de Pablo H, Marmolejo-Rodríguez J. 2009. Record of diagenesis of rare earth elements and other metals in a transitional sedimentary environment. *Marine Chemistry*. 116(1):36–46

Canfield DE. 1989. Reactive iron in marine sediments. *Geochimica et Cosmochimica Acta*. 53(3):619–32

Cao LQ, Arculus RJ. 1995. Data Report: Geochemistry of volcanic ashes recovered from Hole 887A. In *Proc. ODP, Sci. Results*, Vol. 145, eds. DK Rea, IA Basov, DW Scholl, JF Allan, pp. 661–69. College Station, TX (Ocean Drilling Program)

Carter P, Vance D, Hillenbrand CD, Smith JA, Shoosmith DR. 2012. The neodymium isotopic composition of waters masses in the eastern Pacific sector of the Southern Ocean. *Geochimica et Cosmochimica Acta*. 79:41–59

Chen J, Algeo TJ, Zhao L, Chen Z-Q, Cao L, et al. 2015. Diagenetic uptake of rare earth elements by bioapatite, with an example from Lower Triassic conodonts of South China. *Earth-Science Reviews*. 149:181–202

Clark PU, McCabe AM, Mix AC, Weaver AJ. 2004. Rapid Rise of Sea Level 19,000 Years Ago and Its Global Implications. *Science*. 304(5674):1141–44

Cogez A, Meynadier L, Allègre C, Limmois D, Herman F, Gaillardet J. 2015. Constraints on the role of tectonic and climate on erosion revealed by two time series analysis of marine cores around New Zealand. *Earth and Planetary Science Letters*. 410:174–85

Colin C, Frank N, Copard K, Douville E. 2010. Neodymium isotopic composition of deep-sea corals from the NE Atlantic: implications for past hydrological changes during the Holocene. *Quaternary Science Reviews*. 29(19–20):2509–2517

Cook MS, Keigwin LD. 2015. Radiocarbon profiles of the NW Pacific from the LGM and deglaciation: Evaluating ventilation metrics and the effect of uncertain surface reservoir ages. *Paleoceanography*. 30(3):174–95

Crocker AJ, Chalk TB, Bailey I, Spencer MR, Gutjahr M, et al. 2016. Geochemical response of the mid-depth Northeast Atlantic Ocean to freshwater input during Heinrich events 1 to 4. *Quaternary Science Reviews*. 151:236–54

Cuffey KM, Clow GD, Steig EJ, Buizert C, Fudge TJ, et al. 2016. Deglacial temperature history of West Antarctica. *Proceedings of the National Academy of Sciences*. 113(50):14249–54

Curry WB, Oppo DW. 2005. Glacial water mass geometry and the distribution of delta C-13 of Sigma CO2 in the western Atlantic Ocean. *Paleoceanography*. 20(1):PA1017

Daniault N, Mercier H, Lherminier P, Sarafanov A, Falina A, et al. 2016. The northern North Atlantic Ocean mean circulation in the early 21st century. *Progress in Oceanography*. 146:142–58

Davies MH, Mix AC, Stoner JS, Addison JA, Jaeger J, et al. 2011. The deglacial transition on the southeastern Alaska Margin: Meltwater input, sea level rise, marine productivity, and sedimentary anoxia. *Paleoceanography*. 26(2):PA2223

Davies-Walczak M, Mix AC, Stoner JS, Southon JR, Cheseby M, Xuan C. 2014. Late Glacial to Holocene radiocarbon constraints on North Pacific Intermediate Water ventilation and deglacial atmospheric CO2 sources. *Earth and Planetary Science Letters*. 397:57–66

de la Fuente M, Skinner L, Calvo E, Pelejero C, Cacho I. 2015. Increased reservoir ages and poorly ventilated deep waters inferred in the glacial Eastern Equatorial Pacific. *Nature Communications*. 6:7420

de Lavergne C, Madec G, Capet X, Maze G, Roquet F. 2016. Getting to the bottom of the ocean. *Nature Geoscience*. 9(12):857–58

de Lavergne C, Madec G, Le Sommer J, Nurser AJG, Naveira Garabato AC. 2015. On the Consumption of Antarctic Bottom Water in the Abyssal Ocean. *J. Phys. Oceanogr.* 46(2):635–61

de Lavergne C, Madec G, Roquet F, Holmes RM, McDougall TJ. 2017. Abyssal ocean overturning shaped by seafloor distribution. *Nature*. 551(7679):181–86

DeVries T, Holzer M, Primeau F. 2017. Recent increase in oceanic carbon uptake driven by weaker upper-ocean overturning. *Nature*. 542(7640):215–18

DeVries T, Weber T. The export and fate of organic matter in the ocean: New constraints from combining satellite and oceanographic tracer observations. *Global Biogeochemical Cycles*. 31(3):535–55

Du J, Haley BA, Mix AC. 2016. Neodymium isotopes in authigenic phases, bottom waters and detrital sediments in the Gulf of Alaska and their implications for paleo-circulation reconstruction. *Geochimica et Cosmochimica Acta*. 193:14–35

Du J, Haley BA, Mix AC, Walczak MH, Praetorius SK. 2018. Flushing of the deep Pacific Ocean and the deglacial rise of atmospheric CO 2 concentrations. *Nature Geoscience*. 11(10):749–55

Dubois-Dauphin Q, Bonneau L, Colin C, Montero-Serrano J-C, Montagna P, et al. 2016. South Atlantic intermediate water advances into the North-east Atlantic with reduced Atlantic meridional overturning circulation during the last glacial period. *Geochemistry, Geophysics, Geosystems*. 17(6):2336–53

Dunlea AG, Murray RW, Sauvage J, Spivack AJ, Harris RN, D'Hondt S. Dust, volcanic ash, and the evolution of the South Pacific Gyre through the Cenozoic. *Paleoceanography*. 30(8):1078–99

Duplessy JC, Shackleton NJ, Fairbanks RG, Labeyrie L, Oppo D, Kallel N. 1988. Deepwater source variations during the last climatic cycle and their impact on the global deepwater circulation. *Paleoceanography*. 3(3):343–60

Ehlert C, Grasse P, Frank M. 2013. Changes in silicate utilisation and upwelling intensity off Peru since the Last Glacial Maximum – insights from silicon and neodymium isotopes. *Quaternary Science Reviews*. 72:18–35

Elderfield H, Ferretti P, Greaves M, Crowhurst S, McCave IN, et al. 2012. Evolution of Ocean Temperature and Ice Volume Through the Mid-Pleistocene Climate Transition. *Science*. 337(6095):704–9

Elderfield H, Gieskes JM. 1982. Sr isotopes in interstitial waters of marine sediments from Deep Sea Drilling Project cores. *Nature*. 300(5892):493–97

Elderfield H, Pagett R. 1986. Analytical Chemistry in Marine Sciences Rare earth elements in ichthyoliths: Variations with redox conditions and depositional environment. *Science of The Total Environment*. 49:175–97

Elderfield H, Sholkovitz ER. 1987. Rare earth elements in the pore waters of reducing nearshore sediments. *Earth and Planetary Science Letters*. 82(3–4):280–88

Elmore AC, Piotrowski AM, Wright JD, Scrivner AE. 2011. Testing the extraction of past seawater Nd isotopic composition from North Atlantic deep sea sediments and foraminifera. *Geochem. Geophys. Geosyst.* 12(9):Q09008

Emerson S, Hedges J. 2003. Sediment Diagenesis and Benthic Flux. *Treatise on Geochemistry*. 6:625

Emile-Geay J, Cane MA, Naik N, Seager R, Clement AC, van Geen A. 2003. Warren revisited: Atmospheric freshwater fluxes and "Why is no deep water formed in the North Pacific." *Journal of Geophysical Research: Oceans*. 108(C6):3178

Fagel N, Innocent C, Gariepy C, Hillaire-Marcel C. 2002. Sources of Labrador Sea sediments since the last glacial maximum inferred from Nd-Pb isotopes. *Geochimica et Cosmochimica Acta*. 66(14):2569–81

Fagel N, Innocent C, Stevenson RK, Hillaire-Marcel C. 1999. Deep circulation changes in the Labrador Sea since the Last Glacial Maximum: New constraints from Sm-Nd data on sediments. *Paleoceanography*. 14(6):777–88

Farmer GL, Ayuso R, Plafker G. 1993. A Coast Mountains provenance for the Valdez and Orca groups, southern Alaska, based on Nd, Sr, and Pb isotopic evidence. *Earth and Planetary Science Letters*. 116(1–4):9–21

Ferrari R. 2014. Oceanography: What goes down must come up. *Nature*. 513(7517):179–80

Ferrari R, Jansen MF, Adkins JF, Burke A, Stewart AL, Thompson AF. 2014. Antarctic sea ice control on ocean circulation in present and glacial climates. *Proceedings of the National Academy of Sciences*. 111(24):8753–58

Ferrari R, Mashayek A, McDougall TJ, Nikurashin M, Campin J-M. 2016. Turning Ocean Mixing Upside Down. *J. Phys. Oceanogr.* 46(7):2239–61

Frank M. 2002. Radiogenic isotopes: Tracers of past ocean circulation and erosional input. *Reviews of Geophysics*. 40(1):1001

Freslon N, Bayon G, Toucanne S, Bermell S, Bollinger C, et al. 2014. Rare earth elements and neodymium isotopes in sedimentary organic matter. *Geochim. Cosmochim. Acta*. 140:177–98

Friedrich T, Timmermann A, Stichel T, Pahnke K. 2014. Ocean circulation reconstructions from εNd: A model-based feasibility study. *Paleoceanography*. 29(11):1003–23

Froelich PN, Klinkhammer GP, Bender ML, Luedtke NA, Heath GR, et al. 1979. Early oxidation of organic matter in pelagic sediments of the eastern

equatorial Atlantic: suboxic diagenesis. *Geochimica et Cosmochimica Acta*. 43(7):1075–90

Galbraith ED, Jaccard SL. 2015. Deglacial weakening of the oceanic soft tissue pump: global constraints from sedimentary nitrogen isotopes and oxygenation proxies. *Quaternary Science Reviews*. 109(Supplement C):38–48

Galbraith ED, Kienast M, Members TN working group, Galbraith ED, Kienast M, et al. 2013. The acceleration of oceanic denitrification during deglacial warming. *Nature Geoscience*. 6(7):579

Galbraith ED, Kwon EY, Bianchi D, Hain MP, Sarmiento JL. 2015. The impact of atmospheric pCO2 on carbon isotope ratios of the atmosphere and ocean. *Global Biogeochemical Cycles*. 29(3):307–24

Ganachaud A, Wunsch C. 2000. Improved estimates of global ocean circulation, heat transport and mixing from hydrographic data. *Nature*. 408(6811):453–57

Garcia HE, Locarnini RA, Boyer TP, Antonov JI, Baranova OK, et al. 2014. Dissolved Oxygen, Apparent Oxygen Utilization, and Oxygen Saturation. In *World Ocean Atlas 2013*, Vol. 3, eds. S Levitus, A Mishonov, p. 27

Gebbie G. 2014. How much did Glacial North Atlantic Water shoal? *Paleoceanography*. 2013PA002557

Gebbie G, Huybers P. 2010. Total Matrix Intercomparison: A Method for Determining the Geometry of Water-Mass Pathways. *Journal of Physical Oceanography*. 40(8):1710–28

Gebbie G, Huybers P. 2012. The Mean Age of Ocean Waters Inferred from Radiocarbon Observations: Sensitivity to Surface Sources and Accounting for Mixing Histories. *Journal of Physical Oceanography*. 42(2):291–305

German CR, Elderfield H. 1989. Rare earth elements in Saanich Inlet, British Columbia, a seasonally anoxic basin. *Geochimica et Cosmochimica Acta*. 53(10):2561–71

Goldstein SJ, Jacobsen SB. 1987. The Nd and Sr isotopic systematics of river-water dissolved material: Implications for the sources of Nd and Sr in seawater. *Chemical Geology: Isotope Geoscience section*. 66(3):245–72

Goldstein SL, Hemming SR. 2003. Long-lived Isotopic Tracers in Oceanography, Paleoceanography, and Ice-sheet Dynamics. In *Treatise on Geochemistry*, eds. HD Holland, KK Turekian, pp. 453–89. Oxford: Pergamon

Goldstein SL, Onions RK, Hamilton PJ. 1984. A Sm-Nd isotopic study of atmospheric dusts and particulates from major river systems. *Earth and Planetary Science Letters*. 70:221–36

Gourlan AT, Meynadier L, Allègre CJ. 2008. Tectonically driven changes in the Indian Ocean circulation over the last 25 Ma: Neodymium isotope evidence. *Earth and Planetary Science Letters*. 267(1–2):353–64

Gourlan AT, Meynadier L, Allègre CJ, Tapponnier P, Birck J-L, Joron J-L. 2010. Northern Hemisphere climate control of the Bengali rivers discharge during the past 4 Ma. *Quaternary Science Reviews*. 29(19–20):2484–98

Grasse P, Bosse L, Hathorne EC, Böning P, Pahnke K, Frank M. 2017. Short-term variability of dissolved rare earth elements and neodymium isotopes in the entire water column of the Panama Basin. *Earth and Planetary Science Letters*. 475:242–53

Grasse P, Stichel T, Stumpf R, Stramma L, Frank M. 2012. The distribution of neodymium isotopes and concentrations in the Eastern Equatorial Pacific: Water mass advection versus particle exchange. *Earth and Planetary Science Letters*. 353–354:198–207

Gray AR, Johnson KS, Bushinsky SM, Riser SC, Russell JL, et al. 2018a. Autonomous Biogeochemical Floats Detect Significant Carbon Dioxide Outgassing in the High-Latitude Southern Ocean. *Geophysical Research Letters*. 45(17):9049–57

Gray WR, Rae JWB, Wills RCJ, Shevenell AE, Taylor B, et al. 2018b. Deglacial upwelling, productivity and CO 2 outgassing in the North Pacific Ocean. *Nature Geoscience*. 11(5):340–44

Grenier M, Jeandel C, Lacan F, Vance D, Venchiarutti C, et al. 2013. From the subtropics to the central equatorial Pacific Ocean: Neodymium isotopic composition and rare earth element concentration variations. *Journal of Geophysical Research: Oceans*. 118(2):592–618

Grousset FE, Cortijo E, Huon S, Hervé L, Richter T, et al. 2001. Zooming in on Heinrich layers. *Paleoceanography*. 16(3):240–59

Grousset FE, Pujol C, Labeyrie L, Auffret G, Boelaert A. 2000. Were the North Atlantic Heinrich events triggered by the behavior of the European ice sheets? *Geology*. 28(2):123–26

Gulick SPS, Jaeger JM, Mix AC, Asahi H, Bahlburg H, et al. 2015. Mid-Pleistocene climate transition drives net mass loss from rapidly uplifting St. Elias Mountains, Alaska. *PNAS*. 112(49):15042–47

Gutjahr M, Frank M, Stirling CH, Keigwin LD, Halliday AN. 2008. Tracing the Nd isotope evolution of North Atlantic Deep and Intermediate Waters in the western North Atlantic since the Last Glacial Maximum from Blake Ridge sediments. *Earth and Planetary Science Letters*. 266(1–2):61–77

Gutjahr M, Frank M, Stirling CH, Klemm V, van de Flierdt T, Halliday AN. 2007. Reliable extraction of a deepwater trace metal isotope signal from Fe–Mn oxyhydroxide coatings of marine sediments. *Chemical Geology*. 242(3–4):351–70

Gutjahr M, Hoogakker BAA, Frank M, McCave IN. 2010. Changes in North Atlantic Deep Water strength and bottom water masses during Marine Isotope Stage 3 (45–35kaBP). *Quaternary Science Reviews*. 29(19–20):2451–2461

Haley BA, Du J, Abbott AN, McManus J. 2017. The Impact of Benthic Processes on Rare Earth Element and Neodymium Isotope Distributions in the Oceans. *Front. Mar. Sci.* 4:

Haley BA, Frank M, Hathorne E, Pisias N. 2014. Biogeochemical implications from dissolved rare earth element and Nd isotope distributions in the Gulf of Alaska. *Geochimica et Cosmochimica Acta*. 126:455–474

Haley BA, Klinkhammer GP. 2003. Complete separation of rare earth elements from small volume seawater samples by automated ion chromatography: method development and application to benthic flux. *Marine Chemistry*. 82(3–4):197–220

Haley BA, Klinkhammer GP, McManus J. 2004. Rare earth elements in pore waters of marine sediments. *Geochimica et Cosmochimica Acta*. 68(6):1265–79

Haley BA, Klinkhammer GP, Mix AC. 2005. Revisiting the rare earth elements in foraminiferal tests. *Earth and Planetary Science Letters*. 239(1–2):79–97

Halliday AN, Fallick AE, Dickin AP, Mackenzie AB, Stephens WE, Hildreth W. 1983. The isotopic and chemical evolution of Mount St. Helens. *Earth Planet. Sci. Lett.* 63(2):241–56

Haslett J, Parnell A. 2008. A simple monotone process with application to radiocarbon-dated depth chronologies. *Journal of the Royal Statistical Society: Series C (Applied Statistics)*. 57(4):399–418

Hastings DW, Emerson SR, Mix AC. 1996. Vanadium in foraminiferal calcite as a tracer for changes in the areal extent of reducing sediments. *Paleoceanography*. 11(6):665–78

Hein JR, Koschinsky A. 2014. Deep-Ocean Ferromanganese Crusts and Nodules. In *Treatise on Geochemistry (Second Edition)*, eds. HD Holland, KK Turekian, pp. 273–91. Oxford: Elsevier

Hemming SR. 2004. Heinrich events: Massive late Pleistocene detritus layers of the North Atlantic and their global climate imprint. *Reviews of Geophysics*. 42(1):

Hemming SR, Broecker WS, Sharp WD, Bond GC, Gwiazda RH, et al. 1998. Provenance of Heinrich layers in core V28-82, northeastern Atlantic: 40Ar/39Ar ages of ice-rafted hornblende, Pb isotopes in feldspar grains, and Nd–Sr–Pb isotopes in the fine sediment fraction. *Earth and Planetary Science Letters*. 164(1):317–33

Hildreth W, Fierstein J. 2012. *The Novarupta-Katmai Eruption of 1912—Largest Eruption of the Twentieth Century: Centennial Perspective*. U.S. Geological Survey Professional Paper 1791

Hillaire-Marcel C, de Vernal A, Bilodeau G, Weaver AJ. 2001. Absence of deep-water formation in the Labrador Sea during the last interglacial period. *Nature*. 410(6832):1073–77

Horikawa K, Asahara Y, Yamamoto K, Okazaki Y. 2010. Intermediate water formation in the Bering Sea during glacial periods: Evidence from neodymium isotope ratios. *Geology*. 38(5):435–38

Horikawa K, Martin EE, Asahara Y, Sagawa T. 2011. Limits on conservative behavior of Nd isotopes in seawater assessed from analysis of fish teeth from Pacific core tops. *Earth and Planetary Science Letters*. 310(1–2):119–30

Howe JNW, Huang K-F, Oppo DW, Chiessi CM, Mulitza S, et al. 2018. Similar mid-depth Atlantic water mass provenance during the Last Glacial Maximum and Heinrich Stadial 1. *Earth and Planetary Science Letters*. 490:51–61

Howe JNW, Piotrowski AM. 2017. Atlantic deep water provenance decoupled from atmospheric CO 2 concentration during the lukewarm interglacials. *Nature Communications*. 8(1):2003

Howe JNW, Piotrowski AM, Hu R, Bory A. 2017. Reconstruction of east–west deep water exchange in the low latitude Atlantic Ocean over the past 25,000 years. *Earth and Planetary Science Letters*. 458:327–36

Howe JNW, Piotrowski AM, Noble TL, Mulitza S, Chiessi CM, Bayon G. 2016a. North Atlantic Deep Water Production during the Last Glacial Maximum. *Nat Commun*. 7:11765

Howe JNW, Piotrowski AM, Oppo DW, Huang K-F, Mulitza S, et al. 2016b. Antarctic intermediate water circulation in the South Atlantic over the past 25,000 years. *Paleoceanography*. 31(10):1302–14

Howe JNW, Piotrowski AM, Oppo DW, Huang K-F, Mulitza S, et al. Antarctic intermediate water circulation in the South Atlantic over the past 25,000 years. *Paleoceanography*. 31(10):1302–14

Howe JNW, Piotrowski AM, Rennie VCF. 2016c. Abyssal origin for the early Holocene pulse of unradiogenic neodymium isotopes in Atlantic seawater. *Geology*. 44(10):831–34

Hu R, Noble TL, Piotrowski AM, McCave IN, Bostock HC, Neil HL. 2016a. Neodymium isotopic evidence for linked changes in Southeast Atlantic and Southwest Pacific circulation over the last 200 kyr. *Earth and Planetary Science Letters*. 455:106–14

Hu R, Piotrowski AM. 2018. Neodymium isotope evidence for glacial-interglacial variability of deepwater transit time in the Pacific Ocean. *Nature Communications*. 9(1):4709

Hu R, Piotrowski AM, Bostock HC, Crowhurst S, Rennie V. 2016b. Variability of neodymium isotopes associated with planktonic foraminifera in the Pacific Ocean during the Holocene and Last Glacial Maximum. *Earth and Planetary Science Letters*. 447:130–38

Huang K-F, Oppo DW, Curry WB. 2014. Decreased influence of Antarctic intermediate water in the tropical Atlantic during North Atlantic cold events. *Earth and Planetary Science Letters*. 389:200–208

Jaccard SL, Galbraith ED. 2013. Direct ventilation of the North Pacific did not reach the deep ocean during the last deglaciation. *Geophysical Research Letters*. 40(1):199–203

Jacobsen SB, Wasserburg GJ. 1980. Sm-Nd isotopic evolution of chondrites. *Earth and Planetary Science Letters*. 50(1):139–55

Jaeger JM, Gulick SPS, LeVay LJ, the Expedition 341 Scientists. 2014. *Proc. IODP, 341*. College Station, TX (Integrated Ocean Drilling Program))

Jansen MF. 2017. Glacial ocean circulation and stratification explained by reduced atmospheric temperature. *Proceedings of the National Academy of Sciences*. 114(1):45–50

Jansen MF, Nadeau L-P. 2016. The Effect of Southern Ocean Surface Buoyancy Loss on the Deep-Ocean Circulation and Stratification. *Journal of Physical Oceanography*. 46(11):3455–70

Jeandel C, Arsouze T, Lacan F, Techine P, Dutay J. 2007. Isotopic Nd compositions and concentrations of the lithogenic inputs into the ocean: A compilation, with an emphasis on the margins. *Chemical Geology*. 239(1–2):156–164

Jeandel C, Bishop JK, Zindler A. 1995. Exchange of neodymium and its isotopes between seawater and small and large particles in the Sargasso Sea. *Geochimica et Cosmochimica Acta*. 59(3):535–47

Jeandel C, Delattre H, Grenier M, Pradoux C, Lacan F. 2013. Rare earth element concentrations and Nd isotopes in the Southeast Pacific Ocean. *Geochem. Geophys. Geosyst.* 14(2):328–41

Jeandel C, Oelkers EH. 2015. The influence of terrigenous particulate material dissolution on ocean chemistry and global element cycles. *Chemical Geology*. 395:50–66

Jickells TD, An ZS, Andersen KK, Baker AR, Bergametti G, et al. 2005. Global Iron Connections Between Desert Dust, Ocean Biogeochemistry, and Climate. *Science*. 308(5718):67–71

Johannesson KH, Burdige DJ. 2007. Balancing the global oceanic neodymium budget: Evaluating the role of groundwater. *Earth and Planetary Science Letters*. 253(1–2):129–42

Jones CE, Halliday AN, Rea DK, Owen RM. 1994. Neodymium isotopic variations in North Pacific modern silicate sediment and the insignificance of detrital REE contributions to seawater. *Earth and Planetary Science Letters*. 127(1–4):55–66

Jones DC, Ito T, Takano Y, Hsu W-C. 2014. Spatial and seasonal variability of the air-sea equilibration timescale of carbon dioxide. *Global Biogeochem. Cycles*. 28(11):1163–78

Jones KM, Khatiwala SP, Goldstein SL, Hemming SR, van de Flierdt T. 2008. Modeling the distribution of Nd isotopes in the oceans using an ocean general circulation model. *Earth and Planetary Science Letters*. 272(3–4):610–619

Jones MT, Pearce CR, Jeandel C, Gislason SR, Eiriksdottir ES, et al. 2012. Riverine particulate material dissolution as a significant flux of strontium to the oceans. *Earth and Planetary Science Letters*. 355–356:51–59

Jonkers L, Zahn R, Thomas A, Henderson G, Abouchami W, et al. 2015. Deep circulation changes in the central South Atlantic during the past 145 kyrs reflected in a combined 231Pa/230Th, Neodymium isotope and benthic δC13 record. *Earth and Planetary Science Letters*. 419:14–21

Josse J, Husson F. 2016. missMDA: A Package for Handling Missing Values in Multivariate Data Analysis. *Journal of Statistical Software*. 70(1):1–31

Jullien E, Grousset FE, Hemming SR, Peck VL, Hall IR, et al. 2006. Contrasting conditions preceding MIS3 and MIS2 Heinrich events. *Global and Planetary Change*. 54(3):225–38

Kalinowski BE, Schweda P. 1996. Kinetics of muscovite, phlogopite, and biotite dissolution and alteration at pH 1–4, room temperature. *Geochimica et Cosmochimica Acta*. 60(3):367–85

Kawabe M, Fujio S. 2010. Pacific ocean circulation based on observation. *J Oceanogr*. 66(3):389–403

Keigwin LD, Swift SA. 2017. Carbon isotope evidence for a northern source of deep water in the glacial western North Atlantic. *PNAS*. 201614693

Kelemen PB, Hanghøj K, Greene AR. 2014. One View of the Geochemistry of Subduction-Related Magmatic Arcs, with an Emphasis on Primitive Andesite and Lower Crust. In *Treatise on Geochemistry (Second Edition)*, eds. HD Holland, KK Turekian, pp. 749–806. Oxford: Elsevier

Kelemen PB, Yogodzinski GM, Scholl DW. 2004. Along-Strike Variation in the Aleutian Island Arc: Genesis of High Mg# Andesite and Implications for Continental Crust. In *Inside the Subduction Factory*, ed. J Eiler, pp. 223–76. American Geophysical Union

Key RM, Kozyr A, Sabine CL, Lee K, Wanninkhof R, et al. 2004. A global ocean carbon climatology: Results from Global Data Analysis Project (GLODAP). *Global Biogeochemical Cycles*. 18(4):GB4031

Khatiwala S, Primeau F, Holzer M. 2012. Ventilation of the deep ocean constrained with tracer observations and implications for radiocarbon estimates of ideal mean age. *Earth and Planetary Science Letters*. 325–326(0):116–25

Kinsman DJJ. 1969. Interpretation of Sr (super +2) concentrations in carbonate minerals and rocks. *Journal of Sedimentary Research*. 39(2):486–508

Koeve W, Wagner H, Kähler P, Oschlies A. 2015. 14C-age tracers in global ocean circulation models. *Geoscientific Model Development*. 8(7):2079–94

Kostov Y, Armour KC, Marshall J. 2014. Impact of the Atlantic meridional overturning circulation on ocean heat storage and transient climate change. *Geophysical Research Letters*. 41(6):2108–16

Kraft S, Frank M, Hathorne EC, Weldeab S. 2013. Assessment of seawater Nd isotope signatures extracted from foraminiferal shells and authigenic phases of Gulf of Guinea sediments. *Geochimica et Cosmochimica Acta*. 121:414–35

Kurahashi-Nakamura T, Paul A, Losch M. 2017. Dynamical reconstruction of the global ocean state during the Last Glacial Maximum. *Paleoceanography*. 32(4):326–50

Kwon EY, Hain MP, Sigman DM, Galbraith ED, Sarmiento JL, Toggweiler JR. 2012. North Atlantic ventilation of "southern-sourced" deep water in the glacial ocean. *Paleoceanography*. 27(2):PA2208

Lacan F, Jeandel C. 2001. Tracing Papua New Guinea imprint on the central Equatorial Pacific Ocean using neodymium isotopic compositions and Rare Earth Element patterns. *Earth and Planetary Science Letters*. 186(3):497–512

Lacan F, Jeandel C. 2005a. Neodymium isotopes as a new tool for quantifying exchange fluxes at the continent–ocean interface. *Earth and Planetary Science Letters*. 232(3–4):245–57

Lacan F, Jeandel C. 2005b. Acquisition of the neodymium isotopic composition of the North Atlantic Deep Water. *Geochem. Geophys. Geosyst.* 6(12):Q12008

Lacan F, Tachikawa K, Jeandel C. 2012. Neodymium isotopic composition of the oceans: A compilation of seawater data. *Chemical Geology*. 300–301:177–184

Lacerra M, Lund D, Yu J, Schmittner A. 2017. Carbon storage in the mid-depth Atlantic during millennial-scale climate events. *Paleoceanography*. 32(8):780–95

Lambelet M, van de Flierdt T, Crocket K, Rehkämper M, Kreissig K, et al. 2016. Neodymium isotopic composition and concentration in the western North Atlantic Ocean: Results from the GEOTRACES GA02 section. *Geochimica et Cosmochimica Acta*. 177:1–29

Landschützer P, Gruber N, Haumann FA, Rödenbeck C, Bakker DCE, et al. 2015. The reinvigoration of the Southern Ocean carbon sink. *Science*. 349(6253):1221–24

Lang DC, Bailey I, Wilson PA, Chalk TB, Foster GL, Gutjahr M. 2016. Incursions of southern-sourced water into the deep North Atlantic during late Pliocene glacial intensification. *Nature Geosci*. 9(5):375–79

Lauderdale JM, Williams RG, Munday DR, Marshall DP. 2017. The impact of Southern Ocean residual upwelling on atmospheric CO2 on centennial and millennial timescales. *Clim Dyn*. 48(5–6):1611–31

Le Houedec S, Meynadier L, Allègre CJ. 2012. Nd isotope systematics on ODP Sites 756 and 762 sediments reveal major volcanic, oceanic and climatic changes in South Indian Ocean over the last 35 Ma. *Earth and Planetary Science Letters*. 327–328:29–38

Lê S, Josse J, Husson F. 2008. FactoMineR: An R Package for Multivariate Analysis. *Journal of Statistical Software*. 25(1):1–18

Lippold J, Gutjahr M, Blaser P, Christner E, de Carvalho Ferreira ML, et al. 2016. Deep water provenance and dynamics of the (de)glacial Atlantic meridional overturning circulation. *Earth and Planetary Science Letters*. 445:68–78

Lippold J, Luo Y, Francois R, Allen SE, Gherardi J, et al. 2012. Strength and geometry of the glacial Atlantic Meridional Overturning Circulation. *Nature Geosci*. 5(11):813–16

Loose B, McGillis WR, Perovich D, Zappa CJ, Schlosser P. 2014. A parameter model of gas exchange for the seasonal sea ice zone. *Ocean Sci.* 10(1):17–28

Lowson RT, Comarmond M-CJ, Rajaratnam G, Brown PL. 2005. The kinetics of the dissolution of chlorite as a function of pH and at 25°C. *Geochimica et Cosmochimica Acta*. 69(7):1687–99

Lozier MS, Li F, Bacon S, Bahr F, Bower AS, et al. 2019. A sea change in our view of overturning in the subpolar North Atlantic. *Science*. 363(6426):516–21

Lumpkin R, Speer K. 2007. Global Ocean Meridional Overturning. *Journal of Physical Oceanography*. 37(10):2550–62

Lund DC. 2013. Deep Pacific ventilation ages during the last deglaciation: Evaluating the influence of diffusive mixing and source region reservoir age. *Earth and Planetary Science Letters*. 381:52–62

Lund DC, Asimow PD, Farley KA, Rooney TO, Seeley E, et al. 2016. Enhanced East Pacific Rise hydrothermal activity during the last two glacial terminations. *Science*. 351(6272):478–82

Lund DC, Mix AC, Southon J. 2011. Increased ventilation age of the deep northeast Pacific Ocean during the last deglaciation. *Nature Geoscience*. 4(11):771–74

Lund DC, Tessin AC, Hoffman JL, Schmittner A. 2015. Southwest Atlantic water mass evolution during the last deglaciation. *Paleoceanography*. 30(5):477–94

Lynch-Stieglitz J, Valley SG, Schmidt MW. 2019. Temperature-dependent ocean–atmosphere equilibration of carbon isotopes in surface and intermediate waters over the deglaciation. *Earth and Planetary Science Letters*. 506:466–75

Maher K, Steefel CI, DePaolo DJ, Viani BE. 2006. The mineral dissolution rate conundrum: Insights from reactive transport modeling of U isotopes and pore fluid chemistry in marine sediments. *Geochimica et Cosmochimica Acta*. 70(2):337–63

Mahowald NM, Baker AR, Bergametti G, Brooks N, Duce RA, et al. 2005. Atmospheric global dust cycle and iron inputs to the ocean. *Global Biogeochemical Cycles*. 19(4):

Marchitto TM, Lehman SJ, Ortiz JD, Flückiger J, Geen A van. 2007. Marine Radiocarbon Evidence for the Mechanism of Deglacial Atmospheric CO2 Rise. *Science*. 316(5830):1456–59

Marcott SA, Bauska TK, Buizert C, Steig EJ, Rosen JL, et al. 2014. Centennial-scale changes in the global carbon cycle during the last deglaciation. *Nature*. 514(7524):616–19

Marshall J, Plumb RA. 2008. *Atmosphere, Ocean, and Climate Dynamics: An Introductory Text*, Vol. 93. Amsterdam ; [Burlington, MA]: Elsevier Academic Press. 1st ed.

Marshall J, Speer K. 2012. Closure of the meridional overturning circulation through Southern Ocean upwelling. *Nature Geoscience*. 5(3):171–80

Martin EE, Blair SW, Kamenov GD, Scher HD, Bourbon E, et al. 2010. Extraction of Nd isotopes from bulk deep sea sediments for paleoceanographic studies on Cenozoic time scales. *Chemical Geology*. 269(3–4):414–31

Martin EE, Haley BA. 2000. Fossil fish teeth as proxies for seawater Sr and Nd isotopes. *Geochimica et Cosmochimica Acta*. 64(5):835–47

Martin EE, Macdougall JD, Herbert TD, Paytan A, Kastner M. 1995. Strontium and neodymium isotopic analyses of marine barite separates. *Geochimica et Cosmochimica Acta*. 59(7):1353–61

Martínez-Botí MA, Marino G, Foster GL, Ziveri P, Henehan MJ, et al. 2015. Boron isotope evidence for oceanic carbon dioxide leakage during the last deglaciation. *Nature*. 518(7538):219–22

Marzocchi A, Jansen MF. 2017. Connecting Antarctic sea ice to deep-ocean circulation in modern and glacial climate simulations. *Geophys. Res. Lett.* 44(12):2017GL073936

Mashayek A, Ferrari R, Merrifield S, Ledwell JR, Laurent LS, Garabato AN. 2017. Topographic enhancement of vertical turbulent mixing in the Southern Ocean. *Nature Communications*. 8:14197

Masson-Delmotte V, Schulz M, Abe-Ouchi A, Beer J, Ganopolski A, et al. 2013. Information from paleoclimate archives. In *Climate Change 2013: The Physical Science Basis*, eds. TF Stocker, D Qin, G-K Plattner, MMB Tignor, SK Allen, et al., pp. 383–464. Cambridge University Press, Cambridge

Matsumoto K, Oba T, Lynch-Stieglitz J, Yamamoto H. 2002. Interior hydrography and circulation of the glacial Pacific Ocean. *Quaternary Science Reviews*. 21(14–15):1693–1704

McGee D, Marcantonio F, Lynch-Stieglitz J. 2007. Deglacial changes in dust flux in the eastern equatorial Pacific. *Earth and Planetary Science Letters*. 257(1–2):215–30

McLennan SM. 1989. Rare earth elements in sedimentary rocks; influence of provenance and sedimentary processes. *Reviews in Mineralogy and Geochemistry*. 21(1):169–200

McLennan SM. 2001. Relationships between the trace element composition of sedimentary rocks and upper continental crust. *Geochem. Geophys. Geosyst.* 2(4):1021

McLennan SM, Hemming S, McDaniel DK, Hanson GN. 1993. Geochemical approaches to sedimentation, provenance, and tectonics. *Geological Society of America Special Papers*. 284:21–40

McManus JF, Francois R, Gherardi J-M, Keigwin LD, Brown-Leger S. 2004. Collapse and rapid resumption of Atlantic meridional circulation linked to deglacial climate changes. *Nature*. 428(6985):834–37

Meijers AJS. 2014. The Southern Ocean in the Coupled Model Intercomparison Project phase 5. *Philosophical Transactions of the Royal Society A*. 372(2019):20130296

Meinshausen M, Smith SJ, Calvin K, Daniel JS, Kainuma MLT, et al. 2011. *The Paleoclimate Modeling Intercomparison Project Contribution to CMIP5*, Vol. 16

Menard HW, Smith SM. 1966. Hypsometry of ocean basin provinces. *Journal of Geophysical Research*. 71(18):4305–25

Menounos B, Goehring BM, Osborn G, Margold M, Ward B, et al. 2017. Cordilleran Ice Sheet mass loss preceded climate reversals near the Pleistocene Termination. *Science*. 358(6364):781–84

Menviel L, England MH, Meissner KJ, Mouchet A, Yu J. 2014. Atlantic-Pacific seesaw and its role in outgassing CO2 during Heinrich events. *Paleoceanography*. 29(1):58–70

Menviel L, Mouchet A, Meissner KJ, Joos F, England MH. Impact of oceanic circulation changes on atmospheric δ13CO2. *Global Biogeochemical Cycles*. 29(11):1944–61

Menviel L, Spence P, Yu J, Chamberlain MA, Matear RJ, et al. 2018. Southern Hemisphere westerlies as a driver of the early deglacial atmospheric CO 2 rise. *Nature Communications*. 9(1):2503

Menviel L, Yu J, Joos F, Mouchet A, Meissner KJ, England MH. 2016. Poorly ventilated deep ocean at the Last Glacial Maximum inferred from carbon isotopes: A data-model comparison study. *Paleoceanography*. 32(1):2–17

Mix AC, Bard E, Schneider R. 2001. Environmental processes of the ice age: land, oceans, glaciers (EPILOG). *Quaternary Science Reviews*. 20(4):627–57

Mix AC, Fairbanks RG. 1985. North Atlantic surface-ocean control of Pleistocene deep-ocean circulation. *Earth and Planetary Science Letters*. 73(2):231–43

Mokadem F, Parkinson IJ, Hathorne EC, Anand P, Allen JT, Burton KW. 2015. High-precision radiogenic strontium isotope measurements of the modern and glacial ocean: Limits on glacial–interglacial variations in continental weathering. *Earth and Planetary Science Letters*. 415:111–20

Molina-Kescher M, Frank M, Hathorne E. 2014a. Nd and Sr isotope compositions of different phases of surface sediments in the South Pacific: Extraction of seawater signatures, boundary exchange, and detrital/dust provenance. *Geochem. Geophys. Geosyst.* 15(9):3502–20

Molina-Kescher M, Frank M, Hathorne E. 2014b. South Pacific dissolved Nd isotope compositions and rare earth element distributions: Water mass mixing versus biogeochemical cycling. *Geochimica et Cosmochimica Acta*. 127:171–89

Molina-Kescher M, Frank M, Tapia R, Ronge TA, Nürnberg D, Tiedemann R. 2016. Reduced admixture of North Atlantic Deep Water to the deep central South Pacific during the last two glacial periods. *Paleoceanography*. 31(6):651–68

Molnia BF, Hein JR. 1982. Clay Mineralogy of a Glacially Dominated, Subarctic Continental Shelf: Northeastern Gulf of Alaska. *Journal of Sedimentary Research*. 52(2):

Muglia J, Schmittner A. 2015. Glacial Atlantic overturning increased by wind stress in climate models. *Geophysical Research Letters*. 42(22):9862–68

Muglia J, Skinner LC, Schmittner A. 2018. Weak overturning circulation and high Southern Ocean nutrient utilization maximized glacial ocean carbon. *Earth and Planetary Science Letters*. 496:47–56

Muratli JM, McManus J, Mix A, Chase Z. 2012. Dissolution of fluoride complexes following microwave-assisted hydrofluoric acid digestion of marine sediments. *Talanta*. 89:195–200

Murphy DP, Thomas DJ. 2010. The negligible role of intermediate water circulation in stadial–interstadial oxygenation variations along the southern California margin: Evidence from Nd isotopes. *Quaternary Science Reviews*. 29(19–20):2442–50

Naidu AS, Han MW, Mowatt TC, Wajda W. 1995. Clay minerals as indicators of sources of terrigenous sediments, their transportation and deposition: Bering Basin, Russian-Alaskan Arctic. *Marine Geology*. 127(1–4):87–104

Naidu AS, Mowatt TC. 1983. Sources and dispersal patterns of clay minerals in surface sediments from the continental-shelf areas off Alaska. *Geological Society of America Bulletin*. 94(7):841–54

Negre C, Zahn R, Thomas AL, Masqué P, Henderson GM, et al. 2010. Reversed flow of Atlantic deep water during the Last Glacial Maximum. *Nature*. 468(7320):84–88

Ng HC, Robinson LF, McManus JF, Mohamed KJ, Jacobel AW, et al. 2018. Coherent deglacial changes in western Atlantic Ocean circulation. *Nature Communications*. 9(1):2947

Noble TL, Piotrowski AM, McCave IN. 2013. Neodymium isotopic composition of intermediate and deep waters in the glacial southwest Pacific. *Earth and Planetary Science Letters*. 384:27–36

Nokleberg WJ, Parfenov LM, Monger JWH, Norton IO, Khanchuk AI, et al. 2000. Phanerozoic tectonic evolution of the circum-north Pacific. *Open-File Report. 1626*, U.S. Geological Survey,

Okazaki Y, Timmermann A, Menviel L, Harada N, Abe-Ouchi A, et al. 2010. Deepwater Formation in the North Pacific During the Last Glacial Termination. *Science*. 329(5988):200–204

O'Nions RK, Carter SR, Evensen NM, Hamilton PJ. 1979. Geochemical and Cosmochemical Applications of Nd Isotope Analysis. *Annual Review of Earth and Planetary Sciences*. 7(1):11–38

Oppo DW, Fairbanks RG. 1987. Variability in the deep and intermediate water circulation of the Atlantic Ocean during the past 25,000 years: Northern Hemisphere modulation of the Southern Ocean. *Earth and Planetary Science Letters*. 86(1):1–15

Oppo DW, Gebbie G, Huang K-F, Curry WB, Marchitto TM, Pietro KR. 2018. Data Constraints on Glacial Atlantic Water Mass Geometry and Properties. *Paleoceanography and Paleoclimatology*. 33(9):1013–34

Otto-Bliesner BL, Hewitt CD, Marchitto TM, Brady E, Abe-Ouchi A, et al. 2007. Last Glacial Maximum ocean thermohaline circulation: PMIP2 model intercomparisons and data constraints. *Geophysical Research Letters*. 34(12):

Pahnke K, Goldstein SL, Hemming SR. 2008. Abrupt changes in Antarctic Intermediate Water circulation over the past 25,000 years. *Nature Geosci*. 1(12):870–74

Pahnke K, van de Flierdt T, Jones KM, Lambelet M, Hemming SR, Goldstein SL. 2012. GEOTRACES intercalibration of neodymium isotopes and rare earth element concentrations in seawater and suspended particles. Part 2: Systematic tests and baseline profiles. *Limnol. Oceanogr. Methods*. 10(4):252–69

Palmer MR. 1985. Rare earth elements in foraminifera tests. *Earth and Planetary Science Letters*. 73:285–98

Palmer MR, Elderfield H. 1985. Variations in the Nd isotopic composition of foraminifera from Atlantic Ocean sediments. *Earth and Planetary Science Letters*. 73:299–305

Palmer MR, Elderfield H. 1986. Rare earth elements and neodymium isotopes in ferromanganese oxide coatings of Cenozoic foraminifera from the Atlantic Ocean∗. *Geochimica et Cosmochimica Acta*. 50(3):409–17

Parrenin F, Masson-Delmotte V, Köhler P, Raynaud D, Paillard D, et al. 2013. Synchronous Change of Atmospheric CO2 and Antarctic Temperature During the Last Deglacial Warming. *Science*. 339(6123):1060–63

Peck VL, Hall IR, Zahn R, Elderfield H, Grousset F, et al. 2006. High resolution evidence for linkages between NW European ice sheet instability and Atlantic Meridional Overturning Circulation. *Earth and Planetary Science Letters*. 243(3):476–88

Pena LD, Goldstein SL, Hemming SR, Jones KM, Calvo E, et al. 2013. Rapid changes in meridional advection of Southern Ocean intermediate waters to the tropical Pacific during the last 30 kyr. *Earth and Planetary Science Letters*. 368:20–32

Piotrowski AM, Galy A, Nicholl JAL, Roberts N, Wilson DJ, et al. 2012. Reconstructing deglacial North and South Atlantic deep water sourcing using foraminiferal Nd isotopes. *Earth and Planetary Science Letters*. 357–358:289–97

Piotrowski AM, Goldstein SL, Hemming SR, Fairbanks RG. 2004. Intensification and variability of ocean thermohaline circulation through the last deglaciation. *Earth and Planetary Science Letters*. 225(1):205–20

Piotrowski AM, Goldstein SL, Hemming SR, Fairbanks RG. 2005. Temporal Relationships of Carbon Cycling and Ocean Circulation at Glacial Boundaries. *Science*. 307(5717):1933–38

Piotrowski AM, Goldstein SL, Hemming S R, Fairbanks RG, Zylberberg DR. 2008. Oscillating glacial northern and southern deep water formation from

combined neodymium and carbon isotopes. *Earth and Planetary Science Letters*. 272(1–2):394–405

Plank T. 2014. The Chemical Composition of Subducting Sediments. In *Treatise on Geochemistry (Second Edition)*, eds. HD Holland, KK Turekian, pp. 607–29. Oxford: Elsevier

Plank T, Langmuir CH. 1998. The chemical composition of subducting sediment and its consequences for the crust and mantle. *Chemical Geology*. 145(3–4):325–94

Plaza-Morlote M, Rey D, Santos JF, Ribeiro S, Heslop D, et al. 2017. Southernmost evidence of large European Ice Sheet-derived freshwater discharges during the Heinrich Stadials of the Last Glacial Period (Galician Interior Basin, Northwest Iberian Continental Margin). *Earth and Planetary Science Letters*. 457:213–26

Poggemann D-W, Nürnberg D, Hathorne EC, Frank M, Rath W, et al. 2018. Deglacial Heat Uptake by the Southern Ocean and Rapid Northward Redistribution Via Antarctic Intermediate Water. *Paleoceanography and Paleoclimatology*. 33(11):1292–1305

Pöppelmeier F, Gutjahr M, Blaser P, Keigwin LD, Lippold J. 2018. Origin of Abyssal NW Atlantic Water Masses Since the Last Glacial Maximum. *Paleoceanography and Paleoclimatology*. 33(5):530–43

Poulton SW, Canfield DE. 2005. Development of a sequential extraction procedure for iron: implications for iron partitioning in continentally derived particulates. *Chemical Geology*. 214(3–4):209–21

Poulton SW, Raiswell R. 2002. The low-temperature geochemical cycle of iron: From continental fluxes to marine sediment deposition. *Am J Sci*. 302(9):774–805

Poulton SW, Raiswell R. 2005. Chemical and physical characteristics of iron oxides in riverine and glacial meltwater sediments. *Chemical Geology*. 218(3–4):203–21

Praetorius S, Mix A, Jensen B, Froese D, Milne G, et al. 2016. Interaction between climate, volcanism, and isostatic rebound in Southeast Alaska during the last deglaciation. *Earth and Planetary Science Letters*. 452:79–89

Praetorius SK, Mix AC. 2014. Synchronization of North Pacific and Greenland climates preceded abrupt deglacial warming. *Science*. 345(6195):444–48

Praetorius SK, Mix AC, Walczak MH, Wolhowe MD, Addison JA, Prahl FG. 2015. North Pacific deglacial hypoxic events linked to abrupt ocean warming. *Nature*. 527(7578):362–66

Pratt RM, Scheidegger KF, Kulm LD. 1973. Volcanic Ash from DSDP Site 178, Gulf of Alaska. In *Initial Reports of the Deep Sea Drilling Project*, Vol. 18, eds. LD Kulm, R von Huene, pp. 833–34. Washington, D.C.: U.S. Govt. Printing Office

Rae JWB, Burke A, Robinson LF, Adkins JF, Chen T, et al. 2018. CO 2 storage and release in the deep Southern Ocean on millennial to centennial timescales. *Nature*. 562(7728):569

Rae JWB, Sarnthein M, Foster GL, Ridgwell A, Grootes PM, Elliott T. 2014. Deep water formation in the North Pacific and deglacial CO2 rise. *Paleoceanography*. 29(6):645–67

Rahmstorf S, Feulner G. 2013. Chapter 2 - Paleoclimatic Ocean Circulation and Sea-Level Changes. In *International Geophysics*, Vol. 103, eds. G Siedler, SM Griffies, J Gould, JA Church, pp. 31–56. Academic Press

Rashid H, England E, Thompson L, Polyak L. 2011. Late Glacial to Holocene Indian Summer Monsoon Variability Based upon Sediment Records Taken from the Bay of Bengal. *Terr. Atmos. Ocean. Sci.* 22(2):215–28

Rasmussen B, Buick R, Taylor WR. 1998. Removal of oceanic REE by authigenic precipitation of phosphatic minerals. *Earth and Planetary Science Letters*. 164(1–2):135–49

Reimi MA, Marcantonio F. 2016. Constraints on the magnitude of the deglacial migration of the ITCZ in the Central Equatorial Pacific Ocean. *Earth and Planetary Science Letters*. 453:1–8

Rempfer J, Stocker TF, Joos F, Dutay J-C, Siddall M. 2011. Modelling Nd-isotopes with a coarse resolution ocean circulation model: Sensitivities to model parameters and source/sink distributions. *Geochimica et Cosmochimica Acta*. 75(20):5927–5950

Revel M, Sinko J, Grousset F. 1996. Sr and Nd isotopes as tracers of North Atlantic lithic particles: Paleoclimatic implications. *Paleoceanography*. 11(1):95–113

Rickli J, Gutjahr M, Vance D, Fischer-Gödde M, Hillenbrand C-D, Kuhn G. 2014. Neodymium and hafnium boundary contributions to seawater along the West Antarctic continental margin. *Earth and Planetary Science Letters*. 394:99–110

Roberts J, Gottschalk J, Skinner LC, Peck VL, Kender S, et al. 2016. Evolution of South Atlantic density and chemical stratification across the last deglaciation. *Proceedings of the National Academy of Sciences*. 113(3):514–19

Roberts NL, Piotrowski AM. 2015. Radiogenic Nd isotope labeling of the northern NE Atlantic during MIS 2. *Earth and Planetary Science Letters*. 423:125–33

Roberts NL, Piotrowski AM, Elderfield H, Eglinton TI, Lomas MW. 2012. Rare earth element association with foraminifera. *Geochimica et Cosmochimica Acta*. 94:57–71

Roberts NL, Piotrowski AM, McManus JF, Keigwin LD. 2010. Synchronous Deglacial Overturning and Water Mass Source Changes. *Science*. 327(5961):75–78

Robinson LF, Adkins JF, Keigwin LD, Southon J, Fernandez DP, et al. 2005. Radiocarbon Variability in the Western North Atlantic During the Last Deglaciation. *Science*. 310(5753):1469–73

Roden EE, Zachara JM. 1996. Microbial Reduction of Crystalline Iron(III) Oxides: Influence of Oxide Surface Area and Potential for Cell Growth. *Environ. Sci. Technol.* 30(5):1618–28

Rose KA, Sikes EL, Guilderson TP, Shane P, Hill TM, et al. 2010. Upper-ocean-to-atmosphere radiocarbon offsets imply fast deglacial carbon dioxide release. *Nature*. 466(7310):1093–97

Rousseau TCC, Sonke JE, Chmeleff J, Beek P van, Souhaut M, et al. 2015. Rapid neodymium release to marine waters from lithogenic sediments in the Amazon estuary. *Nature Communications*. 6:7592

Rozalen M, Huertas FJ, Brady PV. 2009. Experimental study of the effect of pH and temperature on the kinetics of montmorillonite dissolution. *Geochimica et Cosmochimica Acta*. 73(13):3752–66

Rozalen M, Ramos ME, Gervilla F, Kerestedjian T, Fiore S, Huertas FJ. 2014. Dissolution study of tremolite and anthophyllite: pH effect on the reaction kinetics. *Applied Geochemistry*. 49(Supplement C):46–56

Ruddiman WF. 1977. Late Quaternary deposition of ice-rafted sand in the subpolar North Atlantic (lat 40° to 65°N). *GSA Bulletin*. 88(12):1813–27

Rudnick RL, Gao S. 2014. Composition of the Continental Crust. In *Treatise on Geochemistry (Second Edition)*, eds. HD Holland, KK Turekian, pp. 1–51. Oxford: Elsevier

Rutberg RL, Hemming SR, Goldstein SL. 2000a. Reduced North Atlantic Deep Water flux to the glacial Southern Ocean inferred from neodymium isotope ratios. *Nature*. 405(6789):935–38

Rutberg RL, Hemming SR, Goldstein SL. 2000b. Reduced North Atlantic Deep Water flux to the glacial Southern Ocean inferred from neodymium isotope ratios. *Nature*. 405(6789):935–38

Sabine CL, Feely RA, Gruber N, Key RM, Lee K, et al. 2004. The Oceanic Sink for Anthropogenic CO2. *Science*. 305(5682):367–71

Samson SD, McClelland WC, Patchett PJ, Gehrels GE, Anderson RG. 1989. Evidence from neodymium isotopes for mantle contributions to Phanerozoic crustal genesis in the Canadian Cordillera. *Nature*. 337(6209):705–9

Samson SD, Patchett PJ, Gehrels GE, Anderson RG. 1990. Nd and Sr Isotopic Characterization of the Wrangellia Terrane and Implications for Crustal Growth of the Canadian Cordillera. *The Journal of Geology*. 98(5):749–62

Samson SD, Patchett PJ, McClelland WC, Gehrels GE. 1991a. Nd and Sr isotopic constraints on the petrogenesis of the west side of the northern Coast Mountains batholith, Alaskan and Canadian Cordillera. *Can. J. Earth Sci.* 28(6):939–46

Samson SD, Patchett PJ, McClelland WC, Gehrels GE. 1991b. Nd isotopic characterization of metamorphic rocks in the Coast Mountains, Alaskan and Canadian Cordillera: Ancient crust bounded by juvenile terranes. *Tectonics*. 10(4):770–80

Sarmiento JL, Gruber N. 2013. *Ocean Biogeochemical Dynamics*. Princeton University Press

Sarnthein M, Balmer S, Grootes PM, Mudelsee M. 2015. Planktic and Benthic 14C Reservoir Ages for Three Ocean Basins, Calibrated by a Suite of 14C Plateaus in the Glacial-to-Deglacial Suigetsu Atmospheric 14C Record. *Radiocarbon*. 57(1):129–51

Sarnthein M, Winn K, Jung SJA, Duplessy J-C, Labeyrie L, et al. 1994. Changes in East Atlantic Deepwater Circulation over the last 30,000 years: Eight time slice reconstructions. *Paleoceanography*. 9(2):209–67

Schacht U, Wallmann K, Kutterolf S. 2010. The influence of volcanic ash alteration on the REE composition of marine pore waters. *Journal of Geochemical Exploration*. 106(1–3):176–87

Scheidegger K, Corliss J, Jezek P, Ninkovich D. 1980. Compositions of Deep-Sea Ash Layers Derived from North Pacific Volcanic Arcs - Variations in Time and Space. *J. Volcanol. Geotherm. Res.* 7(1–2):107–37

Scheidegger KF, Kulm LD. 1975. Late Cenozoic volcanism in the Aleutian Arc: Information from ash layers in the northeastern Gulf of Alaska. *Geological Society of America Bulletin*. 86(10):1407–12

Schijf J, Christenson EA, Byrne RH. 2015. YREE scavenging in seawater: A new look at an old model. *Marine Chemistry*. 177, Part 3:460–71

Schlitzer R. 2017. *Ocean Data View*. http://odv.awi.de

Schmitt J, Schneider R, Elsig J, Leuenberger D, Lourantou A, et al. 2012. Carbon Isotope Constraints on the Deglacial CO2 Rise from Ice Cores. *Science*. 336(6082):711–14

Schmittner A, Urban NM, Shakun JD, Mahowald NM, Clark PU, et al. 2011. Climate Sensitivity Estimated from Temperature Reconstructions of the Last Glacial Maximum. *Science*. 334(6061):1385–88

Schulz HD, Zabel M. 2006. *Marine Geochemistry*. Springer Science & Business Media

Shakun JD, Clark PU, He F, Marcott SA, Mix AC, et al. 2012. Global warming preceded by increasing carbon dioxide concentrations during the last deglaciation. *Nature*. 484(7392):49–54

Shaw HF, Wasserburg GJ. 1985. Sm-Nd in marine carbonates and phosphates: Implications for Nd isotopes in seawater and crustal ages. *Geochimica et Cosmochimica Acta*. 49(2):503–18

Sholkovitz ER, Elderfield H. 1988. Cycling of dissolved rare earth elements in Chesapeake Bay. *Global Biogeochem. Cycles*. 2(2):157–76

Sholkovitz ER, Landing WM, Lewis BL. 1994. Ocean particle chemistry: The fractionation of rare earth elements between suspended particles and seawater. *Geochimica et Cosmochimica Acta*. 58(6):1567–79

Sholkovitz ER, Piepgras DJ, Jacobsen SB. 1989. The pore water chemistry of rare earth elements in Buzzards Bay sediments. *Geochimica et Cosmochimica Acta*. 53(11):2847–56

Sholkovitz ER, Shaw TJ, Schneider DL. 1992. The geochemistry of rare earth elements in the seasonally anoxic water column and porewaters of Chesapeake Bay. *Geochimica et Cosmochimica Acta*. 56(9):3389–3402

Siddall M, Khatiwala S, van de Flierdt T, Jones K, Goldstein SL, et al. 2008. Towards explaining the Nd paradox using reversible scavenging in an ocean general circulation model. *Earth and Planetary Science Letters*. 274(3):448–61

Sikes EL, Allen KA, Lund DC. 2017. Enhanced δ13C and δ18O Differences Between the South Atlantic and South Pacific During the Last Glaciation: The Deep Gateway Hypothesis. *Paleoceanography*. 32(10):1000–1017

Sikes EL, Cook MS, Guilderson TP. 2016. Reduced deep ocean ventilation in the Southern Pacific Ocean during the last glaciation persisted into the deglaciation. *Earth and Planetary Science Letters*. 438:130–38

Sikes EL, Samson CR, Guilderson TP, Howard WR. 2000. Old radiocarbon ages in the southwest Pacific Ocean during the last glacial period and deglaciation. *Nature*. 405(6786):555–59

Skinner LC, Fallon S, Waelbroeck C, Michel E, Barker S. 2010. Ventilation of the Deep Southern Ocean and Deglacial CO2 Rise. *Science*. 328(5982):1147–51

Skinner LC, Primeau F, Freeman E, Fuente M de la, Goodwin PA, et al. 2017. Radiocarbon constraints on the glacial ocean circulation and its impact on atmospheric CO_2. *Nature Communications*. 8:16010

Skinner LC, Scrivner AE, Vance D, Barker S, Fallon S, Waelbroeck C. 2013. North Atlantic versus Southern Ocean contributions to a deglacial surge in deep ocean ventilation. *Geology*. 41(6):667–70

Soyol-Erdene T-O, Huh Y. 2013. Rare earth element cycling in the pore waters of the Bering Sea Slope (IODP Exp. 323). *Chemical Geology*. 358:75–89

Steiger RH, Jäger E. 1977. Subcommission on geochronology: Convention on the use of decay constants in geo- and cosmochronology. *Earth and Planetary Science Letters*. 36(3):359–62

Stichel T, Pahnke K, Duggan B, Goldstein SL, Hartman AE, et al. 2018. TAG Plume: Revisiting the Hydrothermal Neodymium Contribution to Seawater. *Front. Mar. Sci.* 5:

Stocker TF, Qin D, Plattner G-K, Tignor M, Allen SK, et al., eds. 2013. *Climate Change 2013. The Physical Science Basis. Working Group I Contribution to the Fifth Assessment Report of the Intergovernmental Panel on Climate Change*. Cambridge University Press, Cambridge, United Kingdom and New York, NY, USA,

Stoll HM, Vance D, Arevalos A. 2007. Records of the Nd isotope composition of seawater from the Bay of Bengal: Implications for the impact of Northern Hemisphere cooling on ITCZ movement. *Earth and Planetary Science Letters*. 255(1–2):213–28

Stone AT, Morgan JJ. 1987. Reductive dissolution of metal oxides. In *Aquatic Surface Chemistry: Chemical Processes at the Particle-Water Interface*, pp. 221–54. John Wiley and Sons, New York.

Struve T, Roberts NL, Frank M, Piotrowski AM, Spielhagen RF, et al. 2019. Ice-sheet driven weathering input and water mass mixing in the Nordic Seas during the last 25,000 years. *Earth and Planetary Science Letters*. 514:108–18

Struve T, van de Flierdt T, Burke A, Robinson LF, Hammond SJ, et al. 2017. Neodymium isotopes and concentrations in aragonitic scleractinian cold-water coral skeletons - Modern calibration and evaluation of palaeo-applications. *Chemical Geology*. 453:146–68

Stuiver M, Polach HA. 1977. Reporting of (super 14)C Data. *Radiocarbon*. 19(3):355–63

Stumpf R, Frank M, Schönfeld J, Haley BA. 2010. Late Quaternary variability of Mediterranean Outflow Water from radiogenic Nd and Pb isotopes. *Quaternary Science Reviews*. 29(19–20):2462–72

Stumpf R, Kraft S, Frank M, Haley B, Holbourn A, Kuhnt W. 2015. Persistently strong Indonesian Throughflow during marine isotope stage 3: evidence from radiogenic isotopes. *Quaternary Science Reviews*. 112:197–206

Tachikawa K, Arsouze T, Bayon G, Bory A, Colin C, et al. 2017. The large-scale evolution of neodymium isotopic composition in the global modern and

Holocene ocean revealed from seawater and archive data. *Chemical Geology*. 457:131–48

Tachikawa K, Athias V, Jeandel C. 2003. Neodymium budget in the modern ocean and paleo-oceanographic implications. *Journal of Geophysical Research: Oceans*. 108(C8):3254

Tachikawa K, Piotrowski AM, Bayon G. 2014. Neodymium associated with foraminiferal carbonate as a recorder of seawater isotopic signatures. *Quaternary Science Reviews*. 88:1–13

Tachikawa K, Toyofuku T, Basile-Doelsch I, Delhaye T. 2013. Microscale neodymium distribution in sedimentary planktonic foraminiferal tests and associated mineral phases. *Geochimica et Cosmochimica Acta*. 100:11–23

Takahashi T, Sutherland SC, Wanninkhof R, Sweeney C, Feely RA, et al. 2009. Climatological mean and decadal change in surface ocean pCO2, and net sea–air CO2 flux over the global oceans. *Deep Sea Research Part II: Topical Studies in Oceanography*. 56(8):554–77

Takahashi Y, Hayasaka Y, Morita K, Kashiwabara T, Nakada R, et al. 2015. Transfer of rare earth elements (REE) from manganese oxides to phosphates during early diagenesis in pelagic sediments inferred from REE patterns, X-ray absorption spectroscopy, and chemical leaching method. *GEOCHEMICAL JOURNAL*. 49(6):653–74

Takebe M. 2005. Carriers of Rare Earth Elements in Pacific Deep-Sea Sediments. *The Journal of Geology*. 113(2):201–15

Talley LD. 2003. Shallow, Intermediate, and Deep Overturning Components of the Global Heat Budget. *Journal of Physical Oceanography*. 33(3):530–60

Talley LD. 2008. Freshwater transport estimates and the global overturning circulation: Shallow, deep and throughflow components. *Progress in Oceanography*. 78(4):257–303

Talley LD. 2013. Closure of the global overturning circulation through the Indian, Pacific, and Southern Oceans: Schematics and transports. *Oceanography*. 21(1):80–97

Talley LD, Feely RA, Sloyan BM, Wanninkhof R, Baringer MO, et al. 2016. Changes in Ocean Heat, Carbon Content, and Ventilation: A Review of the First Decade of GO-SHIP Global Repeat Hydrography. *Annual Review of Marine Science*. 8(1):185–215

Talley LD, Pickard GL, Emery WJ, Swift JH. 2011. *Descriptive Physical Oceanography: An Introduction*. Boston: Elsevier. 6th ed.

Tanaka T, Togashi S, Kamioka H, Amakawa H, Kagami H, et al. 2000. JNdi-1: a neodymium isotopic reference in consistency with LaJolla neodymium. *Chemical Geology*. 168(3–4):279–81

Thornalley DJR, Bauch HA, Gebbie G, Guo W, Ziegler M, et al. 2015. A warm and poorly ventilated deep Arctic Mediterranean during the last glacial period. *Science*. 349(6249):706–10

Toyoda K, Tokonami M. 1990. Diffusion of rare-earth elements in fish teeth from deep-sea sediments. *Nature*. 345(6276):607–9

Turner S, Sandiford M, Reagan M, Hawkesworth C, Hildreth W. 2010. Origins of large-volume, compositionally zoned volcanic eruptions: New constraints

from U-series isotopes and numerical thermal modeling for the 1912 Katmai-Novarupta eruption. *J. Geophys. Res.* 115(B12):B12201

van de Flierdt T. 2003. *The Nd, Hf, and Pb Isotopic Composition of Ferromanganese Crusts and Their Paleoceanographic Implications*. Diss., Naturwissenschaften ETH Zürich, Nr. 15188, 2003

van de Flierdt T, Griffiths AM, Lambelet M, Little SH, Stichel T, Wilson DJ. 2016. Neodymium in the oceans: a global database, a regional comparison and implications for palaeoceanographic research. *Philosophical Transactions of the Royal Society A*. 374(2081):20150293

van der Zee C, Roberts DR, Rancourt DG, Slomp CP. 2003. Nanogoethite is the dominant reactive oxyhydroxide phase in lake and marine sediments. *Geology*. 31(11):993–96

Vance D, Scrivner AE, Beney P, Staubwasser M, Henderson GM, Slowey NC. 2004. The use of foraminifera as a record of the past neodymium isotope composition of seawater. *Paleoceanography*. 19(2):PA2009

VanLaningham S, Pisias NG, Duncan RA, Clift PD. 2009. Glacial–interglacial sediment transport to the Meiji Drift, northwest Pacific Ocean: Evidence for timing of Beringian outwashing. *Earth and Planetary Science Letters*. 277(1–2):64–72

Verplanck EP, Farmer GL, Andrews J, Dunhill G, Millo C. 2009. Provenance of Quaternary glacial and glacimarine sediments along the southeast Greenland margin. *Earth and Planetary Science Letters*. 286(1–2):52–62

von Blanckenburg F. 1999. Tracing Past Ocean Circulation? *Science*. 286(5446):1862–63

Waelbroeck C, Paul A, Kucera M, Rosell-Melé A, Weinelt M, et al. 2009. Constraints on the magnitude and patterns of ocean cooling at the Last Glacial Maximum. *Nature Geosci*. 2(2):127–32

WAIS Divide Project Members. 2013. Onset of deglacial warming in West Antarctica driven by local orbital forcing. *Nature*. 500(7463):440–44

Walinsky SE, Prahl FG, Mix AC, Finney BP, Jaeger JM, Rosen GP. 2009. Distribution and composition of organic matter in surface sediments of coastal Southeast Alaska. *Continental Shelf Research*. 29(13):1565–79

Warren BA. 1983. Why is no deep water formed in the North Pacific? *Journal of Marine Research*. 41(2):327–47

Wei R, Abouchami W, Zahn R, Masque P. 2016. Deep circulation changes in the South Atlantic since the Last Glacial Maximum from Nd isotope and multi-proxy records. *Earth and Planetary Science Letters*. 434:18–29

Weis D, Kieffer B, Maerschalk C, Barling J, de Jong J, et al. 2006. High-precision isotopic characterization of USGS reference materials by TIMS and MC-ICP-MS. *Geochemistry, Geophysics, Geosystems*. 7(8):Q08006

Werner K, Frank M, Teschner C, Müller J, Spielhagen RF. 2014. Neoglacial change in deep water exchange and increase of sea-ice transport through eastern Fram Strait: evidence from radiogenic isotopes. *Quaternary Science Reviews*. 92:190–207

White AF, Brantley SL. 2003. The effect of time on the weathering of silicate minerals: why do weathering rates differ in the laboratory and field? *Chemical Geology*. 202(3–4):479–506

White WM. 2013. *Geochemistry*. Wiley-Blackwell

White WM. 2015. *Isotope Geochemistry*. Wiley-Blackwell

Wilson DJ, Crocket KC, Flierdt T van de, Robinson LF, Adkins JF. 2014. Dynamic intermediate ocean circulation in the North Atlantic during Heinrich Stadial 1: A radiocarbon and neodymium isotope perspective. *Paleoceanography*. 29(11):1072–93

Wilson DJ, Piotrowski AM, Galy A, Banakar VK. 2015. Interhemispheric controls on deep ocean circulation and carbon chemistry during the last two glacial cycles. *Paleoceanography*. 30(6):621–41

Wilson DJ, Piotrowski AM, Galy A, Clegg JA. 2013. Reactivity of neodymium carriers in deep sea sediments: Implications for boundary exchange and paleoceanography. *Geochimica et Cosmochimica Acta*. 109:197–221

Wilson DJ, Piotrowski AM, Galy A, McCave IN. 2012. A boundary exchange influence on deglacial neodymium isotope records from the deep western Indian Ocean. *Earth and Planetary Science Letters*. 341–344:35–47

Winckler G, Anderson RF, Fleisher MQ, McGee D, Mahowald N. 2008. Covariant Glacial-Interglacial Dust Fluxes in the Equatorial Pacific and Antarctica. *Science*. 320(5872):93–96

Wolff-Boenisch D, Gislason SR, Oelkers EH, Putnis CV. 2004. The dissolution rates of natural glasses as a function of their composition at pH 4 and 10.6, and temperatures from 25 to 74°C. *Geochimica et Cosmochimica Acta*. 68(23):4843–58

Wu Q, Colin C, Liu Z, Bassinot F, Dubois-Dauphin Q, et al. 2017. Foraminiferal εNd in the deep north-western subtropical Pacific Ocean: Tracing changes in weathering input over the last 30,000years. *Chemical Geology*. 470:55–66

Wu Q, Colin C, Liu Z, Thil F, Dubois-Dauphin Q, et al. 2015. Neodymium isotopic composition in foraminifera and authigenic phases of the South China Sea sediments: Implications for the hydrology of the North Pacific Ocean over the past 25 kyr. *Geochemistry, Geophysics, Geosystems*. 16(11):3883–3904

Wunsch C. 2003. Determining paleoceanographic circulations, with emphasis on the Last Glacial Maximum. *Quaternary Science Reviews*. 22(2):371–85

Xie RC, Marcantonio F. 2012. Deglacial dust provenance changes in the Eastern Equatorial Pacific and implications for ITCZ movement. *Earth and Planetary Science Letters*. 317–318:386–95

Xie RC, Marcantonio F, Schmidt MW. 2012. Deglacial variability of Antarctic Intermediate Water penetration into the North Atlantic from authigenic neodymium isotope ratios. *Paleoceanography*. 27(3):

Xie RC, Marcantonio F, Schmidt MW. 2014. Reconstruction of intermediate water circulation in the tropical North Atlantic during the past 22,000years. *Geochimica et Cosmochimica Acta*. 140:455–67

Xiong Z, Li T, Algeo T, Chang F, Yin X, Xu Z. 2012. Rare earth element geochemistry of laminated diatom mats from tropical West Pacific: Evidence

for more reducing bottomwaters and higher primary productivity during the Last Glacial Maximum. *Chemical Geology*. 296–297:103–18

Yasuda T, Asahara Y, Ichikawa R, Nakatsuka T, Minami H, Nagao S. 2014. Distribution and transport processes of lithogenic material from the Amur River revealed by the Sr and Nd isotope ratios of sediments from the Sea of Okhotsk. *Progress in Oceanography*. 126:155–67

Yu Z, Colin C, Ma R, Meynadier L, Wan S, et al. 2018. Antarctic Intermediate Water penetration into the Northern Indian Ocean during the last deglaciation. *Earth and Planetary Science Letters*. 500:67–75

Yu Z, Colin C, Meynadier L, Douville E, Dapoigny A, et al. 2017. Seasonal variations in dissolved neodymium isotope composition in the Bay of Bengal. *Earth and Planetary Science Letters*. 479:310–21

Zahn R, Mix AC. 1991. Benthic foraminiferal δ18O in the ocean's temperature-salinity-density field: Constraints on Ice Age thermohaline circulation. *Paleoceanography*. 6(1):1–20

Zemmels I, Cook HE. 1973. Appendix IV; X-ray mineralogy of sediments from the Northeast Pacific and Gulf of Alaska-Leg 18 Deep Sea Drilling Project. In *Initial Reports of the Deep Sea Drilling Project*, Vol. 18, eds. LVD Kulm, R von Huene, pp. 1015–60. Washington, D.C.: U.S. Govt. Printing Office

Zhao Ning, Marchal Olivier, Keigwin Lloyd, Amrhein Daniel, Gebbie Geoffrey. 2018. A Synthesis of Deglacial Deep-Sea Radiocarbon Records and Their (In)Consistency With Modern Ocean Ventilation. *Paleoceanography and Paleoclimatology*. 33(2):128–51

Ziegler CL, Murray RW, Hovan SA, Rea DK. 2007. Resolving eolian, volcanogenic, and authigenic components in pelagic sediment from the Pacific Ocean. *Earth and Planetary Science Letters*. 254(3–4):416–32

Zinder B, Furrer G, Stumm W. 1986. The coordination chemistry of weathering: II. Dissolution of Fe(III) oxides. *Geochimica et Cosmochimica Acta*. 50(9):1861–69

Appendices

Appendix A: Supplementary Materials for Chapter 2

Correcting leachate $^{87}Sr/^{86}Sr$ for carbonate dissolution

Extracted Ca in the leachates is in the range of 0.0004 g/g to 0.06 g/g, consistent with the general observation that carbonate content in GOA sediments is <5% (Bode 1973; Jaeger et al. 2014; Walinsky et al. 2009). This observation supports an assumption that the Ca measured in the leachates is derived entirely from carbonate. On the other hand, the Sr/Ca ratios of HH4 leachates are in the range of 2761 to 33962 ppm, much greater than what is typically found in marine carbonate, indicating the leaching extracted Sr from another source; i.e., there is an excess Sr that cannot be accounted for by carbonate.

We calculate the excess Sr as $[\mathrm{Sr}]_{\mathrm{excess}} = [\mathrm{Sr}]_{\mathrm{leachate}} - \left(\frac{[\mathrm{Sr}]}{[\mathrm{Ca}]}\right)_{\mathrm{carbonate}} \times [\mathrm{Ca}]_{\mathrm{leachate}}$, assuming the only source of Ca is carbonate and use $\left(\frac{\mathrm{Sr}}{\mathrm{Ca}}\right)_{\mathrm{carbonate}} = 0.0012$, or a Sr concentration of 1200 ppm in marine carbonate (Kinsman 1969). Using this equation, the percentage of Sr_{excess} relative to total extracted Sr in HH4 leachates is 73%±10% (1σ), implying that Sr in the leachates was primarily extracted from non-carbonate sources. We can correct our leachate $^{87}Sr/^{86}Sr$ for carbonate dissolution using simple isotope mass balance calculation:

$$^{87}\mathrm{Sr}/^{86}\mathrm{Sr}_{\mathrm{corrected}} = \frac{^{87}\mathrm{Sr}/^{86}\mathrm{Sr}_{\mathrm{leachate}} \times [\mathrm{Sr}]_{\mathrm{leachate}} - {}^{87}\mathrm{Sr}/^{86}\mathrm{Sr}_{\mathrm{carbonate}} \times [\mathrm{Sr}]_{\mathrm{carbonate}}}{[\mathrm{Sr}]_{\mathrm{excess}}}$$

Where $^{87}Sr/^{86}Sr_{carbonate}=^{87}Sr/^{86}Sr_{seawater}=0.7091792$ (Mokadem et al. 2015), $[\mathrm{Sr}]_{\mathrm{carbonate}} = \left(\frac{[\mathrm{Sr}]}{[\mathrm{Ca}]}\right)_{\mathrm{carbonate}} \times [\mathrm{Ca}]_{\mathrm{leachate}}$ and $[Sr]_{excess}$ are calculated above. The corrected values are plotted in Fig. 2.3b and Fig. 2.8 and used in the discussion of Section 4.6. This correction does not affect coretop leachates below 3000 m as these leachates already have seawater-like $^{87}Sr/^{86}Sr$, however, samples shallower than 200 m are strongly affected as these sediments are richer in carbonate. Finally, the assumption that Ca in leachates are entirely derived from carbonate can be relaxed

without affecting our conclusion: a smaller portion of Ca from carbonate will lead to a smaller correction to leachate $^{87}Sr/^{86}Sr$, resulting in even weaker deviation from seawater $^{87}Sr/^{86}Sr$. This, in turn, will only decrease our estimates of detrital contamination to leachate ε_{Nd} (Fig. 2.8).

Estimating Nd release rates

Estimating Nd release rate from authigenic phases

Brantley (2008) compiled published experimental data and showed that reductive dissolution rate of Fe (III) oxide is bounded above by dissolution rate of FeO and below by proton-promoted nonreductive dissolution rate of Fe (III) oxide, and offered pH dependent rate equations (Table EA4). Zinder et al. (1986) reported abiotic reductive dissolution rates of goethite in a pH range of 3 to 4.2 measured in 10^{-3} M ascorbic acid, which is close to our experimental setting. van der Zee et al. (2003) found that the dominant reactive Fe oxyhydroxide mineral in marine sediment is nanogoethite and they suggested its size is similar to 2-line ferrihydrite, which has a specific surface area of 240 m^2/g (Roden & Zachara 1996) although higher numbers were also reported in experiments (Zinder et al. 1986). Based on this information, we calculated Fe release rate from Fe oxyhydroxide and from this calculated Nd release rate assuming the Nd/Fe ratio (0.0014) is the same as in Fe-Mn crusts and nodules (Hein & Koschinsky 2014). Results for the upper and lower limits (Brantley 2008) as well as calculated using the measurements from Zinder et al. (1986) are plotted in Fig. 2.7.

Estimating Nd release rate from detrital minerals

We use the bulk XRD mineralogy data of DSDP Leg 18 Site 178 to 181 that formed a depth-transect (1419 m to 4218 m) in northwestern GOA (Zemmels & Cook 1973) to represent the mineral composition of our GOA samples. Bulk mineralogy is relatively uniform in these sites: mica (32.4%, median), plagioclase (24.4%), quartz (23.0%) and chlorite/kaolinite (11.3%) are the dominant minerals, montmorillonite (4.1%) is present in older sediments and amphibole (4.2%) is an ubiquitous accessory mineral (Zemmels & Cook 1973). Such observations were semi-quantitatively

replicated by shipboard bulk XRD measurements in the recent IODP Expedition 341 in GOA (Jaeger et al. 2014) and are consistent with other studies (Molnia & Hein 1982; Naidu & Mowatt 1983). pH-dependent dissolution rates of these mineral groups are compiled from a variety of sources (Table EA4).

The specific surface areas of minerals can be estimated from grain size. Brantley and Mellott, (2000) reported an equation for impurity-free and nonporous primary silicates: log (specific surface area in cm^2/g) = 5.2–log (grain size in μm). For example, at grain sizes of 4 μm and 1 μm the corresponding specific areas are 4 m^2/g and 16 m^2/g respective. Coretop sediments in the GOA are mostly silty clay and it seems the 4 m^2/g estimation might be reasonable. Maher et al., (2006) reported a specific area of 6.9 m^2/g for plagioclase estimated using α-recoil loss fraction of ^{234}U in sediments from ODP Site 984 in the North Atlantic which agrees roughly with this estimation. This equation, however, is not suitable for non-primary silicates like clay minerals, Maher et al., (2006) also reported 55 m^2/g for clay minerals in their samples.

Using bulk mineralogy and silicate mineral dissolution rates, we can first calculate total Si release rate from detrital silicates and then estimate Nd release rate using the Nd/Si ratio of bulk sediment from DSDP Site 178 in the GOA (Plank 2014). In this calculation, we intentionally chose the most reactive mineral to represent a group so as to give a maximum estimation of detrital contribution to leachate Nd: biotite for the mica group, anthophyllite the amphibole group and anorthite the plagioclase group. In truth, the less reactive illite is perhaps the dominant mica mineral in GOA sediments (Molnia & Hein 1982; Naidu et al. 1995; Naidu & Mowatt 1983). The largest uncertainty in this calculation is the lack of suitable specific surface area data for minerals in marine sediment. If we use 4 m^2/g for the primary silicates and 55 m^2/g for the clay minerals, then the Nd release rate from total detrital minerals is 0.5 ng Nd g^{-1} 0.5 hr^{-1} at pH=4. If a specific surface area of 55 m^2/g is used for all silicate minerals, which must be an overestimation, we get 5 ng Nd g^{-1} 0.5 hr^{-1}, an order of magnitude greater. However, these numbers are all negligible (<1%) comparing to the Nd release rates measured in our HH4 leachates (220 to 2051 ng Nd

g^{-1} $0.5hr^{-1}$), and this supports our findings based on geochemical fingerprinting that nearly all Nd in our leaches comes from Fe-Mn oxyhydroxides.

The definition of reactivity-weighted detrital ε_{Nd}

Detrital sediment, defined here as the non-authigenic and non-biogenic part of the sediment, is made up of components of distinct reactivity and ε_{Nd} (Wilson et al. 2013). Therefore measures of bulk sediment ε_{Nd}, or many other operationally defined ε_{Nd}, do not account possible differences in reactivity when they are used as a source signature. Our definition of "reactivity-weighted detrital ε_{Nd}" depends on the reaction kinetics of these sedimentary components.

Assume the detrital sediment is made of N components *1, 2, 3,…,i,…,N*, and the concentration of the i^{th} component is C_i, measured in unit such as wt%, and the Nd concentration in the i^{th} component is $[Nd]_i$, measured in unit such as μg/g or ppm. Given a rate constant of the i^{th} component (k_i, in unit s^{-1}) and a Nd isotopic composition (ε_{Ndi}), we define

$$\text{reactivity} - \text{weighted detrital } \varepsilon_{Nd} = \frac{\sum_{i=1}^{N} k_i [Nd]_i C_i \varepsilon_{Nd_i}}{\sum_{i=1}^{N} k_i [Nd]_i C_i}.$$

Here we assume first order rate laws for all components, although other reaction kinetics could be incorporated into the definition similarly.

Under this definition, a minor component with low *C* could have significant effects on reactivity-weighted detrital ε_{Nd} during sediment diagenesis and leaching given it has a high reactivity, *i.e.*, if its *k* is large. This can be seen clearly when the reactivity-weighted detrital ε_{Nd} is compared to the non-weighted detrital ε_{Nd} measured by digesting bulk sediment or operationally defined leaching residue.

$$\text{bulk/detrital } \varepsilon_{Nd} = \frac{\sum_{i=1}^{N} [Nd]_i C_i \varepsilon_{Nd_i}}{\sum_{i=1}^{N} [Nd]_i C_i},$$

Better understanding of the distribution of reactivity in detrital sediment is important for future study of the effect of sediment-water interaction on the Nd cycle in the ocean.

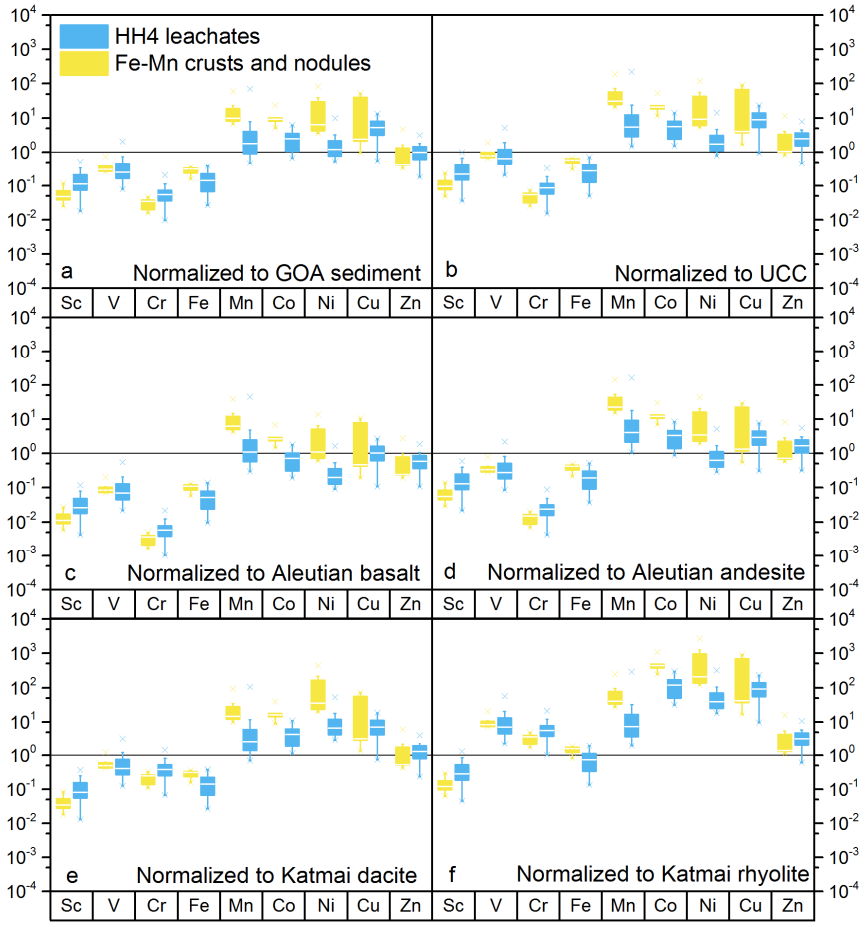

Figure 2.S1. Enrichment factor plots of the first series transitional metals in HH4 leachates normalized to various detrital endmembers and compared to Fe-Mn crusts and nodules.

Fig. 2.5d is the same as in panel (f) here. Regardless of the detrital endmember used for normalization, HH4 leachates show similar non-unity patterns resembling Fe-Mn crusts and nodules. In particular HH4 leachates and Fe-Mn crusts and nodules are typically enriched in Mn, Co, Ni, Cu, Zn and depleted in Sc, V, Cr and Fe

Table 2.S1. GOA bulk mineralogy and dissolution rate parameters for selected minerals

Mineral group	GOA bulk mineralogy (%)[1]	Representative mineral	formula	log k_H (mol mineral m^{-2} s^{-1})[2]	n	Reference
Fe oxyhydroxide		Goethite/reductive	α-FeOOH	-9.72	0.330	Zinder et al., (1986)
		Fe (III) oxide/non-reductive		-10.98	0.430	Brantley, (2008)
		Fe (II) oxide		-5.48	0.400	Brantley, (2008)
Mica	32.4	Biotite	$Si_6O_{20}(OH)_4$	-10.01	0.355	Bandstra and Brantley, (2008)
		Illite	$Si_4O_{10}(OH)_2$	-11.78	0.592	Alekseyev, (2007)
		Muscovite	$Si_6O_{20}(OH)_4$	-11.77	0.140	Kalinowski and Schweda, (1996)
Plagioclase	24.4	Albite	Si_3O_8	-9.62	0.403	Bandstra and Brantley, (2008)
		Anorthite	Si_2O_8	-6.64	0.985	Bandstra and Brantley, (2008)
Quartz	23.0	Quartz	SiO_2	-11.36	0.309	Bandstra and Brantley, (2008)
Chlorite/ Kaolinite	11.3	Chlorite	$Si_3O_{10}(OH)_8$	-9.79	0.490	Lowson et al., (2005)
		Kaolinite	$Si_2O_5(OH)_4$	-11.80	0.129	Bandstra and Brantley, (2008)
Amphibole	4.2	Hornblende	$Si_8O_{22}(OH)_2$	-10.35	0.370	Bandstra and Brantley, (2008)
		Anthophyllite	$Si_8O_{22}(OH)_2$	-10.82	0.200	Rozalen et al. (2014)
		Tremolite	$Si_8O_{22}(OH)_3$	-13.02	0.190	Rozalen et al. (2014)
Smectite	4.1	Montmorillonite	$Si_4O_{10}(OH)_2$	-12.30	0.400	Rozalen et al., (2009)

[1.] (Zemmels & Cook 1973); [2.] Rate equation: $\log(r) = \log(k_H) - n \times \mathrm{pH}$ (Brantley 2008; Brantley & Olsen 2014), where *r* is surface area normalized rate, k_H is the proton-promoted dissolution rate constant and *n* is the reaction order

Appendix B: Supplementary Materials for Chapter 3

The ε_{Nd}-^{14}C twin-tracer approach

The preformed age problem of ^{14}C based circulation age proxies

The challenges of using benthic ^{14}C age as a circulation rate tracer include that (1) the preformed age cannot be reconstructed without a truly independently and absolutely dated, i.e., non-^{14}C based, chronology; (2) the variability of preformed age and mixing are difficult to separate based on observations of benthic ^{14}C age alone. Such impediments are particularly significant in the Southern Ocean. The preformed age here is the highest in the ocean today because of relatively deep wind-driven upwelling of old Pacific and Indian deep waters, and very short surface-water residence time that limits gas exchange and isotope equilibration(Gebbie & Huybers 2012; Jones et al. 2014; Koeve et al. 2015). If the hypothesized changes of Southern Ocean circulation sufficient to modify atmospheric CO_2 in the past are true, the preformed ^{14}C age of deep or bottom waters formed in the Southern Ocean should also be highly variable.

There are four main classes of ^{14}C based age (and their $\Delta^{14}C$ equivalents) proxies for reconstructing circulation rate in paleoceanographic literature: the benthic-planktonic age difference, the benthic-atmospheric age difference, the benthic projection age and the transient-time equilibration-time distribution (TTD-ETD) age(Cook & Keigwin 2015). If the circulation age of a watermass is defined as the time elapsed since its last contact with the atmosphere, then these various ages can be considered circulation ages only under specific assumptions about preformed ^{14}C age and mixing, i.e., to use the benthic-atmospheric age difference as the circulation age requires the assumption of fixed preformed age (or surface reservoir age), and multiple deep watermasses do not mix. These assumptions also apply to the benthic projection age unless the benthic ^{14}C age can be projected onto the (single) source water ^{14}C curve instead of the atmospheric ^{14}C curve. The TTD-ETD approach tries to resolve these issues by treating mixing using the TTD and preformed age using the ETD, but it assumes that the prior probability density functions of these distributions

derived from modern tracer fields can be applied to the ocean in the past, even though these probabilities are presumably circulation-specific.

These challenges show that extra constraints are required to deconvolve ^{14}C-based watermass age proxies to components specific to circulation rate, preformed age and mixing. Because of the relatively low sensitivity of deep-ocean ε_{Nd} to its preformed properties and the relatively high sensitivity to changes in circulation rate (which controls benthic exposure time, Methods), ε_{Nd} can be used to independently constrain circulation rate and thereby deconvolve the preformed age component from ^{14}C records in a relatively simple modeling strategy. In Table 3.S1 we list the definition of ^{14}C related terminology that will be used in the discussions.

Applying ε_{Nd} as a circulation rate tracer

Here we document the budget components and fluxes of Nd relevant to ε_{Nd} in authigenic materials and show (1) the dominance of the benthic flux, (2) the likelihood that this flux is relatively constant on glacial-interglacial cycles, (3) that changes of the surficial fluxes of Nd do not significantly affect the Pacific Nd budget on time scales relevant to our study, and (4) abyssal circulation rate, which controls the conservative transport flux of Nd and modulates the expression of benthic flux in the authigenic component, is the most likely determinant of our ε_{Nd} observations.

Benthic Nd flux and the Pacific Nd budget

Modern Pacific Nd budget

The mass balance of Nd and its isotopes dictates that the seawater ε_{Nd} equals the mass weighted average of the isotope compositions of the sources:

$$\varepsilon_{Nd}^{sw} = \frac{D\varepsilon_{Nd}^{atm} + R\varepsilon_{Nd}^{riv} + B\varepsilon_{Nd}^{ben} + T\varepsilon_{Nd}^{tr}}{D + R + B + T} \quad (1)$$

Where ***D***, ***R, B***, ***T*** are the Nd sources (in g/yr) due to atmospheric deposition (i.e., dust), river discharge (dissolved), benthic source and watermass transport, and ε_{Nd}^{atm}, ε_{Nd}^{riv}, ε_{Nd}^{ben}, ε_{Nd}^{tr} are their respective isotope compositions.

Integrated over the North Pacific, dust flux(Jickells et al. 2005) is 6.75×10^{13} g/yr, leading to a Nd flux of 2.7×10^{7} g/yr (assuming 20 ppm of Nd in dust and 2% solubility(Tachikawa et al. 2003)).

Rivers draining into the North Pacific supply a dissolved Nd flux(Goldstein & Jacobsen 1987) of 8.7×10^{7} g/yr assuming 70% removal in their estuaries(Rousseau et al. 2015). We do not consider the dissolution of river suspended sediments in the estuary(Rousseau et al. 2015) here, as relevant flux data are only available for the Amazon River. If we assume that the ratio of Nd flux due to dissolution of river suspended sediments to dissolved riverine Nd flux (after 70% removal) is the same for North Pacific rivers as the Amazon (ratio = 4), then we may add an additional Nd flux of 3.5×10^{8} g/yr to the river budget, which is still one order of magnitude smaller than the benthic flux estimated later. Further, whether the Nd release due to dissolution of river suspended sediment can outcompete Nd removal due to colloidal coagulation in the high salinity zone of estuary seems river-specific(Rousseau et al. 2015) and is yet to be quantified. If the removal in the high salinity zone is also significant as seen in many rivers(Rousseau et al. 2015), the estimated Nd flux due to dissolution of river suspended sediments would decrease.

The flux due to watermass transport, which represents the preformed and conservative component of Nd budget, is calculated using water fluxes (in volume per time) estimated from geostrophically constrained box inverse models of Talley(Talley 2003, 2008, 2013) as adopted in our model (Fig. 3.S4) and Nd concentrations(van de Flierdt et al. 2016) of the watermasses entering the North Pacific, and it is 7.3×10^{8} g/yr.

Published estimates of benthic Nd flux based on pore water sampling in the Pacific (all from <4000 m water depth)(Abbott et al. 2015b; German & Elderfield 1989; Haley & Klinkhammer 2003) show a statistically significant ($p=0.038$) trend towards increasing flux with water depth (Fig. 3.S1b). Acknowledging the paucity of data available, we consider three hypothetical cases of net benthic flux as a function of water depth, as shown in Fig. 3.S1b. In case 1 we assume benthic Nd flux is

constant with respect to depth and we use the average value of the dataset. In case 2 we use the linear regression line between benthic flux and depth up to 4000 m below which we assume it is constant. In case 3 we adopt the same relationship as in case 2 except that we assume that below 4000 m the benthic flux is zero. Case 3 is unrealistic as there is no reason to believe that the flux should cease below 4000 m, but we use this case to explore the uncertainty range. Using the hypsometry curve(Menard & Smith 1966), the three cases yield depth and area integrated benthic fluxes in the North Pacific of 1.7×10^9 g/yr, 2.9×10^9 g/yr and 1.0×10^9 g/yr respectively.

Using the middle estimate of benthic flux (Case 1), the Nd budget of the North Pacific can be partitioned as following: 1% to dust flux, 3 % to river dissolved flux, 29% to watermass transport, 66% to benthic flux (in Case 2, benthic flux is 78% of the total). The same calculation can be repeated for the entire Pacific, yielding similar results: for Case 1, 1% to dust flux (3.8×10^7 g/yr), 2% to river dissolved flux (1.1×10^8 g/yr), 38% to watermass transport (2.1×10^9 g/yr) and 60% to benthic flux (3.3×10^9 g/yr) (and in Case 2, benthic flux is 72%).

In all three cases, the dust and river fluxes are negligible for the Nd budget (<6% combined). Benthic flux is the most important Nd source in the North Pacific (53-78%), and together with watermass transport accounts for >94% of the total Nd budget. This analysis shows that on basinal scale the non-conservative component (benthic flux) is more important than the conservative component (transport) in the Pacific Nd budget, and thus must be a significant influence on the ε_{Nd} signature of bottom waters and authigenic phases.

The depth distribution of benthic Nd flux

The integrated budget indicates that the marine Nd budget is dominated by benthic Nd flux in the Pacific. Here we further show that the integrated benthic flux is dominated by deep sea sediments >3000 m.

The geometry of the ocean basins determines the distribution of seafloor area and therefore exerts the first order control on the integrated benthic Nd flux. In the Pacific, the seafloor area is largely concentrated between 3000 m and 6000 m, such that seabed below 3000 m contributes to 93% of the depth integrated seafloor area(Menard & Smith 1966) (Fig. 3.S1a).

We examine the depth distribution of benthic Nd flux under the three cases of depth relationship described earlier (Fig. 3.S1b, c, d). Ultimately, the choice of this relationship has little influence on the distribution of depth and area integrated benthic flux, which is to the first order controlled by the distribution of seafloor area (Fig. 3.S1a). Specifically, in all cases deep-sea sediments (water depth > 3000 m) dominate the integrated benthic flux (70-90% of the total; Fig. 3.S1c, d) and accounts for the majority of the Pacific Nd budget.

The stability of benthic Nd flux

We have shown that the integrated benthic flux is dominated by deep sea sediments (>3000 m). Although local sediment changes are possible, the basinal integral is relevant to the Nd budget and ε_{Nd} as a watermass tracer; on this spatial scale sedimentation is stable over glacial-interglacial timescales because large-scale deep-sea sediment provenance is primarily controlled by tectonic activities operating on much longer time scales(McLennan et al. 1993; Ziegler et al. 2007; Dunlea et al.). This also suggests that the basinal benthic flux should be stable on the time scale of glacial-interglacial cycles.

Sediment provenance

Local changes in sediment provenance may also have occurred as glaciers retreated and sea level rose, but this too would have little influence on the depth and area integrated benthic flux of Nd because the seafloor area of the margin is small relative to the broad expanse of abyssal sea floor that dominates the benthic flux[10,11]. Indeed, modern benthic Nd flux in the Pacific from sediments in the range of 0 to 200

m water depth that can be affected by sea-level change during the deglaciation accounts for <2% of the integrated benthic flux (Fig. 3.S1c, d).

The Gulf of Alaska is among the places most susceptible to glacial erosion in the Pacific, where the retreating Cordilleran Ice Sheet caused large changes in sedimentation rate during the deglaciation. However, sediment provenance remained relatively constant with respect to ε_{Nd}, as evidenced by nearly constant bulk sediment (dominantly lithogenic) ε_{Nd} (2σ=0.9 for 85TC/JC/U1419 and 2σ=0.8 for 87JC/U1418, compared to 2σ external analytical uncertainties of 0.3 to 0.5 based on replicate sediment digestions of the two USGS reference materials and two in-house standards). Changes in bulk sediment ε_{Nd} are also not significantly correlated with authigenic ε_{Nd} (Fig. 3.S3d). Consequently, secular changes in our authigenic ε_{Nd} records are not primarily driven by changes in local lithogenic sources of Nd.

Redox State

Early studies on the diagenetic cycle of Rare Earth Elements (REEs) were carried out in reducing coastal environments, leading to a general perception that benthic sources of REEs will increase under reducing conditions where Mn and Fe reduction occurs(Elderfield & Sholkovitz 1987; German & Elderfield 1989). However, recent measurements that represent almost a doubling in total observations are inconsistent with this earlier perception. Transects across the Oregon and California margins showed no increase of benthic Nd flux within in the Oxygen Minimum Zones, nor at shallower depths where organic carbon fluxes are high(Abbott et al. 2015b; Haley & Klinkhammer 2003). In Fig. 3.S1 e, f we show that benthic Nd flux in the Pacific is neither significantly correlated to particulate organic carbon rain rate (p=0.21) nor to bottom water oxygen concentration (p=0.76). For the former comparison, we used the satellite Net Primary Productivity dataset(Behrenfeld & Falkowski 1997), assumed an export ratio of 0.25(DeVries & Weber) and applied a power law (b=0.82) of depth dependence(Berelson 2001) to estimate POC flux at seafloor. Bottom water oxygen concentrations for the latter comparison were reported in the original studies.

Changes of ocean redox state occurred regionally during the deglaciation, but mainly only at shallow water depths(Galbraith & Jaccard 2015) most often associated with sea-level rise onto the continental shelves(Galbraith et al. 2013). The redox state of the deep ocean, instead, was relatively stable(Hastings et al. 1996). And because of the lack of correlation between modern benthic Nd flux and sediment redox state, there is little reason to believe that benthic Nd benthic flux from deep sea sediments should change significantly during the deglaciation. Indeed, during the deglaciation, our intermediate depth site (85TC/JC/U1419) experienced severe hypoxia linked to changing upper-ocean productivity(Praetorius et al. 2015), yet neither these events were related to the subsurface circulation events as recorded in our ε_{Nd} record. If redox changes were the cause of changing authigenic $\varepsilon_{Nd,}$ intermediate sites would exhibit larger ε_{Nd} variabilities than deep sites, and this is not the case (Figure 3.2).

Sedimentation Rate

Large changes of sedimentation rate may also happen locally, but also mostly limited to shallow depths. Because solute transport in sediment is not significantly affected by sedimentation induced advection, this effect is negligible. The dimensionless Péclet number quantifies the ratio of advection to diffusion for transport of solutes in sediments(Berner 1980; Boudreau 1997):

$$Pc = \frac{(1-\varphi)Lw}{\varphi D / (1-\ln(\varphi^2))}, \quad (2)$$

where $\boldsymbol{\varphi}$ is porosity, typically ~0.8 for deep sea sediments; $\boldsymbol{L}$ is the depth scale, typically ~10 cm for early diagenesis; $\boldsymbol{w}$ is sedimentation rate; $\boldsymbol{D}$ is the molecular diffusion coefficient of Nd (88.3 cm^2/yr)(Abbott et al. 2015b); the term $\boldsymbol{1-\ln(\varphi^2)}$ corrects for tortuosity. For typical deep sea sediments, $\boldsymbol{w}$ is ~1 cm/ka, leading to a Péclet number of 0.0001. Even in the case that sediment rate is as high as 1 cm/yr, which is extraordinarily rare for deep sea sediments, the Péclet number is still 0.1, illustrating that deep-sea sediments are dominantly diffusional systems. Large changes in sedimentation rate, say from 1 cm/yr to 1 cm/ka, have negligible effect on the benthic flux of Nd.

Atmospheric Dust Fluxes

Dust flux only contributes to ~1% of the modern Pacific Nd budget and even in regions of relatively high dust flux such as the Northwest Pacific it does not significantly affect water column ε_{Nd}(Amakawa et al. 2004, 2009; Carter et al. 2012; Jeandel et al. 2013; Lacan & Jeandel 2001). During the deglaciation atmospheric deposition could have changed in some areas by a factor of two. For example, records from the East Equatorial Pacific suggest decrease of regional dust fluxes by this amount from LGM to Holocene(McGee et al. 2007; Winckler et al. 2008). The effect of changes of atmospheric flux on seawater ε_{Nd} can be estimated:

$$\Delta\varepsilon_{Nd}^{sw} \approx \frac{\Delta D}{D+R+B+T}\varepsilon_{Nd}^{atm}, \quad (3)$$

where Δ indicates change. If we assume that the atmospheric flux decreased everywhere in the North Pacific by a factor of two during the deglaciation(McGee et al. 2007; Winckler et al. 2008) and that $\varepsilon_{Nd}^{atm} \approx -5$ in the North Pacific(Tachikawa et al. 2003), seawater ε_{Nd} would increase by 0.04 unit, well below our analytical uncertainty (2σ=0.29). For changing dust fluxes to have a significant effect on ε_{Nd}, the magnitude of change would need to be at least an order of magnitude higher than observed and would have to apply everywhere in the Pacific.

More importantly, the sign of the dust effect is opposite to the sense of change in ε_{Nd} we observed in our records. Because dust has more negative ε_{Nd} than seawater (-3.8)(van de Flierdt et al. 2016), decreasing dust flux, if important during the deglaciation, will only lead to more positive seawater ε_{Nd}, in contrast to the negative excursions in our records. This shows that changes in deglacial atmospheric flux of Nd had negligible effect in the North Pacific. South Pacific receives much smaller dust flux (40%) than the North Pacific(Jickells et al. 2005), so the impact of dust on ε_{Nd} must be even smaller there.

Freshwater/Meltwater Fluxes

Deglacial freshwater Nd flux in the North Pacific likely increased in association with meltwater flux released during the collapse of the Cordilleran Ice Sheet (CIS) in Northwest America, but this would not have significantly influenced the North Pacific Nd budget and our ε_{Nd} records on the millennial time-scales of abrupt climate changes. The exact timing, temporal evolution and routing of the meltwater flux remain uncertain and individual flood events generally happen on very short timescales (weeks to decades)(Balbas et al. 2017; Menounos et al. 2017). The events in our ε_{Nd} records in contrast occurred on the timescale of thousands of years, we therefore estimate the potential meltwater Nd flux on this timescale. The total volume of CIS was equivalent to ~6 m of sea level(Menounos et al. 2017), and its collapse during the deglaciation (19-11 ka) would hence supply an average freshwater Nd flux of 1.6×10^6 g/yr (again, considering 20 ppt Nd concentration in fresh water as in modern Columbia River(Goldstein & Jacobsen 1987) and 70% removal before entering the ocean, further assuming all meltwater entered the North Pacific), which is three orders of magnitude smaller than the modern benthic flux in the North Pacific (1.7×10^9 g/yr, Case 1).

Further, we observed no change of ε_{Nd} at our intermediate depth site during the early deglaciation, at the time of large changes of ε_{Nd} in our deep site (Fig. 3.2). If changes in freshwater Nd flux were important we might expect the opposite to happen, as the signal should propagate downward from the surface. Further, the large rivers draining into the Northeast Pacific have more positive ε_{Nd} (-3.0 for the Columbia River, -3.0 for the Fraser River and -3.75 for the Copper River)(Goldstein & Jacobsen 1987; Haley et al. 2014) than deep Pacific seawater, reflecting the radiogenic nature of the terranes they drain. Thus, we would predict that meltwater flux from the CIS, which mainly drains through the Columbia River(Balbas et al. 2017), would drive an increase in seawater ε_{Nd}; Yet we observed negative excursions at our sites.

Hydrothermal processes

Increasing deglacial hydrothermal activity, likely in response to sea-level change, was reported(Lund et al. 2016), but it would have little influence on the marine Nd budget. The effect of hydrothermal activity on modern global ε_{Nd} budget is on the order of 0.1%(2018). Assuming the reported increase of hydrothermal metal flux by a factor of 2 to 3 during the deglaciation(Lund et al. 2016) is applicable to Nd, the resulting change to global Nd budget is merely ~0.3%, which would not have any significant impact on our records far from the hydrothermal source.

Watermass Transport from the Southern Ocean

In contrast to the surficial fluxes, our budget analysis shows that changes of transport (i.e. circulation rate) could significantly influence seawater and authigenic ε_{Nd} in the North Pacific. As described in the Methods, the contribution of this conservative component relative to the non-conservative component is weighted by the factor τ_{Nd}/τ_w. Since we have shown that the benthic flux should be stable on the time scale of interest, i.e. τ_{Nd} is constant, increasing circulation rate will decrease τ_w and consequently increase the "weight" of the conservative component. In short, though benthic flux exerts the first order control on the distribution of ε_{Nd}, its expression is modulated by circulation rate that controls the water residence time and sediment exposure time(Abbott et al. 2015a; Du et al. 2016; Haley et al. 2017).

Given Southern Ocean source waters have more negative ε_{Nd} than North Pacific seawater(van de Flierdt et al. 2016), increasing Southern Ocean water flux (i.e. the conservative component) is the most likely candidate to explain the negative ε_{Nd} excursions found in our North Pacific records during the deglaciation.

Box model

Here we derive the governing equations of ε_{Nd} and watermass age discussed in the Methods and provide details on the modern configuration of the model.

Governing equations of the Nd cycle

The concentration and isotope budgets of Nd in each box are balanced by watermass transport (the conservative component) and the benthic source and sink

(the non-conservative component). We ignore the surficial fluxes of Nd in the model as they do not significantly influence the Pacific Nd budget.

In the derivations of governing equations, we use the PDW box (Fig. 3.S4) as an example. The mass balance in this box is governed by two equations:

$$V_{PDW}\frac{d[Nd]_{PDW}}{dt} = F_4[Nd]_{NAABW} + F_5[Nd]_{AAIW} + F_6[Nd]_{NPIW} - (F_4+F_5+F_6)[Nd]_{PDW} + (B_{PDW} - S_{PDW})A_{PDW}, \quad (4)$$

$$V_{PDW}\frac{d[Nd]_{PDW}\varepsilon Nd_{PDW}}{dt} = F_4[Nd]_{NAABW}\varepsilon Nd_{NAABW} + F_5[Nd]_{AAIW}\varepsilon Nd_{AAIW} + F_6[Nd]_{NPIW}\varepsilon Nd_{NPIW} - (F_4+F_5+F_6)[Nd]_{PDW}\varepsilon Nd_{PDW} + (B_{PDW}\varepsilon Nd_{B\_PDW} - S_{PDW}\varepsilon Nd_{PDW})A_{PDW}, \quad (5)$$

where ***V*** is the volume of the box and ***A*** is the seafloor area in the box; The Nd concentrations ***[Nd]*** (in mass per unit volume) and isotope compositions ε_{Nd} are denoted by the names of the boxes in the subscripts; Water fluxes (in volume per unit time) are noted as ***F*** with subscripts as in Fig. 3.S4; ***B*** and ε_{Nd}***B*** are the magnitude (in mass per unit seafloor area per unit time) and isotope composition of benthic flux; ***S*** is the sink flux (in mass per unit seafloor area per unit time), which has the same isotope composition as seawater in the box.

Equations (4) and (5) can be combined to eliminate the sink term, yielding a single equation of ε_{Nd}:

$$\frac{d\varepsilon Nd_{PDW}}{dt} = \frac{(F_4+F_5+F_6)}{V_{PDW}}\frac{F_4[Nd]_{NAABW}\varepsilon Nd_{NAABW} + F_5[Nd]_{AAIW}\varepsilon Nd_{AAIW} + F_6[Nd]_{NPIW}\varepsilon Nd_{NPIW}}{(F_4+F_5+F_6)[Nd]_{PDW}} + \frac{B_{PDW}A_{PDW}}{V_{PDW}[Nd]_{PDW}}\varepsilon Nd_{B\_PDW} - \left[\frac{(F_4+F_5+F_6)}{V_{PDW}}\frac{F_4[Nd]_{NAABW} + F_5[Nd]_{AAIW} + F_6[Nd]_{NPIW}}{(F_4+F_5+F_6)[Nd]_{PDW}} + \frac{B_{PDW}A_{PDW}}{V_{PDW}[Nd]_{PDW}}\right]\varepsilon Nd_{PDW}, \quad (6)$$

This can be rewritten in the form of Equation (1) in the Methods section using the following definitions: $\tau_{w\_PDW} = \frac{V_{PDW}}{F_4 + F_5 + F_6}$ and $\tau_{Nd\_PDW} = \frac{V_{PDW}[Nd]_{PDW}}{B_{PDW} A_{PDW}}$ are the residence times of water (with respect to water flux) and Nd (with respect to the benthic flux) in the box respectively; $m_{NAABW} = \frac{F_4[Nd]_{NAABW}}{(F_4 + F_5 + F_6)[Nd]_{PDW}}$, $m_{AAIW} = \frac{F_5[Nd]_{AAIW}}{(F_4 + F_5 + F_6)[Nd]_{PDW}}$ and $m_{NPIW} = \frac{F_6[Nd]_{NPIW}}{(F_4 + F_5 + F_6)[Nd]_{PDW}}$ are the concentration weighted mixing ratios of the source waters to the box.

In all simulations, benthic Nd flux and its isotope composition are fixed as today. To solve the model, our default option is to fix the Nd concentration in each box and therefore only Equation (6) is needed. The model can be run with dynamic Nd concentrations if the sink term is specified. In this option, we formulate the sink using a first order rate law:

$$S_{PDW} = k_{PDW}[Nd]_{PDW}, \quad (7)$$

and the rate constant ***k*** is fixed in each box. This is not meant to be a final statement on the geochemical mechanisms of the sink but provides a practical approach to test model sensitivities.

Governing equations of watermass age

The ocean's measured ^{14}C age today (in "true" ^{14}C year, see Table 3.S1), computed using natural ^{14}C concentration, can be approximated within ~50 years as the sum of a circulation age and a preformed age(Koeve et al. 2015). The circulation age is specified to be zero at the surface and subject to mixing and aging by one unit per unit time in the interior. The preformed age is equal to the measured ^{14}C age at the surface and subject to transport but not aging in the interior(Gebbie & Huybers 2012; Khatiwala et al. 2012; Koeve et al. 2015). We adopt the term "*circulation age*" here but note that in the modeling community it is often termed "*ideal age*" or "*mean age*" while in paleoceanography it is often termed "*ventilation age*" (after correction for

preformed properties, although this is often assumed constant). We adopt the term "*preformed age*" to emphasize that all tracers inherit preformed properties while the more commonly used term "*surface reservoir age*" is specific to ^{14}C. The preformed age is equivalent to the "reservoir age" at the surface (except that reservoir age is commonly reported in "conventional" ^{14}C years(Stuiver & Polach 1977) and the preformed age in "true" ^{14}C years).

The interpretation of ^{14}C is more complicated in the paleoceanographic context, because the ^{14}C concentration of the atmosphere was not constant. Therefore, it is necessary to discuss watermass ^{14}C age relative to an atmosphere of fixed ^{14}C age (normally zero) to ensure consistency across time. In our model, we simulate the watermass age with respect to an atmosphere of zero age using this preformed-circulation age decomposition approach(Gebbie & Huybers 2012; Koeve et al. 2015). For the PDW box we have

$$\frac{da_{PDW}}{dt} = \frac{F_4 + F_5 + F_6}{V_{PDW}} \frac{F_4 a_{NAABW} + F_5 a_{AAIW} + F_6 a_{NPIW}}{F_4 + F_5 + F_6} + 1 - \frac{F_4 + F_5 + F_6}{V_{PDW}} a_{PDW}, \quad (8)$$

which can be rewritten in the form of Equation (2) in the Methods section using the aforementioned definitions of water residence time and mixing ratios (except that the mixing ratios no longer contain concentration information).

When comparing modeled watermass age with paleo-^{14}C age records, it is important to make the units consistent: the raw benthic and planktonic ages are reported in conventional ^{14}C years. To convert conventional ^{14}C ages to the true ^{14}C ages requires multiplication by 1.029 (the ratio of the half-lives), i.e., the true ^{14}C age is ~3% older than the conventional age.

The modern distribution of benthic sources and sinks of Nd in the Pacific

When simulating ε_{Nd} in the past we assume the benthic sources are constant in each box equivalent to the modern situation (Methods). Modern observations of Nd sources are rare but given the distribution of Nd concentration and ε_{Nd}, we can use the model to predict a self-consistent distribution of modern sources and sinks assuming

steady state. Nd concentration and ε_{Nd} in each box as well as at the boundaries are specified using modern observations (Table 3.S2). We further specify the isotope compositions of the benthic sources ($\varepsilon_{Nd_{\boldsymbol{B}}}$) assuming they have the isotope compositions the same as modern pore water/core-top authigenic phases. We then solve for the magnitudes of the sources (**B**) and sinks (**S**) in each box. The relevant data and results are presented in Table 3.S2.

In our modern solution, the total benthic Nd flux in the Pacific boxes is 3.8×10^9 g/yr, consistent with the observation-derived estimate of 3.3×10^9 g/yr (Case 1 in Figure 3.S1) discussed earlier. The Nd residence time with respect to benthic flux is ~400 years, consistent with previous estimates(Arsouze et al. 2009; Tachikawa et al. 2003). Benthic source and sink fluxes are on the order of 10 pmol cm^{-2} (seafloor area) yr^{-1} for the North Pacific and AABW boxes, consistent with literature data (Abbott et al. 2015b; Arsouze et al. 2009; Haley & Klinkhammer 2003; Tachikawa et al. 2003). In the AAIW and UCDW boxes these fluxes are on the order of 100 pmol cm^{-2} (seafloor area) yr^{-1}. No measurements of benthic fluxes have yet been made in these regions, but strong benthic source and sink fluxes in these boxes (28ºS-24ºN, 200-3000 m) are consistent with previous arguments that highly weatherable radiogenic materials delivered from the numerous tropical Pacific islands strongly modify seawater ε_{Nd} in this region(Grenier et al. 2013). In our model, the North Pacific boxes that contain our cores are relatively insensitive to the AAIW and UCDW boxes, so our results are robust with respect to such uncertainties.

The modern distribution of watermass ^{14}C age in the Pacific

Using the modern watermass transport in Fig. 3.S4 and boundary conditions in Table 3.S2 we compute the steady state modern distribution of watermass ^{14}C age in the Pacific following the preformed-circulation age decomposition approach. The preformed age is applied as a boundary condition. In the deep Pacific, preformed age is predominantly set up by the Southern Ocean source waters. The modern surface-water reservoir ages of AABW and AAIW are ~1000 years and 700 years respectively(Key et al. 2004). Since our model domain only extends to 28ºS and we

do not model the Southern Ocean, the boundary condition we specify for the South AABW box at 28ºS is necessarily older (1600 years, according to the bomb-corrected GLODAP(Key et al. 2004) database) than the surface reservoir age of AABW, reflecting a combination of aging and mixing of the Southern Ocean watermasses before their transit northward in the deep Pacific. For the surface water of the North Pacific, we use a preformed age of 900 years, consistent with the regional surface reservoir ages calibrated with tephrochronology used in creating the age models of our sediment cores(Davies-Walczak et al. 2014; Praetorius et al. 2015). The results are reported in Table 3.S2.

Transient simulations with other Antarctic-based forcings

In the standard deglacial simulation (Fig. 3.3) we scaled the AABW transport to the rate change of atmospheric CO_2. In Figure 3.4 we report complementary simulations in which we scale the AABW transport to other possible Antarctic forcings, including East Antarctic temperature(Parrenin et al. 2013), West Antarctic temperature(Cuffey et al. 2016) and sea ice (using sea salt sodium ssNa as a sea ice proxy)(WAIS Divide Project Members 2013). We use these simulations to show that our deep ε_{Nd} record is consistent with Antarctic surface buoyancy forcing as a driver of deglacial changes of abyssal circulation in the Pacific and atmospheric CO_2. Compared to the standard deglacial simulation, only the scaling factors applied to the AABW transport were changed.

The Antarctic climate proxies are generally coherent, such that during the deglacial interval CO_2 increased, temperature rose in both East and West Antarctic, while sea ice and/or ice shelf extent decreased (low ssNa) (Fig. 3.4). Consequently, the deep ε_{Nd} simulated using any of these forcings are very similar and all broadly capture the main features of the record, i.e. the rapid negative excursions during the Antarctic warming intervals (Fig. 3.4). However, warming and sea ice (ssNa) retreat in the West Antarctica preceded CO_2 increase and temperature rise in the east. These variables may help to explain the negative ε_{Nd} excursion at the onset of deglaciation (~19 ka) in our deep record that seems unrelated to atmospheric CO_2 change (Fig.

3.2, Fig. 3.4). These early events show that not all circulation changes in the deglacial interval had direct or immediate effects on atmospheric CO_2.

Selection of parameters used in the standard LGM steady-state simulation

We run a set of LGM steady state simulations with the AABW transport scaled to from 0 to doubling of today, and the increase of preformed ε_{Nd} of AABW from 0 to +4.8 ε-units. In these tests, preformed ε_{Nd} of AAIW is fixed to be 1 ε-unit higher than today(Hu et al. 2016a). The results in Fig. 3.S5a show that to explain the increase of LGM ε_{Nd} at our deep site with constant or greater AABW transport it requires the preformed ε_{Nd} of AABW to be implausibly higher than today (>5 ε) than the reported value of 1.8 ε(Hu et al. 2016a). Given this reported increase of the preformed ε_{Nd} of AABW, however, a halving (0.55) of AABW transport would be consistent with our data. This test highlights the competing controls on ε_{Nd} between the conservative component (mixing of preformed ε_{Nd}), and the non-conservative benthic source component. As circulation rate decreases, the benthic exposure time increases and the deep ocean ε_{Nd} becomes less sensitive to the preformed property as the influence of the benthic source prevails.

Following this bottom-up ε_{Nd} constraint on the circulation rate, we next explore the model sensitivity to the preformed ^{14}C age of AABW in the LGM. Simulations show that the LGM deep North Pacific benthic-planktonic age difference would increase nearly linearly with increasing preformed age of AABW (Fig. 3.S5b). Published benthic ^{14}C records from the deep North Pacific, including ours, generally show small LGM-Holocene differences(Broecker et al. 2007; Cook & Keigwin 2015; Lund et al. 2011), at face value suggesting that the AABW preformed and/or circulation age in the LGM cannot be much higher than today. Since our deep ε_{Nd} record indicates that the circulation rate of the deep Pacific was lower in the LGM, we conclude that most likely the LGM preformed age of AABW was slightly younger than today, by ~400 years, to compensate for the increase of circulation age.

The PDW-NPIW exchange in the LGM is best constrained by the ^{14}C rather than the ε_{Nd} record at our intermediate site, because the small LGM PDW-NPIW ε_{Nd} difference means model ε_{Nd} is insensitive to changes in this parameter. Given that the LGM intermediate depth benthic-planktonic age difference is slightly younger (100 years) than the Holocene, our sensitivity tests show that the mixing between PDW and NPIW must have been slightly weaker (0.6) than today (Fig. 3.S5c).

Uncertainty of the LGM ^{14}C data and its influence on the transient simulations

The benthic-planktonic age difference for the LGM used in our study is 1339±132 years (at 20.6 ka in site W8709A-13PC(Lund et al. 2011)). For comparison, the larger Cook and Keigwin compilation of ^{14}C age differences during the LGM (18.4-22 ka)(Cook & Keigwin 2015) excluding outliers is 1393±337 years, consistent with our data. This is also essentially identical to the modern value (1400±280 years) based on the GLODAP bomb-corrected dataset(Key et al. 2004). This comparison indicates that the LGM benthic-planktonic age difference in the deep North Pacific was similar to today.

We use transient sensitivity tests to examine how the uncertainty in the LGM preformed age of AABW influences the model results in the LGM-early deglaciation transition (Fig. 3.S6). We varied both the preformed age anomaly of AABW and the scaling factor applied to AABW transport in the LGM. In these tests we first run steady-state LGM simulations using the various combinations of preformed age and transport of AABW (Fig. 3.S6). We then use these results to initialize transient simulations of the deglacial interval (Fig. 3.3, Methods) using similar parameters except with different LGM initial values.

The uncertainty in the LGM preformed age of AABW does not propagate significantly into the early deglaciation (Fig. 3.S6). Furthermore, even considering the large spread in the LGM benthic-planktonic age dataset, under realistic conditions of AABW transport (from a quarter to doubling of today), high preformed age anomaly (≥1000 years) of AABW in the LGM seems unlikely. To accommodate such high

preformed ages, the deep Pacific circulation must be significant faster (>2) such that the decrease in circulation age can compensate for the increase in preformed age, yet there is little evidence to support this argument. Solely based on ^{14}C one may conclude that the preformed age of AABW in the LGM was most likely within 500 years of today. If the constraint on the LGM AABW transport (half of today) inferred using our ε_{Nd} record is considered, it seems most likely that the AABW preformed age anomaly in the LGM was ~0-500 years lower (Fig. 3.6Sb).

There is no agreement among the existing estimates of Southern Ocean surface reservoir age in the LGM. For example, based on extrapolation of a global LGM ^{14}C dataset using a circulation model, the Antarctic surface reservoir age (>60ºS) was estimated to be ~2000 years(Skinner et al. 2017), about 1000 years higher than today(Key et al. 2004). Alternatively, fitting a circulation model to observations of both $\delta^{13}C$ and $\Delta^{14}C$ in the LGM yielded an estimate of 900~1200 years(Menviel et al. 2016), similar to today's value. The disparities between these estimates seem to result from the fact that changes in preformed age cannot be independently separated from observed watermass ^{14}C data without some *a priori* (and therefore often different) assumption on the circulation itself.

Theoretical calculations have shown that the LGM surface reservoir age might be ~250 years older because of lower pCO_2^{atm}, but this is only true if the surface ocean was in equilibrium with the LGM pCO_2^{atm} and other factors influencing isotope exchange remained constant(Galbraith et al. 2015). Assumption of equilibrium seems unlikely for the Antarctic surface waters, unless watermass transformation in this region was completely ceased. Factors favoring lower Antarctic surface reservoir age in the LGM may include (1) stronger wind(Brady et al. 2012), (2) longer surface water residence time due to stronger stratification(Jansen 2017; Jones et al. 2014), and (3) weak supply of aged water from the abyss due to stronger stratification(Jansen 2017). Increase of ice cover may reduce isotopic equilibration with the atmosphere in the LGM, but if the front of watermass transformation migrated with the ice cover(Ferrari et al. 2014) then this effect might be mitigated. The intricacy of Southern Ocean surface processes makes straightforward prediction

of the reservoir age of Antarctic surface waters difficult. We believe the multi-tracer approach, in which circulation can be separately constrained by non-^{14}C tracers like ε_{Nd} or $\delta^{13}C$, likely yields more realistic estimates of the preformed age of AABW in the LGM.

Model sensitivity to the deglacial preformed ε_{Nd} of AABW and the role of NADW

Here we investigate the sensitivity of modeled deglacial North Pacific data to the preformed ε_{Nd} of AABW, which is a boundary condition in our model. Published data in the South Pacific are generally consistent(Basak et al. 2018; Elderfield et al. 2012; Hu et al. 2016a; Molina-Kescher et al. 2016; Noble et al. 2013) (Fig. 3.S7c), but given the scatter in the data it is best to analyze the model sensitivity. We also consider whether deglacial variability of NADW, via its potential influence on the preformed ε_{Nd} of AABW, may have affected our North Pacific deglacial records (Fig. 3.S7a-b).

We run three scenarios of deglacial sensitivity tests (Fig. 3.S7d). In scenario 1 the deglacial preformed ε_{Nd} of AABW is fixed at today's value of -7.9, serving as a control run. In scenario 2 the AABW preformed ε_{Nd} decreases linearly by 1.8 ε from 17.5 to 11 ka(Hu et al. 2016a), as the South Pacific data suggest and used in our standard deglacial simulation (Methods). In scenario 3 we consider possible variability of the preformed ε_{Nd} of AABW related to the change of NADW. Some South Atlantic deep ε_{Nd} records(Piotrowski et al. 2005), but not all of them(Skinner et al. 2013), were interpreted to reflect abrupt millennial changes associated with the Atlantic Meridional Overturning Circulation(McManus et al. 2004). The preformed ε_{Nd} in this hypothetical scenario is scaled to the North Atlantic $^{231}Pa/^{230}Th$ record, such that when the NADW formation was weak the AABW preformed ε_{Nd} became more positive. Under this scenario we run two experiments using different scaling factors (Fig. 3.S7d). We consider the strong gains case to be unrealistic but use it to test model sensitivity. Apart from this boundary condition, these tests were all run with the same parameter choice as in the standard deglacial simulation.

As shown in Fig. 3.S7e, the constant preformed ε_{Nd} scenario (scenario 1) overestimates the variability in our record, particularly in the early deglaciation, but the main transient features are preserved. This supports our argument that deep Pacific ε_{Nd} is not sensitive to the change in the AABW preformed property under reasonable circulation rate scenarios.

If our deep Pacific ε_{Nd} record mainly reflects changes of the preformed ε_{Nd} of AABW controlled by NADW formation, we would expect the deep Pacific ε_{Nd} to increase during the Heinrich Stadial 1 and Younger Dryas events, as NADW was weaker at these times. This prediction, however, is contradicted by our records: these intervals rather saw rapid negative excursion of ε_{Nd} in the deep North Pacific. Indeed, the scenario of scaling the AABW preformed value to North Atlantic $^{231}Pa/^{230}Th$ record significantly underestimates the variability in our deep record, as it counterbalances the influence of the changes in AABW transport. Only by increasing deglacial AABW transport more than what is already done in our standard simulation (Fig. 3.3) would it be possible to reproduce our data under this scenario (scenario 3). From these sensitivity tests, we conclude that the deglacial variability of the AABW preformed ε_{Nd}, though possibly affected by NADW, had little influence on our deep North Pacific record.

Model sensitivity to deep water formation in the North Pacific

There is no significant deep water formation in the subpolar North Pacific today, because surface salinity is so low that deep convection cannot occur even when surface temperature is close to the freezing point(Emile-Geay et al. 2003; Warren 1983). Instead, a relatively weak intermediate water, NPIW, is formed in the Sea of Okhotsk and subpolar regions, and subsequently subducts in the Oyashio-Kuroshio confluence(Talley et al. 2011). It has often been speculated that the native North Pacific overturning cell might have been stronger during the last ice age, and a variety of hypotheses suggested either more expansive NPIW or full-scale deep convection analogous to the modern North Atlantic(Matsumoto et al. 2002; Okazaki et al. 2010; Rae et al. 2014). The LGM and early deglaciation are two intervals often postulated

as being candidates for such changes in circulation, but these claims remain controversial(Jaccard & Galbraith 2013).

For example, one such study suggested stronger NPIW production in the Bering Sea during the LGM, arguing that highly radiogenic ε_{Nd} in authigenic phases can only result from stronger intermediate/deep water formation in the North Pacific, as only in this region it seems possible to form a watermass with such radiogenic preformed (i.e., surface water) ε_{Nd}(Horikawa et al. 2010). However, we now know that distinct bottom water ε_{Nd} can develop that is not related to mixing of preformed properties(Abbott et al. 2015a; Du et al. 2016; Howe et al. 2016c), and therefore this argument is not necessarily true.

On the other hand, deep water formation in the North Pacific during the LGM seems highly unlikely given that there is little evidence that glacial deep benthic-planktonic ^{14}C age difference was significantly younger than today(Cook & Keigwin 2015). In contrast, there is no consensus even regarding the sign of circulation change inferred from benthic ^{14}C age during the deglaciation(Lund et al. 2011; Okazaki et al. 2010; Rae et al. 2014).

We use model sensitivity tests to examine the response of intermediate and deep water ε_{Nd} and ^{14}C to increasing NPIW/local deep water formation.

We first examine how the intermediate and deep records should respond to North Pacific deep-water formation in the LGM. Model water fluxes associated with the NPIW box, F7 and F6 (Fig. 3.S4b), are set to be equal, and we increase these fluxes to mimic deep water formation. We compute the steady-state solutions at different deep-water formation rates (Fig. 3.S9a, b). Considering that the North Pacific is twice as voluminous as the North Atlantic, deep water formation here need to reach ~40 Sv to possibly have the equivalent influence on benthic exposure time and ^{14}C age as today's NADW(Talley 2003).

We further consider the possibility that the preformed ε_{Nd} of the North Pacific source water might have been different in the past. We use -3.3 as the modern North

Pacific surface preformed ε_{Nd} in our standard model (Table 3.S2), derived from published dataset in the surface subpolar Northwest Pacific (>35ºN, <180ºE, <200 m)(van de Flierdt et al. 2016) where intermediate water subducts today. Considering the distribution of modern surface seawater and lithogenic ε_{Nd} from the possible intermediate/deep water formation regions (Sea of Okhotsk and Bering Sea) in the subpolar North Pacific(Amakawa 2004; Asahara et al. 2012; van de Flierdt et al. 2016; VanLaningham et al. 2009; Yasuda et al. 2014), we choose 3.3, 0, -3.3 (modern) and -6.6 as hypothetical LGM preformed ε_{Nd} of the North Pacific source water in our sensitivity tests. We do not consider 3.3 and -6.6 as necessarily realistic values but use them to explore the parameter space. Except the preformed ε_{Nd} and the formation rate of deep water in the North Pacific, all other parameters in the model sensitivity tests remain the same as the modern case.

If deep convection happened in the North Pacific at a style like the modern North Atlantic, we would expect its surface reservoir/preformed age to be much smaller than today (~900 years). We set this age to be 500 years in these simulations, similar to the modern North Atlantic(Key et al. 2004). The choice of this surface reservoir/preformed age, however, has no effect on the modeled benthic-planktonic age difference, because when the deep and surface waters of the North Pacific are derived from the same source, the surface reservoir/preformed age is subtracted out in the benthic-planktonic age difference.

None of the simulated scenarios that include North Pacific-source watermass formation larger than today agrees with our ε_{Nd} records for the LGM, as these simulations yield stronger or similar ε_{Nd} changes in the intermediate record than in the deep record (Fig. 3.S9a), opposite the pattern in our data (Fig. 3.2). A significant increase of intermediate water production/deep water formation will also lead to much lower benthic-planktic ^{14}C age differences at both intermediate and deep North Pacific in the LGM (Fig. 3.S9b), and this too is inconstant with published records(Davies-Walczak et al. 2014; Lund et al. 2011) which have the LGM benthic-planktonic age differences like today's (Fig. 3.S6).

We next examine how the intermediate and deep records would respond to North Pacific deep-water formation in the early deglaciation. We initialize these simulations using our standard LGM steady-state solution. We ran the model in transient mode through the early deglacial transition, only changing F7 and F6 and the North Pacific preformed ε_{Nd}. In Figure 3.S10c-d we report the differences between model results after 3000 years and the LGM, which can be compared to the difference between 18 ka and 15 ka in our records.

Again, all model scenarios suggest a stronger or similar response of ε_{Nd} at intermediate depth (Fig. 3.S9c), in conflict with our observations that show greater variance at the deeper site (Fig. 3.2). Strong deep-water formation would also require decreasing benthic-planktonic ^{14}C ages at both intermediate and deep sites, in contrast to the large and transient increase of these ages at our sites with the exception of the 16-17 ka interval (Fig. 3.S9d).

Admitting that if the North Pacific surface preformed ε_{Nd} were the same as today, small vertical ε_{Nd} gradient between our intermediate and deep sites would mean that ε_{Nd} is not very sensitive to vertical mixing in the early deglaciation. Under this scenario, increasing NPIW formation is possible between 16-17 ka during which intermediate water ^{14}C age reduced(Okazaki et al. 2010; Rae et al. 2014) (Fig. 3.3h). However, NPIW cannot be very strong (<10 Sv), as our model sensitivity tests show that the reduction of deep water ^{14}C age should be greater than that of the intermediate water with such strong local deep water production (Fig. 3.S9), yet in the Northeast Pacific we find that in this short interval the deep-intermediate water ^{14}C age gradient actually increased (Fig. 3.3f).

Model sensitivity to the formulation of Nd concentration

By default, our model is run with fixed Nd concentrations in each box. Here we compare this option with the option of running Nd concentrations dynamically. In this dynamic option, the Nd sink term is specified using equation (7), and the rate constants ($\boldsymbol{k}$) are fixed and computed as the ratio of modern sinks to Nd concentrations in each box (Table 3.S2); otherwise this run is the same as the

standard deglacial simulation (Figure 3, Methods). The modeled Nd concentrations vary within 25% at the intermediate depth site and 10% and at the deep site (Fig. 3.S10). By allowing Nd concentrations to change, the "buffering capacity" of the Nd system increases, such that the variabilities of ε_{Nd} are slightly reduced. However, the differences (<0.2) between fixed and dynamic Nd runs are smaller than the analytical uncertainty and therefore we consider the assumption of fixed Nd concentrations reasonable.

In summary, we have tested a variety of parameter combinations and hypotheses that previous studies have proposed to explain deglacial North Pacific circulation. We found these hypotheses inconsistent with our data; either with respect to ε_{Nd} or ^{14}C, or both. Therefore, we conclude our interpretation, based on the parameter choice in our standard deglacial simulation (Fig. 3.3) with primary circulation changes emanating from Antarctica, is the most reasonable one.

Figure 3.S1. The distribution of benthic Nd flux in the Pacific and its relationship to sediment redox state.

a, Depth dependence of seafloor area(Menard & Smith 1966). b, Depth dependence of benthic Nd flux. Data are grouped into regions: Oregon Margin (OR)(Abbott et al. 2015b), California Margin (CAL)(Haley & Klinkhammer 2003), British Columbia Margin (BC)(German & Elderfield 1989) and Peru Margin (PR)(Haley & Klinkhammer 2003). Existing data are limited to <4000 m, and yield a statistically significant (p=0.038) relationship of $y=5x+8.3$, where y is the flux in pmol cm^{-2} yr^{-1} and x is depth in km. To fill the data gap >4000 m we consider three hypothetical cases. (1) the benthic flux is uniform with respect to depth (13.9 pmol cm^{-2} yr^{-1}, the mean value of the data); (2) the depth dependent relationship ($y=5x+8.3$) applied to <4000 m and a constant value applied to >4000 m; (3) same as (2) but assuming zero flux >4000 m. **c**, The depth dependence of area integrated benthic Nd flux. **d**. Cumulative percentage of depth and area integrated benthic flux (integration starting from sea-level). Note that in all cases deep sea sediments dominate the integrated benthic flux because it is mainly controlled by the distribution of seafloor area. Relationship between benthic flux and redox state represented by particulate organic carbon (POC) rain rate (**e)** and bottom water O_2 concentration (**f**). Neither correlation is significant (p=0.21 and 0.76 respectively), suggesting that the benthic flux does not depend on sediment redox state(Abbott et al. 2015b,a).

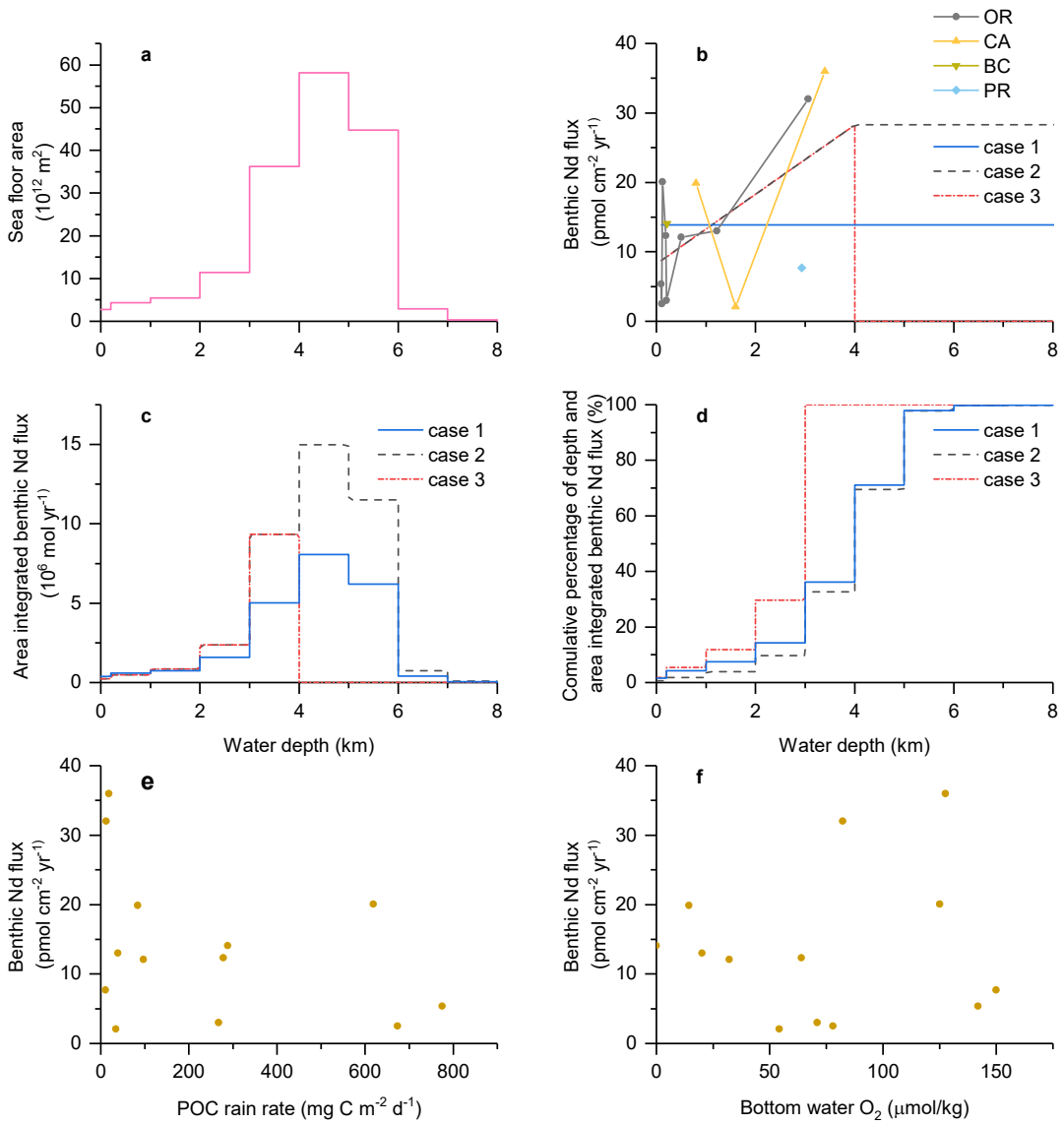

Figure 3.S1. The distribution of benthic Nd flux in the Pacific and its relationship to sediment redox state.

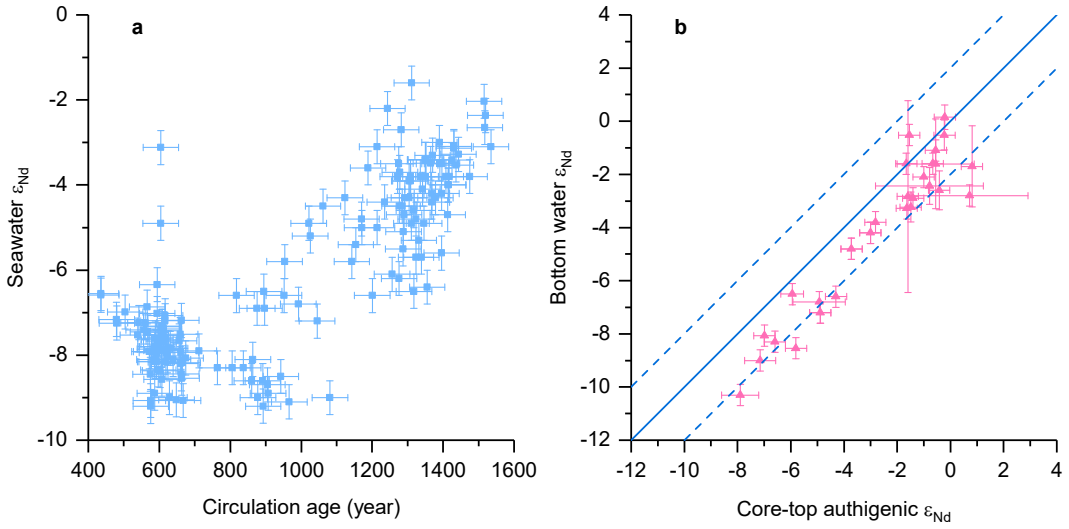

Figure 3.S2. Relationship between (a) modern seawater ε_{Nd} and modern circulation age, (b) core-top authigenic ε_{Nd} and modern bottom water ε_{Nd} in the Pacific.

The relationship between core-top authigenic ε_{Nd} and modern circulation age is plotted in Figure 3.1c. The circulation age(Gebbie & Huybers 2012), or ideal age, is modeled based on ^{14}C and interpolated to the locations of ε_{Nd} data. It is assumed to have an uncertainty of 50 years. Seawater data are from published compilations(Lacan et al. 2012; van de Flierdt et al. 2016). We made a core-top authigenic ε_{Nd} compilation which was different from the recently published one(Tachikawa et al. 2017) in that (1) all decarbonated leach data are excluded, as it is highly likely that decarbonation leads to significant lithogenic contamination(Blaser et al. 2016; Kraft et al. 2013; Wilson et al. 2013; Wu et al. 2015); (2) when leach and foraminifera/fish debris data are both available from a site, only the latter are included; (3) only the top datum is collected when longer Holocene record is available. In making b we divided the ocean into $5^{o}\times5^{o}$ boxes, with thickness increasing from 200 m from the surface to 600 m at depth. Seawater and core-top authigenic data are grouped into these boxes, and when seawater data fall into boxes that contain core-top data they are considered bottom water samples and resulting pairs are plotted. The solid line in b represent the 1:1 line and the dashed lines the ±2 ε envelope. Note that the core-top authigenic ε_{Nd} is consistently more radiogenic that bottom water. All ε_{Nd} data are assumed to have 2σ uncertainty of 0.4, and in b the variance in each ocean box is also considered.

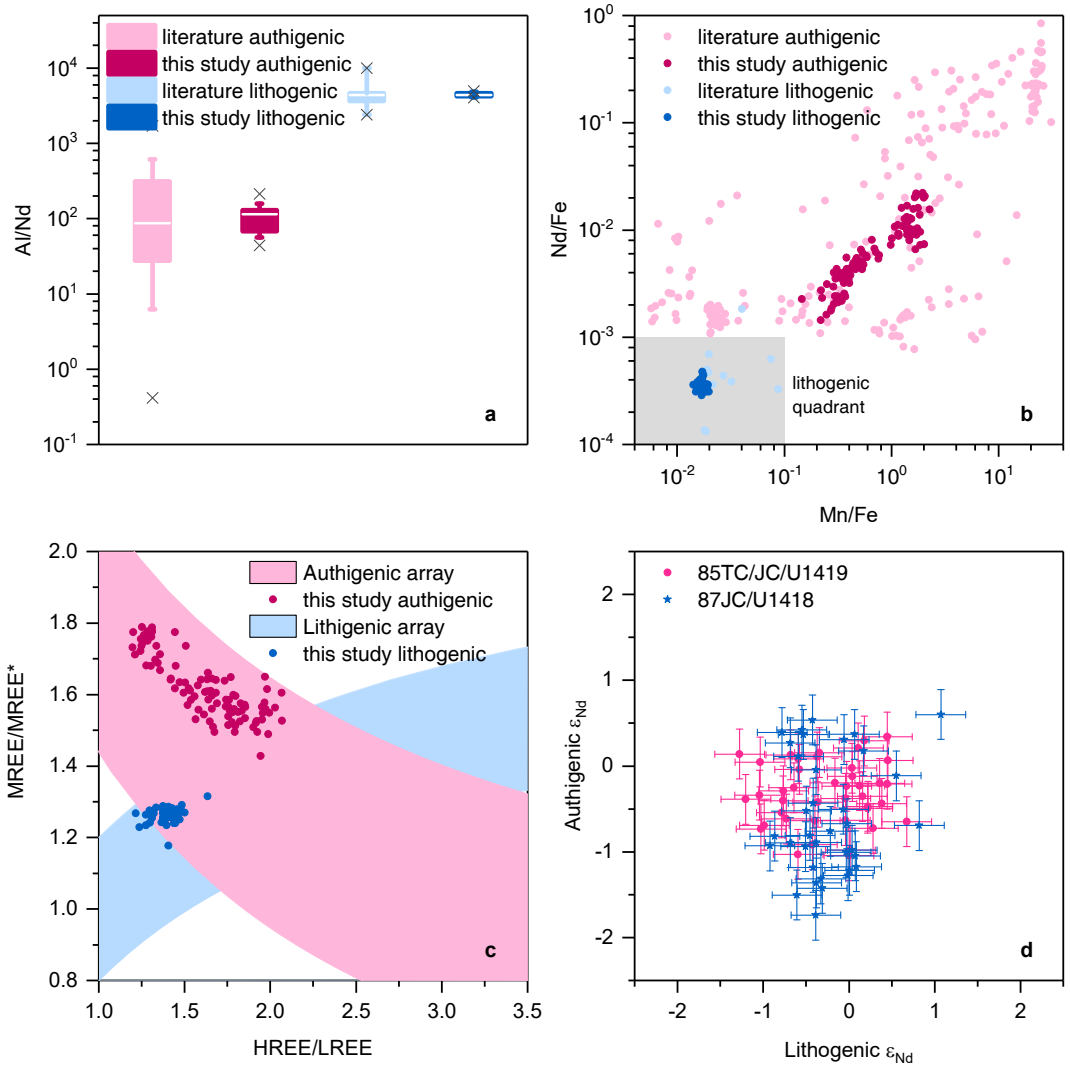

Figure 3.S3. Geochemical evidence of the validity of the method used to generate authigenic ε_{Nd} records in this study.

We provided tools to examine whether bulk sediment leach ε_{Nd} truly records the authigenic components without lithogenic contamination in our published methodology study(Du et al. 2016). These tools distinguish authigenic from lithogenic phases based on their geochemical compositions. Evidence to support the validity of our leaching method includes **a**, low Al/Nd ratios of the authigenic fractions. **b**, high Nd/Fe and Mn/Fe ratios of the authigenic fractions. **c**, the Rare Earth Element patterns of the authigenic fractions follow the Authigenic array instead of the Lithogenic array. MREE/MREE*= 2[Tb + Dy]/[Pr + Nd + Yb + Lu] and HREE/LREE=[Yb + Lu]/[Pr + Nd], using PAAS normalized concentrations. **d**, the lack of correlation (p=0.5) between authigenic and lithogenic (bulk sediment) ε_{Nd}.

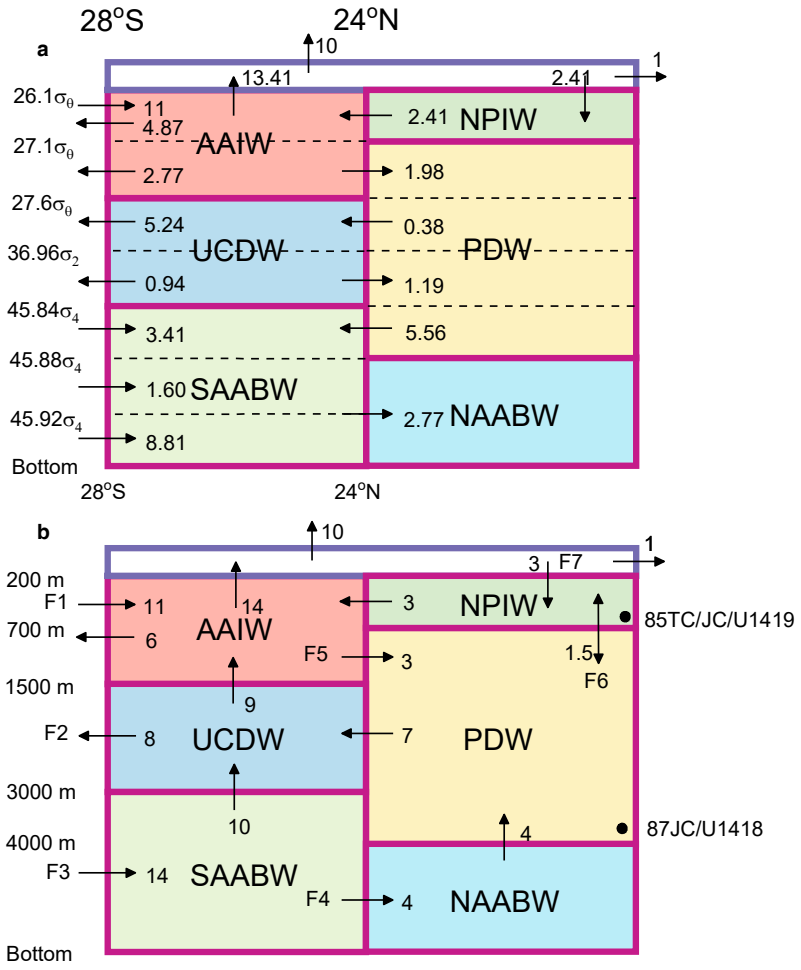

Figure 3.S4. Box model design.

a, the box inverse model of Talley which is defined using density layers and transport across 28°S and 24°N hydrographic sections(Talley 2003, 2008). b, the 6-box model used in this study and site locations. Note that only 7 water fluxes, i.e. F1~F7, are independent. The unit for these fluxes is Sverdrup. These boxes represent: Antarctic Intermediate Water (AAIW), Upper Circumpolar Deep Water (UCDW) and Southern Antarctic Bottom Water (SAABW) between 28°S and 24°N, and North Pacific Intermediate Water (NPIW), Pacific Deep Water (PDW) and North Antarctic Bottom Water (NAABW) north of 24°N. These labels are used heuristically and do not imply that the box boundaries can be assigned precisely to specific physical watermass boundaries, Nevertheless, this simple construct captures the basic water fluxes in the modern Pacific and can be used to illustrate simple but plausible past scenarios. We modified the water fluxes given by Talley slightly to better fit the modern distributions of ε_{Nd} and ^{14}C age. Our deep site 87JC/U1418 lies within the PDW box and the intermediate site 85TC/JC/U1419 lies within the NPIW box.

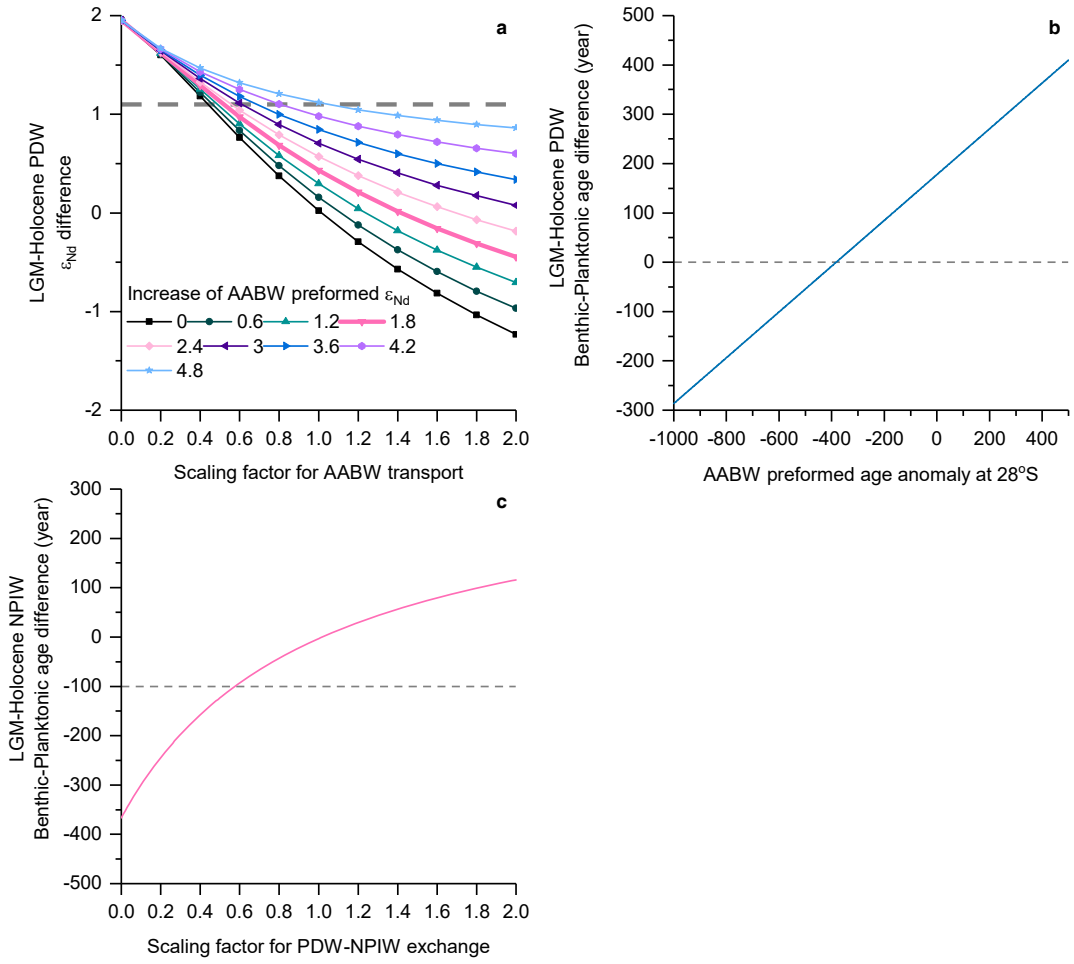

Figure 3.S5. Selection of model parameters for the LGM steady state solution using sensitivity tests.

a, Simulated LGM-Holocene differences of ε_{Nd} in the PDW box with different AABW preformed ε_{Nd} anomalies and scaling factors applied to AABW transports. The thick pink line indicates the model tests using an increase of preformed value (1.8) reported in literature(Hu et al. 2016a). **b,** Dependence of LGM-Holocene benthic-planktonic age difference in the PDW box on the preformed age of AABW at the southern boundary of our box model. **c,** Dependence of LGM-Holocene benthic-planktonic age difference in the NPIW box on the scaling factors applied to PDW-NPIW exchange. Dash lines indicate the observed LGM-Holocene differences in our records.

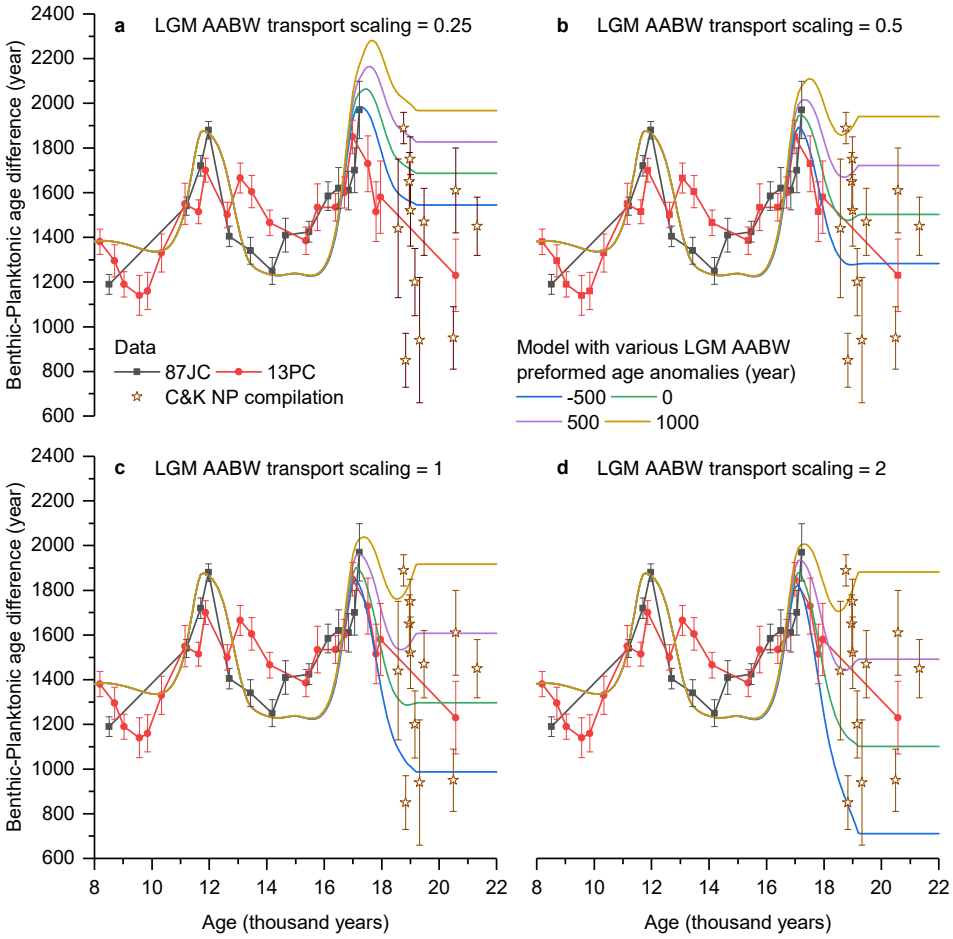

Figure 3.S6. Model sensitivity tests on how the preformed age and transport of AABW affect the benthic-planktonic age difference in the deep North Pacific during the LGM, and how the uncertainty in LGM ^{14}C data affects deglacial transient simulations.

a-d show the model results applying four scaling factors to AABW transport, and in each case the model was run with four scenarios of preformed age anomaly of AABW in the LGM. Modeled results are compared to data from EW0408-87JC and W8709-13PC(Lund et al. 2011), and also the North Pacific LGM data compilation from Cook and Keigwin(Cook & Keigwin 2015). The tests suggest that the preformed age of AABW during the LGM was likely within 500 years of today in accordance with these data, and much larger anomalies (>1000 year) are unlikely, as it would require unreasonable reduction of circulation age (faster circulation) to compensate for the increase of preformed age. Further, the uncertainty in the estimates of the preformed age of AABW during the LGM has little effect on the deglacial transient simulations.

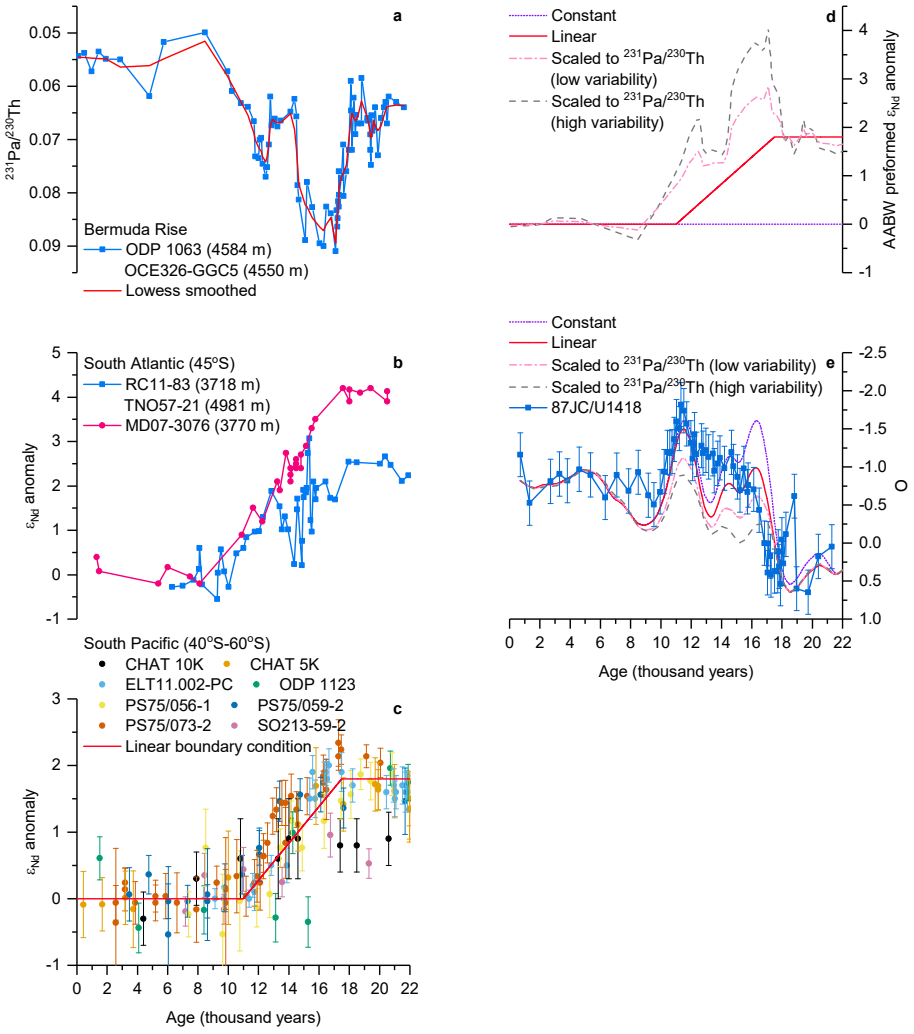

Figure 3.S7. Sensitivity tests on how deglacial evolution of the preformed ε_{Nd} of AABW, possibly related to changes of NADW formation, affects simulated deep North Pacific ε_{Nd}.

a, North Atlantic records of $^{231}Pa/^{230}Th$, a proxy for NADW strength(Böhm et al. 2015; McManus et al. 2004). b, South Atlantic ε_{Nd} records plotted as anomalies relative to the Holocene(Skinner et al. 2013; Piotrowski et al. 2005). c, South Pacific ε_{Nd} records plotted as anomalies relative to the Holocene(Basak et al. 2018; Elderfield et al. 2012; Hu et al. 2016a; Molina-Kescher et al. 2016; Noble et al. 2013). d. Different schemes of deglacial preformed ε_{Nd} of AABW used in sensitivity tests. We consider the following scenarios: (1) constant, (2) fixed LGM-Holocene difference and linear change in between, as seen in the South Pacific records and used in our standard simulation (Methods), and (3) changes scaled to North Atlantic $^{231}Pa/^{230}Th$ records. e, Results of these tests compared to our deep North Pacific record.

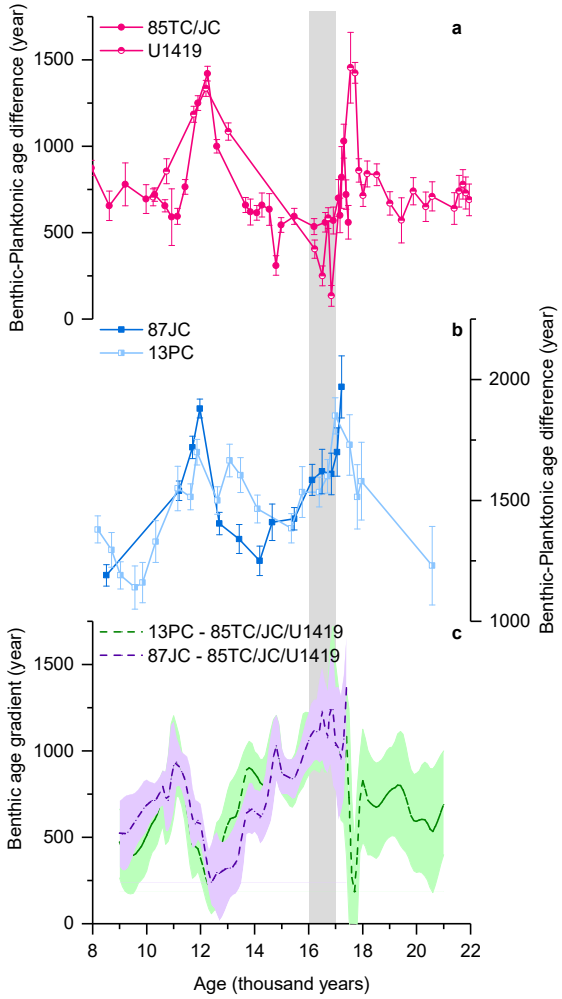

Figure 3.S8. Radiocarbon data from the Northeast Pacific.

a. Benthic-planktonic age difference at intermediate-depth site EW0408-85TC/JC/U1419, same as in Figure 3.3h. **b.** Benthic-planktonic age at deep site EW0408-87JC and W8709A_13PC(Lund et al. 2011), same as in Figure 3.3d. **c.** The deep-to-intermediate benthic age gradients between EW0408-87JC and EW0408-85TC/JC/U1419, and between W8709A_13PC and EW0408-85TC/JC/U1419, same as in Figure 3.3f. The shaded region marks the interval (17-16 ka) during which benthic-planktonic age difference at the intermediate-depth site decreased to values smaller than today, suggesting possible increase of intermediate water formation, but at the same time the deep site benthic-planktonic age difference remained higher than today (despite the reduction) and the deep-to-intermediate benthic age gradients increased to the highest values in the last 22 ka. This suggests that the effect of the possible increase of intermediate water formation did not reach the deep sites.

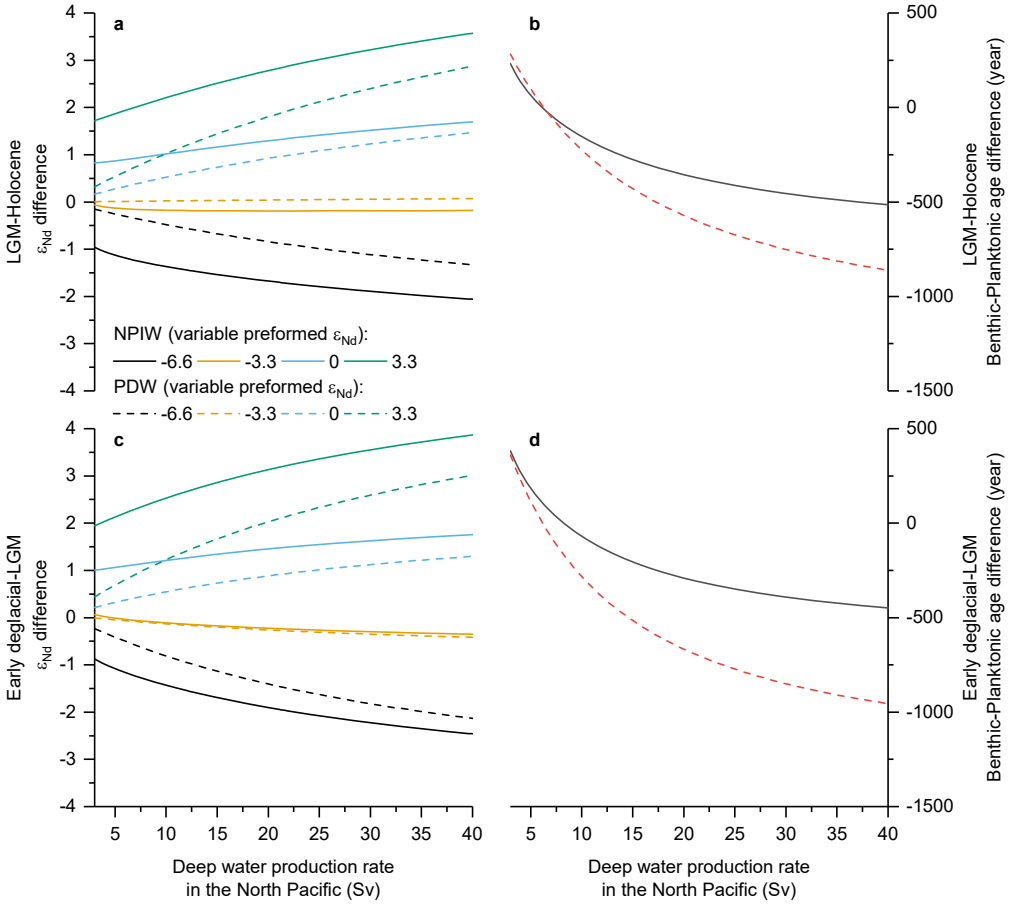

Figure 3.S9. Model sensitivity tests on how enhanced intermediate water formation or formation of local deep water in the North Pacific during the LGM and early deglaciation would affect North Pacific ε_{Nd} and watermass age records.

In a-b we test how stronger intermediate/deep water formation during the LGM affects the North Pacific records. In c-d we test how stronger intermediate/deep water formation during the early deglaciation affects the North Pacific records. a, The dependence of LGM-Holocene steady state differences of ε_{Nd} in the NPIW (solid lines) and PDW (dashed lines) boxes on the formation rate of intermediate/deep water and surface preformed ε_{Nd} (-6.6 ~ +3.3) in the North Pacific. b, The dependence of LGM-Holocene steady state differences of benthic-planktonic age difference in the NPIW (solid line) and PDW (dashed line) boxes on the formation rate of intermediate/deep water. c, Same as in a but for the transient early deglaciation-LGM differences. d, Same as in b but for the transient early deglaciation-LGM differences.

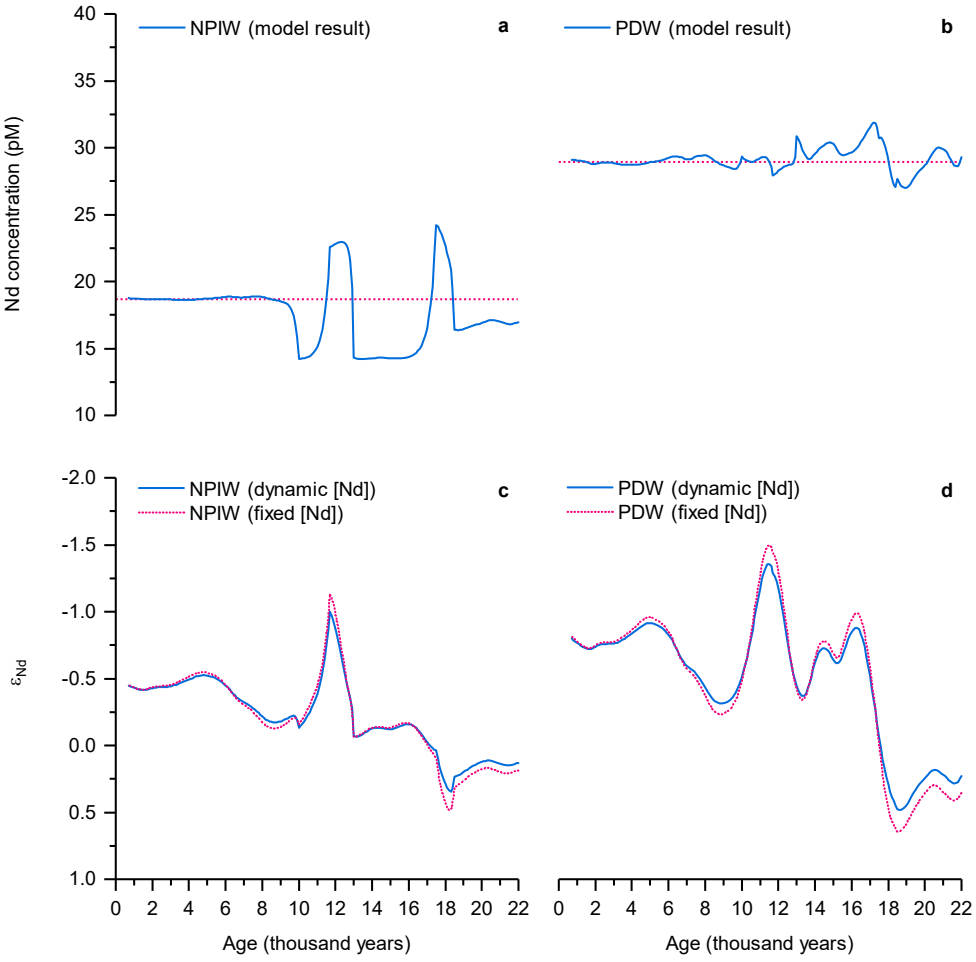

Figure 3.S10. Deglacial transient simulations with dynamic Nd concentrations.

Modeled Nd concentrations in the **a** NPIW and **b** PDW boxes. Dashed lines indicate modern concentrations in these boxes which are used in deglacial transient simulations with fixed Nd concentrations. Simulated authigenic ε_{Nd} in the **c** NPIW and **d** PDW boxes, with dynamic Nd concentrations (solid lines) and fixed concentrations (dashed lines). Note that running Nd concentrations dynamically reduces the variability of modeled ε_{Nd}, but differences are smaller than analytical uncertainties.

Table 3.S1. Radiocarbon terminology used in this study

Term	Definition	Comment
Natural ^{14}C	Pre-anthropogenic ^{14}C concentration unaffected by fossil fuel ^{14}C and nuclear ^{14}C. Often reported as $\Delta^{14}C$.	Few pre-anthropogenic ^{14}C measurements exist. In this study, we rely on the bomb-corrected background ^{14}C in seawater from the GLODAP project (Key et al. 2004).
Conventional ^{14}C years	The unit when ^{14}C age is computed using the Libby half-life of 5568 years.	This is the unit for reporting raw ^{14}C age measurements, such as the raw benthic and planktonic ages.
True ^{14}C years	The unit when ^{14}C age is computed using the true half-life of 5730 years.	This is the unit to be used when using ^{14}C to estimate circulation age.
Surface reservoir age	The natural ^{14}C age of surface ocean water, which is generally non-zero.	This age should be reported in the conventional ^{14}C year unit(Stuiver & Polach 1977). The reservoir age applied to planktonic foraminifera may be equal to or larger than the surface reservoir age, if the planktonic foraminifera calcify in sub-surface habitats.
Calendar age	The age results from ^{14}C calibration, during which the effects of non-constant atmospheric ^{14}C concentration and reservoir age are corrected to yield the actual age of the samples.	The raw ^{14}C age and the surface reservoir age used in calibrations must be in conventional ^{14}C years. Calendar age can also be determined using other absolute dating techniques.
Benthic reservoir age	The natural ^{14}C age of deep ocean water at the growth site of benthic foraminifera at the time they were alive, which is generally non-zero	This age should be reported in the conventional ^{14}C year unit like the surface reservoir age(Stuiver & Polach 1977).
Benthic-planktonic age difference	The age difference between contemporaneous benthic and planktonic foraminifera measured in the same sample.	If calculated using the raw ^{14}C age its unit is the conventional ^{14}C year.
Preformed ^{14}C age	A watermass in the ocean can be decomposed to a mixture of some end-member surface source waters. The weighted average of the ^{14}C ages of these end-members is the preformed ^{14}C age of this watermass.	For a single unmixed watermass, the preformed age is equivalent to the reservoir age (surface or near-surface) at its site of formation, except that its unit is the true ^{14}C year when used in conjunction with the circulation age. Preformed age is tracer-specific.
Circulation age	The time of a watermass elapsed since its last contact with the atmosphere.	Ideal or mean age is the name commonly used in modeling literature. In paleoceanographic literature it is equivalent to ventilation age if these later ages are corrected for preformed age. Circulation age is not specific to a tracer, though it needs to be derived from tracer distributions.
^{14}C age with respect to an atmosphere of zero age	The ^{14}C age of a water or fossil sample corrected to a contemporaneous atmosphere of zero ^{14}C age.	In modern ocean this is equal to the natural ^{14}C age in true year unit (Cook & Keigwin 2015; Koeve et al. 2015), since by convention the natural ^{14}C age of modern atmosphere is zero. In the past, because the ^{14}C age of the atmosphere was not zero relative to today, the measured ^{14}C age of a sample need to be corrected to an atmosphere of fixed ^{14}C age to make paleo-^{14}C age data comparable. At steady state this age can be approximated by the sum of the preformed age and circulation age (Koeve et al. 2015).

Table 3.S2. Configuration of the box model, the modern state and boundary conditions.

The columns are the volume, the seafloor area, modern Nd concentration ([Nd]) and isotope composition (ε_{Nd}), the Nd isotope composition of the benthic flux (ε_{Nd}_B), the magnitudes of benthic flux (B) and sink (S) normalized to the total seafloor area exposed in each box, and the modern ^{14}C age. The boundary conditions are specified at 28oS and the surface of the North Pacific. Box volumes and seafloor areas are estimated using hypsometry curves (de Lavergne et al. 2016; Menard & Smith 1966). Modern observations of [Nd] and ε_{Nd} are from compiled database (80). The numbers used in the model are chosen to be close to the average values in each box as well as giving reasonable results to benthic sources and sinks, and they lie within the range of observed values in each box. The values of ε_{Nd}_B are chosen based on a compiled database of core-top authigenic ε_{Nd}, and they also lie within the range of observed values in each box.

Box	Volume (10^{15} m^3)	Seafloor area (10^{12} m^2)	[Nd] (pM)	ε_{Nd}	ε_{Nd_B}	B (pmol cm^{-2} yr^{-1})	S (pmol cm^{-2} yr^{-1})	^{14}C age (yr)
AAIW	70	2.3	9	-3.1	0	204	378	1498
UCDW	98	4.7	19	-3.4	-1.0	229	326	2178
SAABW	112	47.5	26	-6.5	-3.4	11	10	1854
NPIW	36	1.4	19	-3.2	-1.0	21	8	1647
PDW	99	12.6	29	-3.5	-1.0	16	14	2197
NAABW	45	39	47	-4.5	-2.5	8	2	2210
AAIW at 28°S			10	-6.7				700
SAABW at 28°S			25	-7.9				1600
North Pacific surface water			10	-3.3				900

Appendix C: Supplementary Materials for Chapter 4

Data collection

We created four subsets of the authigenic ε_{Nd} collection: a deglacial time-series dataset, a Holocene time-slice dataset, an LGM time-slice dataset, and a HS1 time-slice dataset. The deglacial time-series dataset includes records that satisfy two criteria: (1) it spans 10 to19 ka, and (2) its average resolution is 1 ka or higher (i.e., the record must have at least 9 data points). Incomplete and very low resolution records were therefore excluded. The Holocene dataset includes authigenic data that either have numerical ages in the range of 0 to 10 ka or are reported as Holocene time-slices. The LGM dataset included authigenic data that either have numerical ages in the range of 19 to 23 ka or are reported as LGM time-slices. The HS1 dataset includes authigenic data that have numerical ages in the range of 15 to 17 ka. The deglacial dataset are used in principal component analysis (see Methods). The Holocene, LGM and HS1 datasets are used to create time-slice section plots in Figure 2, in which we use the mean authigenic ε_{Nd} values at each site in each time-slice.

Detrital sediment ε_{Nd} data were processed similar to the authigenic ε_{Nd} dataset described above, except the following cases. (1) In addition to a Holocene dataset we also included a core-top (defined as within 10 cm of the sediment-water interface) dataset of detrital ε_{Nd} with no age constraints, as few authors made age models for their detrital ε_{Nd} data; In typical oceanic condition (1 cm/kyr sedimentation rate for the deep ocean) the core-top data should be of Holocene age. The core-top and the Holocene detrital datasets are used to create Figure 3a. (2) A deglacial detrital ε_{Nd} record was included as long as it spans 10 to 19 ka and no resolution requirement was made, because few continuous deglacial detrital ε_{Nd} record exist; (3) A Heinrich Layer 1 (HL1) - instead of a HS1 - detrital ε_{Nd} dataset was made, because the stratigraphic constrains on these data were made based on sedimentological evidence rather than numerical dating, as is typical of the studies on detrital ε_{Nd} of HLs(Hemming 2004). These HL detrital ε_{Nd} data are from the subpolar North Atlantic (north of 40^{o}N), mainly in the classically defined ice rafted detritus (IRD) belt (40^{o}N~50^{o}N) but also extending north close to Iceland(Hemming 2004).

In our data collections, we only included sites that are deeper than 500 m. Variabilities in authigenic and detrital ε_{Nd} records from shallower sites are more likely affected by source variabilities rather than circulation. Such shallower sites are also scarce. We also avoided data from the marginal seas where detrital provenance may vary and differ from the open ocean. We did not include the Arctic Ocean because of data scarcity. Our focus is on the global distribution of ε_{Nd} in the main ocean basins (Pacific, Indian and Atlantic, including their Southern Ocean sectors), focusing on intermediate and deep waters.

Box model set up

The seafloor area and volume in each box are determined using the ETOPO1 bathymetry(Amante & Eakins 2009, p. 1). Modern seawater Nd concentrations ([Nd]) and ε_{Nd} of each box are determined using the compiled seawater dataset(Lacan et al. 2012; Tachikawa et al. 2017; van de Flierdt et al. 2016) (Methods). Rather than using the arithmetic means of the data in each box, which is biased toward the surface ocean because of uneven sampling, we used volume-weighted means of [Nd] and ε_{Nd}. To calculate the volume-weighted means we first binned seawater [Nd] and ε_{Nd} data into 500 m depth intervals and computed the mean values for each depth bin. We then binned the ocean volume derived from ETOPO1 bathymetry into the same depth intervals and calculated the volumes in each bin. Because seawater (authigenic and detrital as well) data rarely come from below 5000 m, the depth bins we used did not extend beyond 5000 m. The weights for each depth bin were therefore calculated as the fraction of the ocean volume in that bin with respect to the summed volume of all the bins above 5000 m. This ensures that the weights sum to one and assumes that the ocean below 5000 m has the same [Nd] and ε_{Nd} as the volume-weighted means of the ocean above 5000 m. This calculation was done for each ocean box.

Our box model has three *external* sources: dust flux, dissolved river flux and the sedimentary source (Methods). It also has one *external* sink: scavenging, which is parameterized as a first order rate law of [Nd] in the ocean box, and the ε_{Nd} of the scavenging sink is the same as seawater in the box(Du et al. 2018).

Dust Nd flux in each box was calculated using the gridded global annual mean dust flux in ref.(Mahowald et al. 2005), which was created using observations and global atmospheric models. We calculated the total dust flux entering the surface of each ocean box, and derived the corresponding Nd flux assuming 20 ppm Nd in dust and 2% soluble fraction(Tachikawa et al. 2003). The ε_{Nd} of dust flux in each ocean box followed ref.(Tachikawa et al. 2003). Dissolved river Nd fluxes and their ε_{Nd} were from ref.(Goldstein & Jacobsen 1987).

In each ocean box there are three unknows: the magnitude of the sedimentary source, the ε_{Nd} of the sedimentary source and the scavenging rate constant (k). Among these unknowns, the sedimentary source is better constrained by existing data, and since we are interested in the global budget and its first-order change, we assume that the sedimentary source is uniform globally but allow the ε_{Nd} of the sedimentary source and the scavenging rate constant k to differ in each box. Once this sedimentary source is known, the ε_{Nd} of the sedimentary source and k in each ocean box are uniquely determined given modern observations of [Nd] and ε_{Nd} and assuming steady-state(Du et al. 2018).

A series of tests were performed in which we varied the sedimentary source and calculated the resulting global ocean Nd residence time (τ_{Nd}) (Fig. 4.S1). The results were used to constrain the sedimentary source (Methods).

Variability of global authigenic and detrital ε_{Nd} on glacial-interglacial timescales

Globally, most deep ocean authigenic ε_{Nd} are consistently more positive in the LGM than the Holocene (Fig. 4.S8). A similar temporal change is not seen in detrital ε_{Nd}, suggesting that the glacial-interglacial authigenic ε_{Nd} variability was not caused by a global change in detrital source. Intermediate-depth authigenic ε_{Nd} records from the Atlantic and Pacific do not show significant glacial-interglacial change, nor do the associated intermediate-depth detrital ε_{Nd} records. Only the intermediate-depth authigenic ε_{Nd} records from the North Indian (Bay of Bengal) appears to be anomalous relative to the other ocean basins, which will be discussed separately later.

Variability of Equatorial Pacific authigenic and detrital ε_{Nd} on glacial-interglacial timescales

Detrital ε_{Nd} from the deep Pacific initially appears to be overall more negative in the LGM than the Holocene in Figure S1, but closer examination reveals that this change is only seen in the Equatorial Pacific (Fig. 4.S9). Authigenic ε_{Nd} records from the North and South Pacific show coherent change of ε_{Nd} that is consistent with the global trend (Fig. 4.S8, S9). There is essentially no glacial-interglacial change of detrital ε_{Nd} in these regions, suggesting these authigenic records are not overprinted by detrital variability. In contrast, authigenic ε_{Nd} records from the Equatorial Pacific are anomalously low during the LGM, which is correlated to change in the local detrital ε_{Nd}. Change in the latter been shown to be a result of changing detrital source because of shifting Intertropical Convergence Zone in the past(Reimi & Marcantonio 2016; Xie & Marcantonio 2012). These "anomalous" Equatorial Pacific authigenic ε_{Nd} records are not consistent with the global trend nor with the rest of the Pacific (Fig. 4.S8, S9), suggesting that they were imprinted by the variability of detrital ε_{Nd}.

We corrected these Equatorial Pacific records to remove the detrital influence by subtracting the estimated local detrital ε_{Nd} anomaly (with respect to Holocene, using Loess regression) from the authigenic ε_{Nd} data (Fig. 4.S9). The corrected Equatorial Pacific authigenic ε_{Nd} data immediately fall along the trend of the rest of the Pacific. If accurate, we can infer that the Equatorial Pacific authigenic ε_{Nd} recorded a combined change of ocean circulation and local detrital ε_{Nd}. More sophisticated correction can hopefully be made in the future once better understanding of the mechanism of detrital imprinting is achieved.

Variability of authigenic and detrital ε_{Nd} in the subpolar North Atlantic during the deglaciation

Millennial scale detrital ε_{Nd} variations in the Heinrich Layers (HLs) are documented in the subpolar North Atlantic. The classically defined IRD belt(Hemming 2004; Ruddiman 1977) is mainly restricted to 40^{o}N to 50^{o}N. Highly negative detrital ε_{Nd} implies that the source of HL1 sediment around the IRD belt is

Precambrian materials (ε_{Nd}<–25) from the Canadian Shield(Hemming 2004) (Fig. 4.S10). Further north and at shallower sites, where IRD counts are generally lower, more positive detrital ε_{Nd} implicated Icelandic sedimentary sources (ε_{Nd} >0) can also occur within HL1(Revel et al. 1996). Indeed, this contrasting pattern is reflected in PC2 loadings and PC2 reconstructed HS1-LGM authigenic ε_{Nd} difference (Fig. 4.2), suggesting authigenic records north of 40°N in the North Atlantic were imprinted by the heterogeneous changes in HL-associated detrital ε_{Nd}.

This detrital imprint is seen not only spatially as discussed above but also temporally when comparing authigenic ε_{Nd} time-series and their PC2 components to detrital records during the deglaciation (Fig. 4.S11). For example, in the classic IRD belt the negative shifts of authigenic ε_{Nd} during HS1 and YD correlate to negative shift of detrital ε_{Nd} and increasing IRD counts, while closer to Iceland the positive shifts of authigenic ε_{Nd} during HS1 and YD correlate to increasing volcanic IRD counts. The millennial-scale changes of authigenic ε_{Nd} in these nearby locations cannot reflect watermass differences, so more likely they track the local detrital variability.

Thus, our results indicate that the detrital imprint in the subpolar North Atlantic during the deglacial HEs is ubiquitous rather than limited to the center of the IRD belt, and that this detrital imprint corresponds to heterogenous detrital sources rather than only the Precambrian materials from the Canadian Shield(Blaser et al. 2019). In light of this, we reiterate the importance of decomposing the authigenic ε_{Nd} records and removing the preformed component (PC1) in order to properly evaluate the extent of detrital imprint (Fig. 4.S10, S11).

Variability of authigenic and detrital ε_{Nd} in the North Indian Ocean and its link to the Indian Monsoon

Today, seawater ε_{Nd} in the North Indian Ocean is subject to seasonal variability due to changing terrestrial input linked to monsoon activity, which affects the entire water column in the Bay of Bengal (BoB)(Yu et al. 2017). This observation

raises the question of whether authigenic ε_{Nd} in the BoB records ocean circulation changes or monsoon activity in the past.

Out data compilation shows that the North Indian authigenic ε_{Nd} (mostly from the BoB) behaved anomalously during both the LGM and deglaciation (Fig. 4.S12, S13) compared to the rest of the global ocean. The LGM increase of authigenic ε_{Nd} by as much as ~4.5 ε in the North Indian surpassed everywhere else except the subpolar North Atlantic (Fig. 4.1, 4.2). The deglacial change of authigenic ε_{Nd} in the BoB also surpassed the global ocean except the subpolar North Atlantic (Fig. 4.1, 4.2). Thus, although the general trend of authigenic ε_{Nd} change in the North Indian appears to be aligned with the global ocean, the magnitude of the change cannot be explained by ocean circulation alone.

A plausible explanation lies in variation of the Indian Monsoon since the LGM. Higher LGM authigenic ε_{Nd} here can be explained by reduced terrestrial input from the Himalayas ($\varepsilon_{Nd} \sim -15$, more negative than modern seawater) resulting from a weaker LGM Indian Monsoon(Burton & Vance 2000). The deglacial ε_{Nd} change can also be explained by monsoon activity: for example, if during HS1 and YD the Indian Monsoon became even weaker than the LGM(Rashid et al. 2011), this could have resulted in reduced terrestrial input and more positive authigenic ε_{Nd} excursions(Yu et al. 2018).

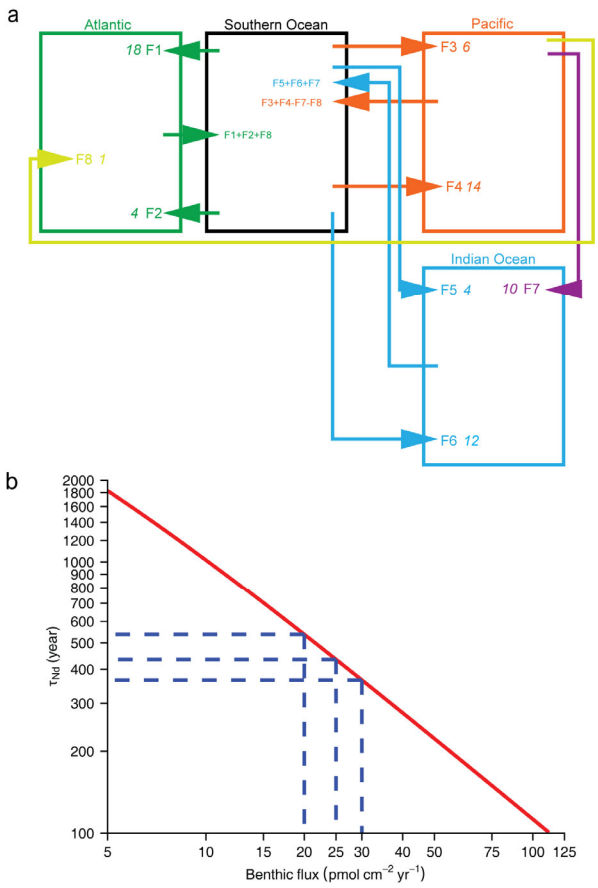

Figure 4.S1. Global box model design.

a, The physical circulation in the model, which flows Talley's geostrophic box-inverse models(Talley 2008, 2013) and shows the "figure 8" pattern of modern GOC. Southern Ocean is separated from the other basins at 30°S, and the related water fluxes are transports across this latitude. *F1* is the surface and intermediate water flux that feeds the production of NADW. *F2*, *F4* and *F6* are the water fluxes entering the deep Atlantic, Pacific and Indian Ocean from the Southern Ocean, being the sources of SOMOC. *F3* and *F5* are the intermediate water fluxes entering the Pacific and Indian Ocean from the Southern Ocean. *F7* is the Indonesian Through Flow and *F8* is the Bering Strait Through Flow. The numbers following the labels are transport in Sverdrup. b, Dependence of global Nd residence time τ_{Nd} on the missing source (assumed to be the benthic flux) in the box model. Note that this is a log-log plot. Independent estimates of τ_{Nd} and benthic flux suggest that the "best" fit to the modern global budget (Methods) is a benthic flux of 20~30 pmol cm^{-2} yr^{-1} and a τ_{Nd} of 300~600 years(Abbott et al. 2015a,b; Arsouze et al. 2009; Du et al. 2018; Rempfer et al. 2011; Tachikawa et al. 2003), which are marked using the blue dash lines.

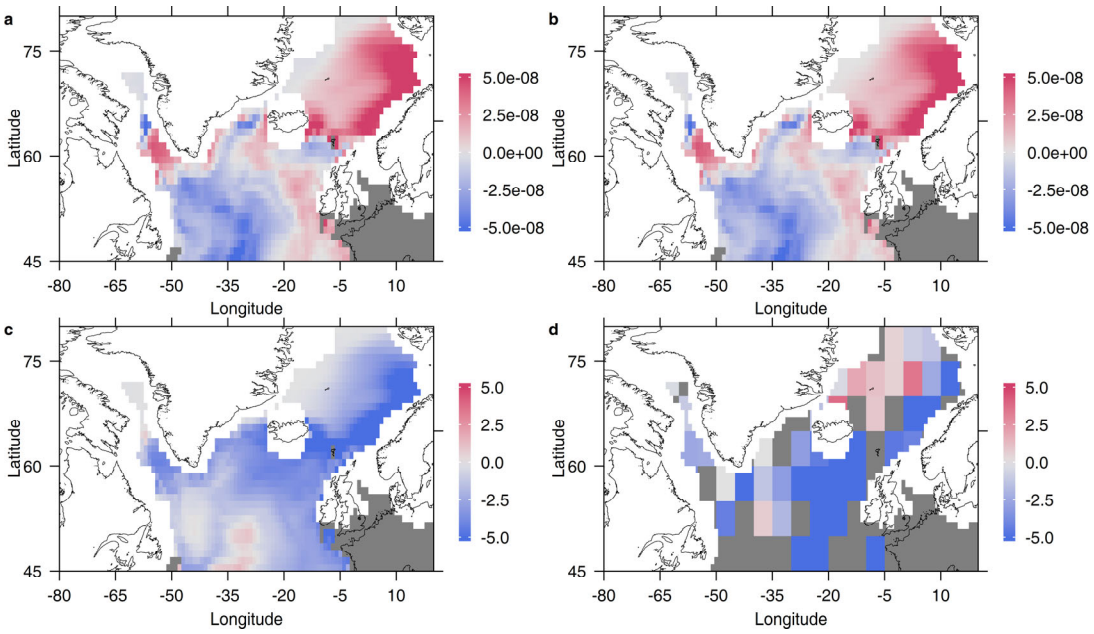

Figure 4.S2. Subpolar North Atlantic surface climate in the LGM.

a, net and b, thermal surface buoyancy flux (in m^2/s^3) anomalies (relative to the pre-industrial control) in the winter (January-February-March average). The data are multi-model median values of PMIP3 results(Meinshausen et al. 2011) (Methods). Red color indicates less buoyancy loss and blue color more. c, LGM winter SST anomaly (in Celsius), also multi-model median values of PMIP3 results(Meinshausen et al. 2011). d, LGM winter SST anomaly from the MARGO project(Waelbroeck et al. 2009). White pixels in the plots indicate LGM ice sheet/shelf in PMIP3 models(Abe-Ouchi et al. 2015). These data show that in the LGM surface buoyancy loss reduced in the Nordic-Labrador Seas but increases south of Iceland, mostly due to the thermal effect related to sea ice (Fig. 4.3) and SST. The results suggest a southward shift of deep water formation locations in the LGM(Otto-Bliesner et al. 2007).

Figure 4.S3. Box model sensitivity tests (Methods).

a, NSW production decreases by 4-fold. b, SSW production increases by 4-fold. c, NSW preformed ε_{Nd} increases by 5 ε_{Nd}. d, SSW preformed ε_{Nd} increases by 5 ε_{Nd}. Among these tests c is consistent with the PC1 pattern and the associated glacial change of authigenic ε_{Nd} (Fig. 4.2), and b is consistent with the PC2 pattern and the associated deglacial change of authigenic ε_{Nd} (Fig. 4.4). Although both "NSW/4" and "SSW*4" results in reduction of NSW mixing ratio, the global responses of ε_{Nd} are different, because the relative contributions of the conservative and non-conservative effects are different in these two tests(Du et al. 2018). In "NSW/4", global ocean residence time (τ_w) increased because of reducing NSW production, which increased the relative contribution of the non-conservative component and caused authigenic ε_{Nd} to converge to the detrital source in each ocean box and thus diverge from each other. In "SSW*4", τ_w decreased because of increasing SSW production, which increased the relative contribution of the conservative component and caused authigenic ε_{Nd} to converge on each other but diverge from the local detrital sources. The results show that changing NSW/SSW production cannot generate a globally uni-directional change of ε_{Nd} as seen in glacial authigenic data (Fig. 4.1, 4.2). On the other hand, the tests "NSW_pref+5" and "SSW_pref+5" show that a globally consistent uni-directional change of ε_{Nd} can be generated by varying the preformed ε_{Nd}, where the resulting perturbation is transmitted globally by circulation. Moreover, because the global Nd residence time (τ_{Nd}) is shorter than τ_w, the magnitude of the perturbation resulting from the change of the preformed ε_{Nd} must decay downstream of the place of its origin(Du et al. 2018), therefore providing a means to identify the origin of change. This points to a change of the preformed ε_{Nd} of NSW, rather than SSW, as the cause of the PC1 pattern.

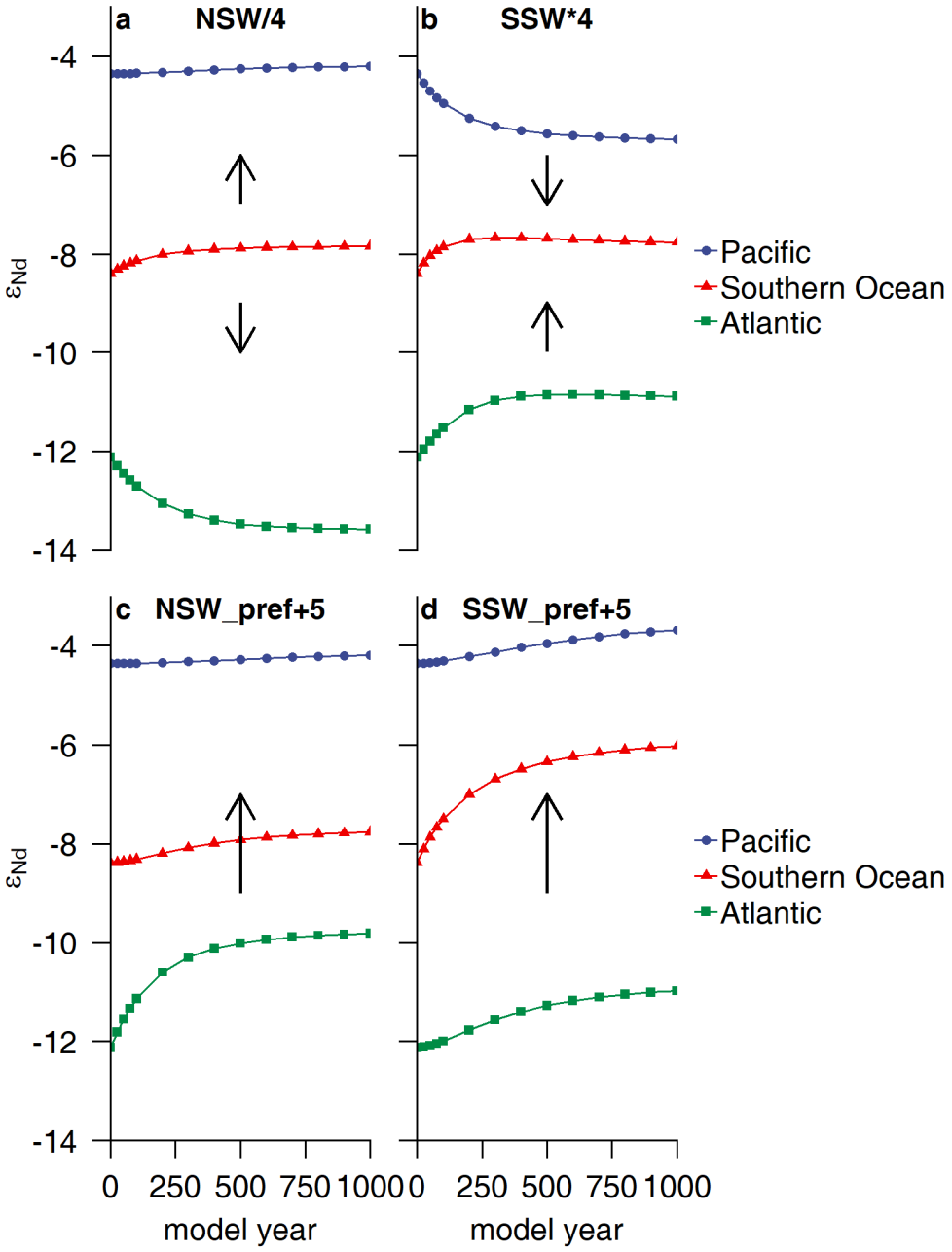

Figure 4.S3. Box model sensitivity tests (Methods).

Figure 4.S4. Transient box model simulations of ε_{Nd} compared to authigenic ε_{Nd} records.

a, The NSW preformed ε_{Nd} anomaly (with respect to the Holocene) scaled to PC1. b, Multiplication factor (with respect to the Holocene) for SOMOC transport scaled to PC2. c, Model results (solid and dashed lines) in the Pacific, Southern Ocean and Atlantic, compared to authigenic ε_{Nd} records (dots indicate raw data, ribbons indicate Loess 95% CIs). Data are from the deep ocean (>1500 m) and not including the subpolar North Atlantic. Subpolar North Atlantic is the source of the preformed ε_{Nd} change on glacial-interglacial timescales while on deglacial millennial timescales authigenic ε_{Nd} here are affected by detrital imprint. "NSW_pref" (solid lines) refers to the simulation in which we used the NSW preformed ε_{Nd} anomaly in a while all other parameters were held constant. "NSW_pref+SOMOC" (dashed lines) refers to the simulation in which we used both the NSW preformed ε_{Nd} anomaly in a and the SOMOC scaling in b while all other parameters were held constant. To facilitate the model/data comparison, we removed the mean ε_{Nd} offset between each individual site and the ocean box mean(Du et al. 2018). In "NSW_pref", an increase of the preformed ε_{Nd} of NSW by 5 ε in the LGM causes the Atlantic mean seawater ε_{Nd} to increase ~2.5 ε in c, consistent with authigenic ε_{Nd} records in the deep Atlantic (reflecting the ocean basin mean) outside the subpolar North Atlantic (the origin of change). Agreeing with the global PC1 pattern, the magnitude of the glacial increase of ε_{Nd} in "NSW_pref" decreases from the Atlantic to the Southern Ocean, and again in the Pacific. "NSW_pref" predicts smaller glacial increase of ε_{Nd} in the Pacific than observed, because the glacial increases of ε_{Nd} in the Pacific must also account for the increasing non-conservative effect associated with sluggish GOC in the LGM(Du et al. 2018). This effect was included in "NSW_pref+SOMOC", which not only explain the LGM Pacific data better but also explains the global deglacial millennial timescale variabilities.

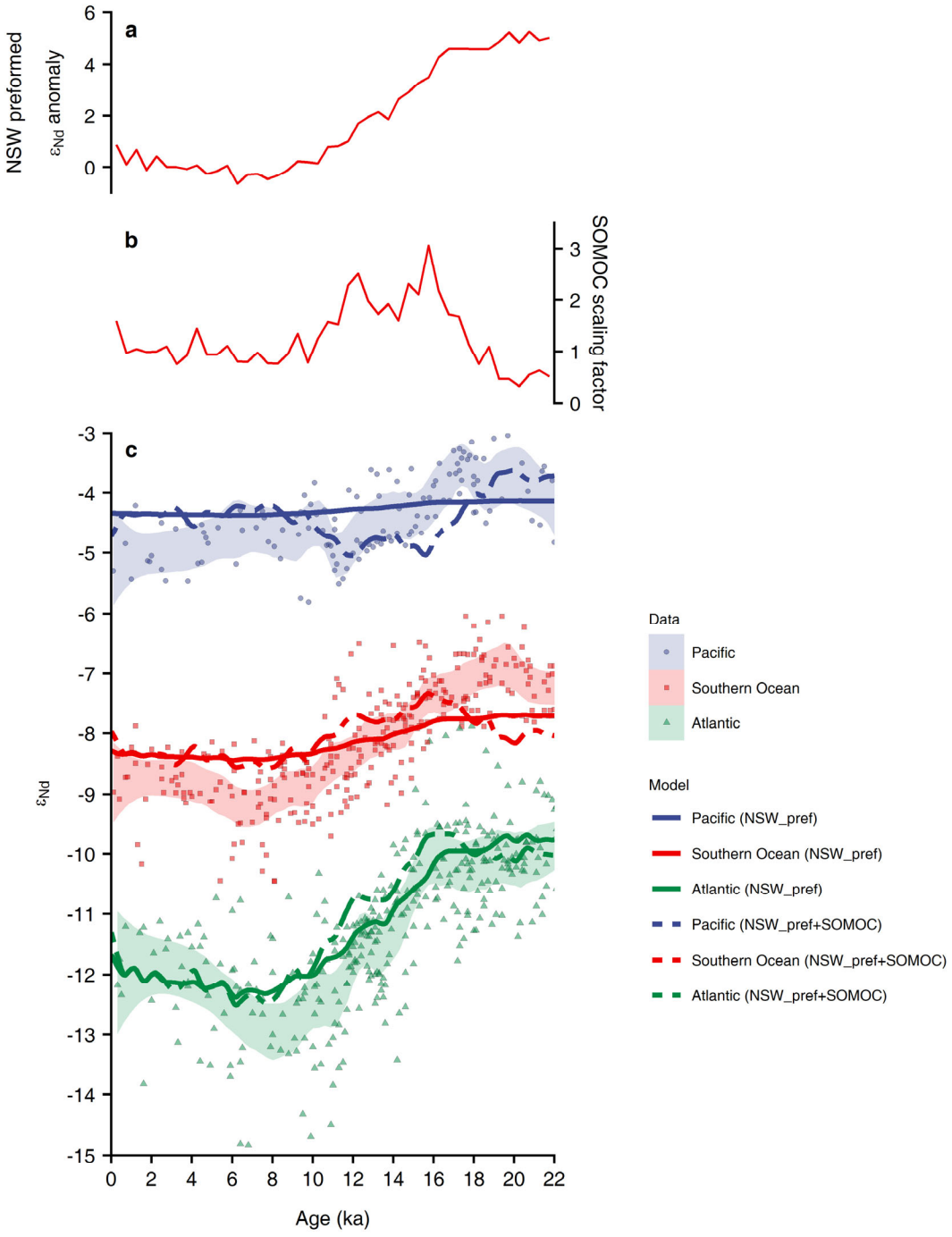

Figure 4.S4. Transient box model simulations of ε_{Nd} compared to authigenic ε_{Nd} records.

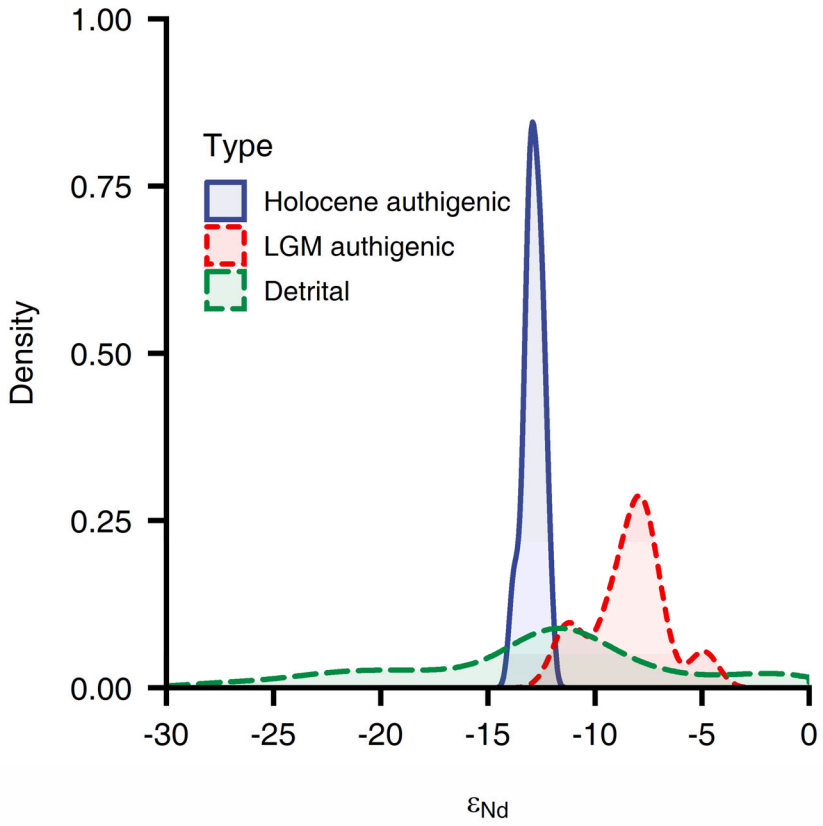

Figure 4.S5. Distributions of detrital, Holocene and LGM authigenic ε_{Nd} in the subpolar North Atlantic (north of 40°N).

The detrital data plotted here include Holocene, LGM and core-top datasets (Methods). There is no statistical difference in the distributions of detrital ε_{Nd} in these three datasets and they are hence merged to show the general detrital background. The Holocene and LGM authigenic ε_{Nd} data are from the same locations, and therefore the difference in their distribution cannot be attributed to sampling bias. The heterogeneity of lithogenic source is shown by the broad distribution of detrital ε_{Nd}. However, strong AMOC and vigorous mixing today largely remove this heterogeneity of the sources, leading to a narrow distribution of authigenic ε_{Nd}. In contrast, in the LGM the distribution of authigenic ε_{Nd} not only shifted toward more positive values, suggesting weaker influence of the low-ε_{Nd} detrital sources, but the distribution of authigenic ε_{Nd} also becomes broader, implying weaker glacial circulation that did not homogenize the detrital influence as efficiently as today.

Figure 4.S6. Transient simulations of εNd compared to the PC2 components of selected records.

a, Multiplication factor (with respect to the Holocene) for SOMOC transport scaled to PC2. b, Multiplication factor (with respect to the Holocene) for AMOC transport scaled to North Atlantic 231Pa/230Th(Ng et al. 2018) (Fig. 4.4). c, Model results (solid, dotted and dashed lines) compared to the PC2 components of representative authigenic ε_{Nd} records (ribbons with 95% CIs). The records are from North Pacific site EW0408-87JC (58.8°N, 144.5°W, 3,680 m)(Du et al. 2018), Southern Ocean site PS75/073_2 (57.2°S, 151.6°W, 3,234 m)(Basak et al. 2018) and North Atlantic site OCE326_GGC6 (33.7°N, 57.6°W, 4,543 m)(Roberts et al. 2010). The mean ε_{Nd} offset between each individual site and the ocean box average is removed to facilitate data-model comparison. Three simulations were performed. In "AMOC−" (dotted lines) only the AMOC scaling factor was used while SOMOC and other parameters were held constant as today. In "SOMOC+" (solid lines) only the SOMOC scaling factor was used while AMOC and other parameters were held constant as today. In "SOMOC+ AMOC−" (dashed lines) both the AMOC and SOMOC scaling factors were used while the other parameters were held constant as today. These results show that increasing SOMOC leads to Atlantic-Pacific convergence while reducing AMOC leads to divergence. To explain the PC2 components of global ε_{Nd} records increasing SOMOC during HS1 and YD is required, especially if AMOC was significantly reduced. The "SOMOC+" simulation is also show in Figure 4.

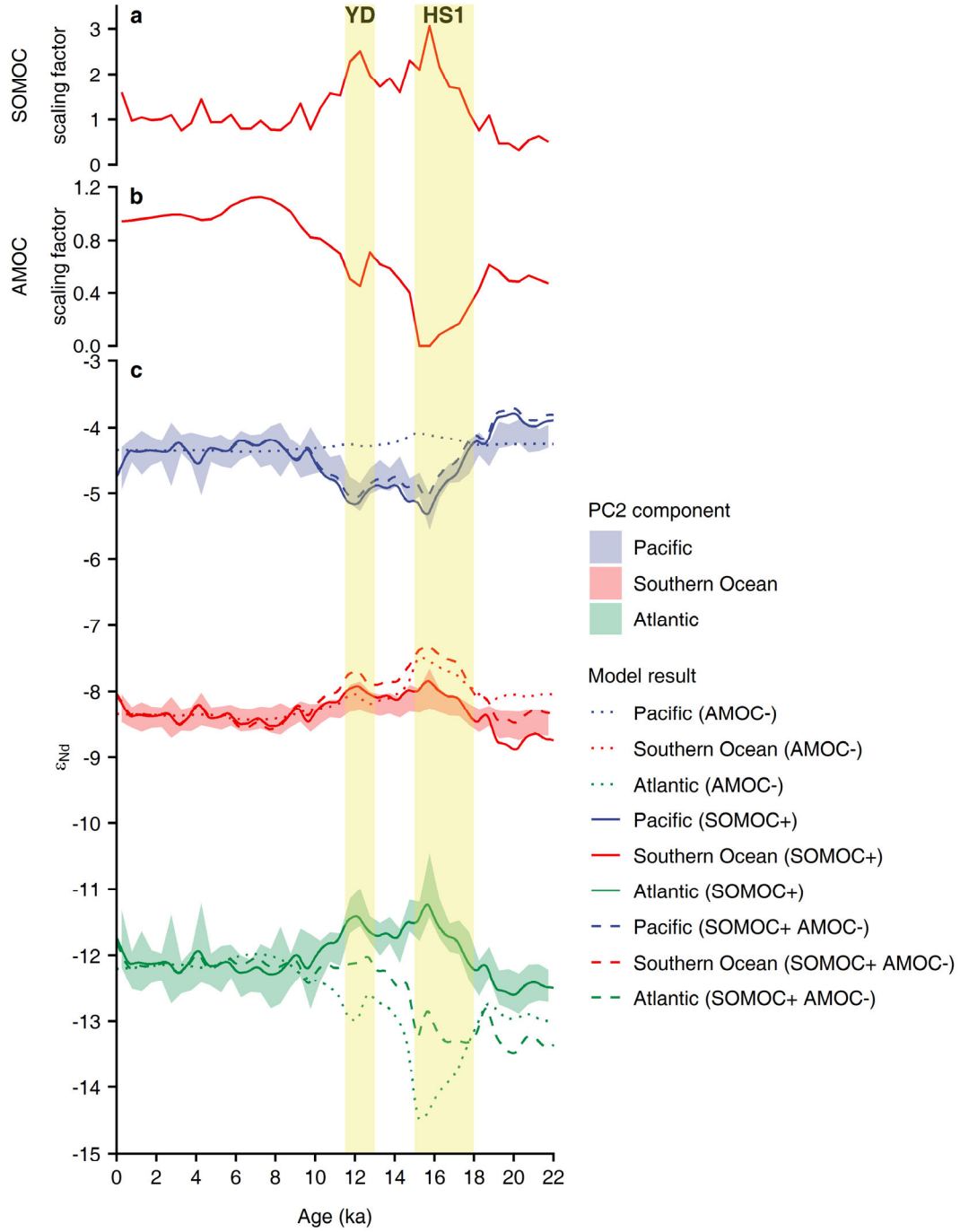

Figure 4.S6. Transient simulations of ε_{Nd} compared to the PC2 components of selected records.

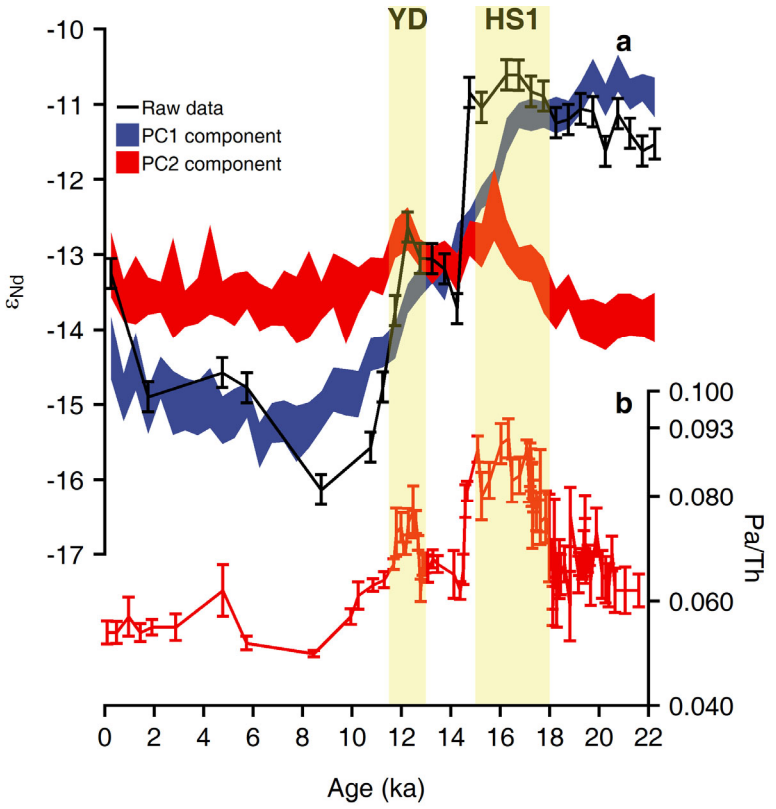

Figure 4.S7. Authigenic ε_{Nd} and sedimentary $^{231}Pa/^{230}Th$ records from the Bermuda Rise site OCE326_GGC6/ODP_1063.

a, authigenic ε_{Nd}(Böhm et al. 2015; Roberts et al. 2010) and its PC1 and PC2 components. b, sedimentary $^{231}Pa/^{230}Th$ record(Böhm et al. 2015; McManus et al. 2004). There is little change of authigenic ε_{Nd} between 22 ka and 15 ka, which has been used as evidence of no change of deep circulation in the North Atlantic during HS1(Roberts et al. 2010). However, after decomposing this authigenic ε_{Nd} record, we find that this apparent lack of change is the result of PC1 (preformed) and PC2 (watermass mixing) components operating in opposite directions. After removing the preformed effect (PC1), authigenic ε_{Nd} (PC2) is highly correlated to $^{231}Pa/^{230}Th$, both consistent with reduction of AMOC and increasing of SOMOC during HS1 and YD.

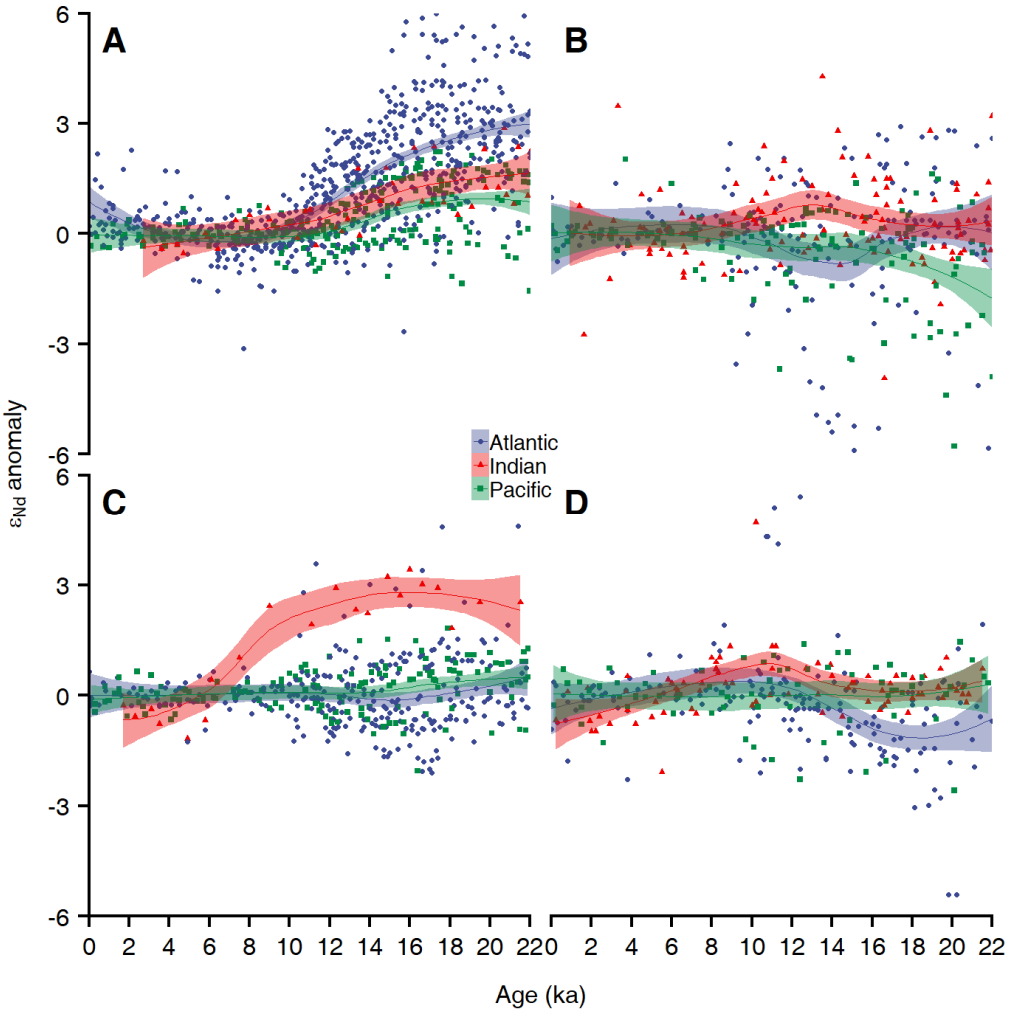

Figure 4.S8. Comparing authigenic and detrital ε_{Nd} in the global ocean since the LGM.

(A) Authigenic ε_{Nd} from the deep ocean (>1500 m). (B) Detrital ε_{Nd} from the deep ocean (>1500 m). (C) Authigenic ε_{Nd} from the intermediate-depth ocean (<1500 m). (D) Detrital ε_{Nd} from the intermediate-depth ocean (<1500 m). We do not make a separate Southern Ocean group in these plots because the geology and detrital compositions of the Southern Ocean sectors of the Atlantic, Pacific and Indian Oceans are more similar to their mother basins than to each other. ε_{Nd} data are plotted in terms of the anomaly with respect to the Holocene mean (<10 ka). The shades lines are loess regression lines with 95% CIs. There is no globally consistent correlation between authigenic and detrital ε_{Nd} on glacial-interglacial timescale.

Figure 4.S9. Comparing authigenic and detrital εNd in the Pacific since the LGM.

(**A**) Equatorial Pacific (25ºS~25ºN) authigenic ε_{Nd}. Filled circles indicate raw data. Open circles indicate corrected data as described in the text. Colors represent different sites. Solid-shaded line is the loess regression line with 95% CI of the raw data. Dash-shaded line is the loess regression line of the corrected data. (**B**) Equatorial Pacific detrital ε_{Nd}. Symbols, lines and colors have the same meaning as in (**A**). (**C**) North Pacific (Gulf of Alaska) and South Pacific (Southern Ocean sector) authigenic ε_{Nd}. Symbols, lines and colors have the same meaning as in (**A**). Note that the corrected Equatorial Pacific authigenic ε_{Nd} data (open symbols) and the regression line (dash-shaded) from (**A**) are also plotted in (**C**) for comparison. (**D**) Gulf of Alaska and Southern Ocean Pacific sector detrital ε_{Nd}. Symbols, lines and colors have the same meaning as in (**A**). ε_{Nd} data are plotted in term of the anomaly with respect to the Holocene mean (<10 ka). In the Equatorial Pacific, (uncorrected) glacial authigenic ε_{Nd} is more negative than the Holocene, corresponding to the same trend in detrital ε_{Nd}. Outside the Equatorial Pacific, glacial authigenic ε_{Nd} is consistently more positive, as authigenic data from the rest of the global ocean are (Fig. S1), and there is no apparent change of detrital ε_{Nd} in these regions. Once corrected (by subtracting the detrital anomaly predicted using loess regression in (**B**)), Equatorial Pacific authigenic ε_{Nd} records fall on the trend of the authigenic ε_{Nd} from the Gulf of Alaska and South Pacific, as well as the global trend (Fig. S1). This correction brings consistency to the Pacific authigenic ε_{Nd} data, and suggests that the authigenic ε_{Nd} from the Equatorial Pacific was imprinted by detrital variability on glacial-interglacial timescale.

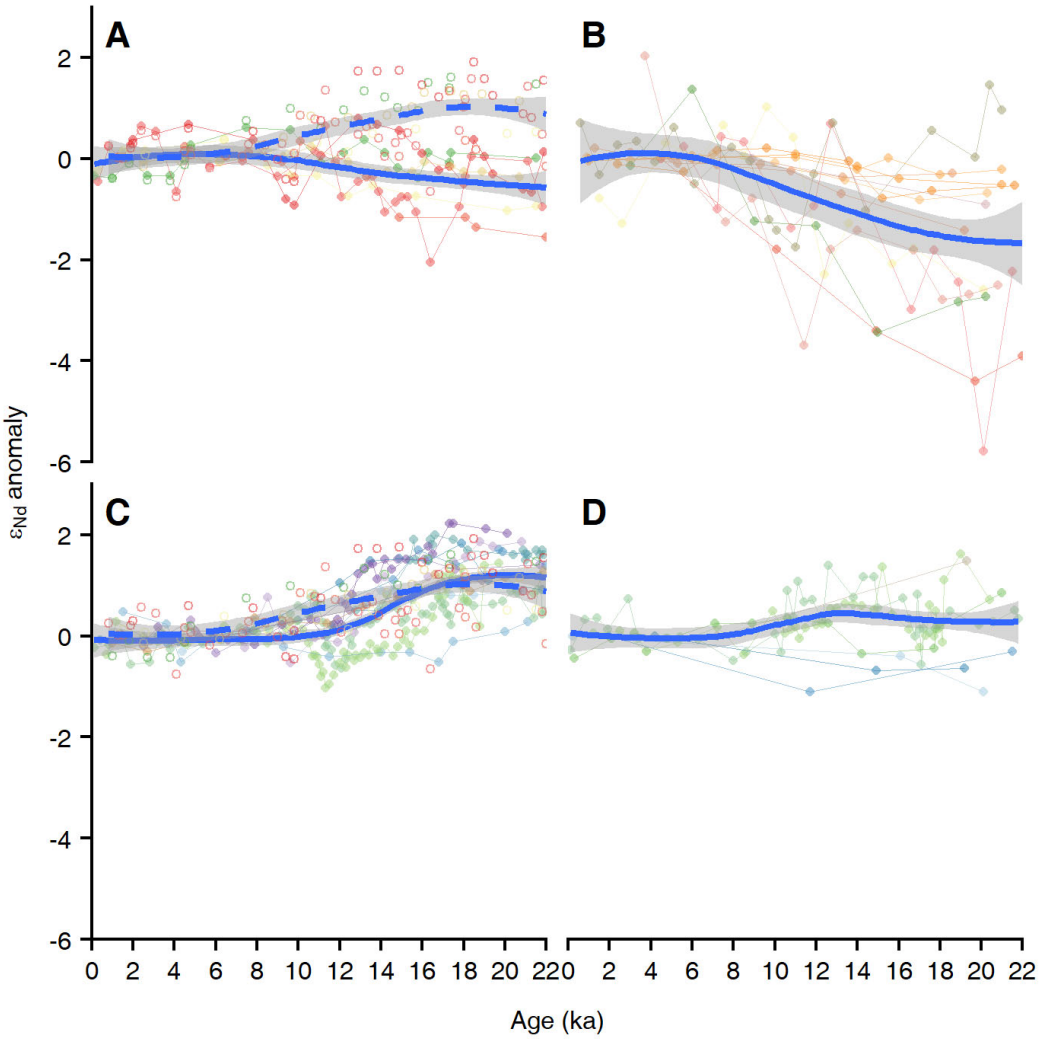

Figure 4.S9. Comparing authigenic and detrital ε_{Nd} in the Pacific since the LGM.

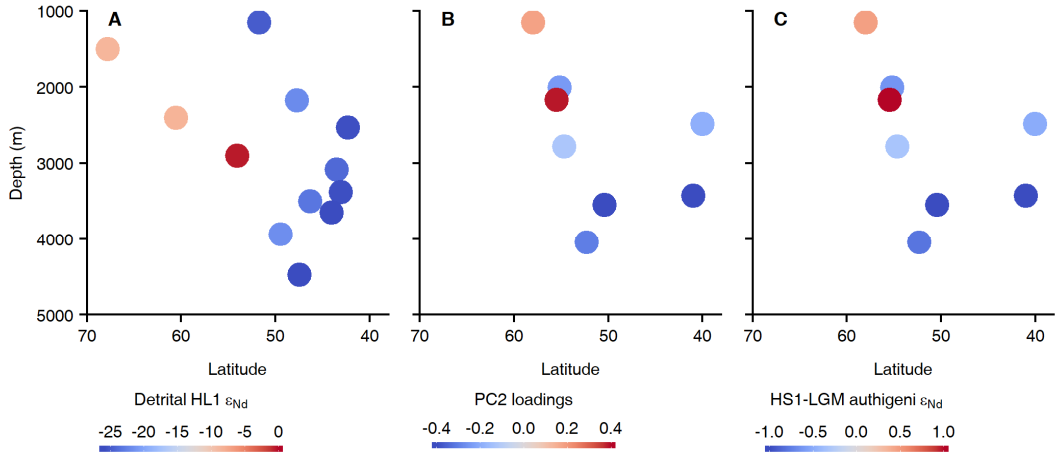

Figure 4.S10. Comparing authigenic and detrital ε_{Nd} in the subpolar North Atlantic around the IRD belt during HS1.

(**A**) Detrital ε_{Nd} of Heinrich Layer 1(Blaser et al. 2016; Grousset et al. 2000, 2001; Hemming et al. 1998; Jullien et al. 2006; Peck et al. 2006; Plaza-Morlote et al. 2017; Revel et al. 1996; Verplanck et al. 2009). (**B**) PC2 loadings of authigenic ε_{Nd} records from Figure 2. (**C**) PC2 reconstructed HS1-LGM authigenic ε_{Nd} difference from Figure 2. The blue color indicates detrital sources and imprints by materials (likely from the Canadian Shield) with ε_{Nd} lower than the preformed ε_{Nd} (–13) of modern NADW. The red color indicates detrital sources and imprints by materials (likely Icelandic) with ε_{Nd} higher than the preformed ε_{Nd} (~ –13) of modern NADW. Note that in the classic IRD belt (40°N~50°N) as defined by refs.(Hemming 2004; Ruddiman 1977) negative detrital ε_{Nd} sources are dominant in HLs(Hemming 2004), but moving closer to Iceland positive volcanic ε_{Nd} sources become important(Revel et al. 1996).

Figure 4.S11. Comparing authigenic ε_{Nd} and detrital records in the subpolar North Atlantic around the IRD belt during the deglaciation.

We use the authigenic ε_{Nd} records of IODP U1313(Lang et al. 2016; Lippold et al. 2016) and ODP 980(Crocker et al. 2016) to illustrate detrital imprints by Canadian Shield materials and Icelandic materials respectively. Site U1313 (41ºN, 33ºW, 3,425 m) is from the southern edge of the classic IRD belt. Its authigenic record and PC decomposition (A, B) are compared to various detrital records from the IRD belt: (C) Detrital ε_{Nd} of site HU91-045-094 (50.2ºN, 45.7ºW, 3,448 m) from the Orphan Knoll(Fagel et al. 2002); (D) Detrital ε_{Nd} of site SU90-09 (43.1ºN, 31.1ºW, 3,375 m) from the Mid-Atlantic Ridge(Grousset et al. 2001); (E) IRD counts at site U1313(Lang et al. 2016) and VM29-191/23-81 (54.27°N, 16.78°W, 2370 m)(Bond et al. 1997). ODP 980 (55.5ºN, 14.7ºW, 2,168 m) is from the Rockall Trough. Its authigenic record and the PC decomposition (F, G) are compared to volcanic IRD counts (H) from the same site(Crocker et al. 2016). The shaded intervals are YD and HS1.

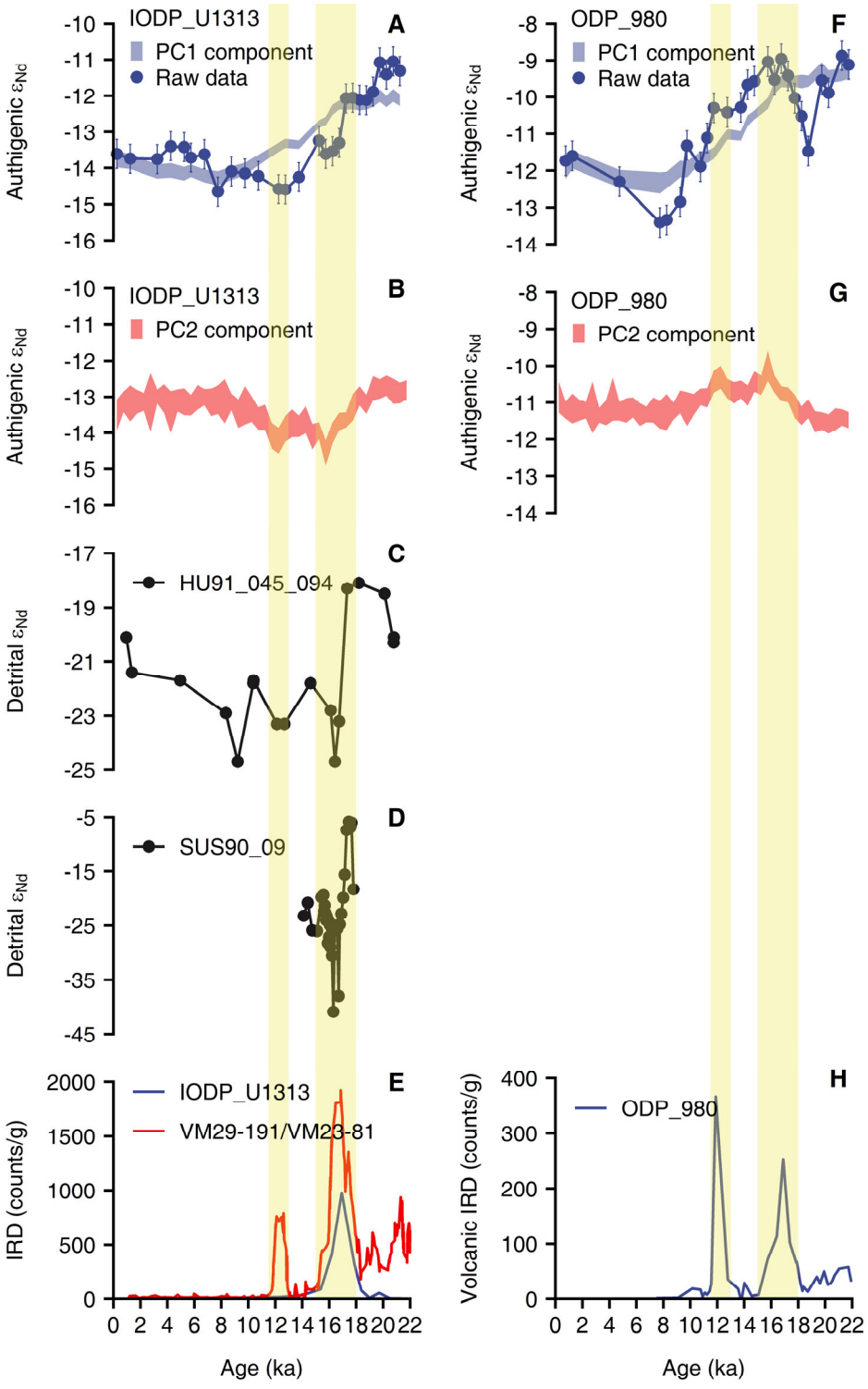

Figure 4.S11. Comparing authigenic ε_{Nd} and detrital records in the subpolar North Atlantic around the IRD belt during the deglaciation.

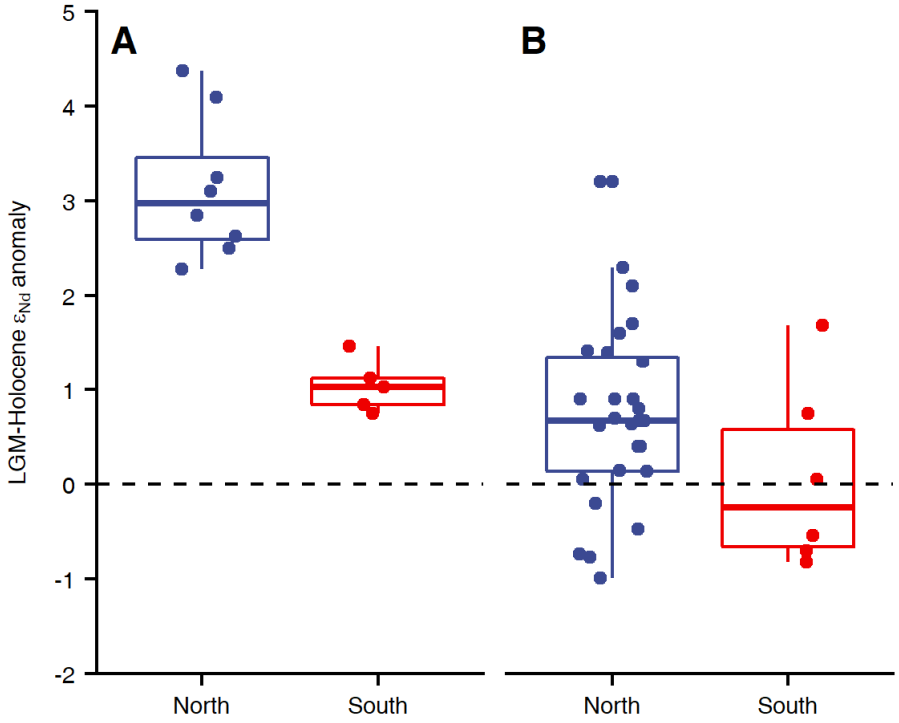

Figure 4.S12. LGM-Holocene authigenic (A) and detrital (B) ε_{Nd} anomalies in the Indian Ocean, separated into the North and South groups.

The dots represent the data, and the box (25%~75% quantiles) and whiskers (minimum and maximum) indicate the statistical summaries. Most of the North Indian Ocean records come from the Bay of Bengal. The glacial increase of authigenic ε_{Nd} is much higher in the North Indian (~3 ε) than the South Indian (~1 ε) and the rest of the global ocean (1~2 ε) (except the subpolar North Atlantic) (Fig. 2). This North Indian Ocean anomaly therefore cannot be explained by circulation. Part, but not all, of this anomaly may be attributed to the slightly greater increase (~1 ε) of detrital ε_{Nd} in the LGM in the North Indian Ocean. On the other hand, higher glacial ε_{Nd} in the North Indian Ocean is consistent with weaker Indian Monsoon that resulted in reduced terrestrial input (either dissolved or particulate) of very negative ε_{Nd} (~ –15) from the Himalayas(Yu et al. 2018; Burton & Vance 2000).

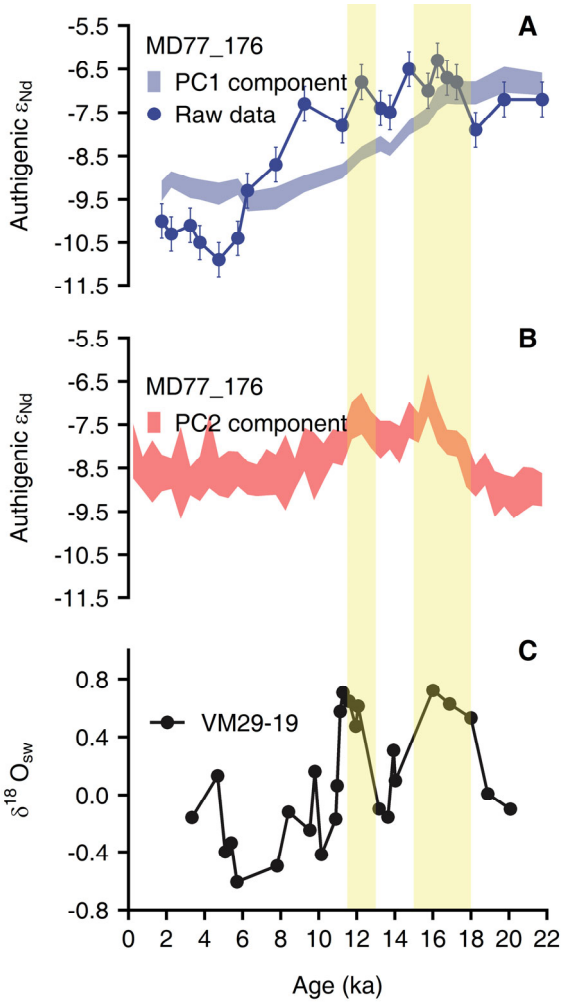

Figure 4.S13. North Indian authigenic ε_{Nd} and its PCs (A, B) compared to Indian Monsoon record (C) during the deglaciation.

The shades intervals mark YD and HS1. Site MD77_176 (14.5°N, 93°E, 1375 m) and VM29-19 (14.7°N, 83.6°E, 3182 m) are both from the northern Bay of Bengal. During HS1 and YD, Indian Monsoon became weaker (more so than the LGM), as indicated by high ice volume corrected surface water $\delta^{18}O_{sw}$ (high salinity) at site VM29-19(Rashid et al. 2011). Weaker monsoon implies reduced terrestrial input from the Himalayan rivers that carry highly negative ε_{Nd} dissolved and particulate materials (~ –15)(Yu et al. 2018). The monsoon activity therefore may explain the positive excursions during YD and HS1 in authigenic ε_{Nd} record at site MD77_176. In contrast, such strong deglacial ε_{Nd} excursions (~2 ε) are not seen anywhere else in the global ocean except the subpolar North Atlantic (Fig. 1, 2, 4), and therefore cannot be fully explained by circulation change.

Table 4.S1. Box model configuration and the modern global marine Nd-ε_{Nd} budget.

Each individual ocean box has four sources of Nd: dust, river (dissolved), benthic flux and transport in (Nd carried by waters entering the box). These sources are balanced by two sinks: scavenging and transport out (Nd carried by waters leaving the box). Note that transport only distributes Nd among the ocean basins and does not provide a net sink/source globally. Only dust, river and benthic flux are external sources and scavenging is the only external sink. In the model the scavenging flux is scaled to Nd concentration and the first order rate law constant k is reported here. The ε_{Nd} of the scavenging flux is the same as seawater. At the end of the table we report the percentage of the individual sources with respect to the external sources (%ES) and the total sources (%TS, i.e., external sources plus transport in). Model description can be found in Methods.

Basin	Atlantic	Pacific	Indian	Southern	Global
Seawater [Nd] (pmol/kg)	25.3	33.3	29.8	26.8	29.5
Seawater ε_{Nd}	-12.1	-4.4	-9.3	-8.4	-7.2
Seafloor area (m^2)	6.12E+13	1.33E+14	3.83E+13	1.1E+14	3.42E+14
Volume (m^3)	2.28E+17	5.3E+17	1.43E+17	4.22E+17	1.32E+18
Dust flux (mol/yr)	4.01E+05	1.48E+05	2.01E+05	6.68E+04	8.17E+05
Dust ε_{Nd}	-12.5	-6.0	-6.0	-8.0	-9.4
River flux (mol/yr)	2.35E+06	7.59E+05	2.70E+05		3.38E+06
River ε_{Nd}	-12.6	-2.9	-8.7		-10.1
Transport in (mol/yr)	1.97E+07	1.69E+07	2.41E+07	5.23E+07	1.13E+08
Transport in ε_{Nd}	-8.2	-8.4	-6.6	-9.4	-8.4
Transport out (mol/yr)	1.84E+07	2.10E+07	2.44E+07	4.91E+07	1.13E+08
Benthic flux (mol/yr)	1.53E+07	3.31E+07	9.59E+06	2.75E+07	8.55E+07
Benthic ε_{Nd}	-17.1	-2.3	-16.0	-6.5	-7.8
Scavenging flux (mol/yr)	1.93E+07	3.00E+07	9.70E+06	3.07E+07	8.97E+07
k (yr^{-1})	3.35E-03	1.70E-03	2.28E-03	2.71E-03	2.30E-03
External sources (mol/yr)	1.80E+07	3.41E+07	1.01E+07	2.75E+07	8.97E+07
Total sources (mol/yr)	3.77E+07	5.10E+07	3.41E+07	7.98E+07	2.03E+08
%ES Benthic	85%	97%	95%	100%	95%
%ES Dust and River	15%	3%	5%	0%	5%
%TS Benthic	41%	65%	28%	34%	42%
%TS Transport in	52%	33%	71%	66%	56%
%TS Dust and River	7%	2%	1%	0%	2%

Table 4.S2. Information of the stations with authigenic ε_{Nd} data used in this study.

Column "Basin" indicates which basin (Atlantic, Pacific or Indian) the station is from. A station is also from the Southern Ocean if it is from south of 30°S. Column "Coverage" indicates data coverage: "D" indicates a station has a deglacial authigenic ε_{Nd} time-series record that was used in the PCA. "H" and "L" indicates a station has Holocene and LGM authigenic ε_{Nd} time-slice data respectively. Column "Lat" is the Latitude of the station. Column "Lon" is the Longitude of the station. Column "Depth" is the water depth (in meter) of the station. Note that we only used stations from below 500 m. Column "Method" indicates the methods/archives used to generate authigenic ε_{Nd} data. The acronyms are as following. "C" for cleaned, "UC" for uncleaned", "CS" for cleaning solution, and these are the methods associated with foraminiferal samples, including "PF" (planktonic foraminifera) and "BF" (benthic foraminifera). "FD" means (cleaned or not) fish debris. "CR" means (cleaned) corals. Note that all the foraminifera, fish debris and corals samples are subject to physical cleaning first, the cleaning methods mentions here refer to chemical (oxidative and/or reductive) cleaning. Sedimentary leach data are classified as "DC" (decarbonated) or "NDC" (non-decarbonate) data, extracted using hydroxylamine hydrochloride (HH) and/or acetic acid (AA). Note that leach data that do not agree consistently with foraminiferal and fish debris data from the same site are excluded in our collection and not included here. The authigenic ε_{Nd} records at many sites were generated using multiple methods/archives. Column "Ref" indicates data source.

Station	Basin	Coverage	Lat	Lon	Depth	Method	Ref
BOFS_10K	Atlantic	D&H&L	54.7	-20.7	2777	C_PF&DC_HHAA&FD&UC_PF	(Piotrowski et al. 2012)(Roberts & Piotrowski 2015)
BOFS_11K	Atlantic	D&H&L	55.2	-20.4	2004	DC_HHAA&FD&UC_PF	(Roberts & Piotrowski 2015)
BOFS_17K	Atlantic	D&H&L	58.0	-16.5	1150	DC_HHAA&UC_PF	(Roberts & Piotrowski 2015)
BOFS_29K	Atlantic	D&H&L	20.6	-21.1	4000	UC_PF	(Howe et al. 2017)
BOFS_30K	Atlantic	D&H&L	19.7	-20.7	3580	UC_PF	(Howe et al. 2017)
BOFS_31K	Atlantic	D&H&L	19.0	-20.2	3300	UC_PF	(Howe et al. 2017)

BOFS_5K	Atlantic	D&H&L	50.4	-21.5	3547	UC_PF	(Roberts & Piotrowski 2015)
BOFS_8K	Atlantic	D&H&L	52.3	-22.0	4045	C_PF&DC_HHAA&UC_PF	(Piotrowski et al. 2012)(Roberts & Piotrowski 2015)
GeoB1515_1	Atlantic	D&H&L	4.2	-43.7	3129	DC_HHAA	(Lippold et al. 2016)
GeoB1523_1	Atlantic	D&H&L	3.8	-41.6	3292	DC_HHAA	(Lippold et al. 2016)
GeoB2104_3	Atlantic	D&H&L	-27.3	-46.4	1500	UC_PF	(Howe et al. 2016a)(Howe et al. 2016b)
GeoB2107_3	Atlantic	D&H&L	-27.2	-46.5	1050	UC_PF	(Howe et al. 2016a)(Howe et al. 2016b)
GL1090	Atlantic	D&H&L	-24.9	-42.5	2225	UC_PF	(Howe et al. 2016a)(Howe et al. 2018)
IODP_U1313	Atlantic	D&H&L	41.0	-33.0	3425	C_PF&DC_HHAA&FD& NDC_AA&NDC_HHAA&UC_PF	(Blaser et al. 2016)(Elmore et al. 2011)(Lang et al. 2016) (Lippold et al. 2016)(Pöppelmeier et al. 2018)
KNR140_2_12JPC	Atlantic	D&H&L	29.1	-72.9	4250	DC_HHAA	(Gutjahr et al. 2008)
KNR140_2_51GGC	Atlantic	D&H&L	32.8	-76.3	1790	DC_HHAA	(Gutjahr et al. 2008)
KNR159_5_33GGC	Atlantic	D&H&L	-27.6	-46.2	2082	UC_PF	(Howe et al. 2018)
KNR159_5_36GGC	Atlantic	D&H&L	-27.5	-46.5	1268	UC_PF	(Howe et al. 2016b)
KNR166_2_26JPC	Atlantic	D&H&L	24.3	-83.3	546	DC_HHAA&FD	(Xie et al. 2012)(Xie et al. 2014)
KNR197_10_GGC17	Atlantic	D&H&L	36.4	-48.5	5010	NDC_HHAA	(Pöppelmeier et al. 2018)
KNR197_3_25GGC	Atlantic	D&H&L	7.7	-53.8	671	UC_PF	(Huang et al. 2014)
KNR197_3_46CDH	Atlantic	D&H&L	7.8	-53.7	947	UC_PF	(Huang et al. 2014)
KNR197_3_9GGC	Atlantic	D&H&L	7.9	-53.6	1100	UC_PF	(Huang et al. 2014)
M35003_4	Atlantic	D&H&L	12.1	-61.2	1299	DC_HHAA	(Lippold et al. 2016)

M39008	Atlantic	D&H&L	36.4	-7.1	577	DC_HHAA	(Stumpf et al. 2010)
M39036	Atlantic	D&H&L	37.8	-9.7	1745	DC_HHAA	(Stumpf et al. 2010)
M78/1_222_9	Atlantic	D&H&L	12.0	-64.5	1018	UC_PF	(Poggemann et al. 2018)
MD99_2198	Atlantic	D&H&L	12.1	-61.2	1330	DC_HHAA	(Pahnke et al. 2008)
OCE326_GGC6/ODP1063	Atlantic	D&H&L	33.7	-57.6	4563	C_PF&DC_HHAA&FD&UC_PF	(Böhm et al. 2015)(Roberts et al. 2010)
ODP_925	Atlantic	D&H&L	4.2	-43.5	3041	UC_PF	(Howe et al. 2016c)(Howe et al. 2016a)
ODP_929	Atlantic	D&H&L	6.0	-43.7	4360	UC_PF	(Howe et al. 2016c)(Howe et al. 2016a) (Howe & Piotrowski 2017)
ODP_980	Atlantic	D&H&L	55.5	-14.7	2168	FD&UC_PF	(Crocker et al. 2016)
SU90_03	Atlantic	D&H&L	40.0	-32.0	2480	UC_PF	(Howe et al. 2016c)(Howe et al. 2016a)
VM12_107	Atlantic	D&H&L	11.3	-66.6	1079	FD	(Xie et al. 2014)
GeoB3603_2	Atlantic/Southern	D&H&L	-34.9	17.6	2840	DC_HHAA&FD	(Wei et al. 2016)
MD02_2594	Atlantic/Southern	D&H&L	-34.7	17.3	2440	DC_HHAA&UC_PF	(Wei et al. 2016)
MD07_3076	Atlantic/Southern	D&H&L	-44.1	-14.2	3786	C_BF&FD	(Skinner et al. 2013)
ODP_1087	Atlantic/Southern	D&H&L	-31.5	15.3	1372	UC_PF	(Hu et al. 2016a)
ODP_1088	Atlantic/Southern	D&H&L	-41.1	13.6	2082	UC_PF	(Howe et al. 2016a)(Hu et al. 2016a)
ODP_1089	Atlantic/Southern	D&H&L	-40.9	9.9	4620	DC_HHAA	(Lippold et al. 2016)
RC11_83	Atlantic/Southern	D&H&L	-41.1	9.7	4718	DC_HHAA	(Piotrowski et al. 2004)(Rutberg et al. 2000a)
TNO57_21	Atlantic/Southern	D&H&L	-41.1	7.9	4981	C_PF&CS_PF&DC_HHAA&UC_PF	(Piotrowski et al. 2005)(Piotrowski et al. 2012)

MD77_176	Indian	D&H&L	14.5	93.1	1375	UC_PF	(Yu et al. 2018)
ODP_758	Indian	D&H&L	5.4	90.4	2925	C_PF&NDC_AA&UC_PF	(Burton & Vance 2000)(Gourlan et al. 2010)
SK129_CR2	Indian	D&H&L	3.0	76.0	3800	DC_HHAA&UC_PF	(Wilson et al. 2015)
WIND_28K	Indian	D&H&L	-10.2	51.8	4147	DC_HHAA&NDC_HHAA&UC_PF	(Wilson et al. 2012)
EW0408_85JC/IODP_U1419	Pacific	D&H&L	59.6	-144.2	682	NDC_HHAA	(Du et al. 2018)
EW0408_87JC/IODP_U1418	Pacific	D&H&L	58.8	-144.5	3680	NDC_HHAA	(Du et al. 2018)
MD01_2385	Pacific	D&H&L	-0.2	134.2	2602	C_PF&UC_PF	(Wu et al. 2017)
MV99_MC19/GC31/PC08	Pacific	D&H&L	23.5	-111.6	705	FD	(Basak et al. 2010)
ODP_1240	Pacific	D&H&L	0.0	-86.5	2921	C_PF	(Pena et al. 2013)
ODP_1241	Pacific	D&H&L	5.8	-86.4	2027	UC_PF	(Hu et al. 2016b)(Hu & Piotrowski 2018)
V21_30	Pacific	D&H&L	-1.2	-89.7	617	UC_PF	(Hu et al. 2016b)(Hu & Piotrowski 2018)
V28_239	Pacific	D&H&L	3.3	159.2	3490	UC_PF	(Hu et al. 2016b)(Hu & Piotrowski 2018)
CHAT_10K	Pacific/Southern	D&H&L	-40.0	180.0	3003	UC_PF	(Noble et al. 2013)
CHAT_16K	Pacific/Southern	D&H&L	-42.5	-178.5	1408	UC_PF	(Hu & Piotrowski 2018)(Noble et al. 2013)
CHAT_5K	Pacific/Southern	D&H&L	-40.8	-171.5	4240	UC_PF	(Hu et al. 2016a)(Noble et al. 2013)
DSDP_594	Pacific/Southern	D&H&L	-45.5	174.9	1204	NDC_AA	(Cogez et al. 2015)
ELT11_002_PC	Pacific/Southern	D&H&L	-56.1	-115.1	3109	UC_PF	(Basak et al. 2018)
PS75/056_1	Pacific/Southern	D&H&L	-55.2	-114.8	3581	FD	(Basak et al. 2018)
PS75/059_2	Pacific/Southern	D&H&L	-54.2	-125.4	3613	FD&UC_PF	(Basak et al. 2018)

PS75/073_2	Pacific/Southern	D&H&L	-57.2	-151.6	3234	FD&UC_PF	(Basak et al. 2018)
SO136_38	Pacific/Southern	D&H&L	-50.2	175.3	1359	UC_PF	(Hu et al. 2016b)(Hu & Piotrowski 2018)
Y9	Pacific/Southern	D&H&L	-48.2	177.3	1267	UC_PF	(Hu et al. 2016b)(Hu et al. 2016a)
BOFS_28K	Atlantic	H	24.6	-22.8	4900	UC_PF	(Howe et al. 2017)
BOFS_32K	Atlantic	H	22.5	-22.0	4500	UC_PF	(Howe et al. 2017)
KNR140_2_21GGC	Atlantic	H	28.2	-74.4	4705	DC_HHAA	(Gutjahr et al. 2008)
KNR140_2_22JPC	Atlantic	H	28.2	-74.4	4712	DC_HHAA	(Gutjahr et al. 2008)
KNR140_2_28GGC	Atlantic	H	30.1	-73.8	4211	DC_HHAA	(Gutjahr et al. 2008)
KNR140_2_29GGC	Atlantic	H	30.0	-73.6	3978	DC_HHAA	(Gutjahr et al. 2008)
KNR140_2_30GGC	Atlantic	H	30.7	-74.5	3433	DC_HHAA	(Gutjahr et al. 2008)
KNR140_2_32GGC	Atlantic	H	30.8	-74.8	3615	DC_HHAA	(Gutjahr et al. 2008)
KNR166_2_31JPC	Atlantic	H	24.2	-83.3	751	DC_HHAA	(Xie et al. 2012)
MD01_2454	Atlantic	H	55.5	-15.7	747	CR	(Colin et al. 2010)
MSM5/5_712	Atlantic	H	78.9	6.8	1491	DC_HHAA	(Werner et al. 2014)
NESM_1.1_1.4	Atlantic	H	38.9	-61.0	1176	CR	(Wilson et al. 2014)
V22_197	Atlantic	H	14.2	-18.6	3170	UC_PF	(Howe et al. 2017)
V14_65	Atlantic/Southern	H	-41.1	7.8	4825	DC_HHAA	(Piotrowski et al. 2008)
MD01_2378	Indian	H	-13.1	121.8	1783	C_PF	(Stumpf et al. 2015)
BNFC_43_PG3	Pacific	H	10.5	-109.0	2874	UC_PF	(Hu et al. 2016b)

ODP_1017	Pacific	H	34.5	-121.1	955	FD	(Murphy & Thomas 2010)
ODP_806	Pacific	H	0.3	159.4	2521	NDC_AA	(Cogez et al. 2015)
ODP_893	Pacific	H	34.3	-120.0	576	FD	(Murphy & Thomas 2010)
RC10_114	Pacific	H	-11.2	-162.9	2791	UC_PF	(Hu et al. 2016b)
RC10_141	Pacific	H	-1.1	156.3	1904	UC_PF	(Hu et al. 2016b)
RC10_143	Pacific	H	-0.3	154.0	3074	UC_PF	(Hu et al. 2016b)
RC10_144	Pacific	H	0.0	152.9	4191	UC_PF	(Hu et al. 2016b)
RC10_163	Pacific	H	32.7	157.5	3550	UC_PF	(Hu et al. 2016b)
RC13_137	Pacific	H	0.9	-96.0	3436	UC_PF	(Hu et al. 2016b)
RC13_81	Pacific	H	-19.0	-124.2	3751	UC_PF	(Hu et al. 2016b)
RC17_178	Pacific	H	1.7	159.4	2591	UC_PF	(Hu et al. 2016b)
V24_148	Pacific	H	-0.8	157.4	1906	UC_PF	(Hu et al. 2016b)
V24_149	Pacific	H	-1.7	157.5	1659	UC_PF	(Hu et al. 2016b)
V24_150	Pacific	H	-2.2	155.7	1849	UC_PF	(Hu et al. 2016b)
V28_168	Pacific	H	13.5	-119.7	545	UC_PF	(Hu et al. 2016b)
V28_294	Pacific	H	28.4	140.0	2308	UC_PF	(Hu et al. 2016b)
V32_130	Pacific	H	35.3	171.9	1193	UC_PF	(Hu et al. 2016b)
DSDP_593	Pacific/Southern	H	-40.5	167.7	1068	NDC_AA	(Cogez et al. 2015)
RC15_65	Pacific/Southern	H	-53.1	-79.0	4111	UC_PF	(Hu et al. 2016b)

RC17_213	Pacific/Southern	H	-51.6	-85.0	4455	UC_PF	(Hu et al. 2016b)
V18_68	Pacific/Southern	H	-54.6	-77.9	3982	UC_PF	(Hu et al. 2016b)
KNR140_2_31GGC	Atlantic	H&L	30.9	-74.5	3410	DC_HHAA	(Gutjahr et al. 2008)
M39058	Atlantic	H&L	39.0	-10.7	1974	DC_HHAA	(Stumpf et al. 2010)
MD96_2085	Atlantic	H&L	-29.7	12.9	3001	UC_PF	(Howe et al. 2016a)
MD96_2086	Atlantic	H&L	-25.8	12.1	3606	DC_HHAA&UC_PF	(Bayon et al. 2002)(Howe et al. 2016a)
MD96_2098	Atlantic	H&L	-25.6	12.6	2910	UC_PF	(Howe et al. 2016a)
Me68_89	Atlantic	H&L	47.4	-9.6	4260	NDC_HHAA	(Blaser et al. 2019)
Me68_91	Atlantic	H&L	47.4	-19.6	4470	NDC_HHAA	(Blaser et al. 2019)
ODP_1061	Atlantic	H&L	29.6	-73.6	4126	C_PF&NDC_HHAA&UC_PF	(Pöppelmeier et al. 2018)(Roberts et al. 2010)
ODP_659	Atlantic	H&L	18.1	-21.0	3070	UC_PF	(Howe et al. 2017)
ODP_668	Atlantic	H&L	4.8	-20.9	2694	UC_PF	(Howe et al. 2016a)
ODP_928	Atlantic	H&L	5.8	-43.7	4015	UC_PF	(Howe et al. 2016a)(Howe et al. 2017)
Po08_23	Atlantic	H&L	47.4	-19.5	3900	NDC_HHAA	(Blaser et al. 2019)
RC13_228	Atlantic	H&L	-22.3	11.2	3204	UC_PF	(Howe et al. 2016a)
RC13_229	Atlantic	H&L	-25.5	11.3	4191	UC_PF	(Howe et al. 2016a)
RC24_10	Atlantic	H&L	-2.2	-11.3	3450	DC_HHAA	(Piotrowski et al. 2008)
SGOC_coral	Atlantic	H&L	35.3	-6.8	538	CR	(Dubois-Dauphin et al. 2016)
V22_174	Atlantic	H&L	-10.1	-12.8	2630	DC_HHAA&UC_PF	(Howe et al. 2016a) (Piotrowski et al. 2008)

V22_175	Atlantic	H&L	-8.8	-14.3	2950	DC_HHAA	(Piotrowski et al. 2008)
V23_100	Atlantic	H&L	22.7	-21.3	4580	UC_PF	(Howe et al. 2017)
CH115_70	Atlantic/Southern	H&L	-30.0	-36.0	2340	UC_PF	(Howe et al. 2016a)
GeoB3808_6	Atlantic/Southern	H&L	-30.8	-14.7	3213	DC_HHAA	(Jonkers et al. 2015)
RC11_86	Atlantic/Southern	H&L	-35.8	18.5	2829	UC_PF	(Howe et al. 2016a)
RC12_267	Atlantic/Southern	H&L	-38.7	-25.8	4144	UC_PF	(Howe et al. 2016a)
RC12_294	Atlantic/Southern	H&L	-37.3	-10.1	3308	UC_PF	(Howe et al. 2016a)
RC13_253	Atlantic/Southern	H&L	-46.6	7.6	2494	UC_PF	(Howe et al. 2016a)
RC13_254	Atlantic/Southern	H&L	-48.5	5.1	3636	DC_HHAA	(Piotrowski et al. 2008)
RC13_259	Atlantic/Southern	H&L	-53.8	-4.9	2677	DC_HHAA	(Piotrowski et al. 2008)
RC13_273	Atlantic/Southern	H&L	-55.1	11.6	4967	DC_HHAA	(Piotrowski et al. 2008)
RC15_94	Atlantic/Southern	H&L	-43.0	-20.9	3762	UC_PF	(Howe et al. 2016a)
TNO57_23	Atlantic/Southern	H&L	-41.0	13.0	2104	DC_HHAA	(Piotrowski et al. 2008)
TNO57_6PC	Atlantic/Southern	H&L	-42.9	8.9	3750	DC_HHAA	(Piotrowski et al. 2004)(Rutberg et al. 2000a)
TTN057_6_PC4	Atlantic/Southern	H&L	-42.9	8.6	3702	UC_PF	(Howe et al. 2016a)
RC12_339	Indian	H&L	9.1	90.0	3010	C_PF	(Stoll et al. 2007)
RC12_341	Indian	H&L	13.1	89.6	2988	C_PF	(Stoll et al. 2007)
RC12_343	Indian	H&L	15.2	90.6	2666	C_PF	(Stoll et al. 2007)
SO93_126KL	Indian	H&L	20.0	90.0	1253	C_PF	(Stoll et al. 2007)

V29_15	Indian	H&L	12.0	88.7	3173	C_PF	(Stoll et al. 2007)
ODP_846	Pacific	H&L	-3.1	-90.8	3296	UC_PF	(Hu et al. 2016b)(Hu & Piotrowski 2018)
ODP_849	Pacific	H&L	0.2	-110.5	3851	UC_PF	(Hu et al. 2016b)
RC10_140	Pacific	H&L	-2.7	157.0	1679	UC_PF	(Hu et al. 2016b)
RC10_174	Pacific	H&L	32.6	157.6	3191	UC_PF	(Hu et al. 2016b)
RC10_65	Pacific	H&L	0.7	-108.6	3588	UC_PF	(Hu et al. 2016b)
RC10_97	Pacific	H&L	-0.9	-134.3	4305	UC_PF	(Hu et al. 2016b)
RC11_210	Pacific	H&L	1.8	-140.1	4420	UC_PF	(Hu et al. 2016b)
RC11_230	Pacific	H&L	-8.8	-110.8	3259	UC_PF	(Hu et al. 2016b)
RC13_114	Pacific	H&L	-1.7	-103.6	3437	UC_PF	(Hu et al. 2016b)(Hu & Piotrowski 2018)
RC13_120	Pacific	H&L	3.8	-107.2	3753	UC_PF	(Hu et al. 2016b)
RC17_177	Pacific	H&L	1.8	159.4	2600	UC_PF	(Hu et al. 2016b)
RC23_50BX	Pacific	H&L	1.0	-104.4	3552	UC_PF	(Hu et al. 2016b)
RC9_124	Pacific	H&L	-28.8	172.6	2540	UC_PF	(Hu et al. 2016b)
V17_42	Pacific	H&L	3.5	-81.2	1814	UC_PF	(Hu et al. 2016b)
V19_25	Pacific	H&L	2.5	-81.7	2404	UC_PF	(Hu et al. 2016b)
V19_27	Pacific	H&L	-0.5	-82.1	1373	UC_PF	(Hu et al. 2016b)
V19_30	Pacific	H&L	-3.4	-83.5	3091	UC_PF	(Hu et al. 2016b)
V19_53	Pacific	H&L	-17.0	-113.5	3058	UC_PF	(Hu et al. 2016b)

V19_55	Pacific	H&L	-17.0	-114.2	3177	UC_PF	(Hu et al. 2016b)
V20_103	Pacific	H&L	34.0	-177.8	3442	UC_PF	(Hu et al. 2016b)
V20_119	Pacific	H&L	48.0	168.8	2739	UC_PF	(Hu et al. 2016b)
V21_29	Pacific	H&L	1.0	-89.4	712	UC_PF	(Hu et al. 2016b)
V21_59	Pacific	H&L	20.9	-158.1	2992	UC_PF	(Hu et al. 2016b)
V24_109	Pacific	H&L	0.4	158.8	2367	UC_PF	(Hu et al. 2016b)
V28_179	Pacific	H&L	4.6	-139.6	4502	UC_PF	(Hu et al. 2016b)
V28_203	Pacific	H&L	1.0	-179.4	3243	UC_PF	(Hu et al. 2016b)
V28_235	Pacific	H&L	-5.5	160.5	1746	UC_PF	(Hu et al. 2016b)
V28_238	Pacific	H&L	1.0	160.5	3120	UC_PF	(Hu et al. 2016b)
V28_255	Pacific	H&L	20.1	142.5	3261	UC_PF	(Hu et al. 2016b)
ODP_1123	Pacific/Southern	H&L	-41.8	-171.5	3290	UC_PF	(Elderfield et al. 2012)
RC12_225	Pacific/Southern	H&L	-53.7	-123.1	2964	UC_PF	(Hu et al. 2016b)
RC9_126	Pacific/Southern	H&L	-33.2	168.7	2060	UC_PF	(Hu et al. 2016b)
SO213_59_2	Pacific/Southern	H&L	-45.8	-116.9	3161	UC_PF	(Molina-Kescher et al. 2016)
ODP_1059	Atlantic	L	31.7	-75.4	2985	NDC_HHAA	(Pöppelmeier et al. 2018)
ODP_1060	Atlantic	L	30.8	-74.5	3481	NDC_HHAA	(Pöppelmeier et al. 2018)
WIND_10K	Indian	L	-29.1	47.5	2871	NDC_HHAA&UC_PF	(Wilson et al. 2012)
WIND_12K	Indian	L	-25.8	47.9	4196	NDC_HHAA&UC_PF	(Wilson et al. 2012)

WIND_24K	Indian	L	-13.1	51.3	4163	NDC_HHAA&UC_PF	(Wilson et al. 2012)
WIND_5K	Indian/Southern	L	-31.6	47.6	3684	NDC_HHAA&UC_PF	(Wilson et al. 2012)
RC10_161	Pacific	L	33.1	158.0	3587	UC_PF	(Hu et al. 2016b)
CHAT_3K	Pacific/Southern	L	-42.7	-167.5	4802	UC_PF	(Noble et al. 2013)
PS75/054_1	Pacific/Southern	L	-56.2	-115.1	4085	UC_PF	(Basak et al. 2018)
SO213_60_1	Pacific/Southern	L	-45.0	-119.6	3471	FD&UC_PF	(Molina-Kescher et al. 2016)

Table 4.S3. Authigenic ε_{Nd} time-series records and their PCs.

Site information can be found in Supplementary Table 1. The black dots indicate raw ε_{Nd} data (with 2σ=0.4) after binning into 500-year intervals. The green dots indicate imputed data (with 95% CIs). The orange ribbons indicate the PC1 components (with 95% CIs). The blue ribbons indicate the PC2 components (with 95% CIs). Station information (basin, site, latitude, longitude and depth) is also printed in the header. The x-axis is age in ka, and the y-axis is authigenic ε_{Nd}.

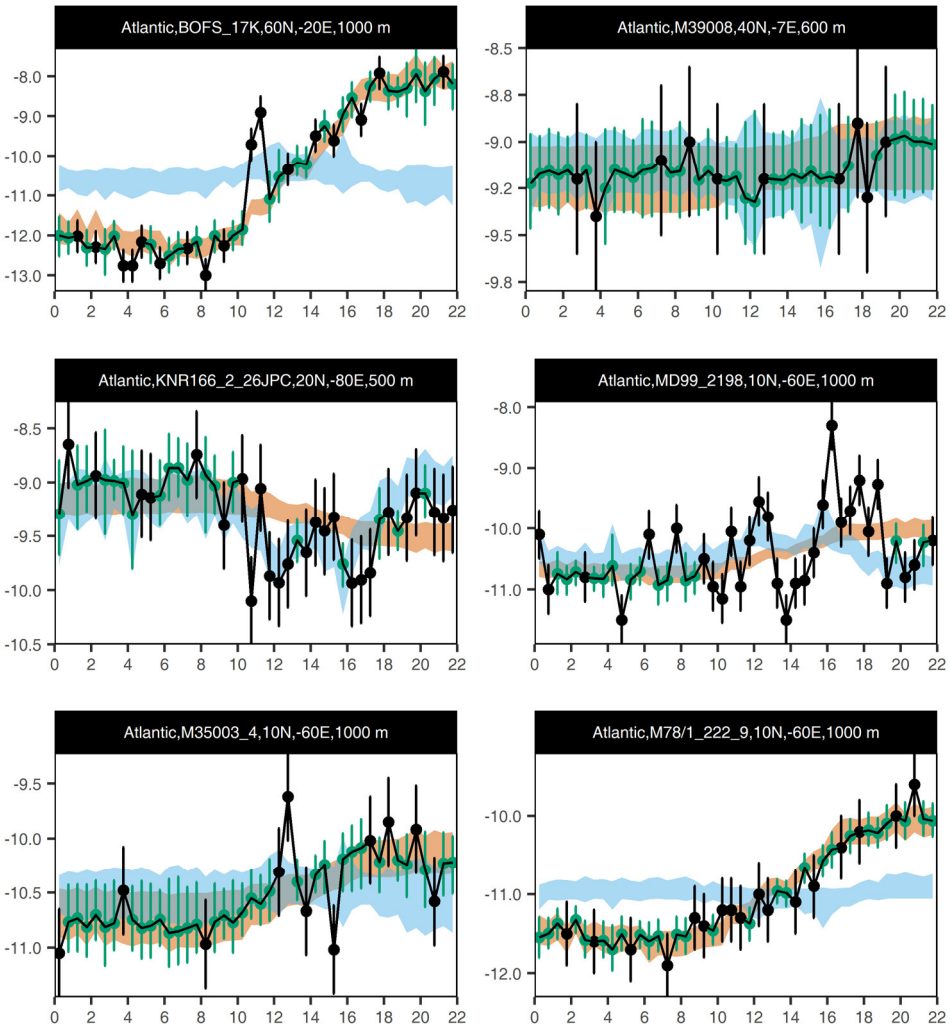

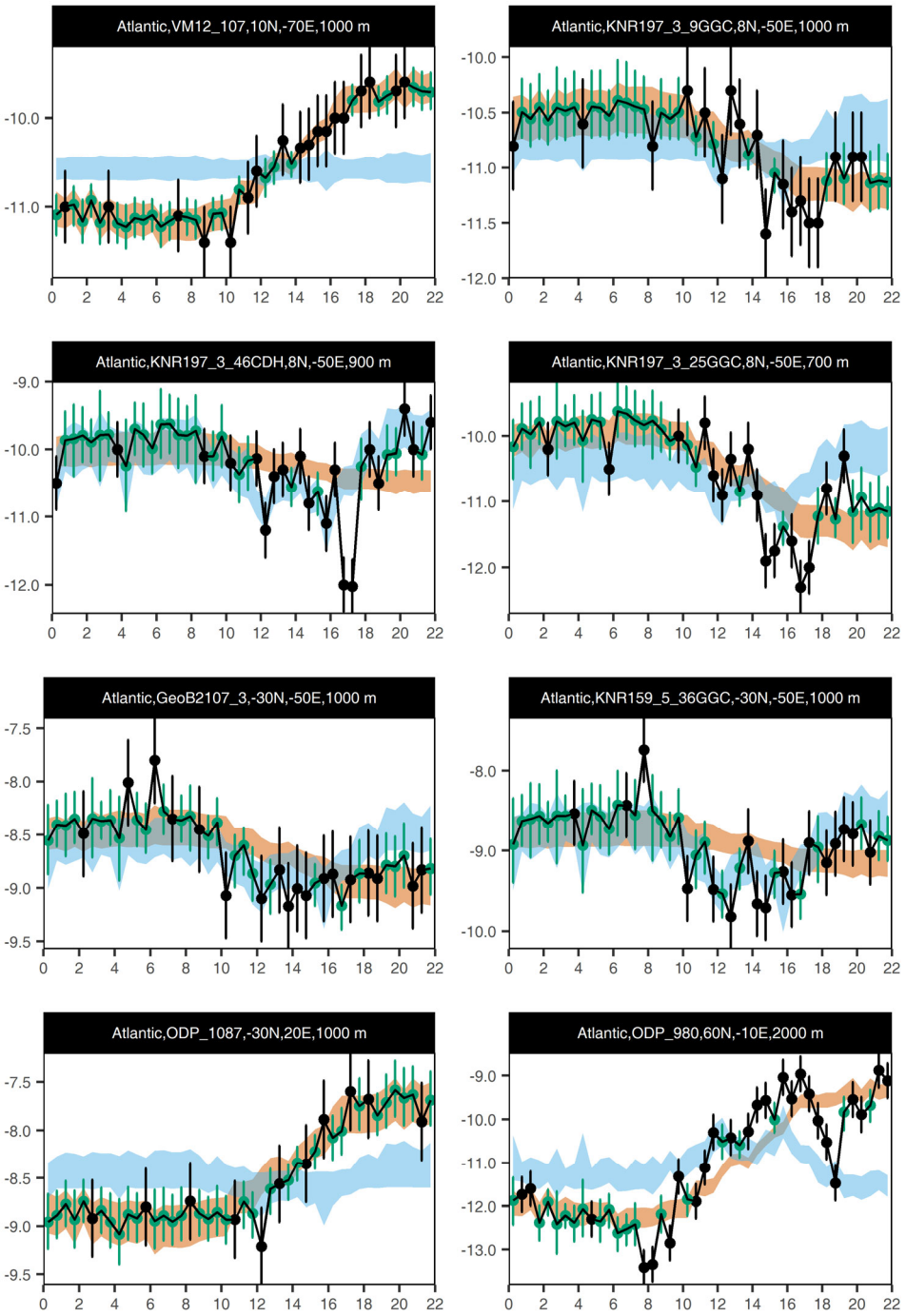
Atlantic,VM12_107,10N,-70E,1000 m
Atlantic,KNR197_3_9GGC,8N,-50E,1000 m
Atlantic,KNR197_3_46CDH,8N,-50E,900 m
Atlantic,KNR197_3_25GGC,8N,-50E,700 m
Atlantic,GeoB2107_3,-30N,-50E,1000 m
Atlantic,KNR159_5_36GGC,-30N,-50E,1000 m
Atlantic,ODP_1087,-30N,20E,1000 m
Atlantic,ODP_980,60N,-10E,2000 m

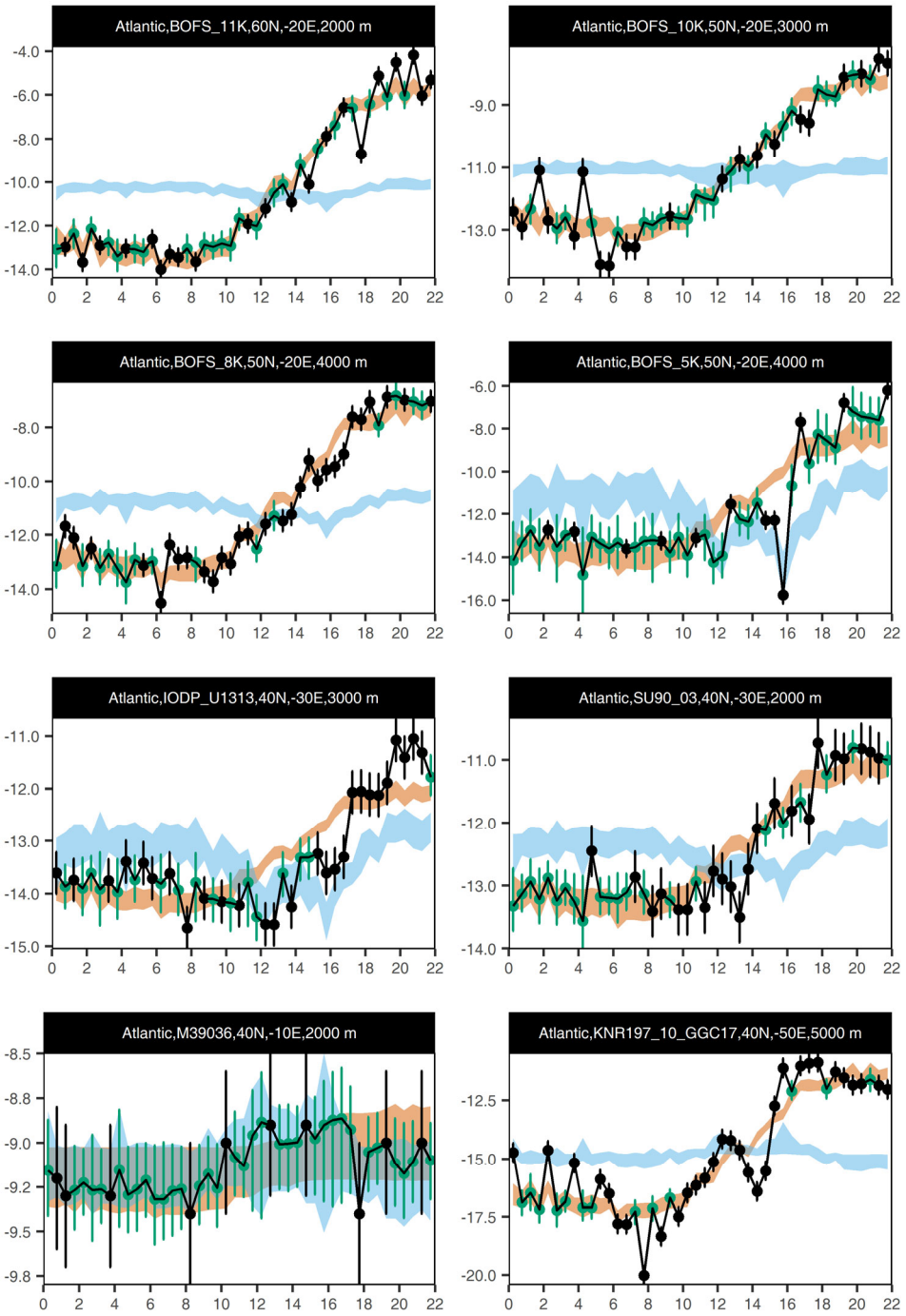
Atlantic,BOFS_11K,60N,-20E,2000 m
Atlantic,BOFS_10K,50N,-20E,3000 m
Atlantic,BOFS_8K,50N,-20E,4000 m
Atlantic,BOFS_5K,50N,-20E,4000 m
Atlantic,IODP_U1313,40N,-30E,3000 m
Atlantic,SU90_03,40N,-30E,2000 m
Atlantic,M39036,40N,-10E,2000 m
Atlantic,KNR197_10_GGC17,40N,-50E,5000 m

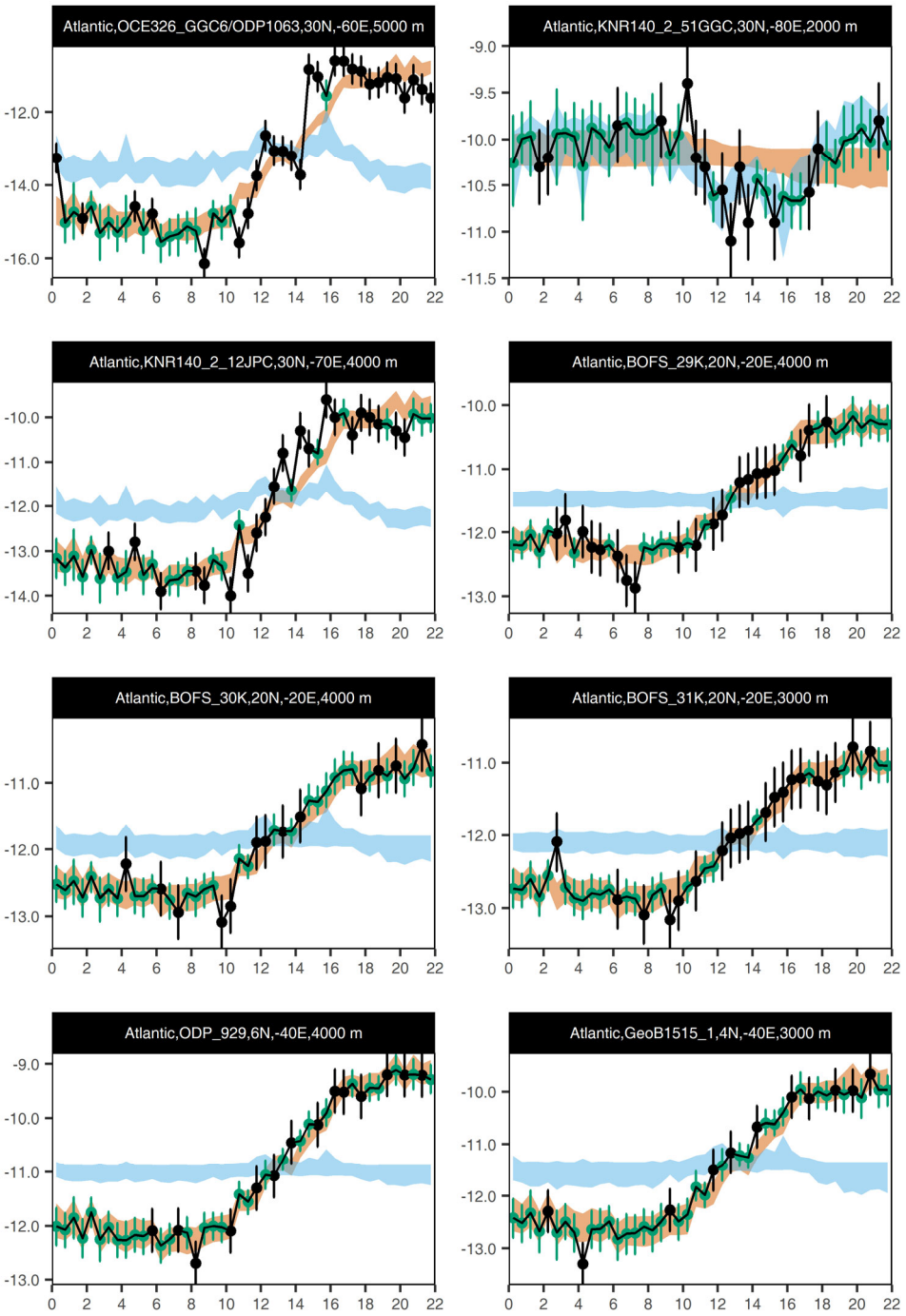
Atlantic,OCE326_GGC6/ODP1063,30N,-60E,5000 m
Atlantic,KNR140_2_51GGC,30N,-80E,2000 m
Atlantic,KNR140_2_12JPC,30N,-70E,4000 m
Atlantic,BOFS_29K,20N,-20E,4000 m
Atlantic,BOFS_30K,20N,-20E,4000 m
Atlantic,BOFS_31K,20N,-20E,3000 m
Atlantic,ODP_929,6N,-40E,4000 m
Atlantic,GeoB1515_1,4N,-40E,3000 m

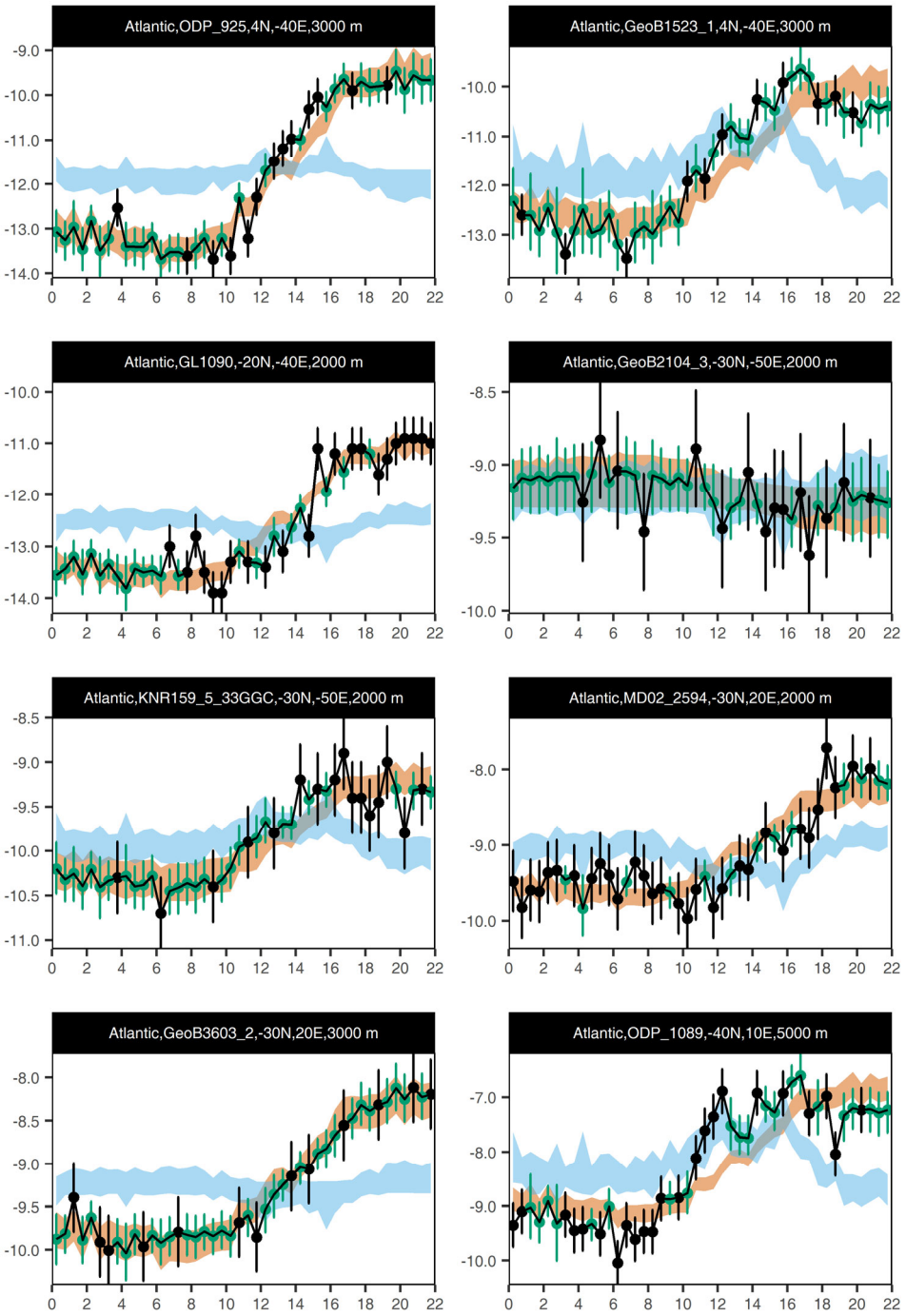
Atlantic,ODP_925,4N,-40E,3000 m
Atlantic,GeoB1523_1,4N,-40E,3000 m
Atlantic,GL1090,-20N,-40E,2000 m
Atlantic,GeoB2104_3,-30N,-50E,2000 m
Atlantic,KNR159_5_33GGC,-30N,-50E,2000 m
Atlantic,MD02_2594,-30N,20E,2000 m
Atlantic,GeoB3603_2,-30N,20E,3000 m
Atlantic,ODP_1089,-40N,10E,5000 m

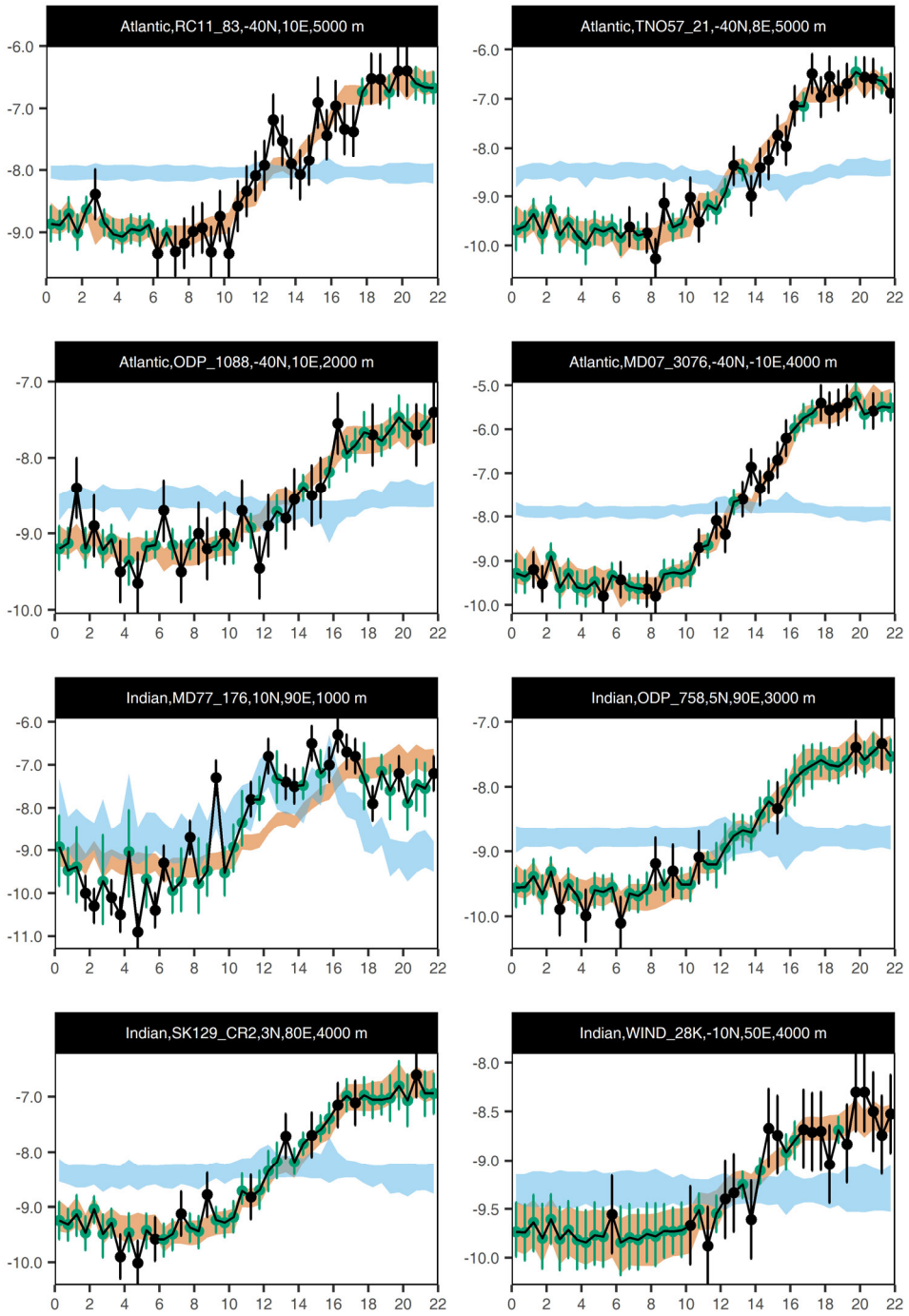
Atlantic,RC11_83,-40N,10E,5000 m
Atlantic,TNO57_21,-40N,8E,5000 m
Atlantic,ODP_1088,-40N,10E,2000 m
Atlantic,MD07_3076,-40N,-10E,4000 m
Indian,MD77_176,10N,90E,1000 m
Indian,ODP_758,5N,90E,3000 m
Indian,SK129_CR2,3N,80E,4000 m
Indian,WIND_28K,-10N,50E,4000 m

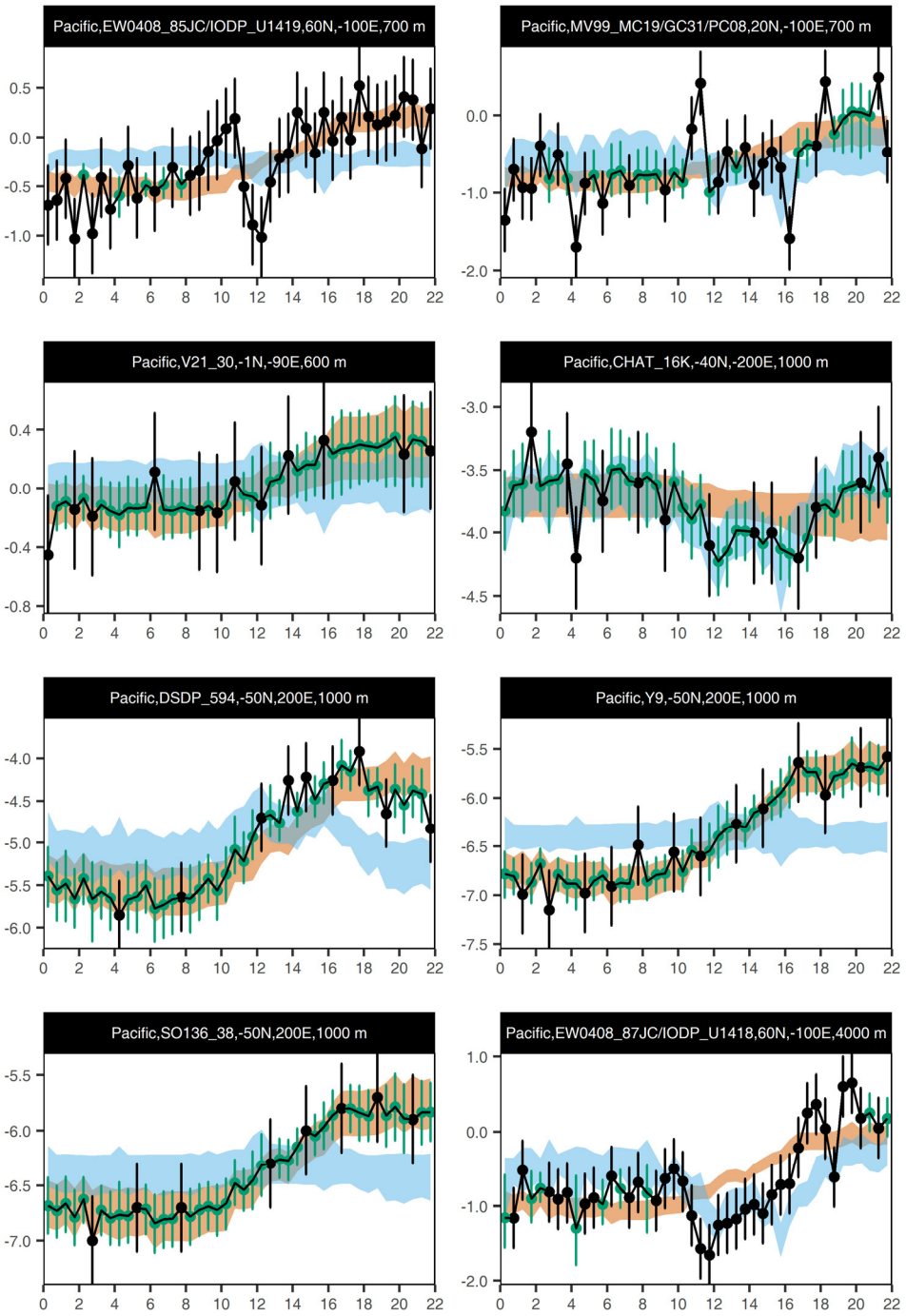
Pacific,EW0408_85JC/IODP_U1419,60N,-100E,700 m
Pacific,MV99_MC19/GC31/PC08,20N,-100E,700 m
Pacific,V21_30,-1N,-90E,600 m
Pacific,CHAT_16K,-40N,-200E,1000 m
Pacific,DSDP_594,-50N,200E,1000 m
Pacific,Y9,-50N,200E,1000 m
Pacific,SO136_38,-50N,200E,1000 m
Pacific,EW0408_87JC/IODP_U1418,60N,-100E,4000 m

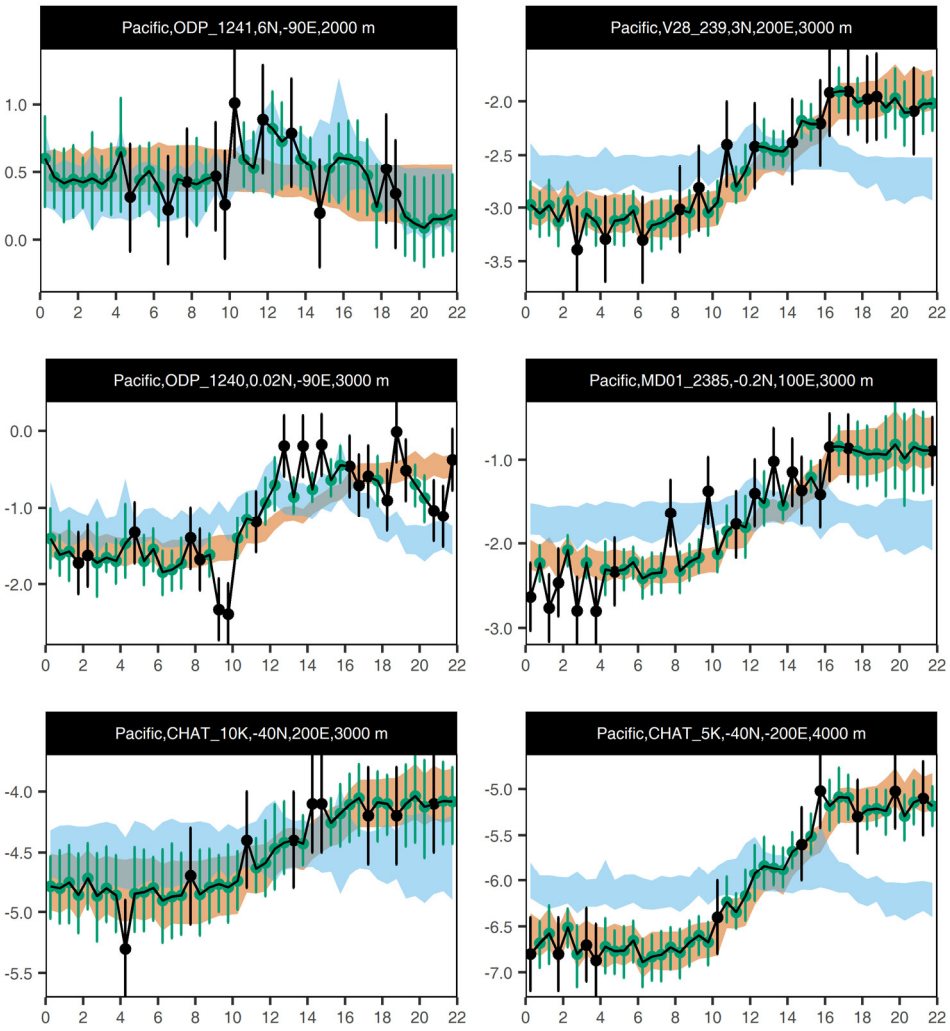
Pacific,ODP_1241,6N,-90E,2000 m
Pacific,V28_239,3N,200E,3000 m
Pacific,ODP_1240,0.02N,-90E,3000 m
Pacific,MD01_2385,-0.2N,100E,3000 m
Pacific,CHAT_10K,-40N,200E,3000 m
Pacific,CHAT_5K,-40N,-200E,4000 m

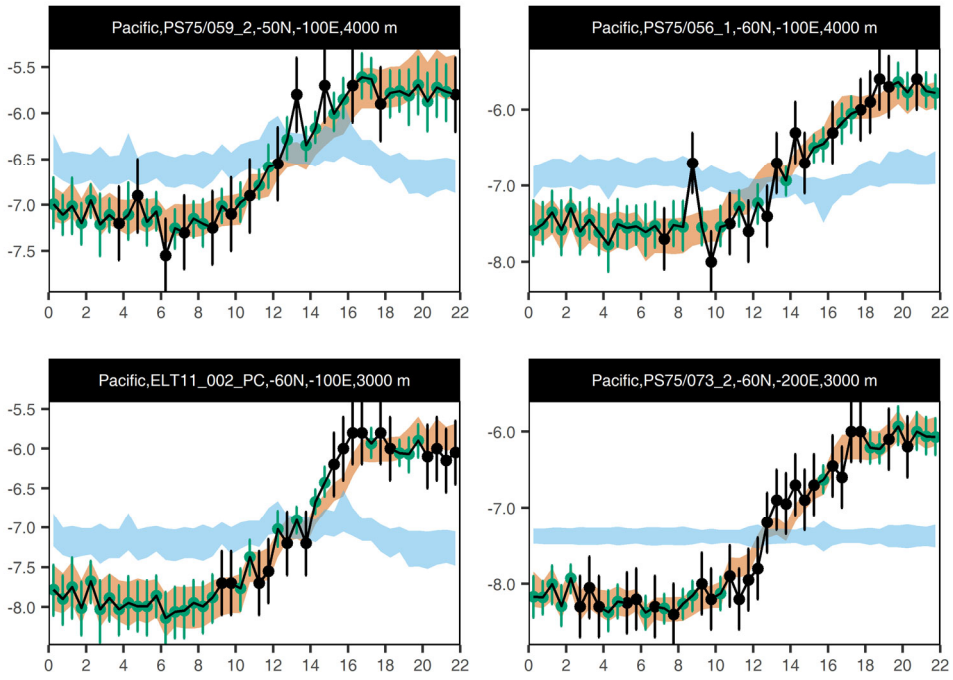
Pacific,PS75/059_2,-50N,-100E,4000 m
Pacific,PS75/056_1,-60N,-100E,4000 m
Pacific,ELT11_002_PC,-60N,-100E,3000 m
Pacific,PS75/073_2,-60N,-200E,3000 m